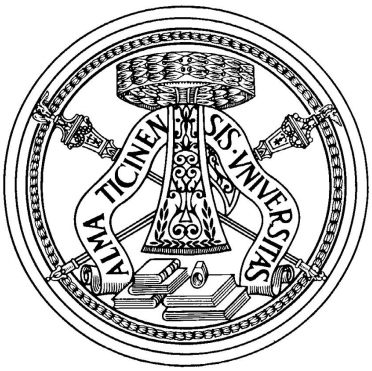

UNIVERSITÀ DEGLI STUDI DI PAVIA

Facoltà di Ingegneria

Dipartimento di Ingegneria Industriale e dell'Informazione

Dottorato di Ricerca in Ingegneria Elettronica, Informatica ed Elettrica

XXXIII Ciclo

Ph.D. Thesis of

SIMONE TACCHINI

High-gain femtosecond Yb-doped multipass amplifiers

Supervisor: Antoniangelo Agnesi

Academic Year 2019/2020

Faber est suae quisque fortunae.

To my family.

Acknowledgements

There are too many people I would like to thank for this journey: where do I start? Firstly, I would like to thank the people from Laser Lab Laboratory. Thank you Jacopo for all the time spent together, for our endless conversations, for your friendship. Thank you Federico for teaching me the laser science, for your enthusiasm and your patience. I would like to thank my supervisor, prof. Antoniangelo Agnesi for the chance to carry out a PhD in collaboration with Spectra-Physics.
A big thank to all the Spectra-Physics Ranwkeil Photonics R&D group. Thank you Annalisa and Johannes for your kind support, thank you Matthias for the tips and good music, thank you Martin for your perseverance, your motivation and your passion. You have helped me a lot and encouraged me in every way. Thank you Juerg for giving me the possibility to work in your group. You have showed me what does it mean to work in a real company.
Thank to my parents, who have always been supportive of my choices in good times and bad times (like the *Led Zeppelin* song). Finally, thank to my lifetime friends: Matteo, Lorenzo, Nicola, Francesco. Thank you for all the time spent together, thank you for the support (especially when it was given with a beer!), thank you for the laughs. This chapter of my life is closing and another is opening - I hope you will be there by my side! Thank you all.

Contents

List of Figures

List of Tables

Introduction

This PhD thesis presents research on industrial ultrafast Ytterbium doped multipass amplifiers. Multipass amplifiers are high gain amplifiers based on the idea of increasing the optical power of the incident signal by geometrically arrange more than one pass in the gain medium. The advantages of this technology are the simplicity of the construction, which defines a fixed optical path, the non requirement of components such as electro-optical modulators, the compactness, and the cost effectiveness.

Studies on semiconductor laser technology started in the early 1960s, but only in the late 1980s laser diodes have reached an acceptable level of reliability, ease of use, stability, output power and time of operation such to be used [6]. Since then, they have been exploited as pumps for solid state lasers, thus creating diode pump solid state lasers (DPSSLs), which had much higher efficiency and compactness with respect to the flash lamp pumped counterparts. On the other hand, the technology of ultrafast lasers ($\approx$ fs - ps range) hit the market at the beginning of 1990s. From then, in less than four decades DPSSLs were able to deliver high energy ultrashort pulses, which have incredibly influenced key sectors of industry such as aerospace and airborne, electronics, automotive, medical, communications and manufacture.
During this time frame the ultrafast laser industry experienced an outstanding evolution, and the tools employed in these sectors have improved their performance in terms of pulse length, average output power, peak power, stability, pulse repetition rate and beam quality near the diffraction limit.
The tight collaboration between universities, research institutions, and industries has been the key of the fast evolution obtained in this field. Moreover, the R&D laboratories have supported this growth and improvement with the study and development of new materials and their fabrication processes, novel design architecture and improved optical components, which have pushed the performance and increased the potential applications of ultrashort-pulse lasers in the real world. Nonetheless, the industry always requires innovative and improved technological solutions. The run for a laser with better characteristics, tailored for a specific task, is always on. The customization of a laser system is now a consolidated reality, opening up the improvements to important aspects such as temperature management, mechanical stability, portability, compactness, repairability and last but not least, costs per performance. As always, research is a key element, both for academy and industry, for technological advancement.
The meaning of this research is to explore and study novel solutions for multipass amplifiers delivering high performances in an industrial environment, taking advantage and continuing the collaboration between academic laboratories and industries. In

particular, this work has been carried out in collaboration with Spectra-Physics Rankweil, a world leading supplier of ultrafast lasers for scientific, medical, and industrial markets.
The scope of the collaboration was to investigate and develop multipass amplifiers to be implemented in real products for manufacturing industry with high gain, high efficiency, increased compactness, reliability and cost effective, involving and employing consolidated and novel schemes, technologies and materials. The purpose of the research was to identify and study the most promising solutions. Moreover, the study aimed to develop a numerical model to help understanding through simulations of the amplification process the experimental results.
In particular I focused my work in collaboration with Spectra-Physics on two amplifier layouts. The first layout was a Yb:YAG multipass amplifier pumped with high-power laser diodes with low brilliance to be exploited in ultrashort pulse amplification. I demonstrated its advantages and capabilities to be used as high performance and low cost amplifier in an industrial product. Moreover I investigated an unusual effect of bandwidth broadening in Yb:YAG, which counteracts a detrimental effect called gain narrowing that reduces the amplified pulse bandwidth. The related results raised interest to such an extent that Spectra-Physics Rankweil decided to set a no public disclosure of 24 months on my PhD thesis.

The second layout was a Yb:CaF_2 multipass amplifier pumped with novel laser diodes with high brilliance. These laser diodes, called Base MiMo, were developed by two companies and two research centres though EU H2020 funding. Here I demonstrated the feasibility of Base MiMos in continuous wave operation as a diode pump for pulse amplification exploiting a multipass configuration. While Base MiMos have a modest output power $\sim$ 14 W, they have a very high beam quality $M^2 < 2$. This property paves the way to a completely different way to amplify pulses and to extract the energy stored in the gain medium.

Contextually with the collaboration with Spectra-Physics, I worked on another project regarding a Yb:LLF multipass amplifier pumped with high-power laser diodes with low brilliance. The gain medium was an innovative material, an SCF Yb:LLF, grown by the micro-pulling down technique, that presents a lot of advantages to be used as gain medium for high-power amplifiers. Here are shown the preliminary results in continuous wave amplification. The research carried out in my PhD brought to published papers ([7, 8]) and may lead to potential patents.

The thesis is organized as follows. The Chapter 1 describes the history of lasers, the technological advancement of the ultrafast lasers and their market; subsequently it is explained why ultrafast lasers are useful in industry and their main applications. The Chapter 2 is devoted to the fundamentals of the laser. It starts with the incompatibility between classical and quantum physics, it follows the schematic description of an atomic system and ends with the definition the laser rate equations. The Chapter 3 describes in detail the laser oscillation, its properties and main parameters, both in continuous wave and pulsed. The Chapter 4 covers the ultrashort pulse amplification, and explains a description of the pulse amplification throughout the gain medium, with the undesired effects experienced by it. The Chapter 5 describes the Ytterbium doped materials exploited as medium, focusing on their main and interesting spectroscopic properties useful for pulse amplification. The Chapter 6, Chapter 7 and Chapter 8 regard the experimental works done in this

research. In the end, Chapter 9 draws the conclusions of this PhD thesis.

Chapter 1

History and Applications

1.1 The Birth of DPSSLs in a Nutshell

The laser set his origin at the beginning of the XX century. The journey started in 1900 when Max Planck published his work in which he deduced two fundamental concepts, the relationship between energy and the frequency of radiation and the discretized amount of energy which could be absorbed or emitted by matter, which he called *quanta*. In 1917 Albert Einstein theorized the radiation-matter process which set the foundation of laser, the stimulated emission. Besides the spontaneous emission and the absorption, which were well known, this third process described the emission of light from an excited atom though stimulation from an incoming electromagnetic wave.
Nonetheless, almost 40 year were needed to experimentally observe this phenomena. In 1951 Charles Hard Townes of Columbia University in New York conceived the MASER (acronym for microwave amplification by stimulated emission of radiation) which was a device that produced coherent electromagnetic waves through amplification by stimulated emission [9]. In 1954, collaborating with Herbert J. Zeiger and James P. Gordon, Townes demonstrated the first maser at Columbia University, which for the first time validated the process proposed by Einstein. While the exploitation of stimulated emission was developed only at microwave frequencies, at the end of 1950s was proposed the idea to operate also at optical and infrared frequencies.
In 1957, Gordon Gould coined the acronym LASER (light amplification by stimulated emission of radiation) and set the ground for a lot of fundamental photonic technologies, among them also optical amplifiers [10]. In 1958, the paper "Infrared and Optical Masers" written by Arthur Leonard Schawlow and Charles Hard Townes was published on the scientific journal Physical Review [9]. This paper opened the possibility of an optical maser and how to accomplish it. After this seminal paper, a lot of laboratories focused their research on the laser. Finally, in May 1960 Theodore Maiman from Hughes Research Laboratory in California built the first laser of mankind, exploiting a photographic flash-lamp as pump source, on a 2 cm long synthetic ruby cylinder with a diameter of 1 cm and with silver-coated surfaces. Maiman wrote a paper which was promptly published by the British Nature in July 1960, with the title "Stimulated Optical Ratiation in Ruby" [11].
The laser hit the commercial market in 1961 through companies such as Trion

Instruments Inc., Perkin-Elmer, and Spectra-Physics. The applications involved the manufacturing, like hole drilling and non-contact measurements, and medical fields, such as dermatology and ophthalmology [10]. From this moment, a lot of effort was spent to discover new materials and active ions, novel techniques and optical components, which increased and expanded the market. A very important milestone for solid state lasers was the development, by Joseph E. Geusic and Richard G. Smith at Bell Labs of the Neodymium-doped YAG laser, Nd:YAG, which assumed a lot of importance due to its unique properties [12].

A major breakthrough was reached in the mid 1970s, when Zhores I. Alferov, from Physico-Technical Institute, and Herbert Koemer, from Bell Labs, developed the first semiconductor laser successfully operated in continuous wave at room temperature in stable conditions. The key of this discovery was the double heterojunction, which lowered the threshold current density of two orders of magnitude at room temperature. Semiconductor lasers, or diode lasers, are compact, inexpensive, highly efficient electrically-driven lasers; their discovery opened up the market to new possibilities and applications. One of the most interesting is the use of the semiconductor lasers as pump source for lasers which need optical pumping, such as solid state lasers. While a solid state laser was already pumped by a diode laser in 1964, the Ur^{3+}:CaF_2, the diode was cryogenically cooled [13]. The 1970s are, in fact, the born of the diode pumped solid state lasers (DPSSLs), which could be pumped much more easily at room temperature.

A more mature semiconductor laser technology led to a lot of improvements regarding the emission wavelength, stability and cost-effectiveness, expanding their usage and the range of solid state active media that could be used as laser materials. These technological progress made the solid state laser competitive with other lasers, such as CO_2, and they developed the born of a new category of solid state lasers, the fiber laser, which will be a driving technology for the laser market.

In the 1980s and 1990s there was another breakthrough in the photonic world. It concerned the study and the generation of stable ultrafast pulses ($\approx$ ps - fs), especially in the sub-picosecond region. In 1986 Peter Moulton published a paper regarding Ti:Sapphire, a material which could sustain femtosecond pulses due to its broadband gain bandwidth [14]. The first solid state lasers able to deliver stable femtosecond pulses used a Ti:sapphire as gain medium; they exploited the passive mode-locking technique with a saturable absorber dye (by Ishida et al., 1990, [15]), and the Kerr Lens mode-locking technique (Spence et al., 1991, [16]). While these techniques aroused a lot of interest around the topic, they didn't provide a self-starting, reliable, stable, and simple laser for the generation of ultrashort pulses.

The solution came in 1992 through the development of a new type of saturable absorber made in semiconductor technology, the semiconductor saturable absorber mirror (SESAM). With respect to other saturable absorbers, a SESAM has several advantages: it generates more stable femtosecond pulses, it can be exploited for reliable self-starting mode locking, it reduces the complexity of the cavity and can be adapted to an existent one, it saturates with respect to the incidence fluence and thus can be used to scale up the average output power, and more importantly it is made in semiconductor technology, which means that its properties can be modified accordingly to the materials used to build it [17, 18].

The next significant breakthrough in the femtosecond pulse generation was the

Figure 1.1: Spirit: A Spectra-Physics High-Power Femtosecond Laser [21].

commercialization of ultrashort DPSSLs exploiting Ytterbium doped materials. While their potential was known since the 1970s, it is only in the early 1990s that the trivalent Ytterbium ions could be exploited. Due to their quasi-three level nature and spectroscopic properties, they needed a very specific pump source. It had to possess an high spectral radiance, to reach the desired level of population inversion, and an emission linewidth capable to match the narrowband spectral region of absorption. This requirement was satisfied when the semiconductor technology found a way to develop laser diodes at 900-990 nm with that given properties, which were made by InGaAs quantum wells.
Until then the most famous and exploited ion was the Neodymium. The Ytterbium ions are so interesting because they have a prolonged energy storage lifetime, much longer than the Neodymium ion; they also possess a reduced quantum defect with respect to Neodymium, which means higher efficiency and less thermal load; they have relatively broad amplification bandwidth, which could sustain a pulse duration from hundreds to few tens of femtoseconds [19, 20].
Since then, technology advancements in laser and amplification design, development in semiconductor lasers and new materials have established Yb-doped femtosecond DPSS sources as a reliable choice for numerous applications.
One of the major breakthrough in amplifier architecture happened in mid 1980s, when Strickland and Mourou invented a technique to efficiently amplify ultrashort laser pulses avoiding optical damages and nonlinear processes [22]. This technique, which is nowadays widely used, is called *chirped pulse amplification* (CPA) and exploits temporal stretchers to reduce the high peak intensity of the ultrashort pulses before entering the gain medium of the amplifier, and successively temporally recompress the pulses after amplification. CPA technique permits to increase the pulse peak power from Kilowatts to Gigawatts without compromising the structural integrity of the amplifier and other optical components.
Today, CPA technique is employed in the majority of high-power femtosecond lasers. These systems are composed by several parts, generally exploiting an architecture called *master-oscillator power amplifier* (MOPA), where the energy of a low-power femtosecond oscillator is increased by adding one or more amplifying stages to the laser system.

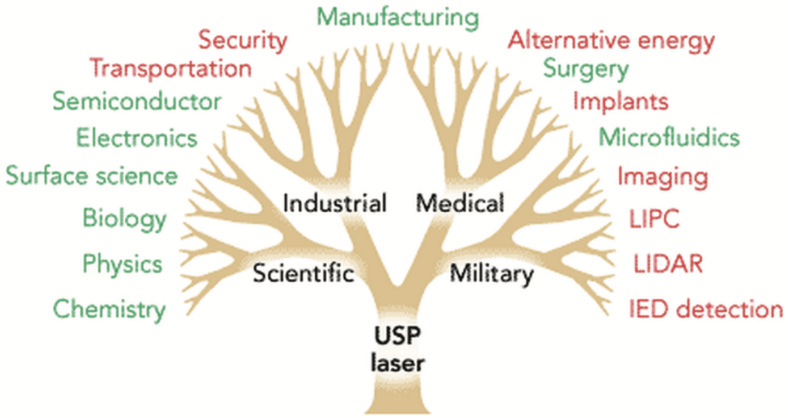

Figure 1.2: Opportunity tree: it shows some areas where ultrafast lasers are in use or will play a role in the future. In green are shown the segments where femtosecond lasers are currently used; in red the segments of likely employment in the next future [24].

In Spectra-Physics portfolio, one of the most important high-power ultrashort lasers is the *Spirit*. It exploits Ytterbium ions thanks to their unique spectroscopic properties. With a diffraction limited beam quality, it has an output power up to 140 W at 1030 nm, with a pulse duration lower than 400 fs, a variable pulse repetition rate from 100 kHz to 30 MHz, and a pulse energy up to 600 μJ. Thanks to these characteristics, it provides impressive versatility and performance in a variety of applications: high-precision industrial manufacturing for micromachining of polymers, thin metals, sapphire, polycrystalline diamond, and other materials, but also in many other applications.

1.2 Importance of Ultrashort Lasers and Their Applications

From previous section it should be evident that ultrashort pulse laser systems have constantly and rapidly progressed during the past decades. A report on ultrafast lasers from BCC Research, a market research company that investigates changes driven by science and technology, shows that the ultrafast lasers global market is expected to grow from 2.7 billion dollars in 2017 to 8.1 billion in 2022, by a compound annual growth rate (CAGR) of 24.7% from 2017 through out 2022 [23]. The ultrafast laser market growth is primarily driven by the increasing demand for material processing and semiconductor industries that in turn find their applications in several end-user industries like automotive, communication and technology, consumer electronics as well as healthcare.
Moreover, advances in the ultrafast laser market are projected to open new avenues of applications outside its core application of micromachining [25]. Most of these applications take advantage of the interaction between femtosecond pulses and matter, which is completely different with respect to longer pulses in the picosecond or nanosecond range [26]. The unique properties provided by ultrashort lasers paved

the way to a wide use in fundamental research and practical applications, which are briefly explained in the following sections.

1.2.1 Scientific Applications

Ultrafast microscopy is a very powerful tool used in several branches of science, from chemistry to biology, astrophysics, and biomedicine. The idea is to exploit the main characteristics of ultrashort pulses: a very high peak power, a moderate average power, a short pulse duration and a broad bandwidth. These unique properties gave access to nonlinear processes, such as high harmonic generation and four wave mixing. Nonlinear optics in microscopy makes possible to obtain spatially resolved spectroscopic measurements, providing information both in time and frequency domain. This technique is called ultrafast laser spectroscopy, which studies the dynamics of materials at molecular level on extremely short time scales. It usually exploit a 'pump-probe' method, where a femtosecond laser is used to excite a molecule's electrons from their ground states to higher-energy excited states. Then, a probing light source and a detector are used to measure over time the absorption spectrum of the molecule. This technique is particularly useful to understand the temporal behaviour of nonradiative, short-lived species such as transition states in chemical reactions [27].

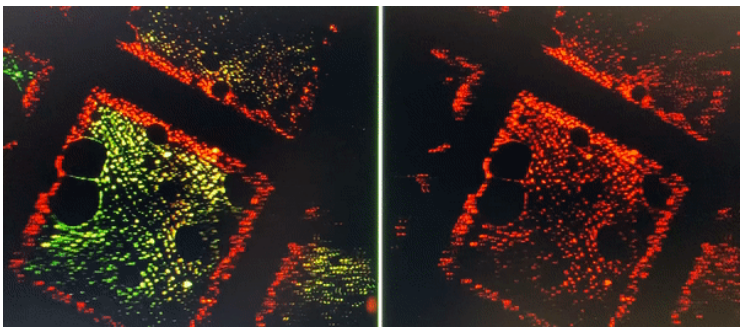

Figure 1.3: 3D reconstruction of carbon net grid with two photon fluorescence. Backscattering: red, forward scattering: green [28].

Moreover, combining this technique with angle-resolved photoemission, it permits to obtain 3D imaging in living tissue without damaging it, since the average power lower than the damage threshold. These are just few examples of the powerfulness of ultrashort pulses combined to imaging and microscopy.

1.2.2 Industrial Applications

Ultrafast lasers have a long history in industrial material processing. The physical phenomena involved during material processing, such as cutting, drilling, lapping and ablating, depend strongly on the timescale of the process itself. Due to their duration, high peak power and beam quality, femtosecond laser pulses generate an ultra high laser intensity, providing localized material ablation or modification of material properties through nonlinear multiphoton absorption. The termal effects, which are detrimental, occur when the laser pulse duration is longer than the electron-lattice relaxation time of the material. Thermal damages in material processing are given

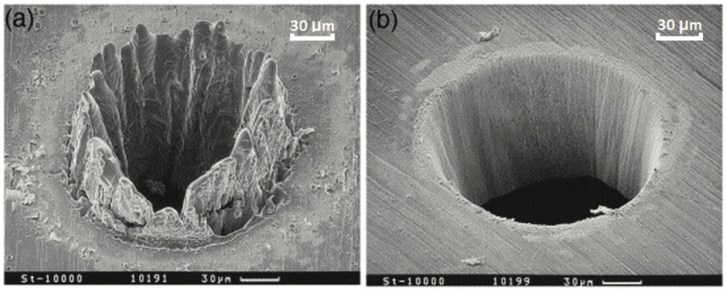

Figure 1.4: Holes drilled in 100 μm thick steel foils by ablation using laser pulses. (a) pulse duration: 3.3 ns, pulse energy: 1 mJ, fluence: 4.2 J·cm^{-2}, λ: 780 nm; (b) pulse duration: 200 fs, pulse energy: 120 μJ, fluence: 0.5 J·cm^{-2}, λ: 780 nm [30].

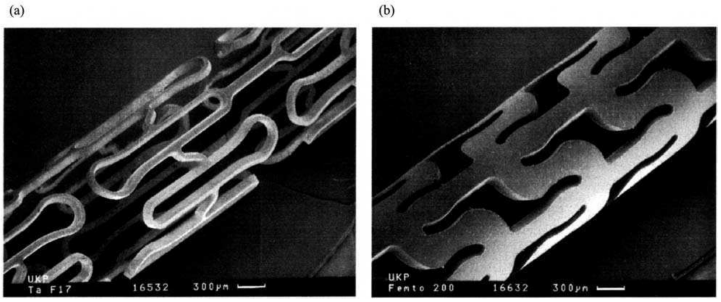

Figure 1.5: Prototypes of medical implants (stents) made of (a) metal (titanium) and (b) a bioresorbable material. In both cases the stents were structured with femtosecond laser pulses [33].

by a heat diffusion that leads to the so-called *Heat affected zone* (HAZ). The HAZ is the area of the material around the processed surface that has suffered stress and consequently alterations of its original properties [29]. Femtosecond pulses, thanks to their duration, allow to minimize the thermal diffusion and to generate a small HAZ around the processed area. Moreover, they drastically reduce the energy threshold necessary to generate an ablation with respect to nanosecond pulses. These properties permit an efficient, rapid and localized energy deposition, ensuring a clean and accurate operation.

The first usage of an ultrafast laser in material processing dates back to 1987, when Srinivasan et al., Küper and Stuke experimentally demonstrated the ablation of polymethylmethacrylate, a transparent thermoplastic, exploiting picosecond pulses from an UV laser [31, 32]. From this demonstration the involvement of ultrafast lasers in material processing drastically increased, especially from a strong research conducted since the 1990s. Ultrashort lasers have the capability to achieve a resolution lower than $\lambda/5$ of its emission wavelength. Thanks to this property, nowadays they are used as an universal tool of microfabrication and micromachining of metal, semiconductors, dielectrics, polymers and also transparent or opaque materials [26]. Ultrafast lasers are exploited in the micro texturing of hard disk drives, video heads and diamond films, preparation of silicon wafers, but also to create microstructures, such as waveguides, in gallium arsenide, lithium niobate, lithium tantalite. They are

also extremely useful in biomedical applications to manufacture stents and micro holes for patient monitoring probes, fabrication of different micro features in MEMS, or micro fluidic channels combined with optical wave guides [33].
Another industrial application of ultrafast lasers is the creation of tridimensional structures and volume processing inside transparent materials in a selective manner exploting nonlinear multiphoton absorption. In a such way it is possible for example to change the refactive index, crystallize particles, or enhance the chemical etching rate [cit]. Regarding photonics, ultrafast lasers are involved in the fabrication of optical couplers, volume Bragg gratings, diffractive lenses and so on.

1.2.3 Medical Applications

Lasers in medicine have been exploited since their commercialization in the 1960s, and they have bought great impact and influence [34]. The first laser medical treatment as been done employing a ruby laser to destroy a retinal tumor, by C.J. Campbell in 1961 [35]. Few years later, lasers were used to treat cancer skin by Goldman [36] and in cardiovascular surgery for atherosclerotic plaques by McGuff [37]. In current days, lasers have a variety of applications in numerous medical disciplines, not only as a cure but also as prevention. Dermatology, cardiology, neurosurgery, dentistry and eye surgery are only few of the branches where the properties of ultrafast lasers can be implemented being minimally invasive.

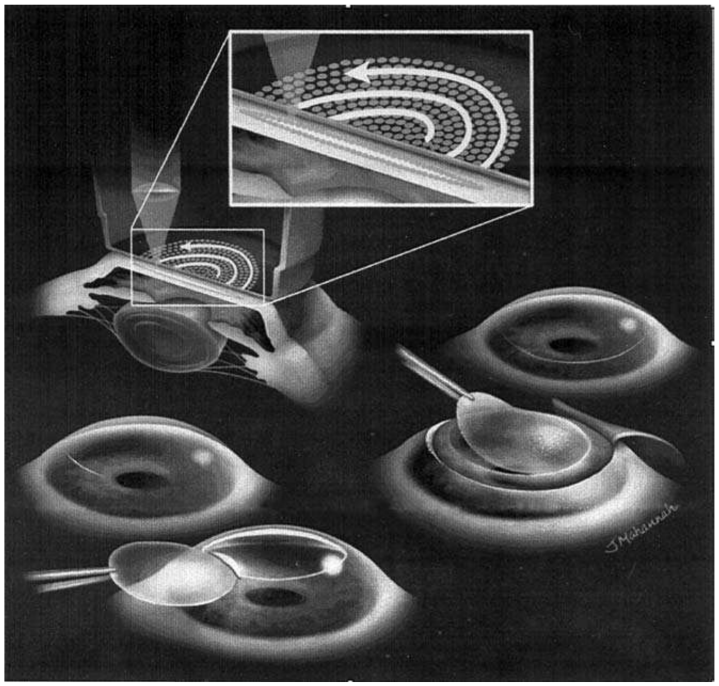

Figure 1.6: LASIK technique: stromal tissue is removed by applying two lamellar resections. The flap is opened with another resection, and the tissue is removed manually [38].

Medical applications exploit several different techniques. Multiphopton excitation is used in photodynamic therapy (PDT) which is a treatment for diseased tissue. In

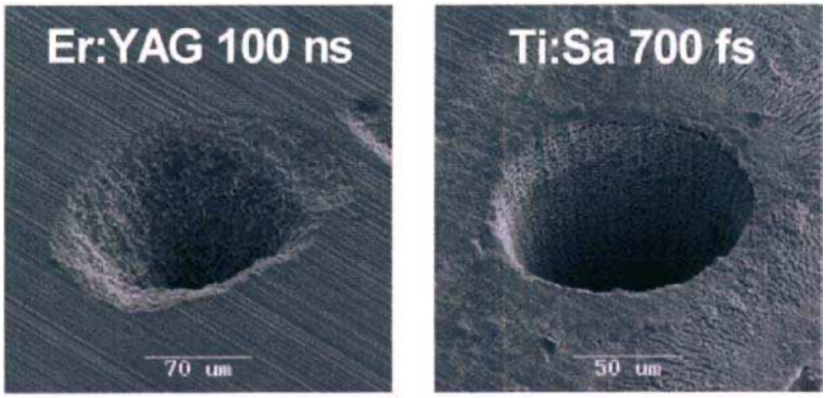

Figure 1.7: Holes drilled in a tooth, respectively with nanosecond and femtosecond pulses, showing the superior ablation quality obtained with ultrashort pulses [33].

PDT, a photosensitive agent is introduced into the afflicted area of tissue, which is then locally illuminated by a light source. This illumination photoactivates the agent, which in turn selectively destroys the diseased tissue, thereby preventing the further spread of the disease [33].

One of the most important area of the medical laser market is represented by ophthalmology. Here, ultrafast laser technology is implemented in surgical devices in cases of cataract, glaucoma, refractive errors and vitreoretinal disorders, diagnostic. The unique properties of femtosecond lasers offer high precision and minimal collateral tissue damage, exploiting soft tissue ablation. With respect to picosecond pulses, it allows to affect up to ≈ 100 time smaller tissue volume around the area of interest [38]. A radiation-matter interaction at femtosecond scale allows direct breaking of molecular bond instead of the photo-thermal processes driven by lasers with a longer time scale [33]. The first employment of femtosecond lasers in ophthalmology was for reshape the eye's cornea in order to improve visual acuity, with a technique called laser-assisted in situ keratomileusis (LASIK).

Laser dentistry is another area of medicine which has been benefited from ultrashort laser pulses. Soft and hard tissue ablation are exploited for a number of procedures such as cavity restoration, preparation and sterilization, but also dental caries removal and prevention, periodontal diseases and the treatment of oral malignancies [33]. Moreover, ultrashort lasers can be used to manufacture medical devices through micromachining, such as stents, heart valves, tridimensional ceramic structures, catheters.

Last but not least, an incredibly powerful imaging technique takes advantage of femtosecond pulses. It is called *optical coherence tomography* (OCT) and performs high-resolution cross-sectional tomographic imaging of the internal microstructure in materials and biological systems by measuring the echo time delay and magnitude of backscattered light (Huang et al., 1991, [39]). This technique provided an increased image resolution of orders of magnitude with respect to conventional ultrasound.

Figure 1.8: DIRCM device from Leonardo Company [41].

1.2.4 Military Applications

Ultrafast lasers are used in military as aircraft defence and detection. For example, an high-energy femtosecond laser is used in a device called Directional Infrared Counter Measures (DIRCM), which protects aircrafts from infrared homing missiles and from man-portable air-defense systems. Similar devices, named Laser Weapon Systems (LaWS), are used to protect ships from different targets such as drones, small ships or missiles. The inherent characteristics of laser weapons, speed of light engagement, precision targeting, rapid shot generation and tunability, offer the opportunity for expanded engagement options against a range of threats [40].
Ultrashort pulses can be useful to detect Improvise Explosive Devices (IED). These devices exploit nonlinear effects, such as Raman and Stokes scattering, to detect material explosives from a safe distance. Moreover, ultrashort laser technology can be implemented in remote sensing and rangefinding to create devices for high speed hyperspectral imaging [42].

1.3 Why Multipass Amplifiers Raise Industrial Interest?

Pulse energy is a critical parameter for most of applications which exploit ultrashort pulses. Unfortunately, the current state-of-the-art femtosecond laser oscillators cannot provide the pulse energy necessary to these applications. In order to be able to do that, the pulse energy has to be increased by using one or more laser amplifiers. There are mainly two techniques to provide high-gain amplification to pulses exploiting stimulated emission in a solid-state active medium: multipass and regenerative amplifiers.
In a multipass amplifier the incident signal pulse passes through the gain medium by a fixed number of multiple passes geometrically arranged, defined by optical components. On the other hand, a regenerative amplifier is a multipass amplifier where the gain medium is positioned in an optical resonator. The incident signal pulse is inserted by using an optical switch, generally made by an electro-optic or

acusto-optic modulator and a polarizer. The signal pulse goes through the gain medium for tens or hundreds of passes, until the majority of the energy stored in the crystal is being depleted. Then, the pulse is ejected with a second optical switch or with the same one used for coupling in. A regenerative amplifier can realize a extremely high amount of gain, and it is the best solution to efficiently amplify the femtosecond pulse energy in most cases [43]. In a matter of fact, they are leaders in the high-gain DPSS amplifiers world.
Nonetheless, while multipass amplifiers are not the most efficient way to amplify an ultrashort pulse [43] or to reach enormous amount of gain they present some characteristics which define them as an incredible feasible solution for industrial products. First of all, even though the amplification gain provided is limited with respect to regenerative amplifiers, it is still in the range of tens of dB. Moreover they do not possess any active component to insert or extract the incident signal pulse, since the beam path is determined by optics. This advantage contains the costs, reduces the complexity and the volume occupied.
In the last decades Ytterbium ions raised a lot of interest due to their spectroscopic properties. Their employment as dopant for solid state gain media became of common usage, both for lasers and amplifier systems. In particular, Yb-doped multipass amplifiers can reach tens of dB of gain. Thanks to the small quantum defect they have an high optical to optical efficiency, with a reduced thermal load, and the broad emission bandwidth sustains the amplification of ultrashort pulses. From an industrial point of view, Yb-doped multipass amplifiers can be an high gain-cost ratio solution in a complex laser system. In an amplifier chain they can be implemented as a low cost, low complexity, but still high gain amplifiers, such as boosters.

Chapter 2

Atomic Transitions

2.1 Energy Levels

In order to understand how a laser works it is necessary to know some principles about the interaction of radiation with matter [44]. Through quantum mechanics it has been proved that electrons in atomic systems occupy stationary states with fixed and discretized energy. These energy levels are called energy states and every atom has its own energy state diagram. A change of the energy state is possible, and in a first approximation it is associated with either an absorption or an emission of a photon, which has a wavelength that depends on the Bohr's frequency relation:

$$E_2 - E_1 = h\nu_{21} \tag{2.1}$$

where E_2 and E_1 are two discrete energy levels of a system, h is the Planck's constant,whose value is 6.62×10^{-34} with dimensions J·s, and ν_{21} is the photon frequency. The Bohr's relation also defines that an electromagnetic wave has to have a ν_{21} frequency to interact with this system.

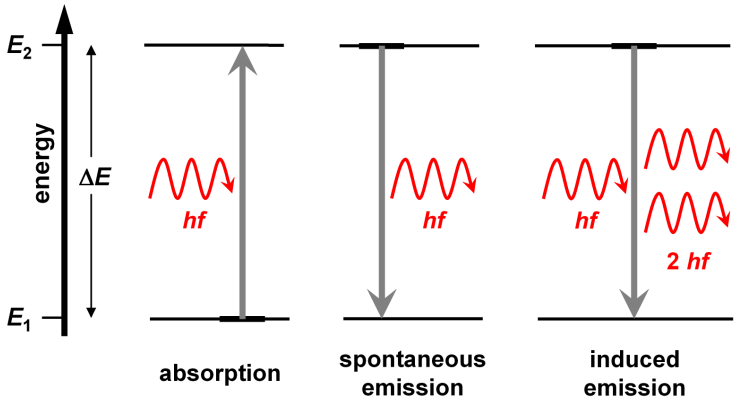

Figure 2.1: Two levels system.

As a first approximation, a solid-state material can be considered as an ensemble of simple and identical atomic systems.

The absorption and emission processes are the foundation of the laser. Nonetheless the theory behind it was not complete until Einstein combined the *Black Body*

Radiation formulated by Planck, which describes the spectral distribution of thermal radiation, and the *Boltzmann's Statistics*, which describes the electronic population of the energy states at any given temperature, to define another process called *stimulated emission*. In the following sections they will briefly discussed.

2.2 Boltzmann's Statistics

Statistical mechanics defines the electronics population of the energy levels of an atomic system at thermal equilibrium. suppose to have a two states system, when a large collection of identical atomic systems are at thermal equilibrium at temperature T, the relative energy levels population is given by the *Boltzmann's ratio*:

$$\frac{N_2}{N_1} = e^{-\frac{(E_2 - E_1)}{k_B T}} = e^{-\frac{h\nu_{21}}{k_B T}} \tag{2.2}$$

where E_1 and E_2 are the energy levels, N_1 and N_2 are the number of atoms in the respective energy levels, k_B is called *Boltzmann's constant* and its value is 1.38×10^{-23} with dimensions J/K. The lower level E_1 is also called *ground state*, whereas the higher level E_2 *upper state*.

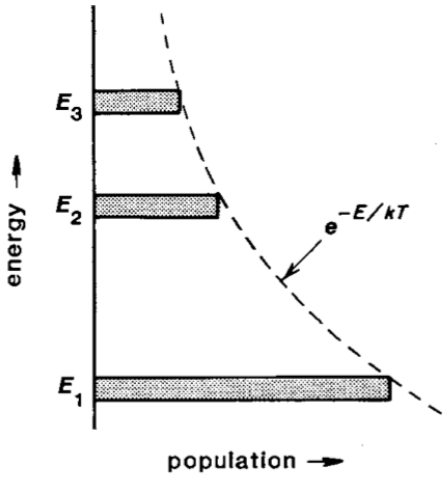

Figure 2.2: Boltzmann's statistics at thermal equilibrium [45].

When the temperature T is the absolute zero, the Boltzmann's statistics says that all the electrons lay in the ground state. At thermal equilibrium part of the electrons will be on the upper state. The ratio between the population of the two states, described by equation 2.2, will be always less than 1. That is because a state with an higher energy will be always less populated than a state with a lower energy. When the energy gap between E_1 and E_2 is considerable that at room temperature:

$$E_2 - E_1 = h\nu_{21} \gg k_B T \tag{2.3}$$

then the ratio expressed by equation 2.2 is close to zero, which means that the upper level E_2 will be almost not populated. At room temperature, $T = 300\,\mathrm{K}$, the product $k_B T \simeq 25\,\mathrm{meV}$, whereas the typical photon energy in the VIS/IR region is $E_\phi \approx 0.5 - 1\,\mathrm{eV}$. This is the case expressed in equation 2.3, and thus the ground state E_1 is nearly the only level populated.
It may happen that two or more energy states have the same energy level, in this case the energy level is called degenerate. The equation 2.2 becomes then:

$$\frac{N_2}{N_1} = \frac{g_2}{g_1}\frac{N_2'}{N_1'} = \frac{g_2}{g_1}\, e^{\dfrac{-(E_2 - E_1)}{k_B T}} \tag{2.4}$$

where g_i is called multiplicity of the i-th level, and it holds the equation $N_i = g_i N_i'$ since the degenerate states are equally populated.

2.3 Black Body Radiation

All baryonic matter which has a temperature above the absolute zero emits thermal electromagnetic radiation, which represents a conversion of the body's internal energy. Conversely, all baryonic matter absorbs electromagnetic radiation by a certain degree.

A black body is a completely opaque, non-reflective and ideal object which therefore absorbs all the electromagnetic radiation falling on it. The black body radiation, which defines a spontaneous process, is the thermal electromagnetic radiation of a black body in thermal equilibrium with its environment; it does not depend upon the material or the shape but only the equilibrium temperature of the body.

Let us suppose to have a cavity filled by an homogeneous and isotropic medium, and let it be at thermal equilibrium, at a temperature T, with the walls of the cavity. Then it is possible to represent the energy density of the electromagnetic field per unit volume introducing the energy density ρ:

$$\rho = \langle \frac{1}{2}\epsilon E^2 \rangle + \langle \frac{1}{2}\mu H^2 \rangle \tag{2.5}$$

where ϵ and μ are the dielectric permittivity and the magnetic permeability of the medium, whereas the symbols $\langle\ \rangle$ defines the energy average over a time cycle period of the radiation. There is a more interesting way to describe the energy density:

$$\rho = \int_0^\infty \rho_\nu \, d\nu \tag{2.6}$$

where $\rho_\nu\, d\nu$ defines the energy density in the $\nu + d\nu$ frequency region. Thus ρ_ν defines the energy per unit volume per unit frequency with dimensions $\mathrm{J{\cdot}s/cm^3}$.

Let us now suppose to have a rectangular cavity, with depth and height $2a$ and width L. Then, through the Maxwell's equations and the boundary conditions imposed at the wall of the cavity it is possible to determine the resonant modes

inside the cavity:

$$N_\nu = 2\frac{\frac{1}{8}\frac{4}{3}\pi\left(\frac{2\pi\nu}{c_n}\right)^3}{\frac{\pi}{2a}\frac{\pi}{2a}\frac{\pi}{L}} = \frac{8\pi\nu^3}{3c_n^3}V \tag{2.7}$$

where N_ν defines the resonant modes between 0 and ν, c_n is the velocity of light in the medium inside the cavity, and V is the volume of the cavity. Let us now define a quantity, called p_ν, the number of resonant modes per unit volume per unit frequency, similarly to what we did at equation2.6, with dimensions # of modes·s/cm^3:

$$p_\nu = \frac{1}{V}\frac{\partial N_\nu}{\partial\nu} = \frac{8\pi\nu^2}{c_n^3} \tag{2.8}$$

Once we have the quantity p_ν it is straightforward to describe ρ_ν as the multiplication of p_ν, which is the number of resonant modes per unit volume per unit frequency, and the average energy of each mode:

$$\rho_\nu = p_\nu\langle E\rangle \tag{2.9}$$

Using a classical approach through the Boltzmann's statistics the average energy of each mode can be calculated as:

$$\langle E\rangle = \frac{\int_0^\infty E\, e^{[-(E/k_BT)]}\, dE}{\int_0^\infty e^{[-(E/k_BT)]}\, dE} = k_BT \tag{2.10}$$

where k_B is the Boltzmann's constant and T is the temperature at thermal equilibrium of the cavity and the medium.
Then the energy density ρ_ν is:

$$\rho_\nu = \left(\frac{8\pi\nu^2}{c_n^3}\right)k_BT \tag{2.11}$$

This equation, which has been derived in a classical way, it is clearly wrong, and fails to adhere to the experimental results; the calculated total energy density ρ, from equation 2.6, would tend to infinite. This non agreement with reality was called *ultraviolet catastrophe*.

The problem was solved by Planck, who introduced the idea of discretized amount of energy light, a *quantum* of energy, which was proportional to the frequency ν of the electromagnetic wave. This package of energy has been called *photon* and its energy is:

$$E_\phi = h\nu \tag{2.12}$$

where h is the Planck's constant. Thus, the energy which can be carried by each mode E cannot be a continue value between 0 and ∞ but has to be a multiple of the photon's energy:

$$E = nh\nu \tag{2.13}$$

where $\forall\, n \in \mathbb{N}$. So the average energy of the mode now is not anymore described by equation 2.10 but is now given by:

$$\langle E \rangle = \frac{\int_0^\infty nh\nu\, e^{[-(nh\nu/k_BT)]}\, dE}{\int_0^\infty e^{[-(nh\nu/k_BT)]}\, dE} = \frac{h\nu}{e^{h\nu/k_BT} - 1} \tag{2.14}$$

This formula, if $h\nu \ll kT$, it becomes the equation 2.10, but when the energy $h\nu$ of the photon is considerably higher, such as in the ultraviolet region, that simplification doesn't hold anymore and the equation 2.14 doesn't tend to infinite as it happened to the equation 2.10 derived in the classical way.
The spectral energy density ρ_ν can be then expressed as:

$$\rho_\nu = \left(\frac{8\pi\nu^2}{c_n^3}\right) \frac{h\nu}{e^{h\nu/k_BT} - 1} \tag{2.15}$$

which perfectly describes the experimental results.

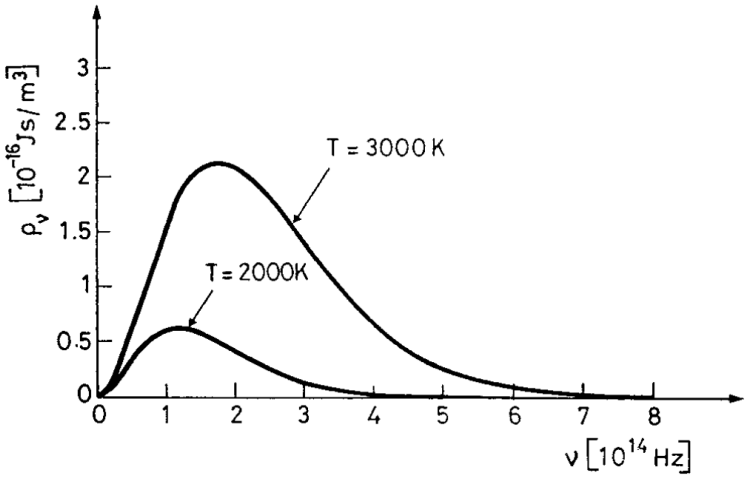

Figure 2.3: Spectral energy density [44].

Let us now suppose to create a hole in the cavity's walls, if the radiation field which escapes the cavity is isotropic, then the spectral intensity and the intensity of the black body radiation can be defined as:

$$I_\nu = \frac{c}{4n}\rho_\nu \qquad I = \frac{c}{4n}\rho \tag{2.16}$$

where n is the refractive index of the material inside the cavity. I_ν has dimensions W·s/cm^2 and I has dimensions W/cm^2. Through equations 2.15 and 2.16 it is possible to derive the *Stefan-Boltzmann's Law*, which describes the intensity in function of the temperature of the black body:

$$I = \sigma T^4 \quad , \quad \sigma = \frac{2\pi^5 k_B^4}{15c^2h^3} \tag{2.17}$$

where σ is a constant whose value is 5.68×10^{-12} with dimensions $\mathrm{W/(cm^2 \cdot K^4)}$. The average number of photons per mode is then defined from equation 2.14:

$$\langle \phi \rangle = \frac{\langle E \rangle}{h\nu} = \frac{1}{e^{h\nu/k_B T} - 1} \tag{2.18}$$

2.4 Einstein's Coefficients

Let us take a two energy level system, the total number of atoms in this system has to be constant:

$$N_1 + N_2 = N_{tot} \tag{2.19}$$

It is possible to identify three types of interaction between an electromagnetic radiation and this atomic system: *absorption*, *spontaneous emission*, *stimulated emission*. All these interactions come from the fact that radiation processes are allowed between two energy levels which differs by some energy $E_2 - E_1 = h\nu_{21}$.

- **Absorption**

  If a quasi monochromatic wave with frequency ν_{21} passes through an atomic system with an energy gap equal to $h\nu_{21}$, part of the radiation will be absorbed. In this case, the lower level will be depleted, because some atoms will be excited to the upper level. This interaction is called absorption and it is described by:

  $$\frac{\partial N_1}{\partial t} = -B_{12}\rho_\nu N_1 \tag{2.20}$$

  where N_1 is the ground state and ρ_ν is the spectral energy density at the frequency transition of the incident radiation. The B_{12}, which is the Einstein B coefficient, it gives the probability per unit time per unit spectral energy density of the electromagnetic wave that there will be an absorption; its dimensions are $\mathrm{cm^3/(s^2 \cdot J)}$. This means that the B coefficient is spectra dependent.
  As can be seen, the lower level population is decreasing, due to absorption, with a rate which depends proportionally on the variables N_1 and ρ_ν. The product $B_{12}\rho_\nu$ has dimensions $\mathrm{s^{-1}}$ and defines the overall probability per unit frequency that the atom absorbs the quantum of energy and leaves the N_1 level. The equation 2.32 can be written in an alternative way:

  $$\frac{\partial N_1}{\partial t} = -\sigma_{12}(\nu)\Phi N_1 \tag{2.21}$$

  where $\sigma_{12}(\nu)$, with dimensions $\mathrm{cm^2}$, is called *absorption cross-section* and represents the photon absorption probability; Φ is the photon flux and it is measured in # of photons/$\mathrm{(s \cdot cm^2)}$. Again, the product $\sigma_{12}(\nu)\Phi$ has dimensions $\mathrm{s^{-1}}$.
  The absorption cross section $\sigma_{12}(\nu)$ depends on frequency, and it is not a Dirac delta, but it is a function of frequency with a shape that is typical of each material. This means that there is a frequency-dependent probability that a photon with an energy sightly different from $h\nu_{21}$ might be absorbed, if it is present in the incident electromagnetic wave.

- **Spontaneous Emission**

  After an atom has been raised from the lower level to the upper level by absorption, it will decay spontaneously to the lower level after some time. If, during this process, it releases energy in the form of an electromagnetic wave, then it defines a *radiative transition*, will be called spontaneous emission and:

$$\frac{\partial N_2}{\partial t} = -A_{21} N_2 \tag{2.22}$$

  As can be seen, the upper level population is decreasing, due to spontaneous emission, with a rate which depends on A_{21} and the population N_2. The process releases a photon of energy $h\nu_{21}$. The value A_{21}, which is the Einstein A coefficient, is called spontaneous transition probability and gives the probability that an atom on the upper level decays to the lower level within a unit of time, spontaneously. As well as $B\rho_\nu$ the A coefficient has dimension s^{-1}, but whilst the latter depends only on the particular transition, the former depends also on the incident radiation intensity.
  Not all the processes where an excited atom goes to the lower level are radiative transitions, it may happen that the released energy doesn't go into an electromagnetic wave, for example in kinetic or internal energy. In this case it is called *non-radiative decay.*
  The photons emitted by spontaneous emission do not have a phase or spatial relation among each other. The emitted radiation has an isotropic spatial distribution and a spectral distribution which is equal to that of absorption cross section $\sigma_{12}(\nu)$. The previous equation has a solution:

$$N_2(t) = N_2(0)\, e^{\left(-\frac{t}{\tau_{rad,21}}\right)} \tag{2.23}$$

  where $\tau_{rad,21}$ is also known as lifetime for the spontaneous emission in the upper level. There is a relationship between this lifetime and the spontaneous transition probability:

$$\tau_{rad,21} = A_{21}^{-1} \tag{2.24}$$

  This relation is understandable because higher is A_{21}, the probability of an emission per unit of time, lower will be the average lifetime $\tau_{rad,21}$ of the atom on the upper level.
  It is worth noticing that the spontaneous emission refers to a radiative transition, but also non radiative decays exist. Since their behaviour is in the form of equation 2.22, they share the same solution 2.23, in which the lifetime is $\tau_{nr,21}$. Moreover:

$$\frac{1}{\tau_{21}} = \frac{1}{\tau_{rad,21}} + \frac{1}{\tau_{nr,21}} \tag{2.25}$$

In the 1916 Einstein observed that, if the system had been in thermal equilibrium, the spontaneous emission and the absorption would have created a total net movement of the electrons between E_1 and E_2 equal to zero. Consequently, it should have been true that:

$$A_{21}N_2 = B_{12}\rho_\nu N_1 \tag{2.26}$$

but since it is known that the Boltzmann's statistics was:

$$\frac{N_2}{N_1} = e^{-\frac{h\nu_{21}}{k_B T}} \tag{2.27}$$

the resulted value of ρ_ν would have been in contrast with the black body radiation theory developed by Planck and the equation 2.15, which would have meant that this thermal equilibrium wasn't true for every temperature.
At this point Einstein theorized another process, called *stimulated emission*.

- **Stimulated Emission**

  A radiative transition takes place not only due to spontaneous processes, but even when an electromagnetic radiation with a particular frequency stimulates the excited atom, thus this is an *induced emission*, which follows the equation:

$$\frac{\partial N_2}{\partial t} = -B_{21}\rho_\nu N_2 \tag{2.28}$$

  where N_2 is the level population, B_{21} is the Einstein coefficient, which defines the probability per unit time per unit spectral energy density that there will be a stimulated emission. During this process the excited atom decays to the lower level and emits a photon with energy $h\nu_{21}$. The variable ρ_ν is the spectral energy density referred to the incident radiation field. The product $B_{21}\rho_\nu$ still has dimensions s^{-1}. Another way to write it:

$$\frac{\partial N_2}{\partial t} = -\sigma_{21}(\nu)\Phi N_2 \tag{2.29}$$

  where $\sigma_{21}(\nu)$ is the *emission cross-section*, with dimensions cm^2. Again, the upper level population is decreasing, this time due to stimulated emission, with a rate which depends proportionally on Φ, the population N_2 and $\sigma_{21}(\nu)$. In this case, the emitted photon has a phase, a polarization, a direction and spectral characteristics equal to the electromagnetic radiation which stimulated the excited atom. This means that there is a amplification of the incident radiation intensity, which is at the base of the laser and the laser amplifier working principle.
  Now, with this third process, at thermal equilibrium we have:

$$A_{21}N_2 + B_{21}\rho_\nu N_2 = B_{12}\rho_\nu N_1 \tag{2.30}$$

Employing the Boltzmann population ratio from 2.4:

$$\rho_\nu = \frac{\dfrac{A_{21}}{B_{21}}}{\dfrac{g_1}{g_2}\dfrac{B_{12}}{B_{21}}e^{(h\nu_{21}/k_BT)} - 1} \tag{2.31}$$

and exploiting the equation of ρ_ν from 2.15:

$$\frac{A_{21}}{B_{21}} = \frac{8\pi h\nu^3}{c_n^3} = h\nu p_\nu \qquad \frac{B_{21}}{B_{12}} = \frac{g_1}{g_2} \qquad \frac{\sigma_{21}(\nu)}{\sigma_{12}(\nu)} = \frac{g_1}{g_2} \tag{2.32}$$

where p_ν is from equation 2.8 and is the number of resonant modes per unit volume per unit frequency, g_i is the degeneracy of the i-th energy level. These equations are known as *Einstein's relations*. If the energy levels are non degenerate then:

$$B_{12} = B_{21} \qquad \sigma_{12}(\nu) = \sigma_{21}(\nu) \tag{2.33}$$

The equations 2.32 and 2.33 show that there is always a relation between A and B coefficients. The relationship between B coefficient and $\sigma_{21}(\nu)$ is:

$$B_{21}\rho_\nu = \sigma_{21}(\nu)\Phi \tag{2.34}$$

which, if it is considered an infinitely narrow transition linewidth 2→1, can be written as:

$$\sigma_{21}(\nu) = \frac{h\nu_{21}}{c_n}B_{21} \tag{2.35}$$

and exploiting equation 2.32:

$$\sigma_{21}(\nu) = \frac{\lambda^2}{8\pi}A_{21} = \frac{\lambda^2}{8\pi\tau_{rad,21}} \tag{2.36}$$

Moreover, the lifetime of the excited atom is:

$$\tau_{rad,21} = A_{21}^{-1} \propto \nu^{-3} \tag{2.37}$$

which means that, for a given system, more energetic transitions have a shorter lifetime.

The absorption, spontaneous emission and stimulated emission processes have been derived for a quasi monochromatic incoming wave, but this is not the most general case. Suppose to have an incident radiation field with a spectral distribution $\Delta\nu$ centered at ν_c, then the equation 2.32 becomes:

$$\frac{\partial N_1}{\partial t} = -N_1 \int B_{12}\rho_\nu \, d\nu \tag{2.38}$$

It can be recalled from equation 2.6 that:

$$\rho = \int \rho_\nu \, d\nu \tag{2.39}$$

where ρ is the energy density of the incident radiation field. The equation 2.38 can be expressed through the cross-section as:

$$\frac{\partial N_1}{\partial t} = -N_1 \int \sigma_{12}(\nu)\phi(\nu) \, d\nu \tag{2.40}$$

The variable $\phi(\nu)$ is the photon flux per unit frequency and it is calculated as:

$$\Phi = \int \phi(\nu) \, d\nu \tag{2.41}$$

where Φ is the photon flux.
Let us now exploit the three radiation-matter interactions described in this section to derive a system of equations, called *Laser Rate Equations*, which define the electronic population on each level of the atomic system.

2.5 Atomic Lineshapes

All the calculations which have been carried out so far took into account that the energy level difference of the system was $E_2 - E1 = h\nu_{21}$ and that the incident radiation was a quasi monochromatic wave with photon energy $h\nu_{21}$. Let us now consider a two level system where there is a finite linewidth transition $\Delta\nu$ and the incoming radiation has a bandwidth $d\nu$.
Due to the existence of this finite linewidth transition it is necessary to define a distribution of the electrons over the two levels. in order to do that it is introduced the atomic lineshape function $g^*(\nu, \nu_0)$, which is centered at ν_0. The linewidth $\Delta\nu$ of this function is measured at full width half-maximum (FWHM) and it values:

$$\Delta\nu \propto g^*(\nu, \nu_0) \tag{2.42}$$

First of all, this distribution must be normalized:

$$\int_0^\infty g^*(\nu, \nu_0) \, d\nu = 1 \tag{2.43}$$

Let us now describe the spectral distribution per unit frequency of the excited electrons by using this function:

$$N(\nu) = g^*(\nu, \nu_0)N_2 \tag{2.44}$$

where N_2 is the upper level of the system. Since the atomic lineshape function is normalized:

$$\int_0^\infty N(\nu) \, d\nu = N_2 \qquad \int_0^\infty N_2 g^*(\nu, \nu_0) \, d\nu = N_2 \tag{2.45}$$

Since it is a distribution, $g^*(\nu, \nu_0)$ defines also the probability per unit frequency that there is an absorption or an emission. We can write equations 2.45 as:

$$N(\nu)d\nu = g^*(\nu, \nu_0)d\nu N_2 \tag{2.46}$$

Since this is a two level system, this equation says, once the g function is known, that $N(\nu)d\nu$ is the number of atoms in the upper level N_2 which can emit a photon in the $[\nu, \nu + d\nu]$ spectral region, or conversely the number of atoms in the ground level N_1 which can absorb a photon in the same region.

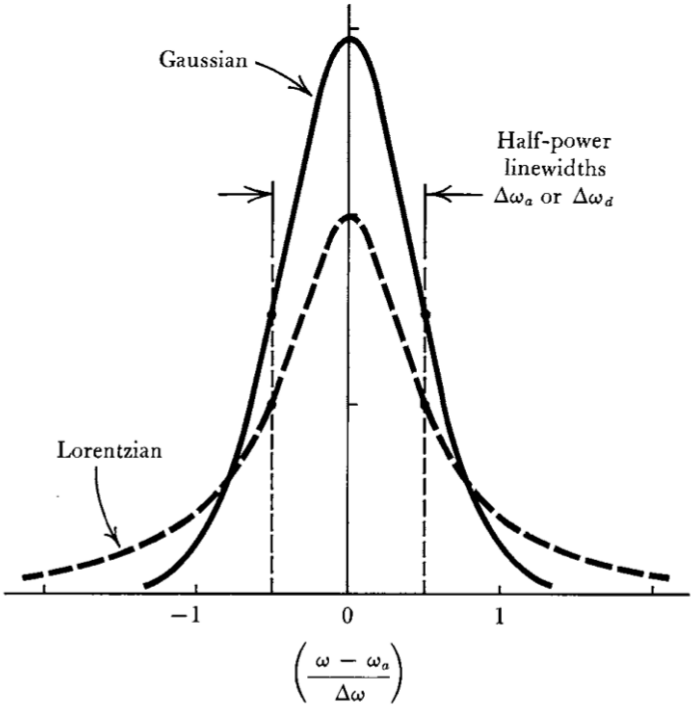

Figure 2.4: Comparison between Gaussian and Lorentzian atomic lineshapes with the same FWHM [45].

The distribution $g^*(\nu, \nu_0)$ defines the probability per unit frequency of a transition, an absorption or an emission. Thus the product $g^*(\nu, \nu_0)d\nu$ is the probability of a transition in the region $[\nu, \nu + d\nu]$ and describes the emission or the absorption of a photon with an energy which falls within the range $[h\nu, h\nu + d\nu]$. When the probability is calculated all over the spectrum the equation 2.43 is obtained.

Combining the equation 2.46 with 2.32, 2.22 and 2.28 it is possible to rewrite the absorption, spontaneous and stimulated processes taking into account the $g^*(\nu, \nu_0)$

distribution:

$$\begin{cases} \frac{\partial N_1}{\partial t} = -B_{12}\rho_\nu g^*(\nu,\nu_0)d\nu N_1 \\ \frac{\partial N_2}{\partial t} = -A_{21}g^*(\nu,\nu_0)d\nu N_2 \\ \frac{\partial N_2}{\partial t} = -B_{21}\rho_\nu g^*(\nu,\nu_0)d\nu N_2 \end{cases} \tag{2.47}$$

Moreover the cross section $\sigma_{21}(\nu)$ changes, since there is a transition which is no more infinitely narrow. So the equation 2.35 now becomes:

$$\sigma_{21}(\nu) = \frac{h\nu_{21}}{c_n}B_{21}g^*(\nu,\nu_0) = \frac{\lambda^2}{8\pi\tau_{rad,21}}g^*(\nu,\nu_0) \tag{2.48}$$

The atomic lineshape function $g^*(\nu,\nu_0)$ highly depends on material properties such as its purity, its state of matter and the interactions among the atoms. These broadening mechanisms are divided in two types, *homogeneous* and *inhomogeneous* line-broadening. The broadening exhibited by a material is unique property and it may be defined by only of one of these effects or by a mix of them. Let us describe these phenomena in details.

2.5.1 The Homogeneously Broadened Line

Suppose to have a system composed by an ensemble of i elements of identical atoms. An homogeneous line-broadening is referred to a mechanism where the lineshape function $g_i^*(\nu,\nu_{i0})$ is equal for each atom i, which means that the frequency response of a single atom is indistinguishable from another. An incident electromagnetic wave will generate the same probability function of transition for every atom in the ensemble. Due to this behaviour, under a strong enough external signal there will be a uniform saturation of the transition. The most important homogeneous broadening processes are the lifetime and the collision broadening, whereas the dipole and thermal broadening show minor effects.

- **Lifetime Broadening**

  It is related to spontaneous transitions between energy levels. Every spontaneous transition, whether it is a radiative decay, such as spontaneous emission, or a non radiative decay, possesses an associated lifetime. Let us focus to a transition from the upper level E_2 to the lower level E_1 in an atomic system with two or more energy levels. It is defined the lifetime τ_2 as the inverse of the population decay rate from E_2 to E_1 and all lower energy levels. In the same way, the lifetime τ_1 is the inverse population decay rate from E_1 to lower levels, if E_1 is not the ground state:

$$\frac{1}{\tau_j} = \sum_{0<i<j}\frac{1}{\tau_{ji}} \tag{2.49}$$

The lifetime τ_e associated to each of these transitions defines a time uncertainty:

$$\frac{1}{\tau_e} = \frac{1}{\tau_1} + \frac{1}{\tau_2} \tag{2.50}$$

The time uncertainty is linked to the frequency uncertainty $\Delta\nu$ through the Fourier transform. The Fourier transform of an exponentially decaying function has a Lorentzian profile. Then, the lifetime broadening linewidth is:

$$\Delta\nu = \frac{1}{2\pi\tau_e} \tag{2.51}$$

which is related to an energy uncertainty of the transitions:

$$\Delta E = h\Delta\nu = \frac{h}{2\pi\tau_e} \tag{2.52}$$

The atomic lineshape function has a normalized Lorentzian shape:

$$g^*(\nu,\nu_0) = \left(\frac{2}{\Delta\nu\pi}\right)\frac{1}{1+\left(\frac{2}{\Delta\nu}\right)^2\left(\nu-\nu_0\right)^2} \tag{2.53}$$

where the $\Delta\nu$ of this function is the linewidth at full width half maximum (FWHM), and the central frequency is ν_0. Thus the peak value is:

$$g^*(\nu_0,\nu_0) = \frac{2}{\Delta\nu\pi} = \frac{0.637}{\Delta\nu} \tag{2.54}$$

- **Collision Broadening**

  The collision broadening arises when the atom collides with particles, such as other atoms, molecules, electrons, or quasi particles, such as phonons. Both elastic and inelastic collision create a homogeneous broadening of the linewidth transition. in particular the elastic collision imparts a random phase shift to the ongoing process. The final result is again a Lorentzian distribution:

$$g^*(\nu,\nu_0) = 2\tau_c\frac{1}{1+4\pi^2\tau_c^2\left(\nu-\nu_0\right)^2} \tag{2.55}$$

  where τ_c is the average time interval between two random collisions, and:

$$\tau_c = \frac{1}{\Delta\nu\pi} \qquad \Delta\nu = \frac{1}{\pi\tau_c} \tag{2.56}$$

  In this case the energy uncertainty is:

$$\Delta E = \frac{h}{\pi\tau_c} \tag{2.57}$$

- **Thermal Broadening**

  This process occurs in liquid and solids, it is called thermal of phonon broadening because it is caused by vibrations in the lattice. The interaction between the phonon and the atom creates a modulation of the instantaneous frequency of the transition, and thus a broadening of the linewidth.
  Since it is governed by lattice vibrations, it has a strong dependence on the lattice temperature. This process may generate a shift of the central transition frequency ν_0, which is therefore called *thermal shift*.

- **Dipolar Broadening**

  When there is an overlapping of the dipolar electric and magnetic field of an atom with other atom's fields its surroundings, the consequent perturbation may create a phase shift. This phase shift results in a line broadening.
  It is almost always negligible because its effect is overwhelmed by the other processes described. Nonetheless it can be observed under particular conditions in materials with strong atomic dipoles.

The sum of these homogeneous broadening processes creates an atomic lineshape function which still has a Lorentzian shape. Neglecting the thermal and dipolar broadening, the $g^*(\nu, \nu_0)$ function is:

$$g^*(\nu, \nu_0) = \left(\frac{2}{\Delta\nu_{tot}\pi}\right) \frac{1}{1 + \left(\frac{2}{\Delta\nu_{tot}}\right)^2 (\nu - \nu_0)^2} \tag{2.58}$$

$$\Delta\nu_{tot} = \frac{1}{2\pi}\left(\frac{1}{\tau_e} + \frac{2}{\tau_c}\right) \tag{2.59}$$

2.5.2 The Inhomogeneously Broadened Line

On the other hand, an inhomogeneous line-broadening is defined as a shift of the atomic resonance frequency of individual atoms of the system. This means that, if this mechanism is present in the atomic ensemble, the lineshape of the function $g_i^*(\nu, \nu_{i0})$ regarding the i-th atom remains the same for all the atoms, but the resonance frequency ν_{i0} of the transition is unique for each i-th atom. So what happens is that there is a distribution of the atomic resonance over a spectral range.

- **Doppler Broadening**

  This mechanism is due to the atomic motion, and thus it is typical of gases. Let us suppose to have an incident electromagnetic wave with frequency ν propagating along the x axis, and let the i-th atom of the material moving along the same axis. Then the frequency of the wave experienced by the atom will be:

$$\nu' = \nu(1 - \nu_{ix}/c_n) \tag{2.60}$$

where c_n is the velocity of light in the material. The absorption of the photon it will happen at the resonance frequency ν_0, so the frequency seen by the atom must be $\nu' = \nu_0$. Manipulating the equation:

$$\nu = \frac{\nu_0}{(1 - \nu_{ix}/c_n)} \tag{2.61}$$

which means that there is a line-broadening of the frequency transition ν_0 related to the i-th atom, and becomes ν_{i0}:

$$\nu_{i0} = \frac{\nu_0}{(1 - \nu_{ix}/c_n)} \tag{2.62}$$

and so it is an inhomogeneous process. It is called after the *Doppler Effect*.

- **Crystal Inhomogeneities**

  The inhomogeneities and impurities in a material create a perturbation on the energy levels, and so on the resonance frequency ν_0, of the atoms in the surroundings through Stark effect. Since this process has a local behaviour it is not equally distributed all over the material and the it is inhomogeneous.

When the resonance distribution follows the Boltzmann's statistics, such as gases, the atomic lineshape function for the inhomogeneous broadening processes has a Gaussian shape:

$$g^*(\nu, \nu_0) = \frac{2}{\Delta\nu}\left(\frac{\ln 2}{\pi}\right)^{\frac{1}{2}} \exp\left[-\frac{4\big(\nu - \nu_0\big)^2}{\Delta\nu}\ln 2\right] \tag{2.63}$$

where ν_0 is the frequency at the center of the line and $\Delta\nu$ is the bandwidth at FWHM. The peak value is of the Gaussian function is:

$$g^*(\nu_0, \nu_0) = \frac{2}{\Delta\nu}\left(\frac{\ln 2}{\pi}\right)^{\frac{1}{2}} = \frac{0.939}{\Delta\nu} \tag{2.64}$$

2.6 Laser Rate Equations

The Laser Rate Equations are a set of differential equations used to describe the temporal evolution of an atomic system. They can describe different situations ongoing in the system, such as an absorption or an optical signal amplification, but they all rely on the three phenomena of radiation-matter interaction just described. Since these processes are not taken anymore singularly, the solution of the problem is non trivial.

It is clear that, if the goal is the amplification of a signal with photon energy $h\nu_{21}$, there is a competition between absorption and emission on the transition $2 \rightarrow 1$. The essential condition is that there are more atoms on the upper level than on the lower level of the transition. This means that:

$$N_2 > N_1 \tag{2.65}$$

So long as the upper level has a smaller population than the lower level, since $B_{21} = B_{12}$, the number of absorption transitions will be higher than the stimulated emission transitions and there will be an overall reduction of the incident radiation. In the system defined by the Boltzmann's equation, the lower level has an higher population than the upper level. For this reason is necessary to reach a situation described by the condition 2.65, which is called *population inversion*, in order to amplify the incident wave. Some sort of energy is provided to the system to move the atoms from thermal equilibrium. The component appointed to do that it is usually another laser and it is called *pump*.
The goal of the laser rate equations is to find the steady state solution of that given set of equations which define the system.

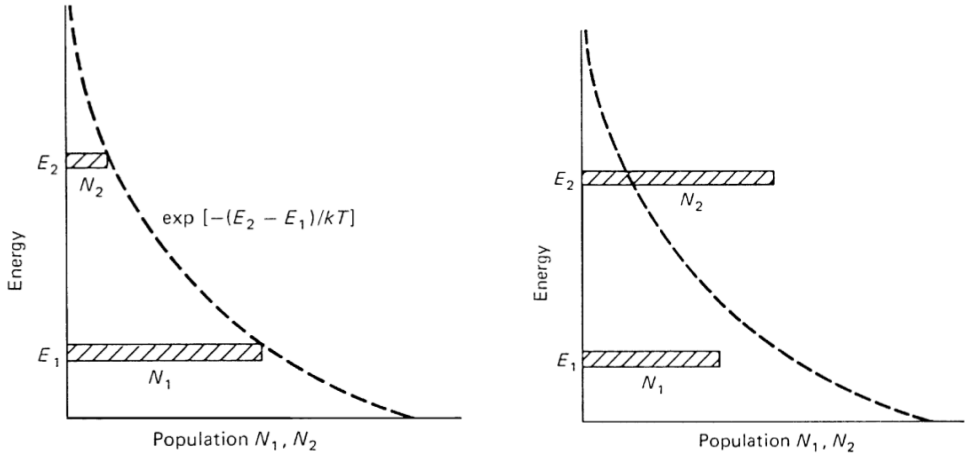

(a) Thermal equilibrium **(b)** Externally excited

Figure 2.5: Boltzmann's statistics for energy level population [45].

First of all it is necessary, for the sake of convenience, exploit a different notation for the transition probability:

$$W_{ji} = B_{ji}\rho_\nu = \sigma_{ji}(\nu)\Phi = \frac{\sigma_{ji}(\nu)I_{ji}}{h\nu_{ji}} \tag{2.66}$$

The quantity W_{ji}, with dimensions s^{-1}, is the probability of the given $j \to i$ transition, $\forall\, j > i \in \mathbb{N}$, either a spontaneous emission, an absorption or a stimulated emission. Then, let us recall:

$$\frac{1}{\tau_{ji}} = \frac{1}{\tau_{rad,ji}} + \frac{1}{\tau_{nr,ji}} \tag{2.67}$$

and $\forall\, j > i \in \mathbb{N}$. Obviously these transitions are linked to the population of their respective energy levels. Since it is known that they refers to the Boltzmann's equation, from 2.2:

$$\frac{\tau_{ji}}{\tau_{ij}} = e^{-\frac{h\nu_{ji}}{k_B T}} \ll 1 \tag{2.68}$$

and thus:

$$\frac{1}{\tau_{ji}} = \frac{1}{\tau_{rad,ji}} + \frac{1}{\tau_{nr,ji}} \qquad \frac{1}{\tau_{ij}} \approx 0 \tag{2.69}$$

This is called *optical approximation.* Moreover, let us from now on define the level population through their density:

$$n_i = \frac{N_i}{V} \tag{2.70}$$

where N_i is the population of the i-th level of the system and V is a unit of volume.

2.6.1 Two Level System

Let us describe a two level system in which there is not interaction with the outside, and the only variation of level population is driven by spontaneous processes. Its laser rate equations are:

$$\frac{\partial n_1}{\partial t} = -\frac{\partial n_2}{\partial t} = -\frac{n_1}{\tau_{12}} + \frac{n_2}{\tau_{21}} \tag{2.71}$$

$$n_{tot} = n_1 + n_2 \tag{2.72}$$

whose solution at steady state is:

$$\Delta n_0 = \frac{\tau_{12} - \tau_{21}}{\tau_{12}\tau_{21}} n_{tot} = n_{tot} \tanh(h\nu_{21}/2k_B T) \tag{2.73}$$

where $\Delta n_0 = n_1 - n_2$ is the difference of level population. This solution derives from thermal equilibrium, and says that almost all the population lies on the lower level E_1 at optical frequencies.

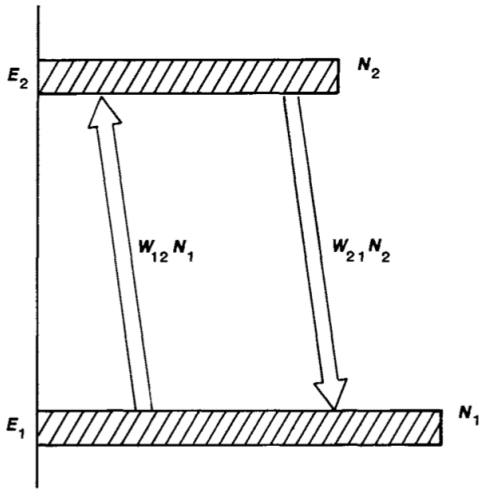

Figure 2.6: Two level system [45].

Suppose now that an incident radiation with frequency ν_{21} is applied. Then the equation 2.71 becomes:

$$\frac{\partial n_1}{\partial t} = -\frac{\partial n_2}{\partial t} = -\frac{n_1}{\tau_{12}} - W_{12}n_1 + \frac{n_2}{\tau_{21}} + W_{21}n_2 \tag{2.74}$$

where W_{ji} is the signal transition probability for i→j. It can be rewritten as:

$$\frac{\partial \Delta n}{\partial t} = -2W_{12}\Delta n - \frac{\Delta n - \Delta n_0}{\tau_{21}} \tag{2.75}$$

where $\Delta n = n_1 - n_2$. The solution at steady state is:

$$\Delta n = \frac{1}{1 + 2W_{12}\tau_{21}}\Delta n_0 \tag{2.76}$$

An alternative way to write it:

$$\frac{\Delta n}{\Delta n_0} = \frac{1}{1 + W_{12}/W_{sat}} \tag{2.77}$$

where $W_{sat} = 1/2\tau_{21}$. It is clear that when there is an incident radiation, the two level system encounters an effect on the level population distribution, called *saturation*. When the applied signal $W_{12} = W_{sat}$, the ratio between Δn and Δn_0 goes to $1/2$. In neither case it is happening what is called a population inversion, and there cannot be any amplification. It might be clear at this point that it is necessary to have a system with more than two energy levels.

2.6.2 Three Level System

Let us have an atomic system with two level E_2 and E_1, which are responsible for the laser transition, and add another level, E_3. That is a three level system. The laser rate equations when it is pumped are:

$$\frac{\partial n_3}{\partial t} = W_p(n_1 - n_3) - \frac{n_3}{\tau_3} \tag{2.78}$$

$$\frac{\partial n_2}{\partial t} = \frac{n_3}{\tau_{32}} - \frac{n_2}{\tau_{21}} \tag{2.79}$$

$$\frac{\partial n_1}{\partial t} = -W_p(n_1 - n_3) + \frac{n_3}{\tau_{31}} + \frac{n_2}{\tau_{21}} \tag{2.80}$$

$$n_{tot} = n_1 + n_2 + n_3 \tag{2.81}$$

where $W_p = W_{30} = W_{03}$ is the pump transition probability and τ_3 is the overall lifetime of the decays from E_3 to all lower levels defined by equation 2.49.

The optical approximation described in 2.69 has been exploited. The steady state solution is:

$$\frac{n_2 - n_1}{n_{tot}} = \frac{(1-\beta)\eta_q W_p \tau_{rad,21} - 1}{1 + (1+2\beta)\eta_q W_p \tau_{rad,21}} \tag{2.82}$$

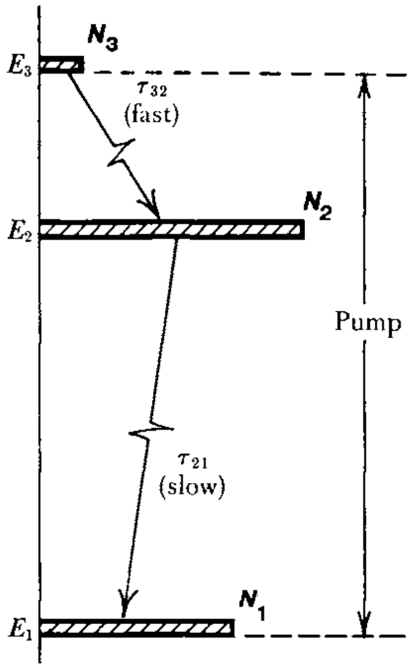

Figure 2.7: Three level system [45].

The factor β is a ratio between population level and also between relaxations time. For a three level system is:

$$\beta = \frac{n_3}{n_2} = \frac{\tau_{32}}{\tau_{21}} \tag{2.83}$$

The value η_q is called *fluorescent quantum efficiency* and describes how many excited atoms from the pump effectively exploit the spontaneous emission 2→1 transition. It is defined as:

$$\eta_q = \frac{\tau_3}{\tau_{32}} \frac{\tau_{21}}{\tau_{rad,21}} \tag{2.84}$$

From equation 2.82 it is possible to see that population inversion is reached if and only if $\beta < 1$ and the pump rate is higher than a given threshold:

$$W_p \tau_{rad,21} \geq \frac{1}{\eta_q(1-\beta)} \tag{2.85}$$

The product $W_p\tau_{rad,21}$ is called *pumping rate*. The best case is reached when $\beta \to 0$ and $\eta_q \to 1$ which means:

$$\tau_{32} \ll \tau_{21} \qquad \tau_{32} \ll \tau_{31} \qquad \tau_{rad,21} \ll \tau_{21} \tag{2.86}$$

These are common for a laser system, since it is needed a long radiative lifetime on the laser transition and a very short decay for all other transitions. The equation

2.107 becomes:

$$\frac{n_2 - n_1}{n_{tot}} \approx \frac{W_p \tau_{rad,21} - 1}{W_p \tau_{rad,21} + 1} \tag{2.87}$$

From this result it is clear the dramatic improvement of having a three level system instead of a two level system in order to get population inversion. This condition it is not easily reached, but it can be fulfilled with a strong enough pump rate.

Let us add now a signal with a transition probability $W_i = W_{21} = W_{12}$ to the laser rate equation from 2.78 to 2.81:

$$\frac{\partial n_3}{\partial t} = W_p(n_1 - n_3) - \frac{n_3}{\tau_3} \tag{2.88}$$

$$\frac{\partial n_2}{\partial t} = \frac{n_3}{\tau_{32}} - \frac{n_2}{\tau_{21}} + W_i(n_1 - n_2) \tag{2.89}$$

$$\frac{\partial n_1}{\partial t} = -W_p(n_1 - n_3) + \frac{n_3}{\tau_{31}} + \frac{n_2}{\tau_{21}} - W_i(n_1 - n_2) \tag{2.90}$$

$$n_{tot} = n_1 + n_2 + n_3 \tag{2.91}$$

From equation 2.89 and 2.90 it is visible that the signal modifies the temporal evolution of the levels population. Also, the term $W_i(n_1 - n_2)$ in equation 2.89 describes a situation in which there is a stimulated emission, and thus an amplification of the radiation at ν_{21} frequency, but also an absorption transition 1→2. This is in fact a reabsorption loss which undermines the amplification. If the assumptions from 2.86 still hold, the steady state solution is then:

$$n_2 - n_1 \approx \frac{\tau_{rad,21} W_p - 1}{1 + \tau_{rad,21} W_p + 2\tau_{rad,21} W_i} n_{tot} \tag{2.92}$$

which can be written as:

$$n_2 - n_1 = \frac{n_0}{1 + \tau_s W_i} \tag{2.93}$$

where:

$$\tau_s \approx \frac{2\tau_{rad,21}}{1 + \tau_{rad,21} W_p} \qquad n_0 \approx \frac{\tau_{rad,21} W_p - 1}{1 + \tau_{rad,21} W_p} n_{tot} \tag{2.94}$$

From equation 2.93 it is clear that a saturation effect appears. The threshold for inversion population is when the pumping rate is $W_p \tau_{rad,21} \geq 1$.
When the pump is very strong, $n_0 \to n_{tot}$ and equation 2.93 gives:

$$n_2 - n_1 = \frac{n_0}{1 + 2W_i/W_p} \tag{2.95}$$

so the population inversion depends both on the pump and signal probability W_p and W_i.

2.6.3 Four Level System

Let us add another level, E_0, in order to have a four level system. This level is going to be at a minor energy than te lower laser level, so $E_0 < E_1$ such that at room temperature $h\nu_{10} \gg k_B T$, which means that at thermal equilibrium almost all the population lies in the ground level E_0. The lower level E_1 and the ground state E_0 does not share the same energy level as in the three level system. This is an advantage because the population inversion is virtually reached already, and thus the four level system has intrinsically a higher efficiency with respect to the three level system. The rate laser rate equations of this system, when there is an incident pump but not a signal are:

$$\frac{\partial n_3}{\partial t} = W_p(n_0 - n_3) - \frac{n_3}{\tau_3} \tag{2.96}$$

$$\frac{\partial n_2}{\partial t} = \frac{n_3}{\tau_{32}} - \frac{n_2}{\tau_2} \tag{2.97}$$

$$\frac{\partial n_1}{\partial t} = \frac{n_3}{\tau_{31}} + \frac{n_2}{\tau_{21}} - \frac{n_1}{\tau_{10}} \tag{2.98}$$

$$\frac{\partial n_0}{\partial t} = -W_p(n_0 - n_3) + \frac{n_3}{\tau_{30}} + \frac{n_2}{\tau_{20}} + \frac{n_1}{\tau_{10}} \tag{2.99}$$

$$n_{tot} = n_0 + n_1 + n_2 + n_3 \tag{2.100}$$

where $W_p = W_{30} = W_{03}$. Again, the optical approximation has been used. The steady state solution for level E_3 is:

$$n_3 = \frac{W_p \tau_3}{1 + W_p \tau_3} n_0 \tag{2.101}$$

for the upper laser level E_2:

$$n_2 = \frac{\tau_3}{\tau_{32}} n_3 \tag{2.102}$$

and for the lower laser level E_1:

$$n_1 = \frac{\tau_{10}}{\tau_{21}} + \frac{\tau_{32}\tau_{10}}{\tau_{31}\tau_2} n_2 = \beta n_2 \tag{2.103}$$

where the β factor this time is defined as:

$$\beta = \frac{\tau_{10}}{\tau_{21}} + \frac{\tau_{32}\tau_{10}}{\tau_{31}\tau_2} = \frac{n_1}{n_2} \tag{2.104}$$

and thus it is directly connected with the population inversion of the system.
From these equations some considerations can be made. If the following hypothesis hold:

$$\tau_{43} \ll \tau_3 \qquad \tau_{10} \ll \tau_{21} \qquad \tau_{31} \approx \infty \tag{2.105}$$

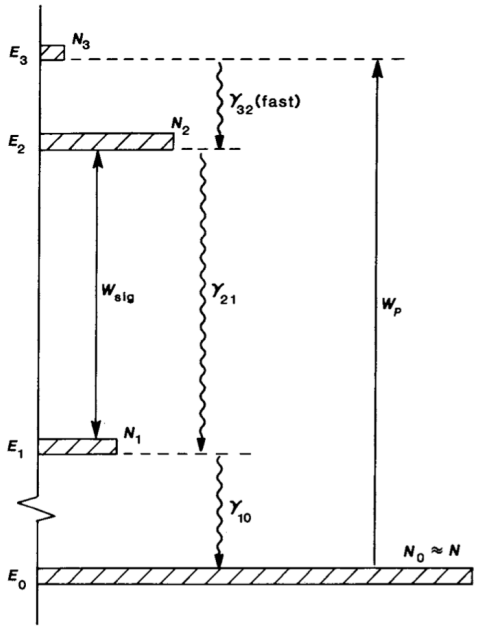

Figure 2.8: Four level system [45].

then:

$$n_2 \gg n_3 \qquad \beta = \frac{n_1}{n_2} \approx \frac{\tau_{10}}{\tau_{21}} \ll 1 \tag{2.106}$$

This means that the decay 4→3 is very fast, such that the pumped atoms quickly go from level E_3 to upper level E_2; the radiative lifetime transition 2→1 is very long in order to exploit the best population inversion conditions; the decay 1→0 is also very fast. The steady state solution of the system is:

$$\frac{n_2 - n_1}{n_{tot}} = \frac{(1-\beta)\eta_q W_p \tau_{rad,21}}{1 + (1+\beta)\eta_q W_p \tau_{rad,21}} \approx \frac{W_p \tau_{rad,21}}{1 + W_p \tau_{rad,21}} \tag{2.107}$$

This result is very important and it shows how a four level system might reach population inversion with a very weak pump, i.e. it is extremely easy to move it from the thermal equilibrium into a population inversion condition. In fact, there isn't a threshold on the pumping rate as in a three level system, which means that a four level system is intrinsically more efficient than a three level system.

Let us add now a signal with a transition probability $W_i = W_{21} = W_{12}$ to the laser rate equation from 2.96 to 2.100:

$$\frac{\partial n_3}{\partial t} = W_p(n_0 - n_3) - \frac{n_3}{\tau_3} \tag{2.108}$$

$$\frac{\partial n_2}{\partial t} = \frac{n_3}{\tau_{32}} - \frac{n_2}{\tau_2} + W_i(n_1 - n_2) \tag{2.109}$$

$$\frac{\partial n_1}{\partial t} = \frac{n_3}{\tau_{31}} + \frac{n_2}{\tau_{21}} - \frac{n_1}{\tau_{10}} - W_i(n_1 - n_2) \tag{2.110}$$

$$\frac{\partial n_0}{\partial t} = -W_p(n_0 - n_3) + \frac{n_3}{\tau_{30}} + \frac{n_2}{\tau_{20}} + \frac{n_1}{\tau_{10}} \tag{2.111}$$

$$n_{tot} = n_0 + n_1 + n_2 + n_3 \tag{2.112}$$

If the assumptions from 2.105 still hold, the steady state solution is then:

$$n_2 - n_1 \approx \frac{\tau_{rad,21} W_p}{1 + \tau_{rad,21} W_p + \tau_s W_i} n_{tot} \tag{2.113}$$

which can be written as:

$$n_2 - n_1 = \frac{n_0}{1 + \tau_s W_i} \tag{2.114}$$

where:

$$\tau_s \approx \frac{\tau_{rad,21}}{1 + \tau_{rad,21} W_p} \qquad n_0 \approx \frac{\tau_{rad,21} W_p}{1 + \tau_{rad,21} W_p} n_{tot} \tag{2.115}$$

Again, from equation 2.114 it can be seen that there is a saturation effect. When there is a very weak pumping rate $W_p \tau_{rad,21} \ll 1$ the equation 2.113 becomes:

$$n_2 - n_1 \approx \frac{\tau_{rad,21} W_p}{1 + \tau_s W_i} n_{tot} \tag{2.116}$$

On the other hand, when the pump contribution is not negligible and tends to infinite, $n_0 \to n_{tot}$ and so:

$$n_2 - n_1 = \frac{n_0}{1 + W_i / W_p} \approx n_{tot} \tag{2.117}$$

which means that virtually all the population tends to lay on the upper level E_2 when $W_i / W_p \ll 1$.

2.6.4 Quasi-Three Level System

A quasi-three level system is an intermediate situation between three and four level system. The level populations N_1 and N_2 do not lie anymore on a single energy level but in an ensemble of slightly different energy levels E_{1j} and E_{1j}, i.e. a manifold. Energy levels in the lower manifold N_1 are so close each other such that:

$$E_{1j} - E_{10} = h\nu_{j0} \gtrsim k_B T \tag{2.118}$$

where T is the room temperature, E_{10} is the energy of the lowest level, formally the ground state, and E_{1j} is the energy level of a generic level in the manifold.
This means that there are some levels close to the lowest one that are thermally populated at room temperature. The population of each energy level in the manifold at thermal equilibrium is described by:

$$N_{1j} = f_{1j} N_1 \qquad N_{2j} = f_{2j} N_2 \tag{2.119}$$

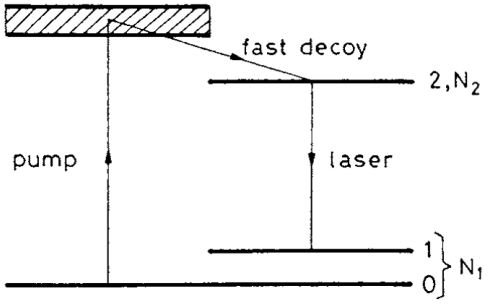

Figure 2.9: Quasi-three level system [44].

where:

$$N_i = \sum_{j=0} f_{ij} N_i \qquad f_{ij} = g_{ij} \frac{e^{\frac{-E_{ij}}{k_B T}}}{\sum_{j=0} g_{ij} e^{\frac{-E_{ij}}{k_B T}}} \tag{2.120}$$

and f_{ij} is the fraction of each j-th level population with g degeneracy with respect to N_i manifold. Through this definition it is possible to describe the population of the energy levels exploited by the laser transition. Let us define the lower level in the upper manifold N_2 and the upper level in the lower manifold N_1:

$$N_{2u} = f_{2u} N_2 \qquad N_{1l} = f_{1l} N_1 \tag{2.121}$$

where N_{2u} is the population of the upper laser level E_u and N_{1l} is the population of the lower laser level E_l. The E_u and E_l energy levels are nothing else that the E_2 and E_1 in the previous notation, as well as u→l transition is the previous 2→1 transition.
Similarly it can be defined the population of the energy levels of the pump transition:

$$N_{2h} = f_{2h} N_2 \qquad N_{1g} = f_{1g} N_1 \tag{2.122}$$

where the level E_g is the ground state of the manifold N_1, whereas the level E_h is the highest level of the upper manifold N_2. Since the lower laser level E_l is thermally populated, the transition u→l, will experience some reabsorption. This behaviour is in between the four level system, in which it is absent, and a three level system, where the reabsorption at laser wavelength is strong since the ground state and the lower laser level share the same energy. Also, the quasi-three level suffers from partial reabsorption at pump wavelength. The laser rate equations for a quasi-three level system vary a lot depending on the specific atomic system taken into account and may become particularly complex. For this reason it has been considered the case of a system with only two manifolds N_1 and N_2 and with negligible non radiative decays within them. In such a way, the population $N_{2h} \approx 0$ since the ions decay very

fast on the lower level E_{2u}. So, the equation with an incident pump and no signal are:

$$\frac{\partial n_2}{\partial t} = W_{ap} n_1 - W_{ep} n_2 - \frac{n_2}{\tau_2} \tag{2.123}$$

$$\frac{\partial n_1}{\partial t} = W_{ep} n_2 - W_{ap} n_1 + \frac{n_2}{\tau_2} \tag{2.124}$$

$$n_{tot} = n_1 + n_2 \tag{2.125}$$

The first thing to notice is that the equation $W_{ij} = W_{ji}$ does not hold anymore; every transition, absorption of emission, possesses its own transition probability W at a given frequency $\nu_{gh} = \nu_p$:

$$W_{ap} = \frac{\sigma_{gh} f_{1g} I_p}{h\nu_{gh}} \qquad W_{ep} = \frac{\sigma_{hg} f_{2h} I_p}{h\nu_{gh}} \tag{2.126}$$

where σ_{gh} and σ_{hg} are the absorption and emission cross sections for g→h and h→g transitions, respectively. Since it has been considered a system without degeneracy, $\sigma_{gh} = \sigma_{hg}$. The lifetime of the radiative transition is $\tau_{rad,ul} = \tau_{rad,21}$. The value I_p is the intensity of the pump radiation, part of which is reabsorbed. The steady state solution is:

$$\frac{n_2 - n_1}{n_{tot}} \approx \frac{\tau_{rad,21} W_{ap} - \tau_{rad,21} W_{ep} - 1}{\tau_{rad,21} W_{ap} + \tau_{rad,21} W_{ep} + 1} \tag{2.127}$$

This equation is similar to the solution 2.87 of the three level system. The difference is the splitting of the probability for the absorption and emission transitions. Moreover it is clear, through the term $\tau_{rad,21} W_{ep}$, that there is a partial reabsorption at the pump wavelength. Let us now add a signal with frequency $\nu_{lu} = \nu_{21}$:

$$\frac{\partial n_2}{\partial t} = W_{ai} n_1 + W_{ap} n_1 - W_{ei} n_2 - W_{ep} n_2 - \frac{n_2}{\tau_2} \tag{2.128}$$

$$\frac{\partial n_1}{\partial t} = W_{ei} n_2 + W_{ep} n_2 - W_{ai} n_1 - W_{ap} n_1 + \frac{n_2}{\tau_2} \tag{2.129}$$

$$n_{tot} = n_1 + n_2 \tag{2.130}$$

Again, the transition probabilities for the pump and the signal are unique:

$$W_{ai} = \frac{\sigma_{lu} f_{1l} I_i}{h\nu_{ul}} \qquad W_{ei} = \frac{\sigma_{ul} f_{2u} I_i}{h\nu_{ul}} \tag{2.131}$$

where I_i is the intensity of the signal radiation, whose wavelength is ν_{21}. The steady state solution is:

$$\frac{n_2 - n_1}{n_{tot}} \approx \frac{\tau_{rad,21} W_{ap} - \tau_{rad,21} W_{ep} + \tau_{rad,21} W_{ai} - \tau_{rad,21} W_{ei} - 1}{\tau_{rad,21} W_{ap} + \tau_{rad,21} W_{ep} + \tau_{rad,21} W_{ai} + \tau_{rad,21} W_{ei} + 1} \tag{2.132}$$

As in the previous solution, there is a reabsorption, not only at pump wavelength but also at signal wavelength. The term W_{ep}, despite being present, is almost negligible,

since $\sigma_{ul} f_{2u} \ll \sigma_{lu} f_{1l}$. In addition, let us suppose that $W_{ai} = W_{ei} = W_i$, then the equation 2.132 becomes:

$$\frac{n_2 - n_1}{n_{tot}} \approx \frac{\tau_{rad,21} W_{ap} - 1}{\tau_{rad,21} W_{ap} + 2\tau_{rad,21} W_i + 1} \tag{2.133}$$

and it is exactly the equation 2.92 found for a three level system in presence of a pump and signal radiation.

2.6.5 Gain Saturation

Let us recall the definition 2.66:

$$W_{ji} = B_{ji}\rho_\nu = \sigma_{ji}(\nu)\Phi = \frac{\sigma_{ji}(\nu) I_{ji}}{h\nu_{ji}} \tag{2.134}$$

A generic atomic system with 2→1 laser transition possesses a temporal variation of the photon density at frequency ν_{21} as:

$$\frac{\partial \rho_\nu}{\partial t} = W_{12}(n_2 - n_1) + \frac{n_2}{\tau_{rad,21}} \tag{2.135}$$

Let us not take into account the emitted photons by spontaneous emission, which do not have the same properties of coherence and directionality of a stimulated photon. Suppose to have a medium composed by and ensemble of this atomic system. Thus, the photon flux Φ along the z direction of the medium is:

$$\partial\Phi(z) = W_{21} n \, \partial z = \gamma(\nu)\Phi \, \partial z \qquad \gamma(\nu) = \gamma_{21} = n\sigma_{21} \tag{2.136}$$

whose solution is:

$$\Phi(z) = \Phi(0) e^{\gamma_{21} z} \tag{2.137}$$

In function of the intensity $I(z)$:

$$I(z) = I(0) e^{\gamma_{21} z} \tag{2.138}$$

The variable $\gamma(\nu)$ is the net gain in the photon flux per unit length, dimensions m^{-1}. Following the equation 2.48 it can be described as:

$$\gamma(\nu) = n\sigma(\nu) = n \frac{\lambda^2}{8\pi\tau_{rad,21}} g^*(\nu, \nu_0) \tag{2.139}$$

where $n = n_2 - n_1$ is the population inversion and $g^*(\nu, \nu_0)$ is the atomic transition lineshape. When $\gamma(\nu)$ is negative, due to a negative population inversion, it is called *absorption coefficient* and it is defined as:

$$\alpha_\nu = -\gamma(\nu) \tag{2.140}$$

On the other hand, when the population inversion is positive, it is called *gain coefficient*:

$$g(\nu) = \gamma(\nu) \tag{2.141}$$

The overall gain along the medium is:

$$G(\nu) = \frac{I(z)}{I(0)} = e^{\gamma(\nu)l} \tag{2.142}$$

where l is the length of the medium. Obviously the gain through the medium does not have the same growth but eventually it will saturate. Let us take the equation 2.93, which describes in general an atomic system with a pump and a signal applied:

$$n_2 - n_1 = \frac{n_0}{1 + \tau_s W_i} \tag{2.143}$$

thus, following the definition of W_i:

$$n = \frac{n_0}{1 + \Phi/\Phi_s} \tag{2.144}$$

where:

$$\frac{1}{\Phi_s} = \tau_s \sigma(\nu) = \frac{\lambda^2}{8\pi} \frac{\tau_s}{\tau_{rad,21}} g^*(\nu, \nu_0) \tag{2.145}$$

is the saturated photon flux. When the photon flux $\Phi = \Phi_s$ the inversion population is half of n_0. Since there is a direct relation between the inversion population and the net gain coefficient $\gamma(\nu)$:

$$\gamma(\nu) = n\sigma(\nu) = \frac{\gamma_0(\nu)}{1 + \Phi/\Phi_s} \tag{2.146}$$

$$\gamma_0(\nu) = n_0 \frac{\lambda^2}{8\pi\tau_{rad,21}} g^*(\nu, \nu_0) \tag{2.147}$$

Or:

$$\gamma(\nu) = n\sigma(\nu) = \frac{\gamma_0(\nu)}{1 + I/I_s} \tag{2.148}$$

$$\frac{1}{I_s} = \frac{\tau_s \sigma(\nu)}{h\nu} = \frac{\lambda^3}{8\pi hc} \frac{\tau_s}{\tau_{rad,21}} g^*(\nu, \nu_0) \tag{2.149}$$

in which $\gamma_0(\nu)$ is the small signal (unsaturated) attenuation or gain coefficient, respectively α_0 and g_0, depending on the fact that it is positive or negative. When the photon flux Φ (or the intensity I) reaches its saturation value, the net gain coefficient decreases to half its maximum value $\gamma_0(\nu)$.
Because the gain is frequency dependent there is also a phase dependent on it. From equation 2.138 it is possible to derive the complex amplitude:

$$E(z) = E(0) e^{\frac{1}{2}\gamma(\nu)z} e^{-j\varphi(\nu)z} \tag{2.150}$$

where $\varphi(\nu)$ is the gain-dependent phase. For a lorentzian atomic function lineshape $g^*(\nu, \nu_0)$ it worth:

$$\varphi(\nu) = \frac{\nu - \nu_0}{\Delta\nu} \gamma(\nu) \tag{2.151}$$

where ν_0 is the peak frequency gain and $\Delta\nu$ the bandwidth FWHM.

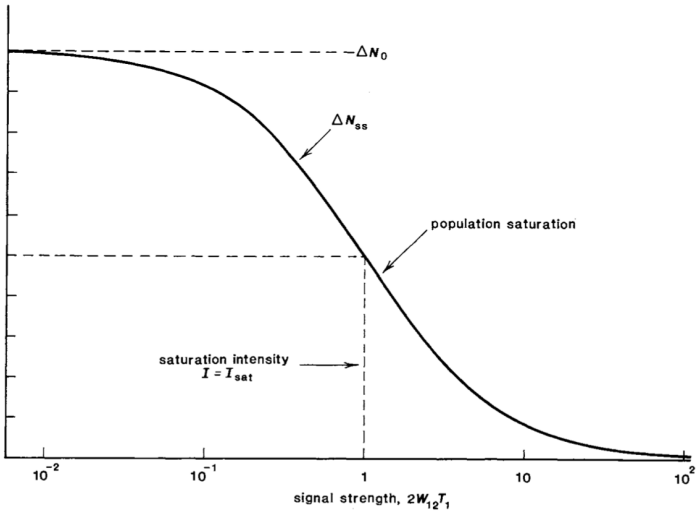

Figure 2.10: Gain saturation [45].

Chapter 3

Laser Oscillation

3.1 The Laser

In the previous chapter it has been introduced the concept of amplification of signals through the laser rate equations. These are a mathematical description of an atomic system and its radiation-matter interactions, and well define how to achieve an amplification of a narrowband incident signal. The laser is an optical oscillator in which an amplifier is put in a positive feedback with its output. Since the feedback is positive, the system is unstable.

In order to obtain a stable output from the oscillator two conditions must be fulfilled:

- The net gain provided by the looped amplifier must be positive
- There must be a complete constructive interference between the signal and the feedback, which means that the total phase added has to be a multiple integer of 2π
- There must be a saturation of the gain

Once that the first two conditions are satisfied, the oscillation begins and the amplifier goes rapidly into a gain saturation behaviour, since the feedback is positive. The stability is found when the gain of the system is equal to the losses. These losses can be various, and may depend on frequency. Moreover, even the gain is frequency dependent, as seen in the previous chapter. This means that at steady state condition there will be a balance between gain and losses in a set of frequencies. Usually this set is very narrow and highly depends on the atomic transition lineshape.

Let us now see more in detail the mechanisms which lead to an output from the laser. Because the ions used for this work can be described by a quasi-three level system, particular emphasis is given to it. A quasi three level system is a system the manifolds n_1 and n_2 are composed by different energy levels E_{ij} very close to each other. In general, the transitions within manifolds are non-radiative and atoms use phonons in order to modify their energy level. It works that:

$$E_{1j} - E_{10} = h\nu_{j0} \gtrsim k_B T \tag{3.1}$$

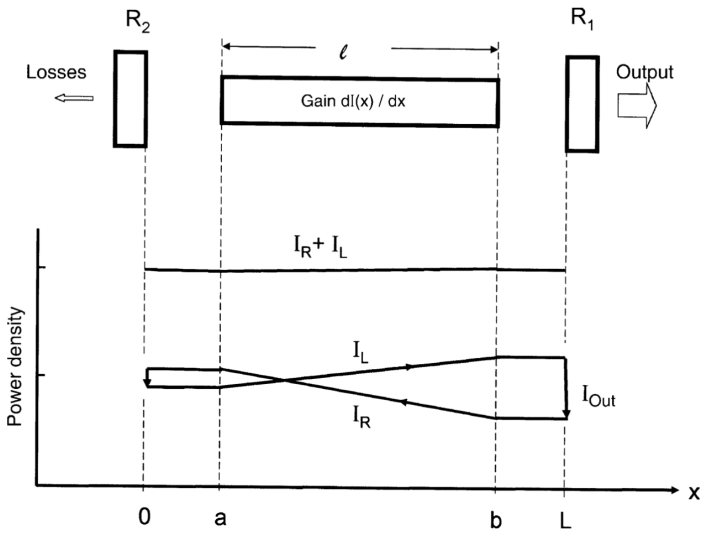

Figure 3.1: Optical Resonator [44].

where T is the room temperature, E_{10} is the energy of the lowest level and E_{1j} is the energy of a generic level in the lower manifold. Let us recall the related laser rate equation for the lower laser level:

$$\frac{\partial n_1}{\partial t} = W_{ei}n_2 + W_{ep}n_2 - W_{ai}n_1 - W_{ap}n_1 + \frac{n_2}{\tau_2} \tag{3.2}$$

in which I_i and I_p are the signal and pump optical intensities, $\tau_2 \approx \tau_{21}$ is the lifetime of an excited atom, and n_1 and n_2 are the atomic densities of the manifolds. moreover:

$$W_{ap} = \frac{\sigma_{ap} f_{1g} I_p}{h\nu_p} \qquad W_{ep} = \frac{\sigma_{ep} f_{2h} I_p}{h\nu_p} \tag{3.3}$$

$$W_{ai} = \frac{\sigma_{ai} f_{1l} I_i}{h\nu_i} \qquad W_{ei} = \frac{\sigma_{ei} f_{2u} I_i}{h\nu_i} \tag{3.4}$$

where σ_{ai} and σ_{ei} are the absorption and emission cross sections at the incident signal frequency, whereas σ_{ap} and σ_{ep} at pump frequency.
Let us manipulate the equation 3.2 and write it in a more explicative manner:

$$\frac{\partial n_1}{\partial t} = \frac{\sigma_{ei} f_{2u} I_i}{h\nu_i} n_2 + \frac{\sigma_{ep} f_{2h} I_p}{h\nu_p} n_2 - \frac{\sigma_{ai} f_{1l} I_i}{h\nu_i} n_1 - \frac{\sigma_{ap} f_{1g} I_p}{h\nu_p} n_1 + \frac{n_2}{\tau_{21}} \tag{3.5}$$

$$n_{tot} = n_1 + n_2 \tag{3.6}$$

Now, combining these equations and the definition of the gain coefficient from 2.139 it is possible to define the latter as:

$$g(\nu) = n\sigma(\nu) = \sigma_{ei} f_{2u} n_2 - \sigma_{ai} f_{1l} n_1 \tag{3.7}$$

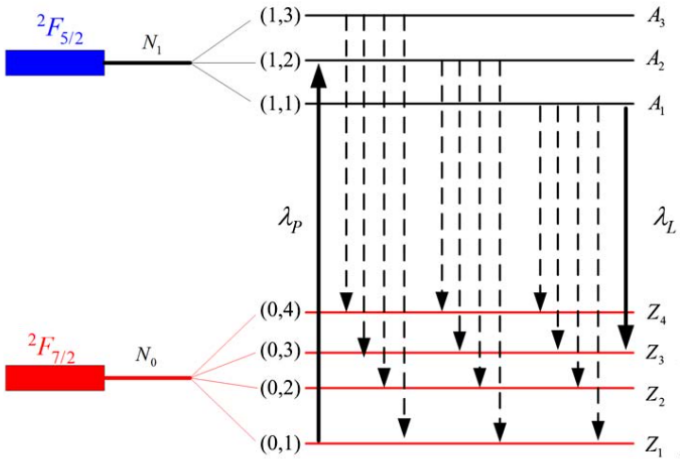

Figure 3.2: Quasi-three level system [46].

which is the optical net gain per unit length, with dimensions m^{-1}. It is possible to see that there is a negative contribution from the reabsorption at laser wavelength. An alternative way to interpret the equation is:

$$g(\nu) = [\sigma_{ei} f_{2u} \beta_r - \sigma_{ai} f_{1l}(1 - \beta_r)] n_{tot} \tag{3.8}$$

where $\beta_r = n_2/n_{tot}$ is called inversion ratio. When $\beta_r = 1$ there is total excitation of the atoms on the lower laser level, there is no reabsorption and the medium acts as a four level system. On the other hand, when $\beta_r = 0$ there is no excitation and the signal is completely absorbed, and it is obtained the formula of the absorption coefficient at laser wavelength a_i. Since the cross sections are frequency dependent, also the gain it is. This means that the spectral shape of the gain coefficient is strictly related to the excitation level, because for each wavelength it is necessary a given β_r in order to fulfill the oscillator conditions.

In a laser, the cavity acts as feedback, and in order to have constructive interference the wave must have the same phase after a round-trip. The threshold conditions for an output are a unitary gain loop and a constructive interference:

$$E_0 e^{i(\omega t - kz)} = E_0 e^{i(\omega t + \omega \Delta t - kz)} \sqrt{R_{oc}(1 - L)}\, e^{\frac{2 g_{th} l_g}{2}} \tag{3.9}$$

where R_{oc} is the output coupler reflectivity, L are additional intracavity losses, such as medium defects and scattering at interfaces, k is the wave number, $\omega \Delta t$ the added phase factor in a round-trip, g_{th} the gain coefficient per unit length at threshold, and l_g the length of the medium. The pump mirror has been set to have a unitary reflectivity.
Let us focus on the threshold round-trip gain g_{th}, with a modulus equal to 1 and a phase which is a 2π multiple:

$$e^{2 g_{th}} R_{oc}(1 - L) = 1 \tag{3.10}$$

This means that the round-trip gain must pair the losses inside the cavity in order to reach threshold. If the R_{oc} is almost unitary and the additional losses are small, it can be rewritten as:

$$2g_{th} = T_{oc} + L \tag{3.11}$$

where $T_{oc} = 1 - R_{oc}$ is the transmittivity of the output coupler. The gain inside the cavity can be found integrating the gain coefficient per unit length through all the medium length:

$$2\int_0^{l_g} \left(\sigma_{ei} f_{2u} n_2 - \sigma_{ai} f_{1l} n_1\right) dz = T_{oc} + L \tag{3.12}$$

where l_g is the crystal length, z is the direction along the medium. The equation 3.7 can be expressed in another way:

$$g(\nu) = \sigma_{ei} f_{2u} n_2 - \sigma_{ai} f_{1l} n_1 = \sigma_{ei} f_{2u} n_2 + \sigma_{ai} f_{1l} n_2 - \sigma_{ai} f_{1l} n_{tot} \tag{3.13}$$

where $n_1 = n_{tot} - n_2$. So:

$$2\int_0^{l_g} \left(\sigma_{ei} f_{2u} + \sigma_{ai} f_{1l}\right) n_2 \, dz = T_{oc} + L + 2\int_0^{l_g} \sigma_{ai} f_{1l} n_{tot} \, dz \tag{3.14}$$

and it is clear that $\sigma_{ai} n_{tot}$ is the reabsorption loss per unit length α_i. The total reabsorption losses per round-trip are called δ:

$$2\int_0^{l_g} \left(\sigma_{ei} f_{2u} + \sigma_{ai} f_{1l}\right) n_2 \, dz = T_{oc} + L + \delta \tag{3.15}$$

The integral can be exploited once the equations 3.5 and 3.6 have been solved in steady-state. Thus n_2 is equal to:

$$n_2 = \frac{\frac{\sigma_{ap} f_{2u} f_{1g} I_p}{h\nu_p} + \frac{\sigma_{ap} f_{1l} f_{1g} I_p}{h\nu_p} + \frac{\sigma_{ei}\sigma_{ai} f_{2u} f_{1l} I_i}{h\nu_i} + \frac{\sigma_{ai}\sigma_{ai} f_{1l} f_{1l} I_i}{h\nu_i}}{\frac{\sigma_{ap} f_{1g} I_p}{h\nu_p} + \frac{\sigma_{ep} f_{2h} I_p}{h\nu_p} + \frac{\sigma_{ei} f_{2u} I_i}{h\nu_i} + \frac{\sigma_{ai} f_{1l} I_i}{h\nu_i} + \frac{1}{\tau_{21}}} n_{tot} \tag{3.16}$$

and the integral can be written as:

$$2\int_0^{l_g} \left(\sigma_{ei} f_{2u} + \sigma_{ai} f_{1l}\right) n_2 \, dz =$$

$$2\int_0^{l_g} \frac{\frac{\sigma_{ei}\sigma_{ap} f_{2u} f_{1g} I_p}{h\nu_p} + \frac{\sigma_{ai}\sigma_{ap} f_{1l} f_{1g} I_p}{h\nu_p} + \frac{\sigma_{ei}\sigma_{ai} f_{2u} f_{1l} I_i}{h\nu_i} + \frac{\sigma_{ai}\sigma_{ai} f_{1l} f_{1l} I_i}{h\nu_i}}{\frac{\sigma_{ap} f_{1g} I_p}{h\nu_p} + \frac{\sigma_{ep} f_{2h} I_p}{h\nu_p} + \frac{\sigma_{ei} f_{2u} I_i}{h\nu_i} + \frac{\sigma_{ai} f_{1l} I_i}{h\nu_i} + \frac{1}{\tau_{21}}} n_{tot} \, dz \tag{3.17}$$

Let us define the signal and pump saturation intensity, respectively I_{si} and I_{sp}, which take into account the fractional level population:

$$I_{si} = \frac{h\nu_i}{(\sigma_{ai} f_{1l} + \sigma_{ei} f_{2u})\tau_{21}} \tag{3.18}$$

$$I_{sp} = \frac{h\nu_p}{(\sigma_{ap} f_{1g} + \sigma_{ep}) f_{2h} \tau_{21}} \tag{3.19}$$

So the equation 3.17, knowing that $I_p \ll I_{sp}$, becomes:

$$2\int_0^{l_g} \big(\sigma_{ei} f_{2u} + \sigma_{ai} f_{1l}\big) n_2 \, dz = 2\int_0^{l_g} \frac{\dfrac{h\nu_i}{h\nu_p}\sigma_{ap} f_{1g}\dfrac{I_p}{I_{si}} + \sigma_{ai} f_{1l}\dfrac{I_i}{I_{si}}}{1 + \dfrac{I_i}{I_{si}}} n_{tot} \, dz \tag{3.20}$$

The intensity ratio can be written as power ratio, moreover since $\sigma_{ai} f_{1l} \frac{I_i}{I_{si}}$ is a lot smaller with respect to the other term can be neglected:

$$2\int_0^{l_g} \big(\sigma_{ei} f_{2u} + \sigma_{ai} f_{1l}\big) n_2 \, dz = 2\int_0^{l_g} \frac{\dfrac{h\nu_i}{h\nu_p}\sigma_{ap} f_{1g}\dfrac{P_p}{P_{si}}}{1 + \dfrac{P_i}{P_{si}}} n_{tot} \, dz \tag{3.21}$$

and exploiting:

$$\alpha_p = (\sigma_{ap} f_{1g} n_1 - \sigma_{ep} f_{2h} n_2) \approx \sigma_{ap} f_{1g} n_{tot} \tag{3.22}$$

$$\alpha_p P_p = -\frac{dP_{p,abs}}{dz} \tag{3.23}$$

where α_p is the absorption coefficient at pump wavelength. Thus:

$$2\int_0^{l_g} \big(\sigma_{ei} f_{2u} + \sigma_{ai} f_{1l}\big) n_2 \, dz = 2\frac{\dfrac{h\nu_i}{h\nu_p}\dfrac{P_{p,abs}}{P_{si}}}{1 + \dfrac{P_i}{P_{si}}} \tag{3.24}$$

So the threshold of the absorbed pump power $P_{th,abs} = P_{p,abs}$ when the gain counteracts the losses, is:

$$P_{th,abs} = \frac{P_{si}}{2}\frac{\lambda_i}{\lambda_p}\big(T_{oc} + L + \delta\big) \tag{3.25}$$

It can be defined the threshold of the incident pump power, i.e. the pump power itself $\eta P_{th,inc} = P_{p,abs}$, so:

$$P_{th,inc} = \frac{P_{si}}{2\eta}\frac{\lambda_i}{\lambda_p}\big(T_{oc} + L + \delta\big) \tag{3.26}$$

This simple formula describes the threshold power $P_{th,inc}$ with little approximation with respect to reality. It depends on few but important variables. The parameter η,

the power saturation at signal wavelength P_{si}, the ratio λ_i/λ_p called *Stokes efficiency* or *quantum defect*, and the total losses, including the reabsorption.
The parameter η, which will be defined in more detail, is the overall efficiency and describes the ability of the cavity to convert the radiation from pump wavelength to laser wavelength.
The ratio λ_i/λ_p is an additional term regarding the efficiency of the system, it is a ratio between the energy of the pump and the laser photon. Usually in quasi-three level system it is close to unity, which means that little part of the pump photon energy is lost outside the laser transition.
The reabsorption losses δ don't exist in four level systems, and thus there will be an higher P_{th} in a quasi-three level system with respect to them. It is not a negligible effect, and in some cases $\delta \approx T_{oc} + L$.
Last but not least let us recall the definition of laser power saturation for a quasi-three level system:

$$P_{si} = \frac{h\nu_i A}{(\sigma_{ei} f_{2u} + \sigma_{ai} f_{1l})\tau_{21}} \tag{3.27}$$

where A is the area of the beam at a given position along the propagation direction. It is then clear that the threshold power relies on two parameters which strictly depend on the medium, i.e. the sum of the cross-sections and the laser transition lifetime. Higher are this values, lower is the laser power saturation and lower is the threshold power. Explicating P_{si} gives a better idea of the players:

$$P_{th,inc} = \frac{h\nu_i A_{eff}}{2\eta(\sigma_{ei} f_{2u} + \sigma_{ai} f_{1l})\tau_{21}} \frac{\lambda_i}{\lambda_p}\big(T_{oc} + L + \delta\big) \tag{3.28}$$

where A_{eff} is a parameter which takes into account the effective area of the signal along all the medium. The threshold gain is:

$$g_{th} = \frac{P_{th,abs}}{P_{si}} \frac{\lambda_p}{\lambda_i} - \delta = \eta \frac{P_{th,inc}}{P_{si}} \frac{\lambda_p}{\lambda_i} - \delta \tag{3.29}$$

where g_{th} is the threshold gain. Once the threshold is reached, it becomes the small signal gain:

$$g_{th} = \frac{P_{abs}}{P_{si}} \frac{\lambda_p}{\lambda_i} \tag{3.30}$$

which is the unsaturated gain. In order to obtain the output power P_{out} it is not possible to neglect the gain saturation. For a quasi-three level system:

$$g(\nu) = \frac{g_0}{1 + I/I_{si}} - \delta/2 \tag{3.31}$$

In a cavity the behaviour is slightly different. There are two standing waves circulating inside it, and thus their effect is doubled, which means that there is a 2 factor that arises in the P_i/P_{si} fraction:

$$g_s = \frac{2g_0}{1 + 2P_i/P_{si}} = T_{oc} + L + \delta \tag{3.32}$$

where g_0 is the small signal gain and g_s is the saturated gain. The g_0 depends on the atomic transition lineshape $g^*(\nu, \nu_0)$, which means that the small signal gain rely on

frequency. So the equation 3.32 describes a set of finite, but continuous, frequencies which can fulfill the equality.
The output power P_{out} is the power coupled out the laser which means the power circulating inside the cavity multiplied by the output coupler transmittivity, $P_{out} = T_{oc}P_i$:

$$P_{out} = \eta \frac{\lambda_p}{\lambda_i} \frac{T_{oc}}{T_{oc} + L} \left(P_{p,abs} - P_{th,abs}\right) \tag{3.33}$$

There is a linear relationship between the output power and the absorbed pump power.
The reabsorption losses increase the threshold power, but do not affect the output power. This is because the energy provided for the reabsorption is not completely lost, but it is used to excite an atom to the upper laser level, which will eventually contribute to output power. So, once some energy has been spent to counteract the reabsorption under threshold, this effect will not influence the output power of the laser.
There is another drawback: the gain medium must be not too long, because otherwise at the end of the crystal there will not be an adequate level of excited atoms, and thus the reabsorption condition will overwhelm the emission. For this reason it is not favorable for a quasi-three level system to have a length in order to fully exploit the pump power absorption.

The derivative of the output power with respect to the absorbed power is called *slope efficiency*:

$$\frac{\partial P_{out}}{\partial P_{abs}} = \eta \frac{\lambda_p}{\lambda_i} \frac{T_{oc}}{T_{oc} + L} \tag{3.34}$$

It is described by the overall efficiency η, the Stokes efficiency λ_p/λ_i and a term which takes into account the intrinsic losses L and the output coupler losses T_{oc}. Increasing the transmission of the output coupler T_{oc} increases the slope efficiency of the output power, but as can be seen from the equation 3.25, even the threshold power is increased.

Let us now focus on the overall efficiency η, which is composed by different terms:

$$\eta = \eta_q \eta_{abs} \eta_f \eta_o \tag{3.35}$$

They are:

- **Quantum efficiency**

  It defines how many pump photons are used to excite one atom on the upper laser level. This efficiency takes into account the non-radiative energy transfer and the cross-relaxation processes between energy levels. It can be very close to unity, and in few special cases is equal to 2.

- **Absorption efficiency**

  It defines how much of the pump power is absorbed by the gain material. It is equal to:

$$\eta_{abs} = 1 - e^{-\alpha_p l} \tag{3.36}$$

where α_p is called absorption coefficient and l is the medium length. This coefficient depends on the absorption cross-section at pump wavelength and on the population of the lower level. In a quasi-three level system it cannot be over 80-90% otherwise the system will experience reabsorption losses.

- **Fresnel efficiency**

  It takes into account the losses due to scattering and reflection of the first mirror of the cavity.

- **Overlap efficiency**

  It describes the overlap between the pump beam and the laser beam inside the medium, so it defines the efficiency of the conversion of the upper level energy in laser output. It is the ratio between the resonator mode volume and the pumped volume of the active material, which means that the overlap efficiency highly depends on the cavity parameters.

3.1.1 Output Coupling Optimization

The output power has the following equation:

$$P_{out} = \eta \frac{\lambda_p}{\lambda_i} \frac{T_{oc}}{T_{oc} + L} \left(P_{p,abs} - P_{th,abs} \right) \tag{3.37}$$

and it depends on the output coupler transmission T_{oc}. It is possible to find a local maximum of this equation, in function of T_{oc}.

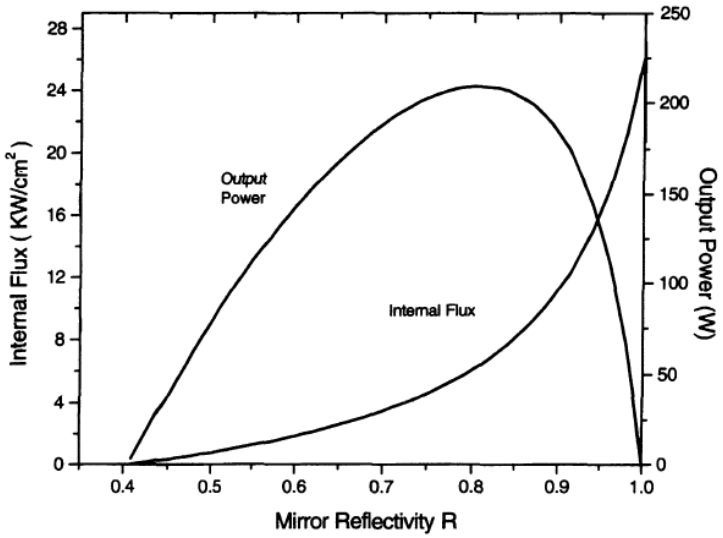

Figure 3.3: Example of output power as a function of mirror reflectivity [44].

The best value for the optimization of the output power is:

$$T_{oc} = \sqrt{2g_0(L + \delta)} - L - \delta \tag{3.38}$$

where g_0 is the small signal gain and L the additional losses. In figure 3.3 is represented the output power in function of T_{oc}. As it can be seen, around the

maximum of the function there is an almost flat behaviour, so there is a set of values of T_{oc} with slightly different output power coupled out.
Eventually it is possible to find the maximum value of optical extraction efficiency with respect to the optimum output coupling:

$$\eta_{opt} = \left[1 - \sqrt{\frac{L+\delta}{2g_0(L+\delta)}}\right]^2 \tag{3.39}$$

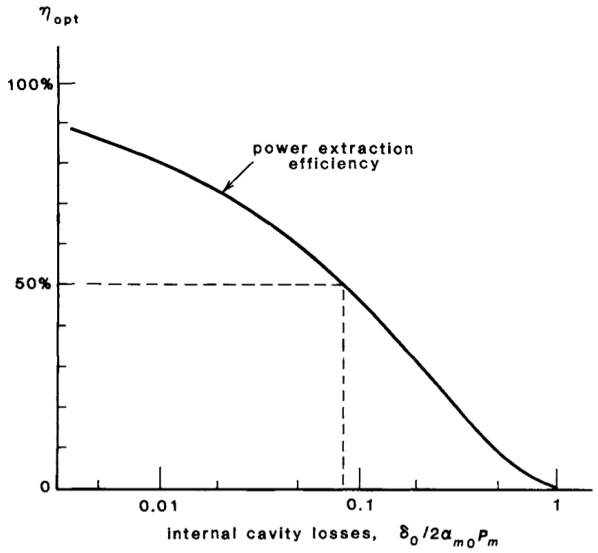

Figure 3.4: Optical extraction efficiency [45].

3.1.2 Emission Spectrum

The first constraint of the laser, regarding the round-trip gain, has been fulfilled. Let us focus about the constructive interference after a round-trip:

$$\mathcal{E}(z,t) = \mathcal{E}(z,t+\Delta t) \tag{3.40}$$

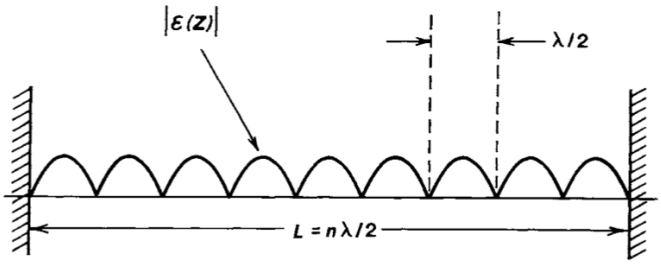

Figure 3.5: Oscillating modes in a optical resonator [45].

where Δt is the time taken by the radiation to complete a cavity trip. This means that:

$$\mathcal{E}_0 e^{i(\omega t - kz)} = \mathcal{E}_0 e^{i(\omega t + \omega \Delta t - kz)} \sqrt{R_{oc}(1-L)}\, e^{\frac{2gl_g}{2}} \tag{3.41}$$

where the added phase factor is:

$$\omega \Delta t = \frac{\omega}{c} 2l_0 \tag{3.42}$$

The cavity length l_0 of a laser is the sum of each path of l length and n refractive index:

$$l_0 = \sum_i^k l_i n_i \tag{3.43}$$

This parameter varies a lot depending on the laser and the cavity length. For long cavities the effect of the crystal refractive index, or other components in the optical path, might be negligible.
The phase added in a round-trip must be a multiple of 2π:

$$\omega \Delta t = q 2\pi \tag{3.44}$$

where $\forall\, q \in \mathbb{N}$, then:

$$2\pi\nu_q = q\frac{\pi c}{l_0} \tag{3.45}$$

So there is a discrete number of frequencies allowed:

$$\nu_q = q\frac{c}{2l_0} \tag{3.46}$$

Each of these ν_q frequencies define the frequency of a so called *longitudinal or axial mode*. The free spectral range (FSR) is defined as the difference between two adjacent allowed frequencies:

$$\Delta\nu = \frac{c}{2l_0} \tag{3.47}$$

with a short cavity the FSR is high, the other way around when the laser cavity is long. An example is given in figure 3.6.
The equation **??** and equation 3.32 have defined a set of finite and continuous frequencies which can generate a small signal gain above the cavity losses. In addition, the phase constructive round-trip interference through the equation 3.46 selects a discrete number of frequencies among this continuous set.
The FSR is important because defines the number of longitudinal modes which are above the gain threshold of the cavity:

$$N_{mod} = \frac{\Delta\nu_{th}}{\Delta\nu} \tag{3.48}$$

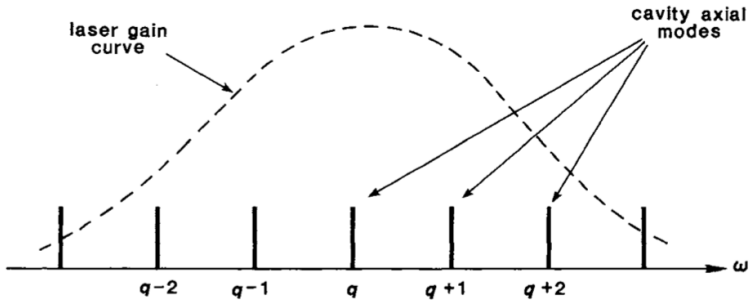

Figure 3.6: Example of frequencies allowed for cavity axial modes [45].

The round-trip time is the inverse of the FSR:

$$\tau_r = \frac{1}{\Delta\nu} = \frac{2l_0}{c} \tag{3.49}$$

and defines how much time takes a photon in order to do a round-trip of the cavity. This parameter is useful to estimate the lifetime of pulsed signals inside the cavity before being coupled out.

3.1.3 Wavelength Selection

As it has been see in the previous sections, there are a finite number of axial modes which can oscillate in the laser cavity, and it depends on the cavity length and the atomic function lineshape $g^*(\nu, \nu_0)$. The laser adjusts itself to oscillate in the axial mode or modes which minimize the cavity losses. This peculiarity can be exploited to select a set of axial modes or even an axial mode. The selection of a single longitudinal mode requires an high complexity, because even with cavities whose length is less than 30 cm the modes are really close to each other, meaning that the selection technique must be fine.
On the other hand, the selection of a set of axial modes, which are adjacent, need a reduced complexity. In order to do that, an element which inserts an angular discrimination with respect to wavelength is inserted in the cavity. This component has the job to deviate the optical path of the beam while introducing the less losses possible to the cavity.
Generally two devices are used. The first is the prism. For a minimum deviation configuration with a single prism, and at Brewster's angle incidence θ_{in}, then the output angle is wavelength dependent and follows [47]:

$$\theta_{out} = -\theta_{in} + 2\left(\left.\frac{\partial n}{\partial \lambda}\right|_{\lambda_0}\right)^2 \Delta\lambda \tag{3.50}$$

where θ_{out} is the output angle, θ_{in} is the input angle, at Brewster's angle incidence; both of them with respect to the normal plane of incidence. The prism's refractive index is wavelength dependent and thus the output angle depends on it. The second is a refractive grating in Littrow configuration. In this position the incident and

the refracted beam share the same optical path but in the opposite direction of propagation. The wavelength dependence then is exploited by [47]:

$$2\sin(\theta_l) = \frac{\lambda}{d} \tag{3.51}$$

where θ_l is the Littrow angle and it is defined with respect to the normal plane of incidence, d is the groove spacing. Both of these elements have the ability to create an angular dispersion, and then with a proper back reflection, it is possible to select only those wavelengths properly aligned. In most cases this is not enough to select a single axial mode, but these devices operate as bandpass filters, and only a narrow bandwidth can oscillate in the cavity.

3.1.4 Resonator Stability

In order to work, a laser needs a laser resonator, namely an optical cavity. Different cavities leads to different mode resonators. The shape of a cavity was studied by Kogelnik and Li, and they found that some constraints are needed in order to have a stable resonator. A stable cavity is interesting because the mode resonator is self-sustainable in time. The stability depends on the cavity length and the mirrors radius of curvature. In Appendix A this problem has been addressed, and it has been simplified applying the matrix formalism to Gaussian beams.
Let us take an optical cavity with two mirrors. In this framework, the condition necessary for stability is:

$$-1 < \frac{A+D}{2} < 1 \tag{3.52}$$

where A and D are components of the round-trip matrix M which defines the optical resonator:

$$M = \begin{bmatrix} A & B \\ C & D \end{bmatrix} = M_- M_+ \tag{3.53}$$

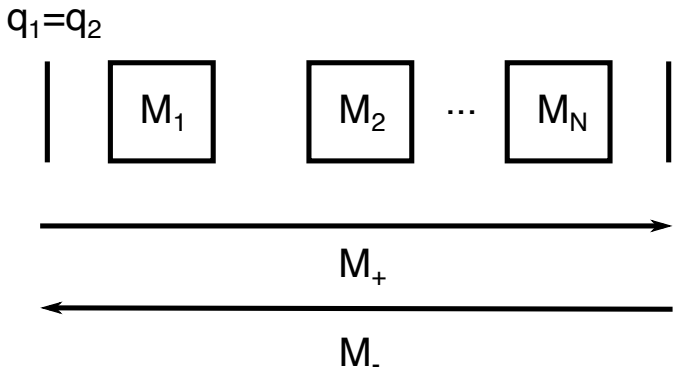

Figure 3.7: Optical Resonator with Matrix Formalism

where M_- and M_+ are the forward and backward matrices:

$$M_+ = \prod_{i=N}^{1} M_i \qquad M_- = \prod_{i=1}^{N} M_i \tag{3.54}$$

For a simple cavity composed by two mirrors and a free-space propagation between them, the round-trip matrix M is:

$$M = \begin{bmatrix} A & B \\ C & D \end{bmatrix} = \begin{bmatrix} 1 & 0 \\ -2/R_1 & 1 \end{bmatrix} \begin{bmatrix} 1 & L \\ 0 & 1 \end{bmatrix} \begin{bmatrix} 1 & 0 \\ -2/R_2 & 1 \end{bmatrix} \begin{bmatrix} 1 & L \\ 0 & 1 \end{bmatrix} \tag{3.55}$$

where R_1 and R_2 are the ray of curvature of the mirrors and L is the cavity length. It leads to:

$$\frac{A+D}{2} = 1 - \frac{2L}{R_1} - \frac{2L}{R_2} + \frac{2L^2}{R_1 R_2} \tag{3.56}$$

which means:

$$\frac{A+D}{2} = 2\left(1 - \frac{L}{R_1}\right)\left(1 - \frac{L}{R_2}\right) - 1 \tag{3.57}$$

Thus, two coefficients are defined, g_1 and g_2:

$$g_1 = 1 - \frac{L}{R_1} \qquad g_2 = 1 - \frac{L}{R_2} \tag{3.58}$$

which leads to:

$$\frac{A+D}{2} = 2g_1 g_2 - 1 \tag{3.59}$$

and exploiting the stability condition from equation 3.52:

$$0 < g_1 g_2 < 1 \tag{3.60}$$

All cavity configurations are unstable unless they correspond to points located inside the area enclosed by the hyperbola $g_1 g_2 = 1$ and the axes, which is called stability zone.

As it can be seen from figure 3.8 on the following page, there are different two mirror resonator configurations which are stable. The stability conditions from and gives information about the cavity but not about the generalized ray of curvature itself. Let us take a general resonator composed by two mirrors with infinite ray of curvature $R = \infty$ and some optical elements in between which are described by a matrix. Thus the M matrix describing the resonator, starting from mirror 1, is:

$$M = \begin{bmatrix} D_+ & B_+ \\ C_+ & A_+ \end{bmatrix} \begin{bmatrix} A_+ & B_+ \\ C_+ & D_+ \end{bmatrix} = \begin{bmatrix} 2A_+D_+ - 1 & 2B_+D_+ \\ 2A_+C_+ & 2A_+D_+ - 1 \end{bmatrix} \tag{3.61}$$

where the properties $A_+ = D_-$, $D_+ = A_-$, $B_+ = B_-$, $C_+ = C_-$ have been exploited. The first consideration is that $A = D$. Moreover, since after a round-trip the

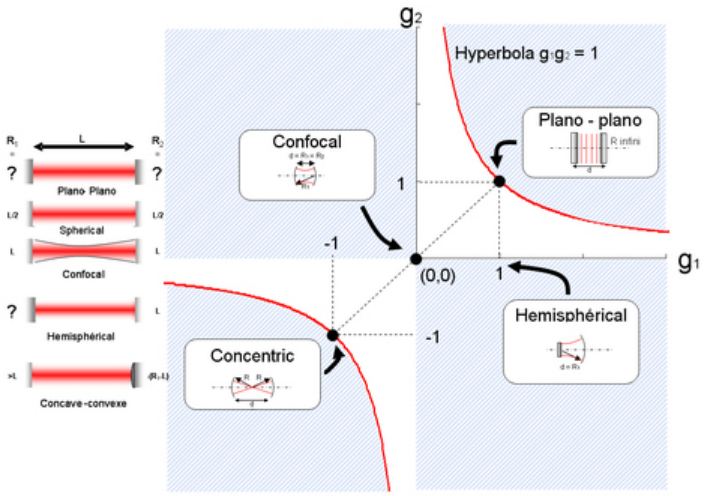

Figure 3.8: Optical resonator stability zones [48].

generalized ray of curvature q must be the same, it has to fulfill the condition from 61:

$$Cq^2 + (D - A)q - B = 0 \tag{3.62}$$

which defines the equality of q after a round-trip. It leads to a condition for q_1 on mirror 1:

$$q_1 = j\sqrt{-\frac{B}{C}} = j\sqrt{-\frac{B_+D_+}{A_+C_+}} \tag{3.63}$$

Since the mirror has $R = \infty$, and q_1 must match the ray of curvature, the generalized ray of curvature is purely imaginary, with $B_+D_+/A_+C_+ < 0$. The same can be done exchanging the matrices M_+ and M_- in order to obtain q_2:

$$q_2 = j\sqrt{-\frac{A_+B_+}{C_+D_+}} \tag{3.64}$$

The same principle applies for q_2, and the condition is $A_+B_+/C_+D_+ < 0$. Let us now define the two-mirror resonator still composed by two mirrors with infinite ray of curvature $R = \infty$, but also with two lenses $f_1 = R_1$ and $f_2 = R_2$.
The results just shown can be still used, and the M_+ matrix can be described as:

$$M_+ = \begin{bmatrix} g_1 & L \\ -\frac{(1-g_1g_2)}{L} & g_2 \end{bmatrix} \tag{3.65}$$

Then, since:

$$\frac{1}{q} = \frac{1}{R} - j\frac{\lambda}{\pi w^2} \tag{3.66}$$

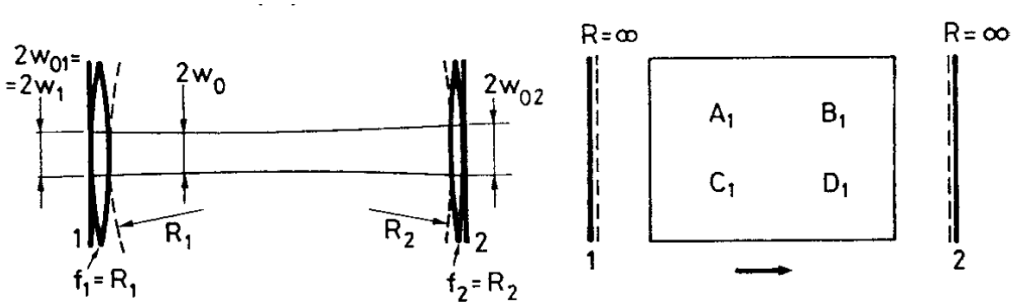

Figure 3.9: Optical resonator stability [44].

It is possible to obtain, exploiting equation 3.63, the beam waist on mirror 1:

$$w_1 = \sqrt{\frac{L\lambda}{\pi}}\left[\frac{g_2}{g_1(1-g_1g_2)}\right]^{1/4} \tag{3.67}$$

The same can be applied exploiting equation 3.64 for mirror 2:

$$w_2 = \sqrt{\frac{L\lambda}{\pi}}\left[\frac{g_1}{g_2(1-g_1g_2)}\right]^{1/4} \tag{3.68}$$

which varies in function of g_1 and g_2. The smallest beam width inside the cavity, called beam waist can be found:

$$w_2 = \sqrt{\frac{L\lambda}{\pi}}\left[\frac{g_1g_2(1-g_1g_2)}{(g_1+g_2-2g_1g_2)^2}\right]^{1/4} \tag{3.69}$$

3.1.5 Laser Beam Properties

Laser light has particular properties, which is what makes the laser so unique with respect to all the light-sources ever encountered in nature. An extended description of laser beams is found in Appendix A. Let us describe the most important:

- **Monochromaticity**

  A laser beam has a very narrow linewidth. It is defined by two factors. The former is the lasing line of the transition 2→1 whose frequency is ν_{21}, with a inhomogeneously or homogeneously broadened gain lineshape $g^*(\nu,\nu_0)$. The latter is the oscillating axial mode which is selected between the modes whose gain is above threshold. Nonetheless there is a lower quantum limit to the bandwidth of a linewidth and it is defined by the Schawlow–Townes equation:

  $$\Delta\nu_l = \frac{\pi h\nu(\Delta\nu_g)^2}{P_{out}} \tag{3.70}$$

  where $\Delta\nu_g^2$ is the resonator gain bandwidth at FWHM. This limit is due to spontaneous emission, which is a quantum phenomena.

- **Spatial Coherence**

  The spatial coherence describes the relationship of the electric field in the transversal plane of the beam. Laser beams have a high spatial coherence, which means that there is a constant phase relationship between two points of the beam, i.e. the wavefronts are well defined.

- **Temporal Coherence**

  The temporal coherence describes the autocorrelation of the electric field at a given position at different time. This means that the coherence of the beam remains the same in time. There is a tight relationship between the temporal coherence and the linewidth of the laser beam, because narrower is the linewidth higher is the temporal coherence, i.e. the phase of the electric field in time. A laser beam possesses both temporal and spatial coherence, which means that there is a constant phase relationship between two points of the wavefront or the temporal profile.

- **Directionality**

  A laser possesses an high directionality, since the laser beam is composed by only those axial modes which can oscillate inside the resonator cavity. Eventually, due to diffraction, the beam will expand. The directionality of a laser beam is defined by its divergence, i.e. how much a the beam size expands in a given amount of space. From Appendix A, the half angle divergence θ is:

  $$\theta = M^2 \frac{\lambda}{\pi w_0} \tag{3.71}$$

  where M^2 is the beam quality and w_0 is the beam waist radius.

- **Brightness**

  The brightness, which stands for radiance in the SI, is a measure of the intensity of a laser beam over a given distance. It is measured in $\mathrm{W{\cdot}cm^{-2}{\cdot}sr^{-1}}$.

- **Polarization**

  The polarization of light describes the behaviour of the temporal electric field in an electromagnetic wave. With respect to the most common light sources a laser beam might possess a well defined polarization, such as linear or circular, and it is easily manipulable. Polarization is important because a lot of radiation-matter interaction relies on it, for example light absorption, reflection and refraction, light scattering.

3.2 Mode-Locking

Until now it has been described the output radiation of a laser in a steady-state condition, where the output power is equal to the average power, so continuous wave (CW). There are techniques to squeezing the output power in order to generate packages of energy, i.e. pulses. A mode of laser operation for obtaining energetic and short pulses is known as *Mode-Locking* (ML). This laser operation creates pulses

in the fs-ps range and in an ordered manner, i.e. a pulse-train, whose repetition rate is linked to the cavity length.
Let us take a laser cavity. The axial modes which can oscillate inside the cavity have a fixed angular frequency:

$$\omega_q = q\frac{\pi c}{l_0} \qquad \Delta\omega = \frac{\pi c}{l_0} \tag{3.72}$$

Let us suppose to have N axial modes oscillating in the cavity, with an amplitude $\mathcal{E}_n$ and a phase φ_n, thus the spatio-temporal evolution of the electric field inside the cavity is:

$$\mathcal{E}(z,t) = \sum_{n=0}^{N-1} \mathcal{E}_n e^{j\varphi_n} e^{j\omega_n(t-z/c)} \tag{3.73}$$

where $\omega_n = \omega_0 + n\Delta\omega$ is the angular frequency of the n-th axial mode and it is defined with respect to a central angular frequency ω_0.
Let us set the modes to have the same amplitude, and an initial phase equal to zero:

$$\mathcal{E}_n = \mathcal{E}_0 \qquad \varphi_n = 0 \tag{3.74}$$

So:

$$\mathcal{E}(z,t) = \sum_{n=0}^{N-1} \mathcal{E}_0 e^{j(\omega_0+n\Delta\omega)(t-z/c)} = N\mathcal{E}_0 \frac{e^{jN\Delta\omega(t-z/c)}-1}{e^{j\Delta\omega(t-z/c)}} e^{jN\omega_0(t-z/c)} \tag{3.75}$$

Then the internal intensity is:

$$I(z,t) = |\mathcal{E}(z,t)|^2 = N^2\mathcal{E}_0^2 \frac{1-\cos(Nk)}{1-\cos(k)} = N^2\mathcal{E}_0^2 \frac{\sin^2(Nk/2)}{\sin^2(k/2)} \tag{3.76}$$

where $k = (\Delta\omega(t-z/c))$. This function intensity is periodic in time and describes a pulse train. It is composed by major peaks, where there is a complete constructive interference among all the modes, and minor peaks, where the constructive interference is only partial. The major peaks have their maximum at $t = kT$, where $\forall\, k \in \mathbb{Z}$, and whose value is N^2 times the amplitude of a mode $\mathcal{E}_0$. The average intensity is $N\mathcal{E}_0^2$. On the sides of these peaks the zeros are at $t = \pm T/N$, moreover between two major peaks there are $N-2$ minor peaks. The axial modes can be seen as part of a Fourier-series expansion of a periodic function, whose period is $T = 1/\Delta\nu = 2l_0/c$, and represents a pulse-train with a pulse repetition rate (PRR) equal to $1/T$.
Let us suppose to have a laser cavity running in continuous wave, the N axial modes oscillating would have a random phase between each other, so the internal laser intensity would be the sum of the intensity of each mode:

$$I_{CW,avg} = I_{CW,max} = \sum_{n=0}^{N-1} I_n = N\mathcal{E}_0^2 \tag{3.77}$$

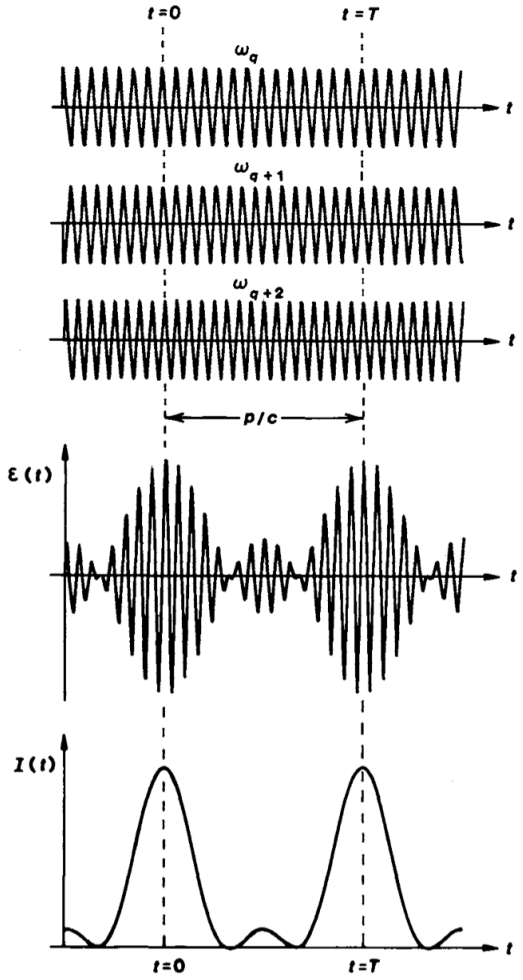

Figure 3.10: Mode coupling with $\varphi_n = 0$ in Mode Locking [45].

which is both the instantaneous, the average intensity and thus the maximum intensity in CW operation. On the other hand, for a mode-locked laser, from 3.76 the maximum intensity is:

$$I_{ML,max} = N^2\mathcal{E}_0^2 \tag{3.78}$$

and the average:

$$I_{ML,avg} = N\mathcal{E}_0^2 \tag{3.79}$$

The ratio between the average and maximum intensity in CW and ML is:

$$\frac{I_{ML,max}}{I_{CW,max}} = N \qquad \frac{I_{ML,avg}}{I_{CW,avg}} = 1 \tag{3.80}$$

so, while the average intensity is the same, the instantaneous intensity is not, and the mode-locking squeezes the energy in pulses which have a peak intensity of N. Moreover, as it can be seen from equation 3.76, increasing the number of the in-phase axial modes N gives not only pulses with higher peak energy but also with shorter duration in time.
If the amplitude of the axial modes $\mathcal{E}_n$ is not equal for all of them but it follows a gaussian distribution, such as for some atomic transition lineshapes $g^*(\nu, \nu_0)$, the result is a pulse train with no minor peaks and with the pulses which have a gaussian shape.
The mode-locking, in order to work, needs a laser cavity which fulfills two conditions:

- There must be a way such that it is possible for all the axial modes above gain threshold to oscillate inside the cavity. It is done through a device which modulates the losses and allows an oscillation under the form of a pulse only when the axial modes are coupled together.

- It is necessary that the axial modes are locked in phase. This requirement arises a fundamental issue regarding the phase mode-locking after a round-trip. The variation of the velocity of the light with respect to its wavelength in the cavity, ie. the chromatic dispersion, cannot be neglected. This effect especially involves the gain medium. When the gain bandwidth is above a certain limit, the resulting pulse dramatically suffers from dispersion, and an additional device is needed to tackle this requirement.

The mode-locking technique is divided in two main methods:

- **Active Mode-Locking**

  It exploits an active modulator, usually an acusto-optic due to its velocity, in order to periodically modify the resonator losses, which have a sinusoidal-like temporal behaviour. A pulse is generated when the resonator losses are minimized, and the increased losses in the other time frames prevent the cavity to oscillate. It can generate pulses with pulse duration of picoseconds. The main limits of this technique is the need of a synchronization with the pulse circulating in the cavity.

- **Passive Mode-Locking**

  It involves a passive element, called saturable absorber, which modulates the inserted losses by the magnitude of radiation fluence at laser wavelength which incides on it. The energy of a generated pulse is enough to saturate the absorber and minimize the losses. Virtually this technique can provide much shorter pulses, because the saturable absorber is a much faster loss modulator.

In this work the passive mode-locking was exploited, only this technique will be explained in detail. So, let us describe the functioning of a saturable absorber in order to properly address the subject.

3.2.1 Saturable Absorbers

A saturable absorber (SA) is an optical element which has a transmission function which depends on the incident intensity at a given wavelength. The material becomes more transparent as the intensity increases, and at high intensity values the losses saturate and the material becomes completely transparent, i.e. it bleaches [49]. At this point, the material has its highest transmission. The bleaching process is due to the saturation of a spectral transition, which depends on the material.

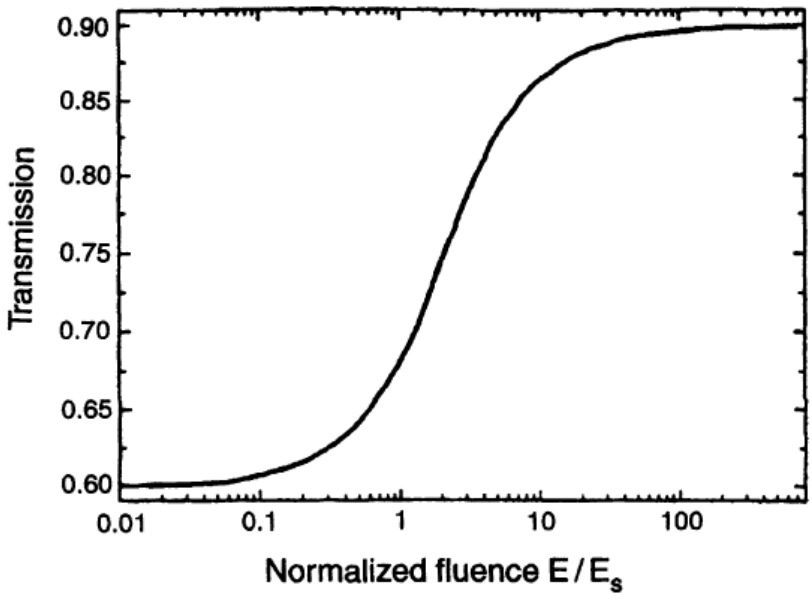

Figure 3.11: Nonlinear transmission of a SA in function of normalized fluence [18].

Such a material can be used to add losses inside a cavity in order to generate short pulses. The saturable absorber must have high absorption at laser wavelength, otherwise it will not work correctly. The most important properties of saturable absorbers are:

- The modulation depth ΔR, which is the maximum possible change in optical loss.
- The non saturable losses l_{ns}, which are the intrinsic losses of the device.

- The saturation energy for the saturable absorber E_{sa}, which is the energy needed to reduce the saturable losses $1/e$ of its initial value. The saturation fluence is the saturation energy divided the mode area, $AE_{sa} = F_{sa}$.

- The recovery time τ_{re} is the time necessary to unsaturate the SA after it has been completely bleached. The relationship between the recovery time and the pulse duration defines the dynamics of SA response. In a mode locked laser the SA does not have a tight constraint on the recovery time.

- The damage fluence, which defines an upper limit of the energy per unit area sustained by the saturable absorber before a permanent phyisical damage.

In order to exploit the mode-locking technique, the saturable fluence of the SA must be much smaller than the saturable fluence of the gain medium [50]. If this is not true, the SA does not saturates losses, and pulse generation isn't possible.

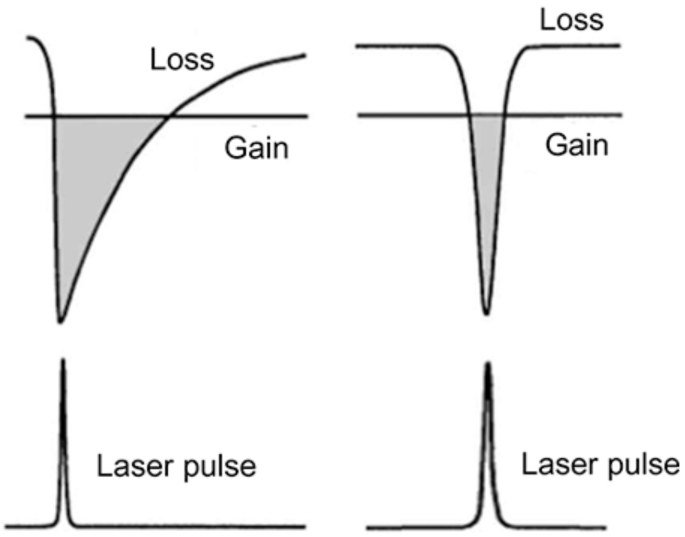

(a) Slow saturable absorber **(b)** Fast saturable absorber

Figure 3.12: Difference in SA recovery time [50]

The behaviour of a saturable absorber can be described by an equation:

$$l_{sa}(t) = l_{ns} + q(t) \tag{3.81}$$

where $l_{sa}(t)$ is the SA loss coefficient, l_{ns} is the non saturable loss coefficient, which takes into account the intrinsic loss of the SA, and $q(t)$ is the saturable loss coefficient. Its temporal variation is:

$$\frac{\partial q(t)}{\partial t} = \frac{q(t) - q_0}{\tau_{re}} - \frac{q(t)P_i(t)}{E_{sa}} \tag{3.82}$$

where q_0 is the small-signal saturable loss coefficient and τ_{re} is the recovery time of the SA. The small-signal saturable loss q_0 is the loss that can be bleached, when the

intracavity intensity is higher than the saturation intensity. The modulation depth of an SA is described as:

$$\Delta R = 1 - e^{-2q_0} \approx 2q_0 \tag{3.83}$$

which holds for $q_0 \ll 1$, a constraint which is usually fulfilled. ΔR is the saturable absorber modulation depth, and defines the maximum amount of variation of optical loss. The $P_i(t)$ and E_{sa} are respectively the intracavity power and the SA saturation energy:

$$E_{sa} = P_{sa}\tau_{re} = \frac{h\nu_i A_{eff,sa}}{\sigma_{ai,sa}} \tag{3.84}$$

From the saturable absorber point of view, $l_{sa}(t)$ can be considered the absorption coefficient, while l_{ns} the non saturable absorption. Moreover:

$$T_{sa} = 1 - l_{ns} - q_0 \tag{3.85}$$

where T_{sa} is the small-signal saturable absorber transmission.
Let us describe two types of SA: fast and slow saturable absorber. The former has a recovery time τ_{re} much smaller than the pulse duration τ_p, the latter has a τ_{re} which can be comparable or even longer than τ_p.
For a fast SA, so $\tau_{re} \ll \tau_p$ the equation 3.82 becomes:

$$0 = \frac{q(t) - q_0}{\tau_{re}} - \frac{q(t)P_i(t)}{E_{sa}} \tag{3.86}$$

which means:

$$q(t) = \frac{q_0}{1 + P_i(t)\tau_{re}/E_{sa}} = \frac{q_0}{1 + P_i(t)/P_{sa}} = \frac{q_0}{1 + I_i(t)/I_{sa}} \tag{3.87}$$

where $P_{sa} = E_{sa}/\tau_{re}$.
So the total losses added by a fast SA are:

$$l_{sa}(t) = l_{ns} + \frac{q_0}{1 + I_i(t)/I_{sa}} \tag{3.88}$$

If the peak intensity of the pulse is much smaller than the saturation intensity of the fast SA a linearization can be carried out:

$$l_{sa}(t) \approx l_{ns} + q_0 - q_0\frac{I_i(t)}{I_{sa}} \tag{3.89}$$

This is not wanted, because the goal of the pulse is to effectively saturate the SA. Anyway, the linearization is useful to obtain an analytical solution, and it will be exploited in the next section.

On the other hand, a slow saturable absorber is approximated by a different equation. Let us recall equation 3.82, but this time $\tau_p \ll \tau_{re}$, which means that it is possible to neglect the recovery of the absorber during the pulse excitation:

$$\frac{\partial q(t)}{\partial t} = -\frac{q(t) - q_0}{\tau_{re}} - q(t)\frac{P_i(t)}{E_{sa}} \tag{3.90}$$

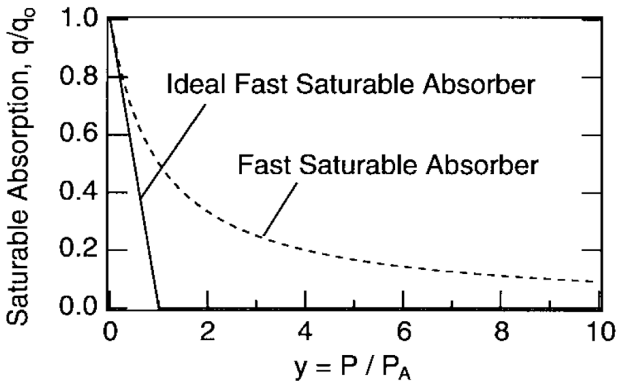

Figure 3.13: Ideal versus real response of a fast SA [51].

This equation obviously tends to 3.102 when $\tau_{re} \to 0$ because it describes a fast SA. An approximation:

$$\frac{\partial q(t)}{\partial t} \approx -\frac{q(t)P_i(t)}{E_{sa}} \tag{3.91}$$

If:

$$P_i(t) = E_p f(t) \qquad \int_0^{\tau_r} f(t)\,dt = 1 \tag{3.92}$$

Then the solution is:

$$q(t) = q_0 \exp\left[-\frac{E_p}{E_{sa}} \int_0^t f(t')\,dt'\right] \tag{3.93}$$

So depends on an integration of the pulse energy E_p over a period, since the recovery time is slower than the pulse itself.

3.2.2 SESAMs

A semiconductor saturable absorber mirror (SESAM) is a mirror structure with an incorporated saturable absorber which is made in semiconductor technology, for example MOCVD technique, MOVPE or MBE [18].

This aspect leads to a complete customization of device parameters such as absorption wavelength, saturation energy and recovery time, once the semiconductor materials are known. On the other hand, the fabrication process is not easy, and it is expensive. They work either in reflection or transmission. The simplest structure of a SESAM is showed in figure 3.14.

The saturable absorber is a quantum well with an energy gap equal to the laser photon energy, while the reflection is made through a Bragg mirror. The quantum well exploits the valence band and conduction band typical of semiconductors. When the intracavity intensity is low, photons are absorbed and the electrons go to the conduction band.

Thus, there are some losses due to absorption. On the other hand, when the intracavity intensity is high, a lot of photons are absorbed and the lower levels of the

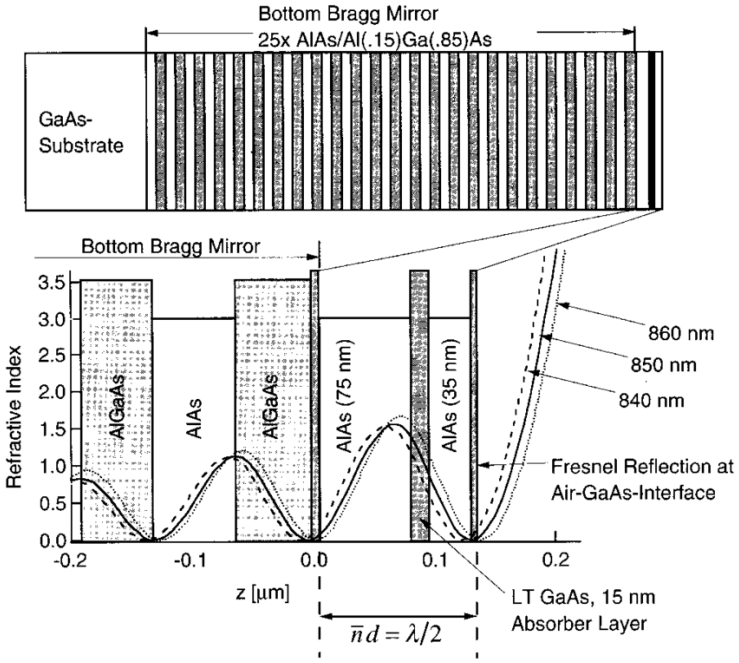

Figure 3.14: Typical SESAM design [18].

conduction band are completely filled, and then the quantum well becomes almost transparent, because it cannot store other electrons in the conduction band. After some time, the quantum well recovers its original absorption.

The phases involved in the process are four. In phase one the optical pulse is absorbed and there is a coherent phase relationship between the pulse and the excitation. If the intracavity intensity is high enough, the SA is bleached. In phase two the carriers start to exchange energy among each other under the form of scattering, this process is called thermalization and is in the range of $\approx$ hundreds of fs. In phase three the carriers which have been involved so far exchange energy with the lattice involving phonons, thus changing its wavenumber within the band; the time frame is $\approx$ ps. The phase four is the electron-hole recombination, which take place in time scales of $\approx$ ns.

It is clear that the total recovery of the absorber from bleaching takes nanoseconds. This can be overcame if the quantum well is provided of a so-called mid-gap trap. It is a intermediate energy state between the conduction and valence band made by defects, which are completely under control with semiconductor technology. These traps work on the sub-ps tome scale allowing to a deplete of the conduction band and then a faster recovery of the absorption capacity of the SA.

It is the quantum well that defines the SESAM modulation depth, recovery time and saturation fluence. In general, all these parameters depend on the laser wavelength, the absorber material and the optical field penetration into the absorber structure. A lot of SESAMs are in the *antiresonant* form. They have an absorber section put on the top which limits the incident intensity on the real saturable absorber. It has a thickness such that the SA has a broadband reflectivity and a very low GDD. Moreover, the intrinsic losses are lowered and the saturation intensity can reach high

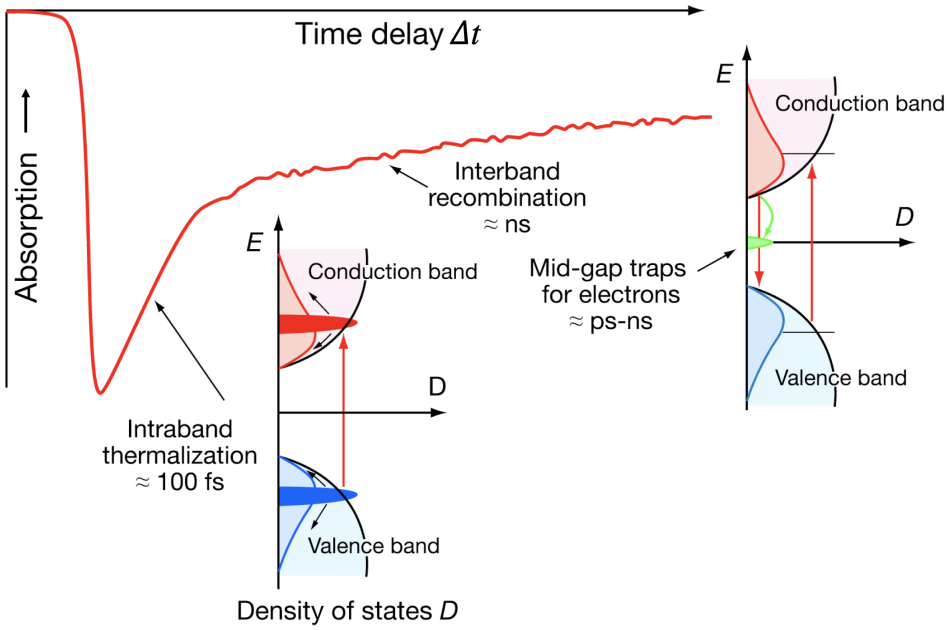

Figure 3.15: Conduction and valence band of a direct gap semiconductor [50].

values, because not all the incident intensity is transmitted to the saturable part of the absorber. The round-trip phase is:

$$\varphi_r = (2m+1)\pi \qquad \forall\, m \in \mathbb{N} \tag{3.94}$$

The most common SESAM is exploited in 1 μm wavelength region. The quantum well is made of InGaAs where the content of indium determines the energy-gap of the SA. The Bragg mirror is made of GaAs and AlAs on a GaAs substrate. The SESAM shown in figure 3.15 is suited for $\approx$ 860 nm and thus it must work at shorter wavelengths. The semiconductors and their composition is properly adjusted.

3.2.3 Quasi-Solitonic Passive Mode-Locking

It involves a SESAM to insert variable losses, and one or more components to counteract the normal intracavity chromatic dispersion in order to sustain a *quasi-solitonic regime*. A pulse in this regime must satisfy the *Haus's master equation* of solitonic mode locking [52]. It is an equation which describes the temporal evolution of the pulse envelope, in SVEA approximation, based on linearized differential operators:

$$\begin{aligned}\frac{\partial \mathcal{E}(\tau_r,t)}{\partial \tau_r}\tau_r = &\left(-jD\frac{\partial^2}{\partial t^2} + j\delta\left|\mathcal{E}(\tau_r,t)\right|^2\right)\mathcal{E}(\tau_r,t) \\ &+ \left(g_s - L - T_{oc} + \frac{g_s}{\Delta\omega_g^2}\frac{\partial^2}{\partial t^2} - q(t)\right)\mathcal{E}(\tau_r,t)\end{aligned} \tag{3.95}$$

Figure 3.16: Typical SESAM

This equation describes the laser dynamics in two time scales, the round-trip time τ_r and the pulse time t. Focusing on the resolution of the equation with respect to t gives the pulse shape solution, which is our goal.
This equation is composed by two terms. The first term is about the chromatic dispersion in the cavity. In particular, $D = 1/2k''z$ is the linearized intracavity GDD, whereas δ is the nonlinear SPM coefficient. The second term regards the overall net gain, and it is defined by the round-trip saturated gain g_s, the intrinsic losses L, the output coupler T_{oc}, the gain dispersion $g_s/\Delta\omega_g^2$, and q_0 the saturable losses of a SA.

Let us forget about the chromatic dispersion and build the second term of the master equation. This part of the equation answers to the first constraint of a mode-locked laser, which is the locking of the axial modes. In the frequency domain the amplification of the electric field after a pass through the gain medium is:

$$\tilde{\mathcal{E}}_{out}(\omega) = \exp\left(\frac{g_s}{2}\frac{1}{1+\left(\frac{\omega-\omega_0}{\Delta\omega_g}\right)^2}\right)\tilde{\mathcal{E}}_{in}(\omega) \tag{3.96}$$

where g_s is the round-trip saturated gain and it follows the equation 2.149, $\Delta\omega_g$ is the medium's gain bandwidth at FWHM, ω_0 is the central wavelength. This is the homogeneously boadened gain medium described by a Lorentzian atomic lineshape. For a laser working in CW, the saturated gain is equal to the losses, which means that it follows the equation 3.11, so $2g_s = L + T_{oc}$. The equation 3.96 can be approximated as:

$$\tilde{\mathcal{E}}_{out}(\omega) \approx \left[1 + \frac{g_s}{2}\left(1 - \left(\frac{\omega-\omega_0}{\Delta\omega_g}\right)^2\right)\right]\tilde{\mathcal{E}}_{in}(\omega) \tag{3.97}$$

In the time domain becomes:

$$\mathcal{E}_{out}(t) \approx \left[1 + \frac{g_s}{2}\left(1 + \frac{1}{\Delta\omega_g^2}\frac{\partial^2}{\partial t^2}\right)\right]\mathcal{E}_{in}(t) \tag{3.98}$$

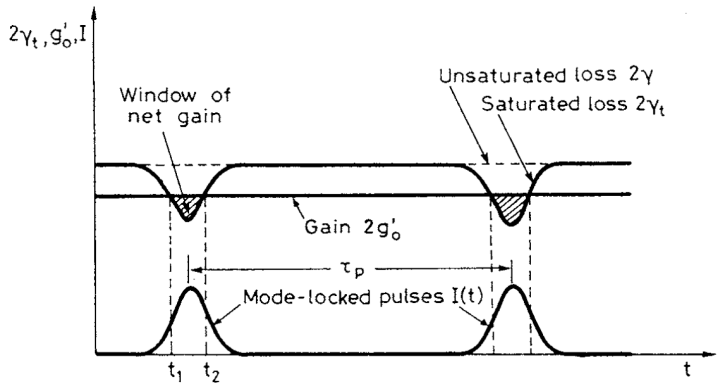

Figure 3.17: Pulse train [45].

On the other hand the round-trip losses are:

$$\mathcal{E}_{out}(t) = \sqrt{1 - L_n - q_0\left(1 - \frac{|\mathcal{E}_{in}(t)|^2}{P_{sa}}\right)}\,\mathcal{E}_{in}(t) \tag{3.99}$$

where $L_n = L + T_{oc} + l_{ns}$ are the intrinsic losses, the output coupler transmittivity and and the non saturable losses of the SA. The saturable losses of a SA are:

$$q(t) = \frac{q_0}{1 + I_i(t)/I_{sa}} \tag{3.100}$$

Moreover:

$$E_p(t) = \int_{-\infty}^{+\infty} |\mathcal{E}_{in}(t)|^2 \, dt \qquad P_i(t) = |\mathcal{E}_{in}(t)|^2 \tag{3.101}$$

where $E_p(t)$ is the pulse energy, $P_i(t)$ is the power intracavity, $|\mathcal{E}_{in}(t)|^2$ is the square modulus of the instantaneous pulse electric field. This means that equation 3.100 can be expressed through the electric field:

$$q(t) = \frac{q_0}{1 + |\mathcal{E}_{in}(t)|^2 / P_{sa}} \tag{3.102}$$

This linearization it is necessary to find an analytical solution, even though it does not adhere to the real behaviour of a fast SA. The last term is the saturable loss of a fast SA linearly approximated from equation 3.87. So:

$$\frac{q_0}{1 + |\mathcal{E}_{in}(t)|^2 / P_{sa}} \approx q_0\left(1 - \frac{|\mathcal{E}_{in}(t)|^2}{P_{sa}}\right) \tag{3.103}$$

Then the round-trip losses can be approximated too:

$$\mathcal{E}_{out}(t) \approx \left[1 - \frac{L_n}{2} - \frac{q_0}{2}\left(1 - \frac{|\mathcal{E}_{in}(t)|^2}{P_{sa}}\right)\right]\mathcal{E}_{in}(t) \tag{3.104}$$

The sum of the amplification process and the losses:

$$\Delta\mathcal{E} = \mathcal{E}_{out}(t) - \mathcal{E}_{in}(t) = \left[g_s + \frac{g_s}{\Delta\omega_g^2}\frac{\partial^2}{\partial t^2} - L_n - q_0 + K_r \left|\mathcal{E}_{in}(t)\right|^2 \right] \mathcal{E}_{in}(t) \tag{3.105}$$

where $K_r = q_0/P_{sa}$. The steady-state condition with respect to pulse time t is then:

$$\Delta\mathcal{E} = 0 \tag{3.106}$$

The equation 3.105 is nothing else than the second term in equation 3.95 solved at time $t \ll \tau_r$, so when the partial derivative with respect to τ_r is zero:

$$\frac{\partial\mathcal{E}(0,t)}{\partial\tau_r}\tau_r = \left(g_s - L - T_{oc} + \frac{g_s}{\Delta\omega_g^2}\frac{\partial^2}{\partial t^2} - q(t) \right) \mathcal{E}(0,t) = 0 \tag{3.107}$$

The solution is a pulse with an hyperbolic secant electric field:

$$\mathcal{E}(t) = A_0 \operatorname{sech}(t/\tau_p) \qquad\qquad A_0 = \sqrt{\frac{E_p}{2\tau_p}} \tag{3.108}$$

where A_0 is the amplitude. So that is the solution for the Haus's master equation without GVD and SPM with fast and ideally fully saturated SA. It describes a *soliton*, a pulse which preserves its spectral and temporal shape along its propagation. The relation between the pulse duration τ_p and the envelope $|\mathcal{E}_{in}(t)|^2$ at FWHM of such a pulse shape is:

$$\tau_{FWHM} = 1.76\tau_p \tag{3.109}$$

Exploiting an hyperbolic secant pulse shape the equation 3.105 at steady-state is:

$$\left[g_s - L_n - q_0 + \frac{g_s}{\Delta\omega_g^2\tau_p^2} \right] \operatorname{sech}(t/\tau_p) - \left[\frac{2g_s}{\Delta\omega_g^2\tau_p^2} - K_r A_0^2 \right] \operatorname{sech}^3(t/\tau_p) = 0 \tag{3.110}$$

where $|\mathcal{E}_{in}(t)|^2 = A_0^2$. It leads to two conditions:

$$g_s = \frac{L_n + q_0}{1 + \dfrac{1}{\Delta\omega_g^2\tau_p^2}} < L_n + q_0 = g_{s,cw} \tag{3.111}$$

$$\frac{2g_s}{\Delta\omega_g^2\tau_p^2} = K_r A_0^2 \tag{3.112}$$

From this point of view it is clear how the mode-locking works. The total losses of the cavity are:

$$L_{tot} = L_n + q_0 = g_s + \frac{g_s}{\Delta\omega_g^2\tau_p^2} \tag{3.113}$$

The saturated gain in mode-locking it is not equal to the counterpart in CW operation, but it is smaller, which means that there could not be an oscillation. The

only way to have an oscillation is under the reduction of the losses, i.e. through saturation losses, due to a pulse circulating in the cavity.
The equation 3.110 can be resolved with respect to:

$$\Delta\omega_g\tau_p = \frac{2(L_n+q_0)}{K_r E_p \Delta\omega_g} + \sqrt{\frac{4(L_n+q_0)^2}{K_r^2 E_p^2 \Delta\omega_g^2} - 1} \tag{3.114}$$

where the pulse energy E_p is the time integration of the intracavity power:

$$E_p = \int_{-\infty}^{+\infty} P_i(t)\,dt = 2A_0^2\tau_p \tag{3.115}$$

Since the gain bandwidth $\Delta\omega_g$ is defined by the medium, the variable is the pulse duration τ_p. The pulse duration is:

$$\tau_p = \frac{4g_s}{\Delta\omega_g^2 K_r E_p} \tag{3.116}$$

The minimum pulse duration is reached when:

$$\frac{2(L_n+q_0)}{K_r E_p \Delta\omega_g} = 1 \tag{3.117}$$

In an alternative way:

$$\tau_{p,min} = \frac{L_n+q_0}{K_r A_0^2 \Delta\omega_g} \tag{3.118}$$

Inserting this result in the equation 3.114 leads to a fundamental relationship between the minimum pulse duration and the gain bandwidth of the medium:

$$\tau_{p,min} = \frac{1}{\Delta\omega_g} \tag{3.119}$$

It is called Fourier-transform limit and a pulse which fulfills this condition is called Fourier-transform limited. With respect to the frequency bandwidth:

$$\tau_{FWHM}\Delta\nu = 0.315 \tag{3.120}$$

It is called Time-Bandwidth product (TBP) of a sech^2 pulse. If the peak of the pulse completely bleaches the saturable losses:

$$q_0 = K_r\,|\mathcal{E}_{in}(t)|^2 \tag{3.121}$$

then, putting together equation 3.109, equation 3.112 and equation 3.121:

$$\tau_{FWHM,min} = 1.76\sqrt{\frac{2g_s}{\Delta\omega_g^2 q_0}} \tag{3.122}$$

which gives a good estimate of the shortest pulse achievable as solution to the Haus's master equation without GVD and SPM taking into account a fast and ideally fully saturated SA.

It is clear from equation 3.119 that it is necessary a broadband gain bandwidth for reaching ultrashort pulses (≈ hundreds of fs). This is connected with the second

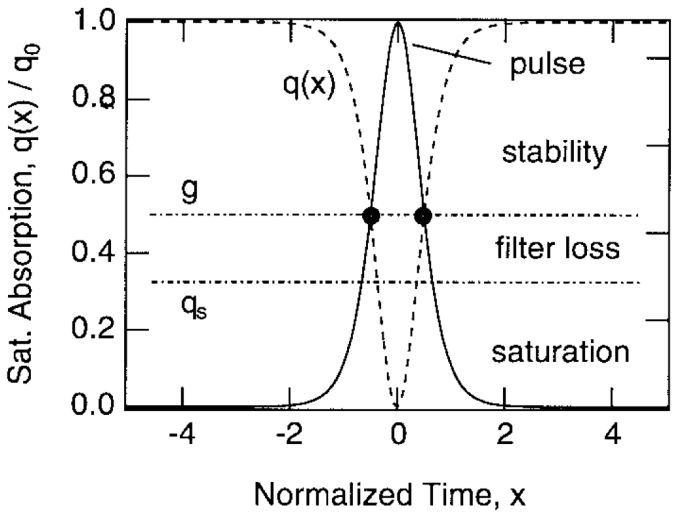

Figure 3.18: Mode locking pulse generation [51].

constraint in the mode-locking technique and the first term in the Haus's master equation 3.95. In order to address this problem, let us recall the chromatic dispersion in Appendix B.
The high intensity inside the cavity arises nonlinearities, especially in the gain medium. The most important phenomena is the *Optical Kerr Effect*, a $\chi^{(3)}$ effect that modifies the refractive index with respect to the intensity:

$$n(\omega, I) = n_0(\omega) + n_2 I(t) \tag{3.123}$$

which means parts of the pulse travel at a different velocity, thus they accumulate a phase difference among each other. It is described in detail in Appendix C. This effect is called Self-Phase Modulation (SPM):

$$\Phi_{tot} = \Phi_0 + \Phi_{SPM}(t) = -n(\omega, I)k_0 z = -(n_0(\omega) + n_2 I(t))k_0 z \tag{3.124}$$

The additional phase is then:

$$\Phi_{SPM}(t) = -k_0 n_2 I(t) z \tag{3.125}$$

and it depends on the pulse shape. The term $\delta = k_0 n_2 z / A_i$ is called SPM coefficient. The phase added through Kerr effect must be counteracted, otherwise the pulse will not physically travel altogether. It can be done though a device which adds a certain amount of chromatic dispersion. Let us recall the first term of the Haus's master equation from 3.95.

$$\frac{\partial \mathcal{E}(\tau_r, t)}{\partial \tau_r} \tau_r = \left(-jD \frac{\partial^2}{\partial t^2} + j\delta \left| \mathcal{E}(\tau_r, t) \right|^2 \right) \mathcal{E}(\tau_r, t) \tag{3.126}$$

It is similar to:

$$\frac{\partial \mathcal{E}(z,t)}{\partial z} = \left(-jD\frac{\partial^2}{\partial t^2} + j\delta \left|\mathcal{E}(z,t)\right|^2 \right)\mathcal{E}(z,t) \tag{3.127}$$

This equation depends on time and space, and it is nothing else than the *Nonlinear Schroedinger Equation* (NSE). The NSE and the first term of the Haus's master equation share the same analytical solution. Recalling:

$$E_p(t) = \int_{-\infty}^{+\infty} \left|\mathcal{E}_{in}(t)\right|^2 dt \qquad P_i(t) = \left|\mathcal{E}_{in}(t)\right|^2 \tag{3.128}$$

The SPM can now written as:

$$\Phi_{SPM}(t) = -k_0 n_2 I(t) z = -\frac{k_0 n_2 z}{A_i}\left|\mathcal{E}_{in}(t)\right|^2 = -\delta\left|\mathcal{E}_{in}(t)\right|^2 \tag{3.129}$$

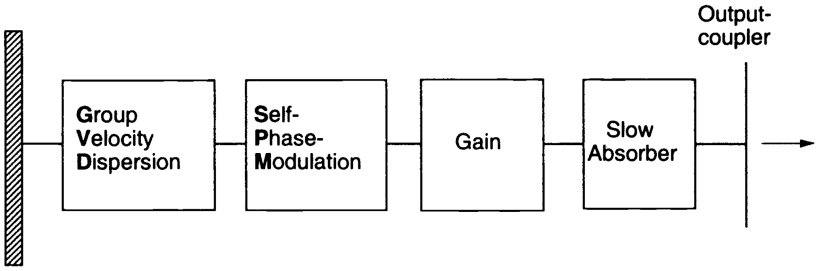

Figure 3.19: Cavity dispersion compensation [53].

The solution of the NSE in the round-trip time is still in the form of an hyperbolic secant:

$$\mathcal{E}(z,t) = A_0 \operatorname{sech}(x(z,t))e^{-j\Phi(z,t)} \tag{3.130}$$

This equation describes again a soliton. Moreover:

$$A_0 = \sqrt{\frac{E_p}{2\tau_p}} \qquad \Phi_{SPM,t} = \frac{\Phi_{SPM,max}}{2} \tag{3.131}$$

The phase added by dispersion is derived from Appendix B and it is:

$$\Phi_{disp} = \frac{D}{\tau_p^2} = \frac{1}{2\tau_p^2}k'' z \tag{3.132}$$

where k'' is the GVD or the GDD per unit length. The minimum pulse duration is reached when there is autoconsistency, meaning that the SPM by the Kerr effect and the added dispersion cancels each other out:

$$\Phi_{SPM,t} + \Phi_{disp} = 0 \tag{3.133}$$

There are also other contributions, i.e. third order effects, but their order of magnitude is lower. Their role it has been neglected. So:

$$\frac{\delta}{2}\left|\mathcal{E}_{in}(t)\right|^2 = \frac{1}{2\tau_p^2}k^{''}z \tag{3.134}$$

This equation can be simplified if the distance z along the phenomena occur is the same. Then, exploiting the definition of pulse energy $E_p = 2A_0^2\tau_p$ from equation 3.115 and equation 3.131:

$$\delta = \frac{2k^{''}z}{\tau_p E_p} \qquad\qquad k_0 n_2 = \frac{2k^{''}}{\tau_p E_p} \tag{3.135}$$

Thus the pulse duration at FWHM is, for a soliton:

$$\tau_{FWHM} = 1.76\frac{2|k^{''}|}{k_0 n_2 E_p} \tag{3.136}$$

The total solution of the Haus's master equation 3.95 for a soliton pulse is then:

$$\mathcal{E}(t) = A_0\left[\operatorname{sech}(t/\tau_p)\right]^{1+j\Phi_s} \tag{3.137}$$

where Φ_s is the overall phase accumulated by dispersion, i.e. GVD and SPM. If these two effect cancels each other out, $\Phi_s = 0$, then:

$$\mathcal{E}(t) = A_0\operatorname{sech}(t/\tau_p) \tag{3.138}$$

Then the pulse duration is equal to the connection of the solution provided by the Haus's master equation without SPM and GVD 3.116 and the solution by NSE from 3.136:

$$\tau_p = \frac{4g_s}{\Delta\omega_g^2 K_r E_p} = \frac{2|k^{''}|}{k_0 n_2 E_p} \tag{3.139}$$

which is the pulse duration for an ideally fast SA. The condition which must hold for the zero dispersion, and thus for a quasi-soliton mode locking, is:

$$\frac{|k^{''}|z}{2\delta} = \frac{g_s}{\Delta\omega_g^2 K_r} \tag{3.140}$$

Again, this equation holds for an ideally fast SA. The technique is called *quasi-soliton* because inside the laser cavity there is not a real soliton, the SPM and GVD are not counteracted all over the cavity, but they are lumped at certain points, i.e. the SPM in the crystal and the GVD at the dispersion compensation device.

The solution is more complex to find for a slow saturable absorber. In this case, the solution to the Haus's master equation without chromatic dispersion from 3.95, instead of being the equation 3.116, is:

$$\tau_{FWHM,min} \approx \frac{1.5}{\Delta\nu_g}\sqrt{\frac{g_s}{2q_0}} \tag{3.141}$$

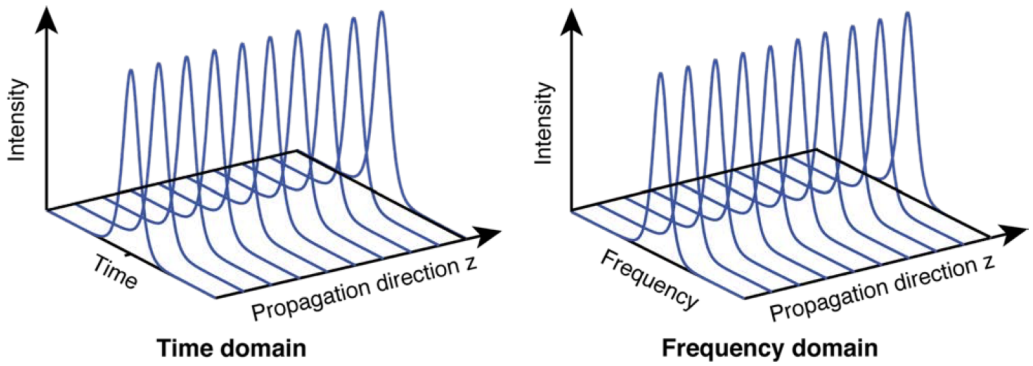

Figure 3.20: Soliton Pulse Propagation [50].

and with GDD and SPM, exploiting the solution by NSE from 3.136:

$$\tau_{FWHM} = 1.76 \frac{k''}{k_0 n_2 E_p} \tag{3.142}$$

which is half of the value obtained in the case of an ideal fast SA from 3.139.

3.2.4 Dispersion Compensation

Since $k_0 > 0$, the parameter k'' has to be negative, it means that there must be an overall anomalous dispersion inside the cavity. The intrinsic positive GVD of the cavity is defined by the sum of all its contributions, such as air, mirrors, optical components, but mainly the medium. In order to obtain a negative GVD, which overcomes the intrinsic positive GVD, it is necessary to use additional devices. It is worth noticing that the quasi-soliton mode locking is stable with a negative amount of GDD but not the other way around. The minimum pulse duration will be reached when the overall dispersion (GDD, TOD...) is zero. The complete discourse on the subject is done in the Appendix D. The anomalous dispersion is obtained mainly with the following methods:

- **Angular Dispersion**

  This technique can be exploited both in refraction, with prisms, and diffraction, with gratings. It exploits the natural wavelength-dependence of a device. So, regarding the sign of the parameter k'' of a given material, the angular dispersion provided is always negative. Let us take a prism. Then the GDD is:

$$\text{GDD} = \frac{\partial^2 \Phi}{\partial \omega^2}\bigg|_{\omega_0} = \frac{\lambda^3}{2\pi c^2} \frac{\partial^2 P}{\partial \lambda^2}\bigg|_{\lambda_0} \approx -\frac{P\omega_0}{c} \left(\frac{\partial \theta}{\partial \Omega}\bigg|_{\omega_0} \right)^2 \tag{3.143}$$

  where ω_0 is the central wavelength, θ the angle created by dispersion, which is directly connected with the refractive index $n(\omega)$ of the material, and P is the path length. The actual solution relies on two prisms: the first creates the

angular dispersion, the second fixes the wavelengths on the same wavefront, but spatially separated on the transversal plane. The GDD is far more complex:

$$\begin{aligned}\mathrm{GDD} = \frac{L_g}{c}\left[2\frac{\partial n}{\partial \omega}\bigg|_{\omega_0} + \omega_0 \frac{\partial^2 n}{\partial \omega^2}\bigg|_{\omega_0}\right] \\ - \frac{\omega_0}{c}\left(\frac{s}{\cos(\theta_3)}\right)\left(\frac{\partial^2 \theta_3}{\partial \omega^2}\bigg|_{\omega_0}\right)^2 - \frac{n\omega_0 L_g}{c}\left(\frac{\partial^2 \theta_1}{\partial \omega^2}\bigg|_{\omega_0}\right)^2\end{aligned} \tag{3.144}$$

where the positive terms take into account the positive GDD along the L_g path glass in the prisms, and the negative terms are the GDD created through angular dispersion at the interfaces. The biggest negative contribution to GDD is the dispersion accumulated between the two prisms.

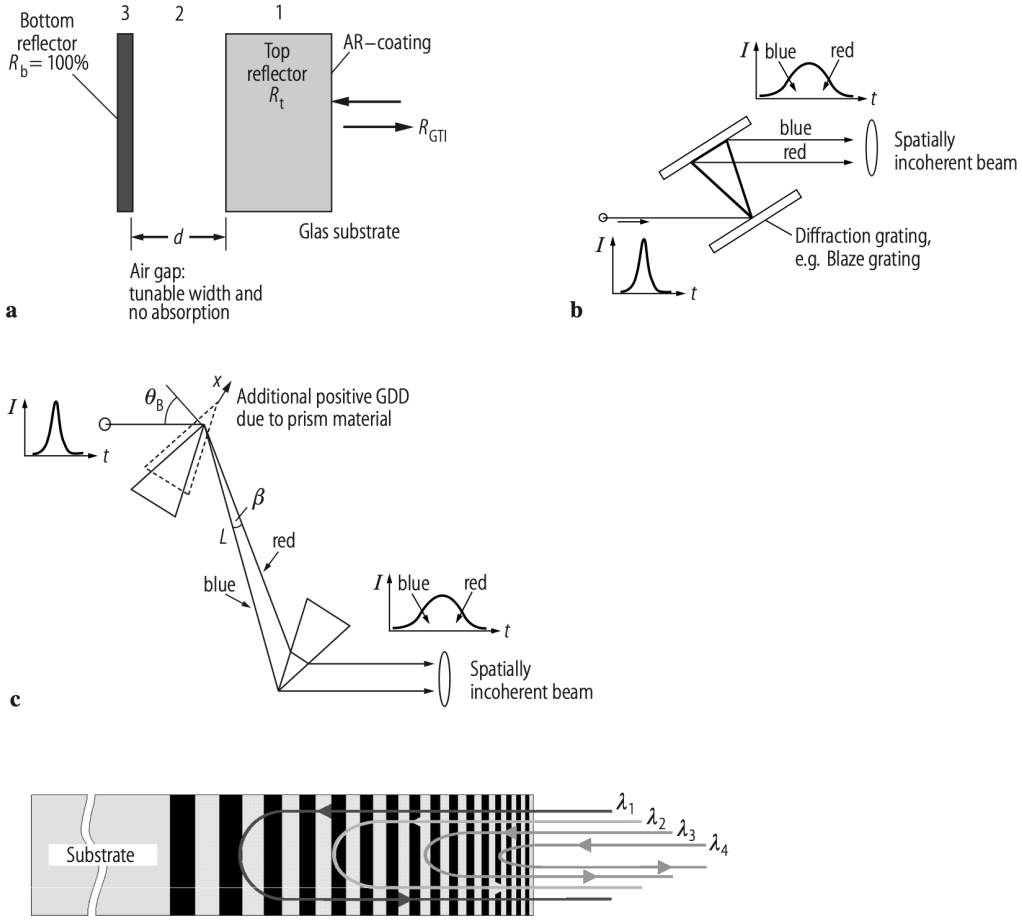

Figure 3.21: Dispersion compensation devices: (a) GTI, (b) grating pairs, (c) prism pairs, (d) chirped mirror [50].

On the other hand, the gratings exploit their wavelength-dependent diffraction of the incident beam to create an angular dispersion. It can produce a bigger

angular dispersion with respect to prisms.

$$\text{GDD} = \left.\frac{\partial^2 \Phi}{\partial \omega^2}\right|_{\omega_0} = -\frac{\lambda^3}{2\pi c d^2} \frac{L}{\cos^3(\beta(\omega_0))} \tag{3.145}$$

where L is the normal distance between the gratings, $\beta(\omega_0)$ is the diffraction angle, d is the grating constant. The prisms are preferable inside a laser cavity because they have a very low insertion loss with respect to gratings, which are usually exploited outside the cavity, where an higher GDD may be useful.

- **Dispersive Dielectric Devices**

  These are devices built with the purpose of adding a negative amount of dispersion. There are two main objects, the Gires-Tournois Interferometer (GTI) and the chirped mirrors.
  A GTI is a standing wave resonator similar to a Fabry-Perot interferometer created to work in reflection. It is composed by a low reflectivity mirror, a layer of non absorbing material, and a total reflective mirror. The free spectral range of the device is:

$$\text{FSR} = \Delta\nu = \frac{c}{2nd} \tag{3.146}$$

  where n and d are respectively the refractive index and the length of the material between the mirrors. The GDD:

$$\text{GDD} = \left.\frac{\partial^2 \Phi}{\partial \omega^2}\right|_{\omega_0} \propto d^2 \qquad \Delta\nu \propto \frac{1}{d} \tag{3.147}$$

  The GTI works within the FSR, which means that it can work with limited bandwidth pulses by design. Moreover, there is an inverse relationship between the BW available and the amount of GDD added by the GTI, so a trade off must be found for each application.
  A chirped mirror is a modified dielectric Bragg mirror with quarter-layer slices of a material with a given refractive index. They are designed to reflect the shorter wavelengths before, while the longer wavelengths propagate though the mirror, and thus increase their phase with respect to the wavelengths already reflected. This wavelength discrimination is done by modifying the slices length through the mirror in order to adjust the reflection at that given wavelength.

3.2.5 Mode-Locking Instabilities

There are different reaesons due to instability in a mode-locked laser, and mostly depend on the type of technique, the propagation of the pulse and the saturable absorber used. For a quasi-soliton mode locking, exploited with a fast SA, instabilities might arise from:

- **Excess of SPM**

An excessive amount of SPM in the cavity. Since it is mainly produced in the gain medium, a great amount of nonlinear phase shift could modify the spectral shape of the pulse.

- **Pulse Break-up**

  The cavity always adjust itself in the position of the minimum losses. It might happen that the soliton pulse breaks-up in two or more pulses, which have obviously less energy and less BW, but enough to counteract the less saturated losses of the SA. This is mainly due to the fact that pulses, beyond a certain energy, cannot sustain the gain from the limited bandwith of the gain material. So, shorter the pulse, lower is this energy threshold for pulse break-up. Moreover it may happens if the SA is too strongly saturated.

- **Continuum**

  The gain dispersion and the losses of the cavity are the reason due to the soliton loss of energy. They are called *continuum* and can be treated as a perturbation. It is a narrowwidth signal with low energy, it suffers from GDD but not SPM. Even though it is low energy, it has more gain than the actual soliton, because it experiences only the gain at the line peak. Eventually it can become more energetic and generate instability. Its importance can be reduced if the saturable absorber is fast enough to let the continuum suffer from the highest amount possible of losses.

- **Q-Switching Mode-Locking**

  If some conditions are fulfilled, the SA provides less losses to the resonator in a picosecond time scale, generating an instability in the mode-locking regime which leads to a Q-Switching behaviour [54]. It is called Q-Switching mode-locking (QML). The condition to prevent it is:

$$E_p^2 > E_{si} E_{sa} \Delta R \tag{3.148}$$

  so the pulse energy E_p must be greater than a critical value, defined by the saturation energy of the gain medium E_{si}, the saturation energy of the SA E_{sa} and its modulation depth ΔR.

  In the femtosecond regime this constraint is different. An increase in the pulse energy would increase the SPM effects, leading to a broader spectrum and thus a lower gain. This is clearly a negative feedback which makes more difficult Q-Switching instability. Thus:

$$E_{si}^2 g K^2 + E_p^2 > E_{si} E_{sa} \Delta R \qquad K = \frac{0.315}{1.76} \frac{4\pi n_2 l_g}{k'' A_i \lambda_0 \Delta \nu_g} \tag{3.149}$$

  where the QML threshold is now lowered by a factor which takes into account this negative feedback.

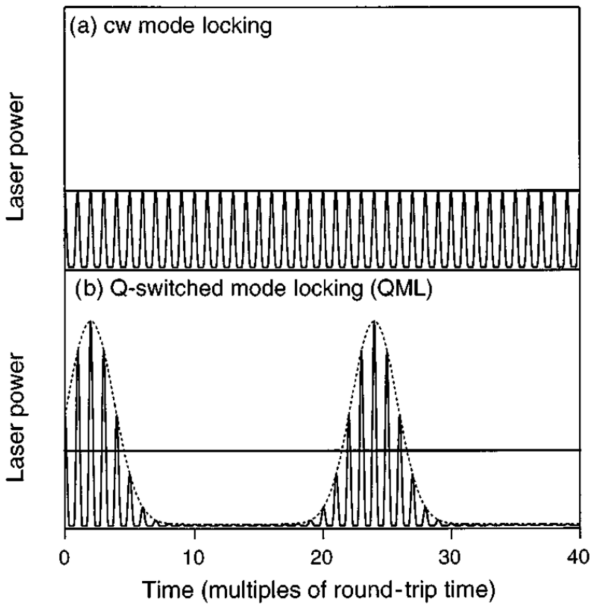

Figure 3.22: Q-Switching Mode-Locking [54]

3.2.6 Mode-Locking Guidelines

Let us describe some of the variables which have to be taken into account for a soliton passive mode-locking laser:

- There must be a trade-off when choosing the modulation depth ΔR of the SA. An high ΔR leads to shorter pulses, from equation 3.116, but also at Q-switching instabilities, from equation 3.149. So the modulation depth should be as small as possible to obtain a pulsed operation. Typically $\Delta R \approx 1\%$ or less.
- The non saturable losses l_{ns} of the SA are regarded as intrinsic losses of the cavity, lower they are, higher is the output power and efficiency of the laser.
- There is not a tight constraint on the recovery time τ_{re} of the SA. SAs with different τ_{re} lead to a different pulsed behaviour of the laser; a slow SA might help a self-start of the mode-locking.
- The pulse repetition rate (PRR) is directly related to the cavity's length. Low PRRs are difficult to reach since the cavity must be excessively long and instabilities arise.
- The typical amount of nonlinear phase shift Φ_{SPM} in a quasi-solitonic mode-locking is few millirad, above this amount instabilities in the soliton regime might arise.

Chapter 4

Laser Amplification

In this chapter it will be addressed the amplification of a laser signal and the main problems which affect it. Amplification is a process which consists in an increase of the amplitude of a given incident signal, i.e. its optical power, while preserving some of the signal characteristics. The main properties which have to be mantained from the input signal, depending on the applications, are the pulse duration, the signal bandwidth, the polarization and the beam quality. There are different ways to do that, the one presented in this chapter is laser amplification through stimulated emission, the same process exploited for lasers. Thus, an external energy source, i.e. a pump, excites the atoms in the gain medium, which will increase the optical power of the signal through energy extraction. The main difference with a laser is the cavity, which is not present for an amplifier.

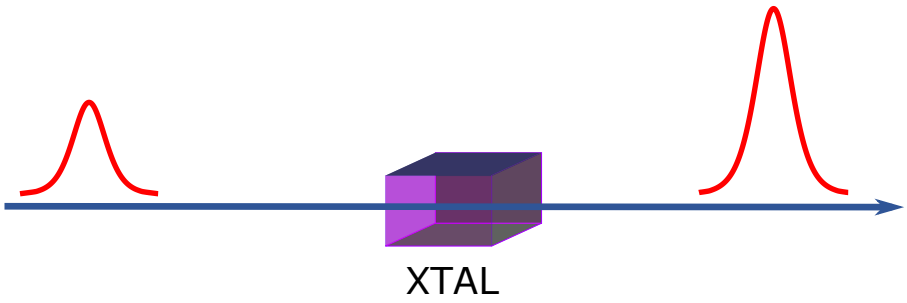

Figure 4.1: Single Pass Amplification

On the contrary, an oscillation in the system is an unwanted effect, because it depletes the gain medium from the excited atoms needed for amplification. This and other adverse effects will be described. In the next sections the focus will be on monochromatic and polychromatic amplification processes and their numerical implementation.

4.1 Pulse Amplification

Let us describe the amplification of a laser signal under the form of a periodic pulsed signal. Since the main work of this thesis has been done with a quasi-three level material, this is the energy system which will be exploited. The pulse repetition

rate is taken such that $1/f_p \ll \tau_f$ which means that the amplifier's medium has a fluorescence time much longer than the time between two signal pulses. It also means that the gain medium does not have enough resolution to discriminate two signal pulses, and then it acts like the signal was CW. The pump has to been CW because it needs to be fast enough to provide strong optical pumping between two pulses. Then, the amplification process is divided in two distinct phases:

- **Pulse Amplification**

  Initially the gain medium excited by the pump. The pulse passes through the medium in a time frame $t \ll 1/f_p$ and it depletes the gain while being amplified. In this phase the pump and fluorescence contributions for the upper level population are neglected.

- **Gain Restoration**

  After the pulse passage there is a time window $T \approx 1/f_p$ in which the gain can be restored though the energy of the pump. Still, the fluorescence and obviously the signal contribution for the upper level population are neglected.

Let us recall the rate equations for a quasi-three level system. From equation 3.5 and 3.6, the variation of the lower laser level is:

$$\frac{\partial n_1}{\partial t} = \frac{\sigma_{ei} f_{2u} I_i}{h\nu_i} n_2 + \frac{\sigma_{ep} f_{2h} I_p}{h\nu_p} n_2 - \frac{\sigma_{ai} f_{1l} I_i}{h\nu_i} n_1 - \frac{\sigma_{ap} f_{1g} I_p}{h\nu_p} n_1 + \frac{n_2}{\tau_{21}} \tag{4.1}$$

$$n_{tot} = n_1 + n_2 \tag{4.2}$$

and the gain coefficient from equation 3.7 is:

$$g(\nu) = n\sigma(\nu) = \sigma_{ei} f_{2u} n_2 - \sigma_{ai} f_{1l} n_1 \tag{4.3}$$

Phase 1: Pulse Amplification

Let us suppose to have a linear, homogeneously broadened gain medium. This phase starts with the gain medium, of length l, which is already considered in steady-state, with a given population on the upper laser level due to the optical pumping. The steady-state condition is obtained neglecting the signal in the equation 4.1:

$$\frac{\partial n_2}{\partial t} = -\frac{\sigma_{ep} f_{2h} I_p}{h\nu_p} n_2 + \frac{\sigma_{ap} f_{1g} I_p}{h\nu_p} n_1 - \frac{n_2}{\tau_{21}} \tag{4.4}$$

whose result is:

$$n_2 = \frac{\dfrac{\sigma_{ap} f_{1g}}{\sigma_{ap} f_{1g} + \sigma_{ep} f_{2h}} \dfrac{P_p(z)}{P_{sp}}}{1 - \dfrac{\sigma_{ep} f_{2h}}{\sigma_{ap} f_{1g} + \sigma_{ep} f_{2h}} \dfrac{P_p(z)}{P_{sp}}} n_1 \tag{4.5}$$

Alternatively, exploiting the inversion ratio β:

$$\beta = \frac{\sigma_{ap} f_{1g}}{\sigma_{ap} f_{1g} + \sigma_{ep} f_{2h}} \frac{\frac{P_p(z)}{P_{sp}}}{1 + \frac{P_p(z)}{P_{sp}}} \tag{4.6}$$

The pump absorption is:

$$P_p(z) = P_p(0) e^{-\alpha_p z} \tag{4.7}$$

where:

$$\alpha_p = (\sigma_{ap} f_{1g} n_1 - \sigma_{ep} f_{2h} n_2) \approx \sigma_{ap} f_{1g} n_{tot} \tag{4.8}$$

The saturation power is:

$$P_{sp} = \frac{h\nu_p A_{eff}}{(\sigma_{ep} f_{2h} + \sigma_{ap} f_{1g})\tau_{21}} \qquad P_{si} = \frac{h\nu_i A_{eff}}{(\sigma_{ei} f_{2u} + \sigma_{ai} f_{1l})\tau_{21}} \tag{4.9}$$

The inversion ratio is exceptionally useful in a quasi-three level system to describe a numerical model of an amplifier, especially when the model is polychromatic, as it will be done in the following sections.
The phase 1 is the pulse amplification, and thus it is necessary to describe the gain dynamics in the quasi-three level system. Since the pulse amplification acts on a very short time scale, the pump and the fluorescence contributions are neglected. Thus, equation 4.1 becomes:

$$\frac{\partial n_1}{\partial t} = \frac{\sigma_{ei} f_{2u} I_i}{h\nu_i} n_2 - \frac{\sigma_{ai} f_{1l} I_i}{h\nu_i} n_1 = \frac{g(\nu)}{l} \frac{I_i}{h\nu_i} \tag{4.10}$$

Then the $g(\nu)$ temporal variation is:

$$\frac{\partial g(\nu)}{\partial t} = \frac{\sigma_{ei} f_{2u} I_i}{h\nu_i} \frac{\partial n_2}{\partial t} - \frac{\sigma_{ai} f_{1l} I_i}{h\nu_i} \frac{\partial n_1}{\partial t} \tag{4.11}$$

Exploiting equation 4.2:

$$\frac{\partial g(\nu)}{\partial t} = -(\sigma_{ei} f_{2u} + \sigma_{ai} f_{1l}) \frac{g(\nu) I_i}{h\nu_i} \tag{4.12}$$

and:

$$\frac{\partial g(\nu)}{\partial t} = -g(\nu) \frac{I_i}{I_{si}} \tag{4.13}$$

where I_{si} is the laser signal saturation intensity. This equation can be solved. Thus, the gain coefficient at a given position z changes with respect to the time t in the pulse time frame:

$$g(\nu)(z,t) = g(\nu)(z,0) e^{-E_p(t)/E_{si}} = g_i e^{-E_i/E_{si}} \tag{4.14}$$

where $g(\nu)(z,0) = g_i$ is the initial gain coefficient, $E_p(t) = E_i$ is the pulse energy at time t, and E_{si} is the saturation energy of the medium at laser wavelength. Along

the propagation through the medium the pulse energy is affected by a gain which depends on the ratio between its own energy, which increases, and the saturation energy of the medium. An alternative solution exploits the fluence:

$$g(\nu)(z,t) = g_i e^{-F_p(t)/F_{si}} = g_i e^{-F_i/F_{si}} \tag{4.15}$$

While at a given position the gain in the medium changes with the passage of the pulse, its energy, while travelling, increases. The pulse fluence in a dz length is:

$$F(z+dz,t) = \int_{-\infty}^{t} I(z+dz,t')\,dt' = \int_{-\infty}^{t} I(z,t')e^{g(\nu)(z,t)dz}\,dt' \tag{4.16}$$

In a dz length holds the following approximation holds:

$$e^{g(\nu)(z,t)dz} \approx 1 + g(\nu)(z,t)dz \tag{4.17}$$

and thus:

$$F(z+dz,t) = \int_{-\infty}^{t} I(z+dz,t')\,dt' + \int_{-\infty}^{t} I(z,t')g(\nu)(z,t)\,dz\,dt' \tag{4.18}$$

which can be written, exploiting equation 4.15:

$$F(z+dz,t) = F(z,t) + g(\nu)(z,0)dz \int_{-\infty}^{t} e^{-F_i/F_{si}}\,dF \tag{4.19}$$

which can be seen as:

$$\frac{\partial F}{\partial z} = g_i F_{si}(1 - e^{-F_i/F_{si}}) \tag{4.20}$$

The solution of this equation is:

$$F(z,t) = F_{si} \ln\left[1 + e^{g_0}(e^{F_i/F_{si}} - 1)\right] \tag{4.21}$$

or using energy instead of fluence:

$$E(z,t) = E_{si} \ln\left[1 + e^{g_0}(e^{E_i/E_{si}} - 1)\right] \tag{4.22}$$

where g_i is the initial gain coefficient and g_0 is the small-signal gain. This equation describes the pulse amplification through the gain medium [55]. If the pulse fluence is $F_i \ll F_{si}$, then from equation 4.21 the output fluence is $F(z,t) \approx e^{g_0} F_i$, which describes a situation of pulse amplification without saturation. In this condition there is the linear amplification regime. On the other hand, when $F_i \gg F_{si}$, again from equation 4.21, the amplification is not linear anymore, since there is a saturation effect and $F(z,t) \approx F_i + g_i F_{si} l \approx g_i F_{si} l$.
The output intensity can be found as:

$$I(z,t) = \frac{e^{g_0} e^{E_i/E_{si}}}{1 + e^{g_0}(e^{E_i/E_{si}} - 1)} I_i \tag{4.23}$$

where $I_i = I(0,t)$ is the initial pulse intensity. The inversion ratio β during amplification is equal to:

$$\beta(z,t) = \frac{g_0/(n_{tot})l}{(\sigma_{ei}f_{2u} + \sigma_{ai}f_{1l})} + \frac{\sigma_{ai}f_{1l}}{(\sigma_{ei}f_{2u} + \sigma_{ai}f_{1l})} \tag{4.24}$$

Phase 2: Gain Restoration

During the phase 2, the pulse has depleted the stored energy in the gain medium and thus the pump has to excite again the atoms to the upper laser level. This happens in a time frame $T < 1/f_p$, while there is no signal. The phase of interest is the transient of the gain medium, which is going into the steady-state condition described in 4.5. There are two equations to take into account, the first is the population temporal variation of n_2, from 4.4:

$$\frac{\partial n_2}{\partial t} = -\frac{\sigma_{ep}f_{2h}I_p}{h\nu_p}n_2 + \frac{\sigma_{ap}f_{1g}I_p}{h\nu_p}n_1 - \frac{n_2}{\tau_{21}} \tag{4.25}$$

The second is the pump absorption along the medium:

$$\frac{\partial I_p(z,t)}{\partial z} = -(\sigma_{ep}f_{2h}n_2 - \sigma_{ap}f_{1g}n_1)\frac{I_p}{h\nu_p} \tag{4.26}$$

where I_p is the initial pump intensity. Then, the pump absorption over a Δz length is:

$$P_p(z+\Delta z,t) = P_p(z,t)\exp\Big\{-\Big[\sigma_{ap}f_{1g}n_1 - \sigma_{ep}f_{2h}n_2\Big]\Delta z\Big\} \tag{4.27}$$

Alternatively, exploiting the inversion ratio β:

$$P_p(z+\Delta z,t) = P_p(z,t)\exp\Big\{-\Big[\sigma_{ap}f_{1g}(1-\beta(z,t)) - \sigma_{ep}f_{2h}\beta(z,t)\Big]n_{tot}\Delta z\Big\} \tag{4.28}$$

The gain restoration, which is directly connected to the inversion ratio, must happen before the arrival of another pulse, i.e. $T < 1/f_p$, $1/f_p < \tau_{21}$. Then, the transient of the upper laser level population is:

$$n_2(z,t+T) = \left(1 - \frac{T}{\tau_{21}}\right)n_2(z,t) + \frac{\Big[\sigma_{ap}f_{1g}n_1 - \sigma_{ep}f_{2h}n_2\Big]}{h\nu_p A_{eff}}P_p(z,t)T \tag{4.29}$$

If $\beta(z,t)$ is the inversion ratio after the depletion of a pulse, its transient is:

$$\beta(z,t+T) = \left(1 - \frac{T}{\tau_{21}}\right)\beta(z,t) + \frac{\Big[\sigma_{ap}f_{1g}(1-\beta(z,t)) - \sigma_{ep}f_{2h}\beta(z,t)\Big]}{h\nu_p A_{eff}}P_p(z,t)T \tag{4.30}$$

Both $n_2(z,t+T)$ and $\beta(z,t+T)$ tend to the steady-state described in equation 4.5 and 4.6.

4.1.1 Extraction Efficiency

The equations proposed so far rely on the small signal gain g_0, which has not been explicitly described. In order to do that it is necessary to know the steady-state condition of the gain medium before the pulse. It comes from equation 4.5. Neglecting the losses from emission at pump wavelength:

$$n_2 \approx \frac{\sigma_{ap} f_{1g} I_p \tau_{21}}{h\nu_p} n_1 \tag{4.31}$$

Then, since:

$$\alpha_p \approx \sigma_{ap} f_{1g} n_1 = \frac{\partial P_{p,abs}}{\partial z} \tag{4.32}$$

It can be written as:

$$n_2 = \frac{\tau_{21}}{h\nu_p A_{eff}} \frac{\partial P_{p,abs}}{\partial z} \tag{4.33}$$

where A_{eff} is the signal area along the medium at a given position. The small signal gain can be found through the integration of the gain coefficient over a length l:

$$g_0 = \int_0^l g(\nu)(z,0)\, dz = \int_0^l g_i\, dz \tag{4.34}$$

where l is the medium length. Exploiting equation 4.3 and neglecting reabsorption losses:

$$g(\nu)(z,0) = \sigma_{ei} f_{2u} n_2 + \sigma_{ai} f_{1l} n_2 \tag{4.35}$$

Then:

$$g_0 = \int_0^l (\sigma_{ei} f_{2u} + \sigma_{ai} f_{1l}) n_2\, dz \tag{4.36}$$

and:

$$g_0 = \int_0^l (\sigma_{ei} f_{2u} + \sigma_{ai} f_{1l}) \frac{\tau_{21}}{h\nu_p A_{eff}} \frac{\partial P_{p,abs}}{\partial z}\, dz \tag{4.37}$$

Finally the small signal gain is:

$$g_0 = \eta \frac{\lambda_p}{\lambda_i} \frac{E_{p,abs}}{E_{si}} \tag{4.38}$$

where E_{si} is the saturation energy of the medium at signal laser wavelength, $E_{p,abs}$ is the pump absorbed energy and η is the overall efficiency, just like in the small-signal gain formula for a laser. The saturation energy worth:

$$E_{si} = \frac{h\nu_i}{\sigma_{ei} f_{2u} + \sigma_{ai} f_{1l}} \tag{4.39}$$

These formulas can be used to obtain a description of the efficiency of the signal to extract the energy inserted in the gain medium through the pump:

$$\eta_{ext} = \frac{E_{out} - E_{in}}{E_{p,abs}} \tag{4.40}$$

The parameter η_{ext} is called *extraction efficiency*. When the pulse fluence is very low with respect to saturation, $F_i \ll F_{si}$ then $F(z,t) \approx e^{g_0} F_i$, which can be approximated as $F(z,t) \approx (1+g_0)F_i \approx g_0 F_i$, then, after the conversion to energy, the extraction efficiency is:

$$\eta_{ext} = \frac{E_{out} - E_{in}}{E_{p,abs}} = \eta \frac{\lambda_p}{\lambda_i} \frac{E_{in}}{E_{p,abs}} \tag{4.41}$$

which describes η_{ext} depending on the initial pulse energy. On the other hand, when $F_i \gg F_{si}$ then $F(z,t) \approx g_i F_{si} l \approx g_0 F_{si}$, which can be easily converted into energy:

$$\eta_{ext} = \frac{E_{out} - E_{in}}{E_{p,abs}} \approx \frac{g_0 E_{si}}{E_{p,abs}} = \eta \frac{\lambda_p}{\lambda_i} \tag{4.42}$$

and this is the highest estraction efficiency possible; it is obtained when the amplifier in highly saturated.

4.2 Frantz-Nodvik Numerical Model Implementation

The previous formulas can be used to build a set of equations, called *Frantz-Nodvik equations*, which describe the pulse amplification along the gain medium [55]. Here it is presented its numerical implementation. Firstly, the gain medium is divided in q slices of Δz length, with k being the k-th slice. Then, the stored fluence $F_{sto,k,in}$ and the small signal gain $g_{0,k,in}$ for each k-th slice are calculated in steady-state, without the signal to amplify, through the pump absorption.

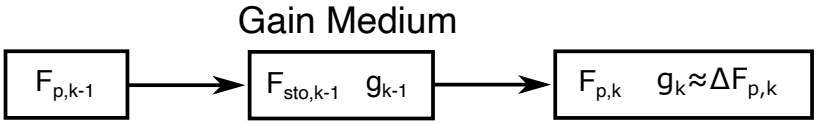

Figure 4.2: Frantz-Nodvik Model

Since for a maximum extraction efficiency the amplifier must be in saturation, $F_{sto,0,in} = g_{0,k,in} F_{si}$. Successively the amplified pulse fluence $F_{p,k,out}$ after the passage in the k-th slice is defined:

$$\begin{cases} g_{0,k,out} = g_{0,k,in} e^{-\frac{F_{p,k,in}}{F_{si}}} \\ \\ F_{p,k,out} = F_{si} \ln \left[1 + e^{g_{0,k,in}} \left(e^{\frac{F_{p,k,in}}{F_{si}}} - 1 \right) \right] \end{cases} \tag{4.43}$$

From this energy extraction the stored fluence before the passage of the pulse, $F_{sto,k,in}$, and after the passage of the pulse, $F_{sto,k,out}$, are calculated. The stored

fluence then contributes to update the small signal gain $g_{0,k,out}$. Finally, from the pulse fluence after the q slices of the gain medium it is straightforward to calculate the pulse energy and the average power. Between the pulses, the gain is restored as described above to return to steady-state condition. An alternative description is:

$$\begin{cases} F_{p,k,out} = F_{si} \ln \left[1 + e^{\frac{F_{sto,k,in}}{F_{si}}} \left(e^{\frac{F_{p,k,in}}{F_{si}}} - 1 \right) \right] \\ \\ F_{sto,k,out} = F_{sto,k,in} - (F_{p,k,out} - F_{p,k,in}) \end{cases} \tag{4.44}$$

4.3 Polychromatic Numerical Model Implementation

A model which takes into account the spectral dependence of parameters is interesting because it gives the chance to describe spectral effects such as gain narrowing [56]. The main limitation of the Frantz-Nodvik equations is the difficulty to operate with a polychromatic model.

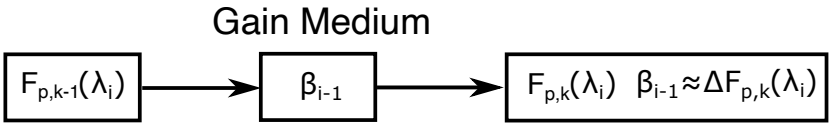

Figure 4.3: Modified Frantz-Nodvik Model

While the description of the stored fluence $F_{sto,k}$ in the k-th slice is straightforward for the monochromatic model, its wavelength-dependent analogous $F_{sto,k}(\lambda)$ is much more complex to describe. An alternative way, which can be exploited also in the monochromatic model, is to describe the variation of the stored fluence $F_{sto,k}(\lambda)$ in the k-th slice through the inversion ratio $\beta(\lambda)$. Then, the gain $g_{0,k,in}(\lambda)$ is calculated from $\beta(\lambda)$. If the broadening of the gain medium is homogeneous, the inversion ratio β is practically wavelength-independent, even though the gain is not.
The workflow is very similar to the one described for the Frantz-Nodvik model. Firstly, the gain medium is divided in q slices of Δz length, with k being the k-th slice. Then, regarding the spectral dependence of the model, the emission and absorption cross-sections of the gain medium, $\sigma_a(\lambda)$ and $\sigma_e(\lambda)$, are divided in r slices of $\Delta\lambda$ length, with i being the i-th slice, as well as the pulse signal with its initial fluence $F_i(\lambda_i)$.
An initial guess of the inversion ratio $\beta_{0,k}$ is done through equation 4.6:

$$\beta_{0,k} = \frac{\sigma_{ap}(\lambda_i) f_{1g}}{\sigma_{ap}(\lambda_i) f_{1g} + \sigma_{ep}(\lambda_i) f_{2h}} \frac{\frac{P_{p,k}(\lambda_i)}{P_{sp}(\lambda_i)}}{1 + \frac{P_{p,k}(\lambda_i)}{P_{sp}(\lambda_i)}} \tag{4.45}$$

where the initial inversion ratio is set $\beta_k = \beta_{0,k}$. Then, the spectral small signal gain $g_{0i,k}$ is calculated for each $\Delta\lambda$ and Δz slice:

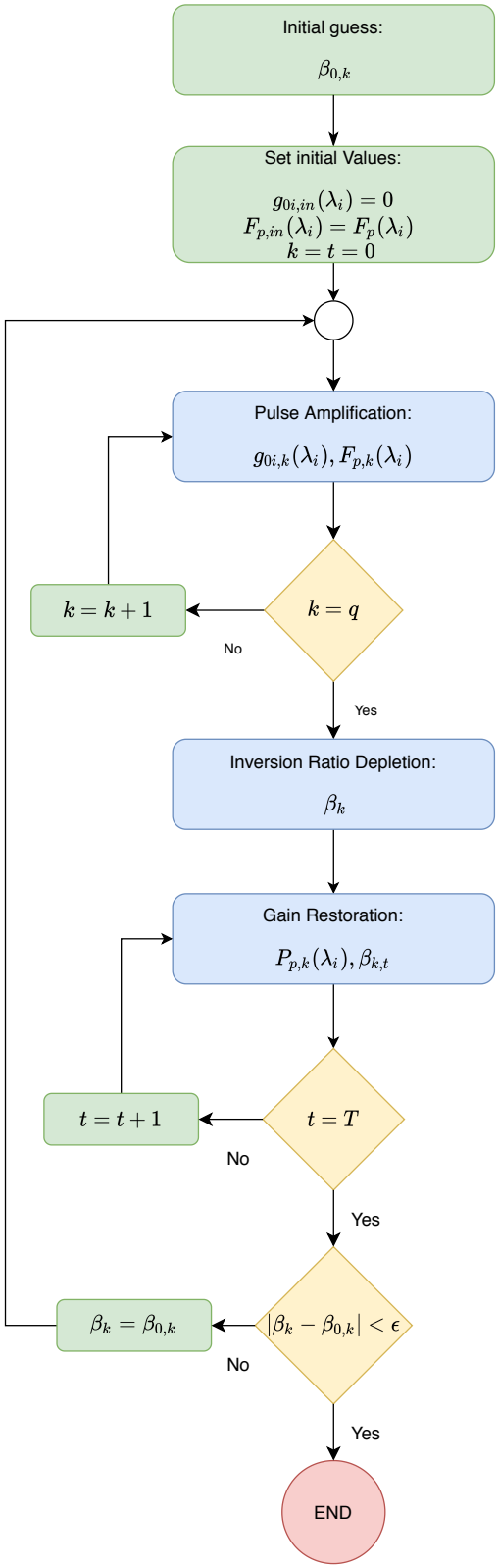

Figure 4.4: Flowchart Polychromatic Numerical Model for Single-Pass Pulse Amplification.

$$g_{0i,k-1}(\lambda_i) = \Big[\sigma_{ap}(\lambda_i) f_{1g}(1-\beta_{0,k-1}) - \sigma_{ep}(\lambda_i) f_{2h}\beta_{0,k-1}\Big] n_{tot}\Delta z \tag{4.46}$$

$$g_{0i,k}(\lambda_i) = g_{0,k-1}(\lambda_i) e^{-\frac{F_{p,k-1}(\lambda_i)}{F_{si}(\lambda_i)}} \tag{4.47}$$

Successively the amplified pulse fluence $F_{p,k}(\lambda_i)$ is calculated for each $\Delta\lambda$ and Δz slice:

$$F_{p,k}(\lambda_i) = F_{si}(\lambda_i) \ln\left[1 + e^{g_{0i,k}(\lambda_i)}\left(e^{\frac{F_{p,k-1}(\lambda_i)}{F_{si}(\lambda_i)}} - 1\right)\right] \tag{4.48}$$

and the pulse fluence amplification in the k-th slice is the sum of the all spectral contributions for the r slices:

$$F_{p,k} = \sum_i F_{p,k}(\lambda_i) \tag{4.49}$$

The depletion of the upper laser level β_k is described by the inversion ratio from equation 4.24:

$$\beta_k = \frac{g_{0i,k}/(n_{tot})l}{(\sigma_{ei}(\lambda_i) f_{2u} + \sigma_{ai}(\lambda_i) f_{1l})} + \frac{\sigma_{ai}(\lambda_i) f_{1l}}{(\sigma_{ei}(\lambda_i) f_{2u} + \sigma_{ai}(\lambda_i) f_{1l})} \tag{4.50}$$

This is the end of the amplification; the gain restoration is necessary in a time frame $T < 1/f_p$, $1/f_p < \tau_{21}$. This period of time T is composed by t slices of length Δt. The equations 4.28 and 4.30 are exploited. Firstly, the pump absorption is described through the depleted inversion ratio β_k:

$$P_{p,k}(\lambda_i) = P_{p,k-1}(\lambda_i) \exp\Big\{-\Big[\sigma_{ap}(\lambda_i) f_{1g}(1-\beta_{k,t}) - \sigma_{ep}(\lambda_i) f_{2h}\beta_{k,t}\Big] n_{tot}\Delta z\Big\} \tag{4.51}$$

Then the inversion ratio β_k is restored:

$$\beta_{k,t} = \left(1 - \frac{\Delta t}{\tau_{21}}\right)\beta_{k,t-1} + \frac{\Big[\sigma_{ap}(\lambda_i) f_{1g}(1-\beta_{k,t-1}) - \sigma_{ep}(\lambda_i) f_{2h}\beta_{k,t-1}\Big]}{h\nu_p A_{eff}} P_{p,k}\Delta t \tag{4.52}$$

Thus, this becomes the new inversion ratio $\beta_k = \beta_{k,t}$ for the pulse amplification phase. The cycle composed by amplification and gain restoration continues until a condition about the final inversion ratio is fulfilled:

$$|\beta_k - \beta_{0,k}| < \epsilon \tag{4.53}$$

which means that the system converged to its steady-state. If it is not, the cycle starts again and $\beta_k = \beta_{0,k}$.

4.4 Multipass Amplifier

The multipass amplifier, which has been introduced in Chapter 1, describes a technique in which the signal passes through the gain medium several times, with a beam path fixed by optical components, enhancing the amplification process. It is a straightforward extension of the single pass amplification, and thus all the boundary conditions and the formulas which have been seen so far can be applied to it.

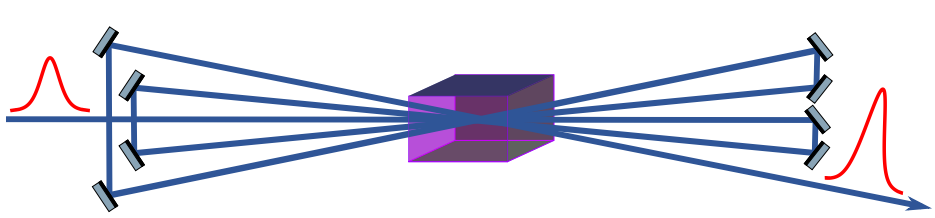

Figure 4.5: Multipass Amplifier

Let us introduce a p passes multipass amplifier. In its most general form, the j-th pass is considered as an independent process with respect to the previous passes; this means that a p passes multipass amplifier can be seen as the cascade of p single pass amplifiers. Depending on how many amplification steps the signal undergoes in the gain medium, more stored energy can be extracted, increasing the overall efficiency with respect to a single pass amplification with the same geometrical properties.
In flowchart 4.6 is described the polychromatic model of a multipass amplifier with p passes. The first pass is exactly the same as a single pass amplification described before. On the other hand, the second pass is different, since the pulse is counter-propagating with respect to all the N slices of the crystal, each of them having their own energy stored from the pump. This is true for each odd and even passes of the overall p passes of the multipass amplifier. Moreover, between the passes there is not gain restoration.

4.5 Undesired Effects

Since the goal of a pulse amplifier is to generate a pulse with a very high intensity, there are different detrimental effects which affect its performances. It is of fundamental importance to know them in order to counteract their negative effects [27]. The processes of our interest are the following. Gain narrowing, which decreases the bandwidth of the optical transition with respect to the gain of the amplifier; amplified spontaneous emission (ASE) which depletes the upper state level when a gain threshold is exceeded; nonlinear phenomena, which modify the temporal and spectral shape and evolution of the pulse depending on its intensity in the gain medium; and thermal lensing, which reshapes the pulse wavefront given the characteristics of the crystal. Let us describe them in detail.

4.5.1 Gain Narrowing

Suppose to have a gain medium with an homogeneous broadened lineshape, i.e. a Lorentzian lineshape, From equation 2.53:

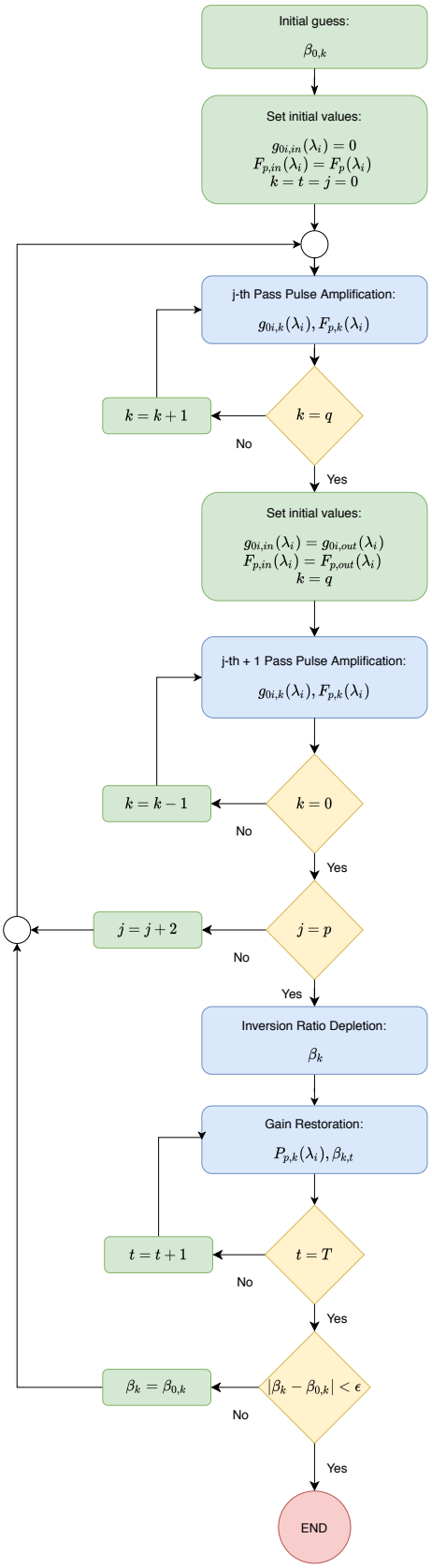

Figure 4.6: Flowchart Polychromatic Numerical Model for Multi-Pass Pulse Amplification.

$$g^*(\nu,\nu_0) = \left(\frac{2}{\Delta\nu_0\pi}\right)\frac{1}{1+\left(\frac{2}{\Delta\nu_g}\right)^2(\nu-\nu_0)^2} \tag{4.54}$$

which has a given bandwidth at FWHM $\Delta\nu_0$ and a central frequency ν_0 . The gain coefficient of the amplifier, from equation 2.139, depends on the broadening:

$$g(\nu)(z,t) = n\frac{\lambda^2}{8\pi\tau_{21}}g^*(\nu,\nu_0) \tag{4.55}$$

Thus the amplifier gain is frequency dependent. The frequencies nearer the central frequency ν_0 will be affected by an higher amplification. The result is that the lorentzian lineshape of the amplifier gain has a $\Delta\nu_0$ which is narrower. For a Lorentzian lineshape, the amplifier gain at FWHM is [45]:

$$G_{dB}(\nu) = \frac{G_{dB}(\nu_0)}{1+\left(\frac{2}{\Delta\nu_0}\right)^2(\nu-\nu_0)^2} \simeq G_{dB}(\nu_0) - 3 \tag{4.56}$$

where $G(\nu) = e^{g(\nu)(z,t)l}$ is the amplifier gain at FWHM and $G(\nu_0) = e^{g(\nu_0)(z,t)l}$ is the amplifier gain at central wavelength. They were calculated in dB, where $-3\,\text{dB} \simeq 0.5$ in power. Then, with respect to the initial bandwidth, the amplified bandwidth at FWHM is:

$$\Delta\nu_{3\,dB} = \Delta\nu_0\sqrt{\frac{3}{G_{dB}(\nu_0)-3}} \tag{4.57}$$

The gain bandwidth $\Delta\nu_{3\,dB}$ of the amplifier, which is the bandwidth at FWHM, is inversely proportional to the gain. At high gain the reduction in the amplifier gain bandwidth is significantly reduced. For this reason, this effect is called *gain narrowing*.

An incoming pulse, whose bandwidth is $\Delta\nu_p < \Delta\nu_0$ with the same central frequency, will experience a reduced bandwidth with respect to the gain acquired by the amplifier.
Let us mathematically describe it as a Fourier limited Gaussian pulse $\tilde{\mathcal{E}}_0(\omega)$ amplified through gain medium with Lorentzian lineshape $G(\omega)$:

$$\tilde{\mathcal{E}}(\omega) = G(\omega)\tilde{\mathcal{E}}_0(\omega) \tag{4.58}$$

If the input pulse has a FWHM BW equal to $\Delta\omega_{p0}$ and a pulse duration τ_{p0}:

$$\tilde{\mathcal{E}}_0(\omega) = A_0\exp\left(-\frac{\omega^2}{\omega_i^2}\right) \tag{4.59}$$

The amplified pulse is:

$$\tilde{\mathcal{E}}(\omega) = A_0\exp\left[\frac{g(\omega_0)}{1+\left(\frac{1}{\Delta\omega_0}\right)^2(\omega-\omega_0)^2}\right]\exp\left(-\frac{\omega^2}{\omega_i^2}\right) \tag{4.60}$$

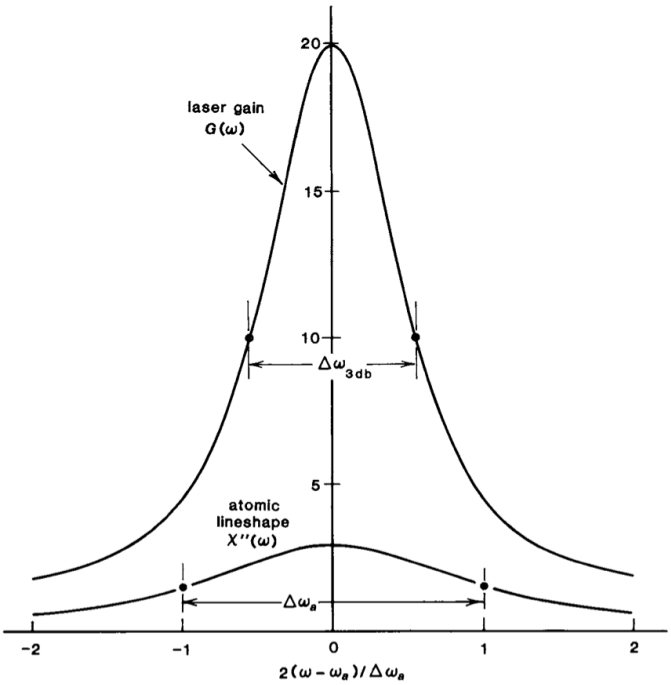

Figure 4.7: Gain Narrowing [45].

where $\Delta\omega_0$ is the gain medium FWHM BW. It can be approximated as:

$$\tilde{\mathcal{E}}(\omega) = A_0 \exp\left[g(\omega_0)\left(1 - \left(\frac{1}{\Delta\omega_0}\right)^2 (\omega - \omega_0)^2\right)\right] \exp\left(-\frac{\omega^2}{\omega_i^2}\right) \tag{4.61}$$

Thus it is possible to extract some information on the pulse bandwidth with respect to the reduction of the gain bandwidth [45]:

$$\Delta\omega_p \simeq \frac{\Delta\omega_{p0}}{\sqrt{\left(\frac{\omega_g}{\omega_i}\right)^2 + g(\omega_0)}} \tag{4.62}$$

Since the Gaussian pulse was Fourier limited, the pulse duration increases too:

$$\tau_p \simeq \tau_{p0}\sqrt{1 + g(\omega_0)\left(\frac{\omega_i}{\omega_g}\right)^2} \tag{4.63}$$

4.5.2 Amplified Spontaneous Emission

The main goal of an amplifier is to amplify an incident signal, a pulse in our case. One of the main limitations to an high amplifier gain is the *Amplified Spontaneous Emission* process, or ASE. It has been said that the spontaneous emission is a

quantistic process and the decay of the excited atom is described by a probability:

$$\frac{\partial n_2}{\partial t} = -\frac{n_2}{\tau_{rad,21}} \tag{4.64}$$

While in a laser this process is necessary, since it generates an optical noise useful to self-starting the cavity modes, in an amplifier it is an unwanted and very detrimental, because it depletes the gain medium from the excitated ions. In practice,, in a high gain pulse amplifier it limits the maximum inversion ratio possible, and thus the small signal gain. ASE has quasi-coherent properties since it is spontaneous radiation amplified by stimulated emission.
ASE spectral linewidth depends on the optical transition in which the decay happens and on its strength, while its direction is random, either forward or backward along the gain medium. Nonetheless, it has some properties of directionality. It is possible to describe the solid angle of emission with respect to the direction of propagation [44]. Let us suppose that the medium's length is much smaller than its height and width, $D \ll l$, where D is the cross sectional area. Regarding the forward direction:

$$\Omega = \frac{\pi D^2}{4l^2} \tag{4.65}$$

While for the backward direction, if there is a unitary reflectivity mirror:

$$\Omega' = \frac{\pi D^2}{16l^2} \tag{4.66}$$

It is important to remember that the output solid angle is multiplied by the medium refractive index n for the forward direction and n^2 for the backward direction, which is reflected back.

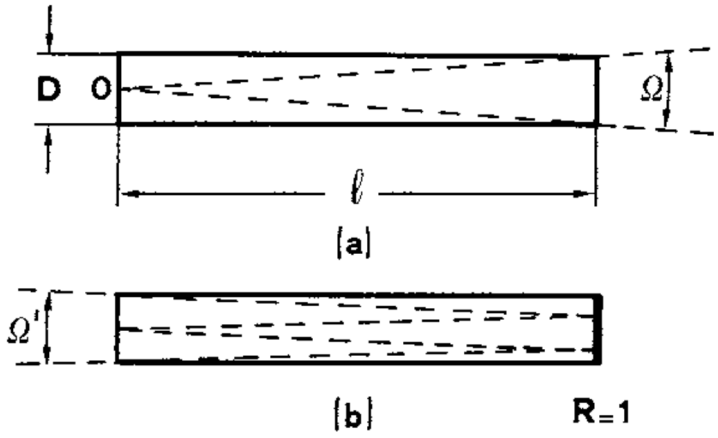

Figure 4.8: ASE Solid Angle [44].

If some optical component in the setup generates enough positive feedback, such as what happens in an oscillator, a cascade effect might start and the amplifier may act as a laser. At this point, the ASE, which has been transformed in laser emission, is

a narrowidth CW signal, has an enormous gain and depletes significantly the gain medium.
A threshold-like gain G necessary to ASE to become a laser radiation has been studied by Svelto et al., and Casperson. The spectral ASE intensity with respect to the propagation axis is defined by a stimulated process and a spontaneous process:

$$\frac{\partial I(\nu)}{\partial z} = \big(\sigma_{a(\nu)} - \sigma_{e(\nu)}\big) n_2 I(\nu) + \frac{n_2}{\tau_{rad,21}} \frac{\Omega(z)}{4\pi} \tag{4.67}$$

where $\Omega(z)$ is the solid angle for each dz component along the axis. Lorentzian lineshape, the ASE intensity of the forward beam is:

$$I = \eta_q I_{s,p} \left(\frac{\Omega}{4\pi} \right) \frac{(G-1)^{3/2}}{[G \ln(G)]^{1/2}} \tag{4.68}$$

where η_q is the fluorescence quantum efficiency, which describes the number of emitted photons with respect to the excited atoms, $I_{s,p}$ is the saturation intensity of the gain medium at peak, since it is exploited by ASE, Ω is the solid angle, G is the peak gain:

$$I_{s,p} = \frac{h\nu}{(\sigma_{a,p} + \sigma_{e,p})\tau} \qquad G = e^{(\sigma_{e,p} n_2 - \sigma_{a,p} n_1) l} \tag{4.69}$$

The bandwidth of the ASE, for a Lorentzian lineshape, is:

$$\Delta\nu_{ASE} = \left[\frac{G-1}{G \ln(G)} \right]^{1/2} \Delta\nu_0 \tag{4.70}$$

where $\Delta\nu_0$ is the lineshape FWHM BW. The bandwidth of the ASE emission decreases with respect to the gain G. The threshold gain G for a closed loop is:

$$G^2 = \frac{4\pi^{3/2}}{\eta_q \Omega} [\ln(G)^2]^{1/2} \tag{4.71}$$

which describes the maximum gain reachable by the amplifier before starting ASE. Let us define for a given amplifier system $k = 4\pi^{3/2}/\eta_q$. Thus, for two different configurations with a given solid angle Ω_i:

$$G_1^2 = \frac{k}{\Omega_1} [\ln(G_1)^2]^{1/2} \qquad G_2^2 = \frac{k}{\Omega_2} [\ln(G_2)^2]^{1/2} \tag{4.72}$$

which means that the ratio between solid angles can be defined just through the gain threshold for ASE:

$$\frac{\Omega_2}{\Omega_1} = \frac{G_1^2}{G_2^2} \sqrt{\frac{\ln(G_2)}{\ln(G_1)}} \tag{4.73}$$

4.5.3 Nonlinear Phenomena

Nonlinear effects play an important role in pulse amplifiers. The most important for the subject is the optical Kerr effect, which describes the variation of the medium's refractive index given by the intensity of a pulse propagating through it:

$$n = n + n_2 I \tag{4.74}$$

The nonlinear refractive index n_2 derives from the third order susceptibility χ^3 of the medium and the refractive index variation is proportional to the pulse intensity. A parameter, called *B integral parameter*, is usually used to describe the amount of accumulated nonlinear phase shift of a pulse which is being amplified:

$$\mathrm{B} = \frac{2\pi}{\lambda} \int n_2 I(z)\, dz \tag{4.75}$$

where $I(z)$ is the beam intensity along the propagation axis z. If the B integral exceeds some values, i.e. $\mathrm{B} > 3 - 5$, the temporal and spectral shape of the pulse degrades. The majority of the contribution in nonlinearity is given by the gain medium. A more detailed description is found in Appendix C.

4.5.4 Thermal Lensing

A very important effect for solid-state lasers is called *thermal lensing*. When a laser beam passes through the gain medium some part of the power is absorbed by the ions, some part is transmitted along the beam axis and some part is dissipated through the crystalline host. For this reason the gain medium is hotter on the beam axis, compared with the surrounding regions, which leads to different effects that modify the optical path of the light inside the crystal. In a high gain amplifier the necessary pumping power is substantial, which means an elevated dissipated power may be required, so this effect cannot be neglected.
One of these effects is the variation of refractive index with respect to temperature. With a different refractive index along the gain medium cross section, the crystal itself acts as a lens. The focal length of the lens depends on the material, on the pumping method and on the cooling system. It can be positive or negative.

Having a lens-like object inside the amplifier gain medium modifies the seeder beam propagation. This is detrimental for an efficient amplification and its gravity depends on the amplifier setup. Depending on the actual amplifier setup it may or may not be more robust against perturbations of the seeder beam propagation. The strength of thermal lens f_{th} depends on the equation 4.76, which expresses the dioptric power:

$$f_{th}^{-1} = \frac{\eta_h P_{abs} \chi}{2\pi w_p^2 K_c} \tag{4.76}$$

where η_h is the fractional thermal load, P_{abs} is the absorbed power, πw_p^2 is the pumped area, K_c is the thermal conductivity and χ is the thermo-optic coefficient [58]. The

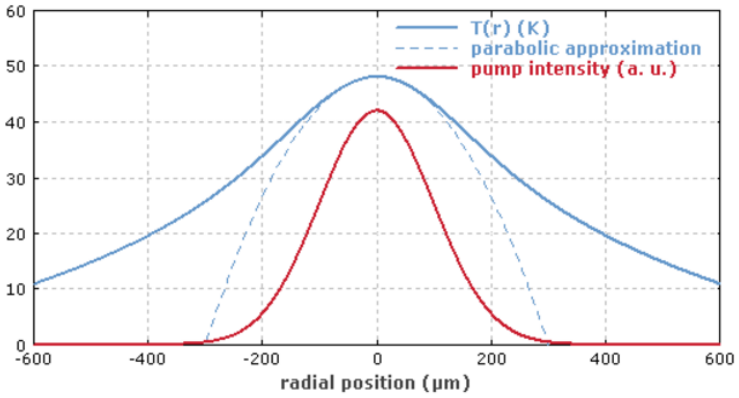

Figure 4.9: Transverse pump intensity distribution (red) and thermal profile (blue), simulated for an 8 mm long end-pumped Nd:YAG rod with 14 W of dissipated power. The distribution in the beam direction is assumed to be homogeneous [57].

previous formula is valid within the paraxial approximation (i.e. $f_{th} \gg L$, where L is the crystal length). The thermo-optic coefficient is defined as:

$$\chi = (n_0 - 1)(1 + \nu)\alpha_T + 2n_0^3 \alpha_T C'_{r,\theta} + \left(\frac{\partial n}{\partial T}\right)_\epsilon \tag{4.77}$$

where ν is the Poisson ratio of the material, α_T is the thermal expansion coefficients tensor, $C'_{r,\theta}$ is the photoelastic constant and n_0 is the crystal refractive index. The thermo-optic coefficient determines the sign of the thermal lens and it is composed of three contributions, which may be understood as follows:

- $(n_0 - 1)(1 + \nu)\alpha_T$ is related to the bulging end-faces of the crystal. Due to the temperature changing, a stress is applied to the crystal. This stress depends on the thermal expansion coefficients tensor α_T. Generally in all crystals it is positive, and this means that with an increased temperature, the crystal expands and the end-faces become bulged. In this case, the optical path is increased.

- $2n_0^3 \alpha_T C'_{r,\theta}$ refers to the photoelastic effect. When the crystal increases its temperature, a strain is created inside it, which modifies the refractive index. It is clearly visible that the photoelastic effect depends both on the thermal expansion coefficient α_T and the photoelastic constant $C'_{r,\theta}$.

- $\left(\partial n/\partial T\right)_\epsilon$ is the partial derivative of the refractive index with respect to the temperature at constant strain. If the crystal was a perfectly rigid body, this would be the only contribution to the thermo-optic coefficient.

In practice, the bulging effect together with the partial derivative of the refractive index determines the thermal lens sign, since the photoelastic effect is a minor contributor.

Chapter 5

Ytterbium Doped Materials

A very broad emission bandwidth is the most important property an active medium has to possess in order to generate and amplify ultrashort pulses. Thus, the choice of the active ion and the crystal host in which it is inserted are of fundamental importance. There are two main categories of active ions exploited for ultrashort pulse sources: metallic ions and rare earths ions. Metallic ions, such as Ti^{3+} and Cr^{3+}, naturally have a broadband emission spectrum, independently on the crystal host. On the other hand, rare earth ions cover almost every region of the visible and near-infrared portions of the electromagnetic spectrum but with very sharp fluorescent transitions [59]. Once the rare earth ion is inserted into the crystal host, the perturbation generated by the local electric field of the crystal matrix splits and shifts the electronic transitions of the ion, namely Stark effect. This effect produces a broadening of the emission spectrum. So, the rare earth ions are perfect candidates as dopants for solid state materials to exploit stimulated emission for ultrashort pulses, with different characteristics depending on the crystal host they are into.

The ground-state electronic configuration of a rare earth atom is equal to Xenon's one plus other electrons. The electronic configuration of Xenon is the following:

$$1\,s^{22}s^{22}p^{63}s^{23}p^{63}d^{104}s^{24}p^{64}d^{105}s^{25}p^{6}$$

In Xenon the first 3 shells are fully covered, while the shell n = 4 is completely filled except for 4f subshell. However, the shell n = 5 have some electrons, which fill 5s and 5p subshells.
Rare Earth ions are elements beyond Xenon, which have lost some electrons, usually three. Their electronic configuration is very simple. The only difference between them is the number of electrons in 4f orbital, as shown in table 5.1.
For example, the outer electronic configuration for Nd^{3+} is:

$$Nd^{3+} : \ldots 4\,f^{35}s^{25}p^{6}$$

The fluorescence spectrum of a rare earth ion si given by electronic transitions between the levels of the partially filled 4f orbital. Electrons present in the 4f orbital can be excited by incoming light and be raised into unoccupied 4f levels. After that, with a stimulated emission process, the electron will return to its original orbital. Nonetheless the crystal host modifies the spectrum emission lines of the ion, the ion's emission spectrum is only slightly different from one host to another due to the

Element number	Trivalent rare earth	Number of 4f electrons	Ground state
58	Cerium, Ce^{3+}	1	$^2F_{5/2}$
59	Praseodymium, Pr^{3+}	2	$^3H_4$
60	Neodymium, Nd^{3+}	3	$^4I_{9/2}$
61	Promethium, Pm^{3+}	4	$^5I_4$
62	Samarium, Sm^{3+}	5	$^6H_{5/2}$
63	Europium, Eu^{3+}	6	$^7F_0$
64	Gadolinium, Gd^{3+}	7	$^8S_{7/2}$
65	Terbium, Tb^{3+}	8	$^7F_6$
66	Dysprosium, Dy^{3+}	9	$^6H_{15/2}$
67	Holmium, Ho^{3+}	10	$^5I_8$
68	Erbium, Er^{3+}	11	$^4I_{15/2}$
69	Thulium, Tm^{3+}	12	$^3H_6$
70	Ytterbium, Yb^{3+}	13	$^2F_{7/2}$
71	Lutetium, Lu^{3+}	14	$^1S_0$

Table 5.1: Electronic configuration of trivalent rare earths

shield generated by the outer shells, 5s and 5p. For this work, particular emphasis was given to Ytterbium Yb^{3+} ions.

5.1 Ytterbium Yb^{3+}

The born and the development of semiconductor diode technology has brought a very important breakthrough in the laser field, especially in high-power and ultrashort pulse laser sources. Until the creation of semiconductor diodes the active media were generally pumped through flash-lamps, which had a very broad emission spectrum.

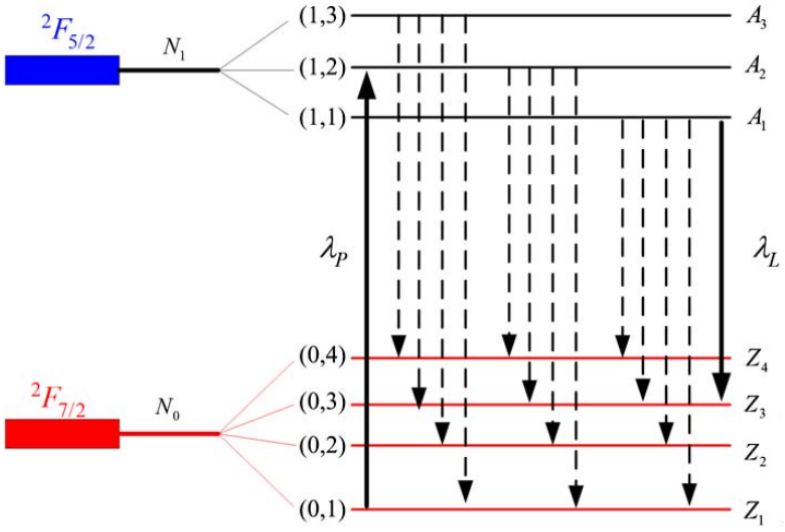

Figure 5.1: Yb:YAG energy level diagram [46].

The replacement of flash-lamps with laser diodes, which have a much narrower emission spectrum, opened the possibility to better match the absorption of the gain media, leading to significant increase of the efficiency, compactness, reliability and cost of the laser source. Moreover it paved the way to the exploitation of new materials and laser transitions, such as the ones found in rare earth ions.

Among rare earths two ions arose with an emission spectrum around 1 μm, Ytterbium and Neodimium. The trivalent ion Yb^{3+} is a rare earth with a very simple two level electronic structure, ${}^2F_{5/2}$ the upper laser level and ${}^2F_{7/2}$ the lower laser level. Once it is inserted in a crystal host, the electronic levels are splitted in two manifolds by Stark effect and it can be considered as a quasi-three level system. This electronic structure avoids most of the unwanted phenomena, such as upconversion, excited-state absorption and concentration quenching. Through laser diodes Yb^{3+} can be pumped at 940 nm or 980 nm, where there are reliable and powerful laser diodes available at competitive cost prices. The relative energy difference between a pump and a laser photon is very reduced, typically less than 10%. It is called *quantum defect* or *Stokes efficiency*:

$$\eta_{qu} = 1 - \frac{\lambda_p}{\lambda_l} \tag{5.1}$$

This is an enormous advantage since it limits the energy dissipated in the crystal host and gives the chance to reach very high optical to optical efficiency. With respect to Neodimium, which has to be pumped at 808 nm or 880 nm, the quantum defect is from tree to five times lower. Moreover it has a longer lifetime which may allow a better storage of the pump energy.

Let us recall the definition of upper manifold ${}^2F_{5/2}$ is N_2, the lower manifold ${}^2F_{7/2}$ is N_1 and their sublevels, N_{1j} and N_{2i}, respectively. From equation 2.119 and 2.120, the electronic structure of a generic Yb-doped crystal, such as Yb:YAG depicted in figure 5.1, is:

$$N_{1j} = f_{1j}N_1 \qquad N_{2i} = f_{2i}N_2 \qquad N_i = \sum_{j=0} f_{ij}N_i \tag{5.2}$$

and:

$$N_1 = \sum_{j=0} f_{1j}N_1 \qquad N_2 = \sum_{i=0} f_{2i}N_2 \tag{5.3}$$

$$f_{1j} = \frac{e^{\frac{-E_{1j}}{k_B T}}}{\sum_{j=0} e^{\frac{-E_{1j}}{k_B T}}} \qquad f_{2i} = \frac{e^{\frac{-E_{2i}}{k_B T}}}{\sum_{i=0} e^{\frac{-E_{2i}}{k_B T}}} \tag{5.4}$$

Where, in the case of Yb:YAG, the lower manifold N_1 has $j = 4$ sublevels, whereas the upper manifold N_2 has $i = 3$ sublevels.

5.2 Host Materials

Solid-state host materials must have defined properties in order to be a suitable host for a given rare earth ion. In particular, the host must have good optical and thermo-mechanical properties to withstand the severe operating conditions of lasers. Moreover they should have other properties such as hardness, chemical inertness, ease of fabrication and so on.
Not every host crystal can be used with every ion, because several interactions between them may give undesirable results. In order to select a crystal suitable for a laser ion host one have to consider the following criteria:

- The crystal must possess favourable optical properties. One of these properties it is the homogeneity of the refractive index, which prevents to have a poor optical quality.
- The crystal must possess thermo-mechanical properties that will permit to use it with high-average powers. Fundamental importance is given to few parameters as thermal conductivity, hardness and so on.
- The crystal must have lattice sites that can accept the dopant ions and that have local crystal fields of symmetry and strength needed to induce the desired spectroscopic properties.
- It is necessary that, with industrial processes, a scalable growth of the impurity-doped crystal is possible, in order to maintain high optical quality and high yield.

5.3 Thermal Load and Thermal Conductivity

A broad emission bandwidth is not the only property an active medium it has to posses in order to be a good candidate for ultrashort pulses sources. Another important criteria to take into account is the thermal properties of the active medium. Especially in quasi-three level active media, a too high temperature would mean problems of efficiency, stability or crystal fracture. It is then imperative to know and understand the crystal's ability to conduct the heat and the induced thermo-mechanical stress. The temperature inside the crystal essentially depends on three factors: the active medium, such as its thermal properties and its shape; the pump intensity and wavelength; the thermal management defined by the actual setup in which the crystal is positioned.

Let us describe, in a first approach, the quantity of energy which does not contribute to the stimulated emission. The fractional thermal load η_h, following T.Y. Fan [60], is defined as the absorbed pump power converted into lattice vibrational energy, i.e. heat:

$$\eta_h = 1 - \eta_p \left[(1 - \eta_l)\eta_r \frac{\lambda_p}{\lambda_f} + \eta_l \frac{\lambda_p}{\lambda_l} \right] \tag{5.5}$$

Where λ_l is the laser or amplification wavelength, λ_p is the pump wavelength and λ_f is the average fluorescence wavelength. The term η_p is the pump quantum efficiency,

which describes how many ions of the active medium contribute to the radiative process we are interested in with respect to each absorbed pump photon. Generally it is very close to unity and it is lowered by nonradiative processes or through pump absorption by the crystal host. The term η_r is the radiative quantum efficiency for the upper manifold, it describes the fraction of excited ions which have a radiative decay without stimulated emission. The main phenomena that may happen to reduce to less than unity the η_r are the concentration quencing and the multiphonon nonradiative decay. On the other hand η_l is the laser extraction efficiency, and defines the fraction of excited ions which contribute to the stimulated emission process. The laser extraction efficiency can be lowered by impurities in the crystal, lattice defects or other energy transfer processes. When $\eta_l = 0$ there is not any stimulated emission, and thus no laser extraction; on the other hand, when $\eta_l = 1$, there is complete laser extraction.
The quantum radiative efficiency can be recalled from 2.67:

$$\eta_r = \frac{\tau_{rad}}{\tau_{nr} + \tau_{rad}} \tag{5.6}$$

The laser extraction efficiency:

$$\eta_l \approx \frac{\sigma_e(\nu_i)I}{\sigma_e(\nu_i)I + \frac{1}{\eta_r \tau_{rad}}} \tag{5.7}$$

An increase in temperature inside the active medium has important implications, especially for a quasi-three level system such as Ytterbium [58]:

- The Ytterbium ions are described by a quasi-three levels system, which has been studied in sub section 2.6.4 . This means that the lower manifold is thermally populated and it follows the Boltzmann's Law. Increasing the temperature leads to an increase in the population of the upper levels of the lower manifold, which might reduce the population inversion at a given laser transition. This is a detrimental effect since it increases the laser threshold and it can reduce the gain provided by the active medium.

- A temperature gradient modifies the physical dimensions of the active medium, but since it is positioned in a holder it causes the crystal to be under stress and thus a strain. The strain of the crystal matrix might lead to an instability in the cavity, a degradation of the beam quality and in worst cases to a fracture.

- The ellipsoid of the crystal index can be modified by the induced thermo-mechanical stress. This is a deleterious effect especially in isotropic crystals, since it creates a strain-induced birifringence which leads to depolarization losses.

- A thermal lens effect might be induced by a temperature gradient along the crystal. The thermal lens focal length has been described in sub section 4.5.4 and it is defined by equation 5.8:

$$f_{th}^{-1} = \frac{\eta_h P_{abs} \chi}{2\pi w_p^2 K_c} \tag{5.8}$$

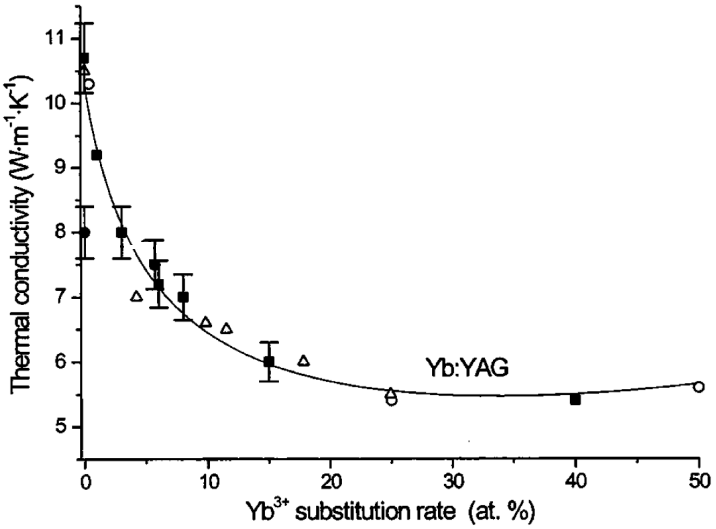

Figure 5.2: Variation of Thermal Conductivity versus doping concentration in Yb:YAG [60].

where η_h is the fractional thermal load, P_{abs} is the absorbed power, πw_p^2 is the pumped area, K_c is the thermal conductivity and χ is the thermo-optic coefficient [58].

The thermal conductivity K_c is of fundamental importance because it defines how efficiently the active medium transports the heat. It usually depends on the doping concentration, since the ions can be seen as an impurity inside the crystal lattice. The thermal conductivity can be defined by the following equation:

$$K_c = \frac{1}{\pi a}\sqrt{\frac{2k_B v_s K_0}{\delta}}\arctan\left[\pi a\sqrt{\frac{K_0\delta}{2k_B v_s}}\right] \tag{5.9}$$

$$\delta = \sum_{k=1}^{n} c_i\left(\frac{M_i - M}{M}\right)^2 \quad M = \sum_{k=1}^{n} c_i M_i \quad a = 2\sqrt[1/3]{\frac{3M}{4\pi N n \rho}} \tag{5.10}$$

Where a is an average interatomic distance, k_B is the Boltzmann's constant, v_s is the speed of sound in the active medium, K_0 is the thermal conductivity of the crystal host without doping, M and n are respectively the molar mass and the number of atoms per formula unit, N is the Avogadro's constant and ρ is the density of the atoms in the crystal lattice. The δ represents the mass variance of the lattice substitution sites of average mass M that have an occupation probability c_i to be occupied with ions i with m ass M_i [61].

The thermal shock resistance R_T is another parameter of fundamental importance which depends on thermal conductivity. It describes the induced thermo-mechanical stress and the capacity of the active medium to resist to thermal solicitations avoiding a fracture:

$$R_T = \frac{(1-\nu)KK_c}{E\alpha} \tag{5.11}$$

where K_c and α are the thermal conductivity and thermal expansion of the active medium, K is the material toughness, E is the Young's modulus and ν is the Poisson's ratio.

5.4 Ytterbium Doped Crystals

Ytterbium doped crystals are an attractive solutions for high-power diode-pumped systems and laser amplifiers for ultrashort pulses. They possess very broad emission bandwidths, a long fluorescence lifetime, good thermo-optical properties, an incredible small quantum defect and a mature semiconductor diode technology which can provide an efficient way to pump them. Moreover, since the Ytterbium electronic structure is very simple, there are not present detrimental effect such as upconversion, excited state absorption and concentration quencing. In this section are reported the main properties of the active media which have been employed during the experiments.

5.4.1 Yb:KYW

Yb-doped Potassium Ittrium Tungstate (Yb^{3+}:$KY(WO_4)_2$) or Yb:KYW is one of the most employed and common laser material for industrial femtosecond diode pumped solid-state lasers. Rare earth potassium tungstates are biaxial crystals which crystallize in the monoclinic structure [62]. While the tungstate matrices are used in active media since the second half of 1960, the KYW crystals appeared only at the beginning of 1970 [63]. Their usage as crystal hosts for Ytterbium ions started to be common at the beginning of 1990 [64].

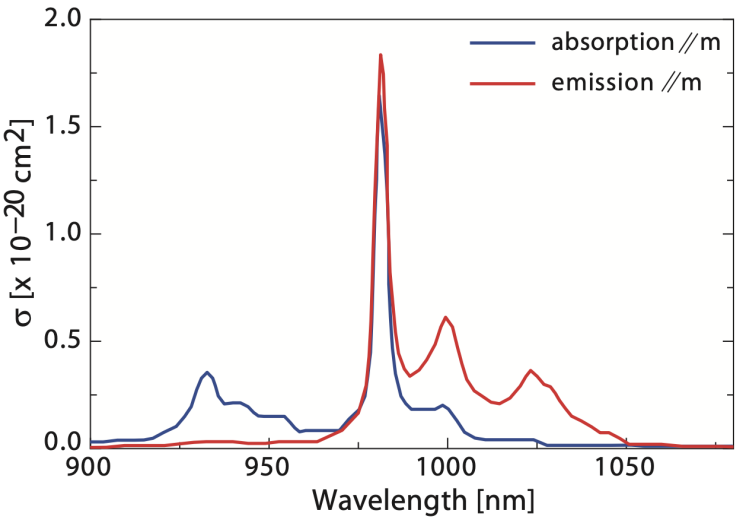

Figure 5.3: Polarized absorption and emission spectra of Yb^{3+}:KYW at room temperature, $\mathbf{E}||N_m$ [1].

The interest in Yb:KYW arose due to its favourable spectroscopic properties as gain medium. Since it is a biaxial crystal, the absorption and emission cross sections depend on the orientation of the crystallographic axes with respect to light polarization. The Yb:KYW axes are defined as N_m, N_p and N_g; generally it is found

as N_g-cut, thus exploiting N_m and N_p as axes for absorption and emission of light. The N_m axis experiences the highest absorption and emission cross sections. When the incoming light polarization is parallel to the N_m axis, depicted in figure 5.3, the absorption cross section of Yb:KYW at 981 nm is $\sigma_a = 13.3 \cdot 10^{-20}$ cm^2, whereas the emission cross section at 1025 nm is $\sigma_e = 3 \cdot 10^{-20}$ cm^2.

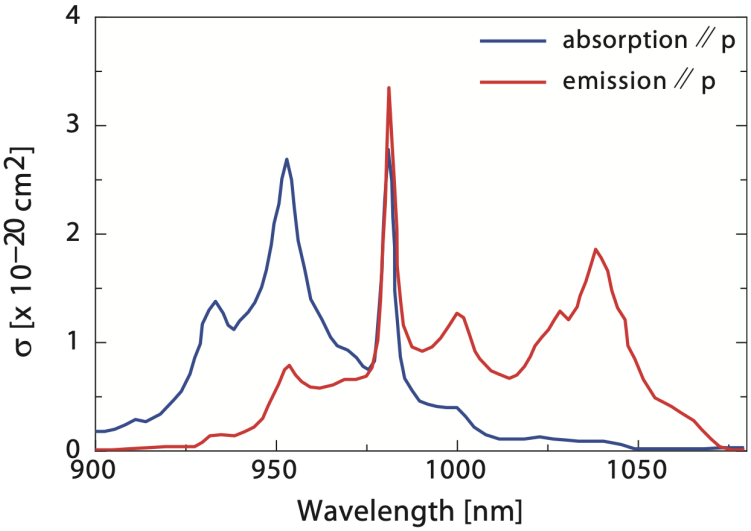

Figure 5.4: Polarized absorption and emission spectra of Yb^{3+}:KYW at room temperature, $\mathbf{E}||N_p$ [1].

It has an emission wavelength between $1020 - 1060$ nm, and a useful emission bandwidth FWHM of about 24 nm, which allows to generate ultrashort pulses in the sub 100 fs range. The Yb:KYW crystals are pumped at 981 nm, where there is a peak of absorption with a bandwidth FWHM of about 3.5 nm. Since the emission wavelength is around 1030 nm, it possess an incredible small quantum defect, about 5%, allowing Yb:KYW crystal the capability to reach high optical to optical efficiency and extremely low thermal load. Moreover it has as a doped material a quite high thermal conductivity of about 3 W·m^{-1}K^{-1}. These characteristics make Yb:KYW an incredible gain media for high power lasers [65]. Nonetheless, a careful thermal management of the system is necessary. The monoclinic structure of Yb:KYW is not symmetric, thus the thermo-optic coefficients along the crystallographic axes are and non uniform. Moreover, as a fluoride crystal it has negative thermo-optic coefficients while the thermal expansion coefficients are positive, leading to a slightly negative and weak thermal lens effect. The consequent thermo-optical distortions can lead to instabilities, reduced output beam quality of crystal fracture [65].
In table 5.2 are reported the main spectroscopic and thermo-mechanical properties of Yb:KYW.

5.4.2 Yb:YAG

Yb-doped Yttrium aluminium garnet or Yb:YAG is one of the first hosts ever used in laser history, starting from 1960s. It is an oxide crystal with a cubic and isotropic structure. Only in the 1990s with the development of semiconductor laser technology

Table 5.2: Spectroscopic and thermo-mechanical properties of Yb:KYW [1].

Material Properties	**Units**	**Value**
Crystal Structure	–	Monoclinic
Lattice Constant	Å	$a = 8.05$, $b = 10.35$, $c = 7.54$
Growth	–	Modified Czochralski
Density	g/cm^2	6.5
Hardness	Mohs	$4 - 5$
Laser Properties	**Units**	**Value**
Possible dopant concentrations	%	$1 - 20$
Pump wavelength (λ_p)	nm	981
Emission wavelength (λ_i)	nm	$1020 - 1060$
Absorption bandwidth FWHM	nm	3.5
Emission bandwidth FWHM	nm	24
Quantum defect (η_q)	%	5
Peak absorption cross section (@ 981 nm, N_m) (σ_a)	10^{-20} cm^2	13.3
Peak emission cross section (@ 1025 nm, N_m) (σ_e)	10^{-20} cm^2	3
Fluorescence lifetime τ	μs	300
Refractive index (n)	–	$n_p = 1.98$, $n_p = 2.02$, $n_g = 2.06$
Nonlinear refractive index (n_2)	10^{-16} cm^2/W	25 $\mathbf{E}\|\|N_m$, 20 $\mathbf{E}\|\|N_p$
Thermo-mechanical Properties	**Units**	**Value**
Thermal shock resistance parameter (R_T)	W$\cdot$ m^{-1}	–
Thermo-optic coefficients (@ 1064 nm) (dn/dT)	10^{-6} K^{-1}	$\mathbf{E}\|\|N_p = -14.6$, $\mathbf{E}\|\|N_m = -8.9$, $\mathbf{E}\|\|N_g = -12.4$
Thermal expansion coefficient (@ 373 K) (α)	10^{-6} K^{-1}	$\alpha_p = 2$, $\alpha_m = 10.3$, $\alpha_g = 15.9$
Young's modulus (E)	GPa	–
Thermal conductivity (average) (K_c)	W$\cdot$m^{-1}K^{-1}	3 (at 2% doping)
Poisson's ratio (ν)	–	-0.25

the Yb:YAG became a feasible industrial solution [66]. The Yb:YAG crystals are grown with Czochralski and Bridgman method, but also with Temperature-gradient technology. Yttrium ions in YAG can be replaced with laser-active rare earth ions without strongly affecting the lattice structure.

Among the numerous Yb-doped oxide and fuoride crystals, Yb:YAG crystal plays an important role since it possesses many attractive characteristics. It has very good thermo-mechanical properties, with a high thermal conductivity of about 7 $W{\cdot}m^{-1}K^{-1}$ at 5%, a positive thermo-optic coefficient, $7.8 \cdot 10^{-6}$ K^{-1}, and a thermal expansion coefficient of $8 \cdot 10^{-6}$ K^{-1}. Moreover it possesses a long fluorescence lifetime, ≈ 1 ms, and has a favourable absorption cross section for semiconductor laser pumping. Thus, from the beginning of its discovery it gained popularity for its versatility and has been intensively investigated.

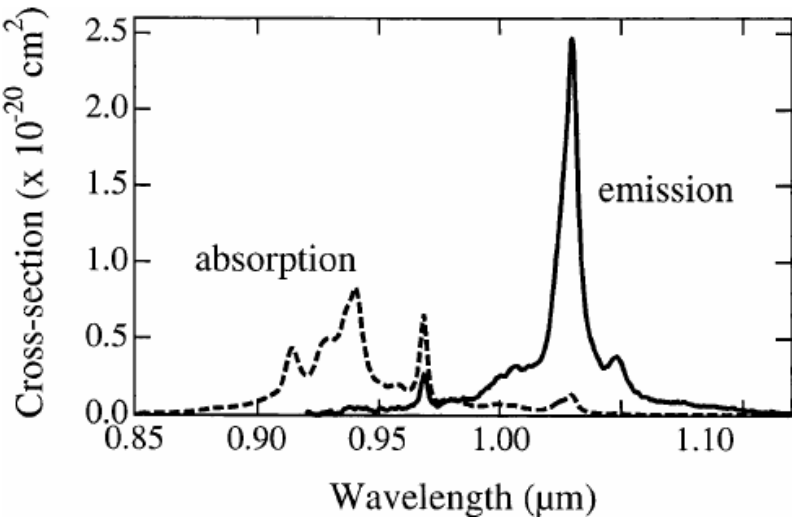

Figure 5.5: Absorption and emission spectra of Yb^{3+}:YAG at room temperature [2].

Yb:YAG has two peaks of absorption. The most exploited peak is at 940 nm, where the available bandwidth is 18 nm, and the absorption cross section is $\sigma_a = 0.82 \cdot 10^{-20}$ cm^2. The second peak is at 969 nm, where the available bandwidth is reduced at 2.7 nm, which limits the adoptable solutions to pump it. At this wavelength the absorption cross section is $\sigma_a = 0.8 \cdot 10^{-20}$ cm^2, but the reduced quantum defect with respect to pumping at 940 nm, 6% instead of 9%, gives advantages to the overall laser system. The emission cross section has its peak at 1030 nm where it worth $\sigma_e = 2.1 \cdot 10^{-20}$ cm^2. On the other hand, the emission bandwidth of 9 nm is much narrower with respect to other crystals such as Yb:CaF_2 or Yb:KYW, leading the Yb:YAG not to be a feasible solution for the generation of ultrashort pulses under 150 fs.

The positive sign of the thermo-optic and thermal expansion coefficient leads to a positive and not negligible thermal lens effect. Moreover, due to the isotropic structure of the crystal, under thermal solicitations the Yb:YAG suffers from strain-induced birifringence, lowering the output beam quality and the polarization extinction ratio. Thus, all the high-power systems where there is involved an Yb:YAG crystal have to take into account some countermeasures to mitigate these detrimental effects.

Table 5.3: Spectroscopic and thermo-mechanical properties of Yb:YAG [2].

Material Properties	**Units**	**Value**
Crystal Structure	–	Cubic
Lattice Constant	Å	$a = 12.01$
Growth	–	Czochralski, Bridgman Temperature-gradient
Density	g/cm^2	4.56
Hardness	Mohs	8.5
Laser Properties	**Units**	**Value**
Possible dopant concentrations	%	$0.5 - 30$
Pump wavelength (λ_p)	nm	940/969
Emission wavelength (λ_i)	nm	1030
Absorption bandwidth FWHM	nm	18/2.7
Emission bandwidth FWHM	nm	9
Quantum defect (η_q)	%	9/6
Peak absorption cross section (@ 940/969 nm) (σ_a)	10^{-20} cm^2	0.82/0.8
Peak emission cross section (@ 1030 nm) (σ_e)	10^{-20} cm^2	2.1
Fluorescence lifetime τ	μs	960
Refractive index (n)	–	1.82
Nonlinear refractive index (n_2)	10^{-16} cm^2/W	3.8
Thermo-mechanical Properties	**Units**	**Value**
Thermal shock resistance parameter (R_T)	$W\cdot m^{-1}$	800
Thermo-optic coefficient (@ 1064 nm) (dn/dT)	10^{-6} K^{-1}	7.8
Thermal expansion coefficient (@ 373 K) (α)	10^{-6} K^{-1}	≈ 8
Young's modulus (E)	GPa	335
Thermal conductivity (average) (K_c)	$W{\cdot}m^{-1}K^{-1}$	7 (at 5% doping)
Poisson's ratio (ν)	–	0.3

5.4.3 Yb:CaF_2

Yb-doped calcium-fluoride or Yb:CaF_2 is one of the oldest hosts used in solid state lasers [67]. The CaF_2 is an alkaline-earth fluoride crystal with a cubic and isotropic structure. Since the first half of 1960 it has been exploited with different ions, such as Uranium, Thulium or Neodymium. In more recent years, with the advent of Ytterbium, it has been rediscovered. This crystalline material has shown to compete with oxides and glasses regarding the thermal conductivity and the ease to grown by using the standard Czochralski or Bridgman technique. When a trivalent ion such as Yb^{3+} is substituted to Ca^{2+} in the crystal matrix a charge compensation is needed to reach the electrical neutrality. In order to do that he Ytterbium ions form a cluster, whose dimensions and complexity depends on the ion concentration. At low dopant concentration the clustering of the Yb^{3+} ions generates some ion-ion energy transfer effects which are detrimental for an active media. Increasing the dopant concentration ($> 1\%$) the generated clusters are free of these deleterious effects and the Yb^{3+} ion clusters resemble in a glass-like disorder, leading to broad and relatively smooth absorption and emission spectra [67].

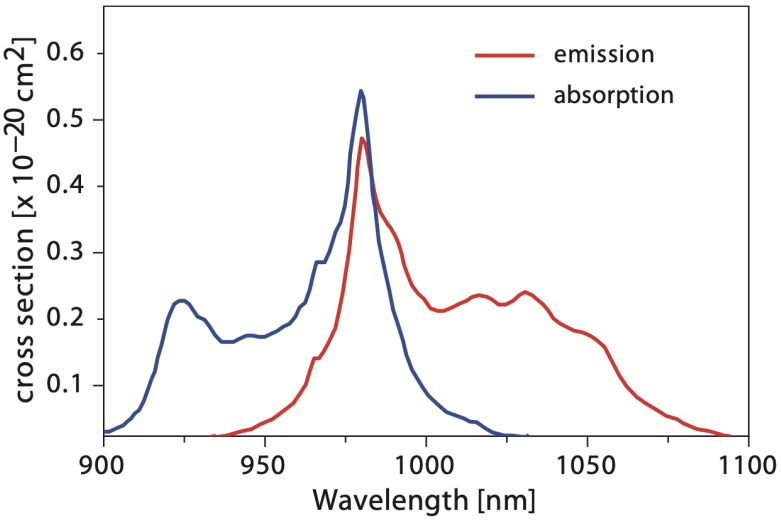

Figure 5.6: Absorption and emission spectra of Yb^{3+}:CaF_2 at room temperature [1].

The peak of absorption of Yb:CaF_2 is at 979.6 nm and its cross section is $\sigma_a = 0.56 \cdot 10^{-20}$ cm^2. In CW operation the laser wavelength is about 1049 nm. At this wavelength the emission cross section is $\sigma_e = 0.16 \cdot 10^{-20}$ cm^2. The relatively low absorption and emission cross sections are compensated by a very long fluorescence lifetime of about 2400 μs. The presence of Yb^{3+} ions decreases the thermal conductivity with respect to their concentration level. Even though, the Yb:CaF_2 has a very high value of 5.4 W·m^{-1}K^{-1} at 2.5% of doping.
Yb:CaF_2 shares the same properties of other fluoride crystals, it has a negative thermo-optic coefficient and a very low thermal shock parameter, which lead it to be sensitive to fracture. Then, in high-power system it has to be treated carefully.
In table 5.4 are reported the main spectroscopic and thermal properties of Yb doped CaF_2.

Table 5.4: Spectroscopic and thermo-mechanical properties of Yb:CaF_2 [1,3].

Material Properties	**Units**	**Value**
Crystal Structure	–	Cubic
Lattice Constant	Å	$a = 5.462$
Growth	–	Czochralski, Bridgman Temperature-gradient
Density	g/cm^2	3.18
Hardness	Mohs	4
Laser Properties	**Units**	**Value**
Possible dopant concentrations	%	$1 - 15$
Pump wavelength (λ_p)	nm	979.6
Emission wavelength (λ_i)	nm	$1033 - 1055$
Absorption bandwidth FWHM	nm	10
Emission bandwidth	nm	70
Quantum defect (η_q)	%	5
Peak absorption cross section (@ 979.6nm) (σ_a)	10^{-20} cm^2	0.54
Peak emission cross section (@ 1025 nm) (σ_e)	10^{-20} cm^2	0.16
Fluorescence lifetime τ	μs	2400
Refractive index (n)	–	1.429
Nonlinear refractive index (n_2)	10^{-16} cm^2/W	1.9
Thermo-mechanical Properties	**Units**	**Value**
Thermal shock resistance parameter (R_T)	$W\cdot m^{-1}$	242
Thermo-optic coefficient (@ 1064 nm) (dn/dT)	10^{-6} K^{-1}	-17.8
Thermal expansion coefficient (@ 373 K) (α)	10^{-6} K^{-1}	18
Young's modulus (E)	GPa	$146.4 < 100 >$, $89.6 < 111 >$
Thermal conductivity (average) (K_c)	$W{\cdot}m^{-1}K^{-1}$	5.4 (at 2.5% doping)
Poisson's ratio (ν)	–	0.21

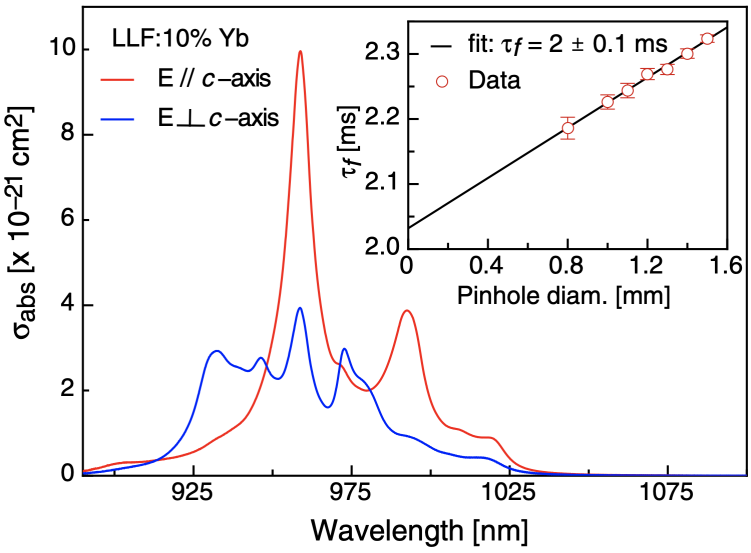

Figure 5.7: Room temperature polarized absorption cross section of Yb:LLF. Inset: lifetime measurement obtained with the pinhole method [8].

5.4.4 Yb:LiLuF$_4$

Yb-doped lutetium-lithium-fluoride or Yb:LiLuF$_4$ is a uniaxial crystal with a tetragonal structure. While a various number of fluoride Yb-doped crystals have been studied since 1960s, Yb:LLF raised interest only in the 2000s [68], with the advent of Ytterbium ions and more famous fluoride crystals. It is isomorphic to Yb:LiYF$_4$, which has been widely studied as laser material [8]. However, relatively recent works involving materials with Lu^{3+} instead of Y^{3+} or codoped with Yb^{3+} ions showed reduced solarization effects and improved laser performance [69]. Moreover, Yb:LLF showed its potentiality as laser material with the complementary advantage to be grown with large size and good optical quality since LLF melt congruently while YLF does not [68]. As other fluorides crystals, is has excellent thermo-optical properties. It offers a weak and negative thermo-optic coefficient (dn/dT is equal to $\mathbf{E}||c = -6$ 10^{-6} K^{-1}, $\mathbf{E}\perp c = -3.6$ 10^{-6} K^{-1}), low phonon energy and low refractive index (≈ 1.46). These properties are favourable for high-energy and high-power lasers in continuous-wave and pulsed regime.
Yb:LLF presents a peak of absorption at 960 nm. While at this wavelength presents high cross section values, the region at 976 nm is exploited by semiconductor technology. At 976 nm, the absorption cross section is $\sigma_{e,||c} = 0.21$ 10^{-20} cm^2 and $\sigma_{e,\perp c} = 0.23$ 10^{-20} cm^2 for the polarization parallel and perpendicular to the c-axis, respectively. The wavelength emission spans across 1010-1050 nm. The peak of emission is at 1010 nm where the emission cross section is $\sigma_{e,||c} = 0.84$ 10^{-20} cm^2 and $\sigma_{e,\perp c} = 0.41$ 10^{-20} cm^2.

Table 5.5: Spectroscopic and thermo-mechanical properties of Yb:$LiLuF_4$ [4, 5].

Material Properties	**Units**	**Value**
Crystal Structure	–	Tetragonal
Lattice Constant	Å	$a = 5.13$, $c = 10.55$
Growth	–	Czochralski, μ-PD Bridgman
Density	g/cm^2	6.19
Hardness	Mohs	–
Laser Properties	**Units**	**Value**
Possible dopant concentrations	%	1–
Pump wavelength (λ_p)	nm	960/976
Emission wavelength (λ_i)	nm	$1010 - 1050$
Absorption bandwidth FWHM (@ 976 nm, $\mathbf{E}\|\|c$)	nm	20
Emission bandwidth FWHM	nm	20
Quantum defect (η_q)	%	6/5
Peak absorption cross section (@ 976nm) (σ_a)	10^{-20} cm^2	$\mathbf{E}\|\|c = 0.21$, $\mathbf{E}\perp c = 0.23$
Peak emission cross section (@ 1018 nm) (σ_e)	10^{-20} cm^2	$\mathbf{E}\|\|c = 0.84$, $\mathbf{E}\perp c = 0.41$
Fluorescence lifetime τ	μs	2000
Refractive index (n)	–	$n_c = 1.46$
Nonlinear refractive index (n_2)	10^{-16} cm^2/W	–
Thermo-mechanical Properties	**Units**	**Value**
Thermal shock resistance parameter (R_T)	W$\cdot$ m^{-1}	–
Thermo-optic coefficients (dn/dT)	10^{-6} K^{-1}	$\mathbf{E}\|\|c = -6$, $\mathbf{E}\perp c = -3.6$
Thermal expansion coefficient (α)	10^{-6} K^{-1}	–
Young's modulus (E)	GPa	–
Thermal conductivity (average) (K_c)	W$\cdot$m^{-1}K^{-1}	$\mathbf{E}\|\|c = 6.3$, $\mathbf{E}\perp c = 5$
Poisson's ratio (ν)	–	–

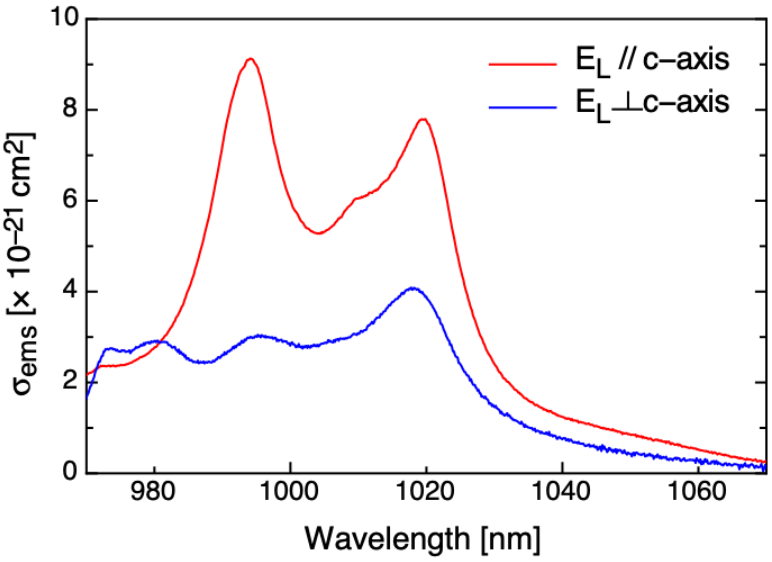

Figure 5.8: Room temperature polarized emission cross section of Yb:LLF [8].

Chapter 6

High Power Yb:YAG Multipass Amplifier

The first part of my work has been devoted to the study of a high-power Yb:YAG multipass amplifier. The Yb:YAG crystal is a well-known crystal with a mature growth technology. It has very good thermo-optic properties, outstanding thermo-mechanical properties, a high emission cross section and relatively broad bandwidth to sustain femtosecond pulses amplification. This leads to some consequences. The passages required to reach a desired high amplification gain are few, since the emission cross section has an high value. On the other hand, the Yb:YAG transition lineshape limits the bandwidth of the amplified ultrashort pulses due to gain narrowing effect. The main focus of this research was to investigate the feasibility of an ultrashort pulses Yb:YAG multipass amplifier in an industrial context. The system layout consisted in a 2-Pass Yb:YAG amplifier which was tested in continuous wave and in pulse regime, exploiting a homemade tunable Yb:KYW oscillator which was easily modified to work in CW and subsequently in solitonic mode locking, generating ≈ 200 fs pulses. The system amplifier showed excellent amplification performances, a very good optical quality and a robustness to thermal effects such as thermal lensing and depolarization losses. On the other hand, the relatively broad bandwidth of Yb:YAG in ultrashort pulse amplification severely limited the output pulse bandwidth due to a strong gain narrowing effect. Thus, I implemented a technique of pulse spectral shaping with the aim of mitigate gain narrowing. While this method seemed to be noneffective or even deleterious in terms of output power and pulse duration in some situations, it led to an interesting bandwidth conservation effect when the incident pulse was centered at 1026 nm. A numerical investigation through polychromatic simulation of the amplification process was carried out in order to help understanding the experimental results.

6.1 CW and Mode-Locked Yb:KYW Seeder

The first part of the work was devoted to build a laser oscillator for the amplification measurements which could be easily switched from continuous wave to mode-locking regime. It had to possess tunability over a wide range of wavelengths centered around 1030 nm and be near diffraction limit. The tunable continuous

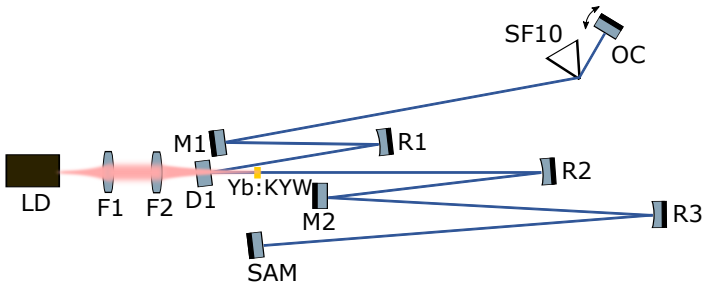

Figure 6.1: Solitonic Mode-Locking Tunable Yb:KYW Seeder Setup. M1, M2: High reflectivity (HR) flat mirror at 1000-1100 nm; R1: r=150 mm spherical mirror HR at 1000-1100 nm; R2: r=400 mm spherical mirror HR at 1000-1100 nm, R3: r=400 mm spherical mirror HR at 1000-1100 nm; D1: Dichroic Mirror (DM) Highly Transmitting (HT) at 980 nm and HR at 1000-1100 nm; OC: Output coupling mirror T=1.7%; F1, F2: f=30 mm achromatic lenses, Anti Reflection (AR) coated at 980 nm.

wave seeder was designed as an X-shaped cavity and exploited a fiber coupled diode pumped 5% doped, 2 mm long, Ng-cut, Yb:KYW crystal. The crystal was wedge and AR coated. The gain medium was positioned on a water-cooled copper heat sink at a constant temperature of 15 °C. The crystal was set such that the tangential plane was $\mathbf{E}||N_m$ whereas the sagittal plane was $\mathbf{E}||N_p$.
The laser diode was fiber coupled, providing 5 W at $\lambda_p = 981$ nm. An half wave plate was inserted along the pump beam optical axis in order to modify its polarization and match the peak of absorption of the Yb:KYW crystal along N_p axis with an extinction ratio of $\approx 13:1$.
The diode pump was focused through a telescope on a 60 μm waist radius by means of two achromatic lenses, F1 and F2, AR coated at 976 nm, with a focal length of 30 mm. On the other hand the resonant mode radius in the crystal was 50 μm. The maximum output power was 0.8 W at 1030 nm with an output coupler transmittivity $T_{OC} = 1.7\%$. The continuous wave seeder was tunable from 1024 nm to 1037 nm with a linear horizontal polarization exploiting N_m emission cross section; the laser emission from 1037 nm to 1040 nm was with a linear vertical polarization exploiting N_p emission cross section. The resonant mode had a beam radius of $w_s \approx 400$ μm on the OC.
The continuous wave oscillator was successively modified to operate in mode-locking regime by inserting a saturable absorber and an optical component to compensate the second order dispersion. The tunable femtosecond seeder, which is depicted in figure 6.1, was designed as a single-prism oscillator [70] including a SESAM for passive mode-locking in a X-shaped cavity. The SESAM was provided by Spectra-Physics with a saturation fluence of $F_{ss} \simeq 400$ μJ·cm^{-2}. The GVD necessary to compensate through the single-prism technique was $\simeq 2500$ fs^2 per round trip.

The femtosecond oscillator was smoothly tunable from 1025 nm to 1036 nm, as depicted in figure 6.2. The pulse repetition rate (PRR) was 108 MHz with a pulse energy up to ~ 5 nJ, output power 0.5 W, exploiting an output coupler transmittivity $T_{OC} = 1.7\%$. The single-prism at Brewster's angle forced the resonant mode to have a linear horizontal polarization, parallel to N_m axis. The pulse shape and duration

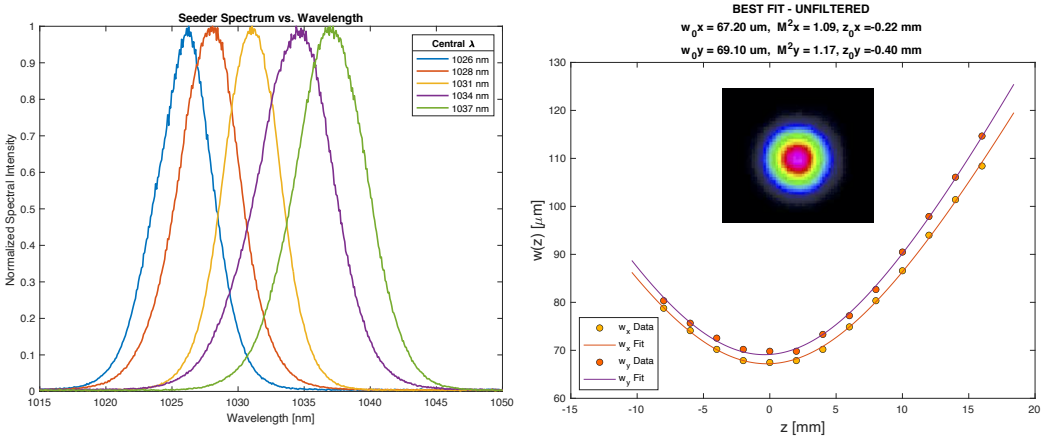

(a) Autocorrelation trace

(b) Beam Quality

Figure 6.2: Spectrum and Beam quality of mode locked Yb:KYW seeder

was measured though an APE Pulsecheck autocorrelator and is depicted in figure 6.3. The pulse duration was about 200 fs FWHM all over the tunability range with a spectrum FWHM of about $5.5 - 7$ nm and a time-bandwidth product (TBP) of 0.37. After the output coupler, a prism pair was added to suppress spatial chirp, however this was not an issue given the not-too-short pulse width, nor was the output direction critically dependent on center wavelength, owing to the relatively narrow tuning range used for the experiment.
The beam quality of the seeder was measured through a CCD camera positioned along the focal plane of a spherical lens with f=125 mm. The beam quality resulted was $M_x^2 \times M_y^2 = 1.09 \times 1.17$ and is depicted in figure 6.2.
The tunability was obtained in two ways, both of them relying on the net gain provided at a given frequency. The SF10 prism creates an angular dispersion which is wavelength dependent. By rotating the output coupler the peak wavelength was selected as the wavelength which generated the highest net gain after a roundtrip. Alternatively, the peak wavelength was selected by moving along the transverse axis the focusing pump lens F2. In this way the resonant mode was forced to change the peak wavelength to oscillate.

6.2 High Power Yb:YAG Multipass Amplifier

The multipass amplifier layout employed in the experiments is shown in figure 6.4. It exploited a Yb:YAG crystal in a 2-Pass configuration with the seeder/pump beams non collinear. The crystal was pumped by a fiber-coupled laser diode mounted on a water-cooled heat sink at 15 °C. The pump module provided up to 120 W in a multimode fiber with a core diameter $2w = 105$ μm with an NA= 0.22. The estimated beam quality was $M^2 \simeq 40$. The pump wavelength was not stabilized by means of a fiber Bragg grating (FBG). Its wavelength had a continuous drift from $\lambda_p = 927$ nm at minimum driving current to $\lambda_p = 940$ nm at maximum driving current, 12 A. Nonetheless, the maximum driving current was set at 10 A due to thermal effects. The spectral bandwidth FWHM was 2.5 nm. The incident and

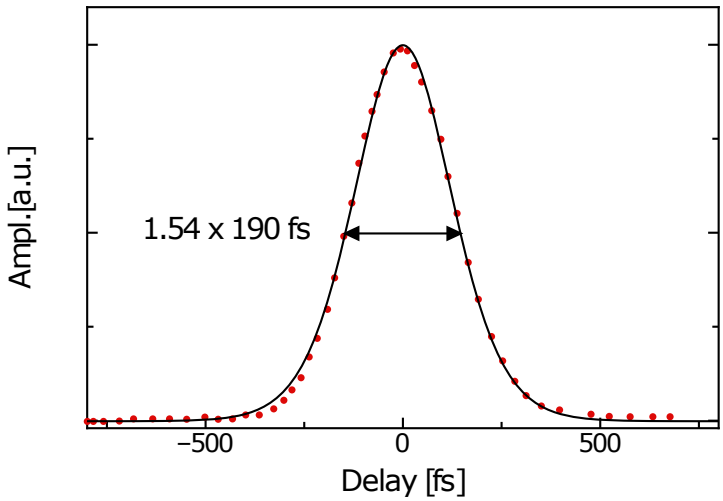

Figure 6.3: Autocorrelation trace of mode locking Yb:KYW oscillator pulse

absorbed pump power characteristics are depicted in figure 6.5. The absorbed pump power was ≈ 80% of the incident pump power. The pump beam was coupled in the amplifier by using a telescope composed by two achromatic lenses, F1 with a focal length of 40 mm, F2 with a focal length of 75 mm, both AR coated at 940 nm. The beam spot radius realized in the active medium was $w_p = 100$ μm.

The gain medium exploited by the amplifier was a 12 mm long Yb:YAG 3% doped. The crystal was wrapped in indium foils and then soldered in a water-cooled copper holder. The water was kept at 15 °C. The seeder output beam was collimated by means of a spherical lens with a focal length of 1000 mm, which is not shown in figure 6.4, and focused by a spherical lens F3 of focal length 250 mm in the gain medium with a beam spot radius of $w_s = 82$ μm. Between the two lenses there were positioned two telescopes with a unitary magnification with the sole aim to mantain the beam collimated (not shown in the amplifier layout). The F3 spherical lens was mounted on a millimetric stage to perfectly match the pump spot size in the gain medium. Moreover, the seeder beam hit the F3 lens off-axis in order to be non collinear with the pump beam in the crystal.

The seeder beam then was inserted into the amplifier gain medium by a dichroic mirror (D1) highly transmitting at $1000 - 1100$ nm, after the first pass was then reflected by another dichroic mirror (D2) along the retroinjection arm, which is composed by a telescope and an HR 0° broadband plane mirror M3, with the purpose to reflect back the amplified seeder beam for the second pass though the gain medium. The amplified seeder beam was reflected by the dichroic mirror D2 with an angle $2\theta \approx 10°$ which still led to high reflectivity $> 95\%$. The telescope was composed by two spherical lenses, F4 with a focal length of 300 mm and F5 with a focal length of 100 mm, both AR coated. The distance F5 lens−M3 mirror was adjustable to take into account thermal lensing in the amplifier. The first pass amplified beam was then reflected back into the gain medium, again in a non collinear situation with respect to the pump. Successively the amplified beam was extracted after the spherical lens F3, which was hit off-axis, by means of M4, an HR 45° broadband plane mirror.

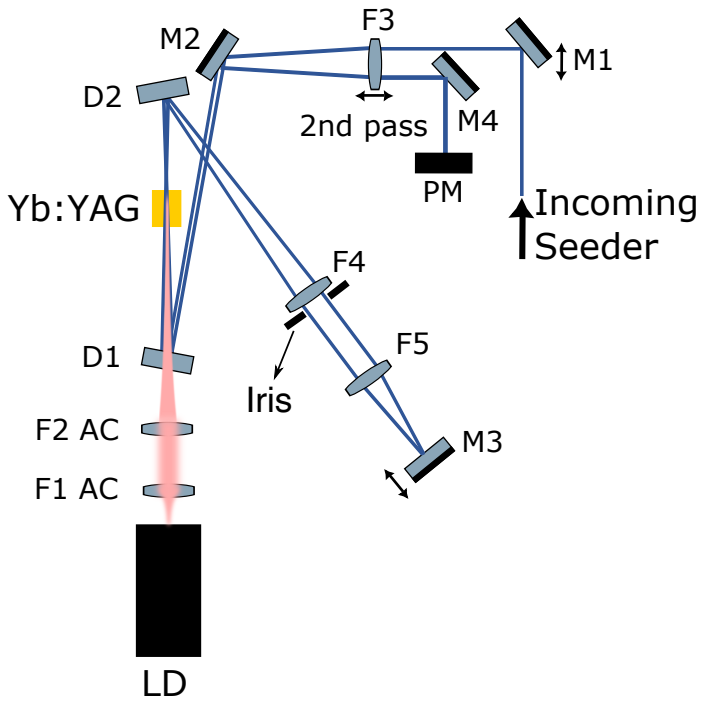

Figure 6.4: 2-Pass Yb:YAG Amplifier.F1, F2: achromatic lenses, f1=40 mm, f2=75 mm, AR coated at 940 nm; F3, F4, F5: spherical lenses, f3=250 mm, f4=300 mm, f5=100 mm, AR coated at 1030 nm; M1, M2, M4: HR 45° broadband plane mirrors; M3: HR 0° broadband plane mirror; D1, D2: dichroic mirrors, HT at 976 nm and HR at 1000-1100 nm; PM: power meter.

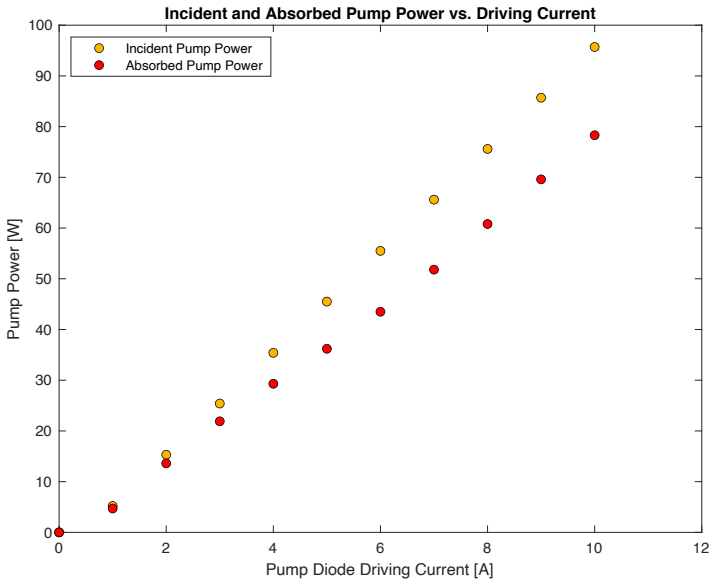

Figure 6.5: Yb:YAG Incident and Absorption Pump Power

In the following sections there is a detailed analysis of the work I performed with the mentioned multipass Yb:YAG amplifier.

6.3 ASE Control

An extensive work has been carried out to control the amplified spontaneous emission (ASE). As described in Section 4.5.2, ASE is one of the main detrimental effects in a high gain amplifier. It is a quasi-coherent process which amplifies through stimulated emission the spontaneous radiation. In a high gain amplifier ASE depletes the energy stored in the gain medium and eventually becomes laser radiation if there is a positive feedback in the amplifier system, such as a reflection from optical components. This event is called *Self-Lasing*. While ASE cannot be completely avoided, in a multipass amplifier is important to avoid an oscillation since it dramatically decreases the amplification efficiency. The threshold gain G for a closed loop is:

$$G^2 = \frac{4\pi^{3/2}}{\eta_q \Omega}[\ln(G)^2]^{1/2} \tag{6.1}$$

where η_q is the fluorescence quantum efficiency and Ω is the solid angle of the ASE back reflected into the gain medium. The equation describes the maximum gain reachable by the amplifier before starting laser oscillation due to ASE. The only parameter which can be modified to increase the maximum amplifier gain without transform ASE into laser radiation is the solid angle Ω. This parameter only depends on the amplifier system layout and the crystal shape. For two different amplifier configurations with a given solid angle Ω_i:

$$G_1^2 = \frac{k}{\Omega_1}[\ln(G_1)^2]^{1/2} \qquad G_2^2 = \frac{k}{\Omega_2}[\ln(G_2)^2]^{1/2} \tag{6.2}$$

where $k = 4\pi^{3/2}/\eta_q$. Thus, the ratio between solid angles can be defined just through the gain threshold for ASE:

$$\frac{\Omega_2}{\Omega_1} = \frac{G_1^2}{G_2^2}\sqrt{\frac{\ln(G_2)}{\ln(G_1)}} \tag{6.3}$$

In this work I studied how to avoid laser radiation by ASE. In order to do that, I increased the threshold gain G by reducing the solid angle of the back scattered ASE. At first I studied the optical components in the amplifier system which backreflected even a minimum quantity of light in the gain medium. The retroinjection arm, composed by the spherical lenses F4 and F5 and by a M3, a HR 0° broadband plane mirror, represented the major contributors to this effect. The ASE possesses quasi-coherent properties, and thus also directionality. Moreover, since it exploits laser transitions, its wavelength is near the peak of the emission cross sections of the gain material, which means that in our scheme it is reflected by the dichroic mirror D2 and inserted into the retroinjection arm. Thus, the angle of acceptance of the spherical lens F3 defines the solid angle of the ASE backreflected into the crystal by the retroinjection arm. I implemented different methods to decrease the angle Ω.

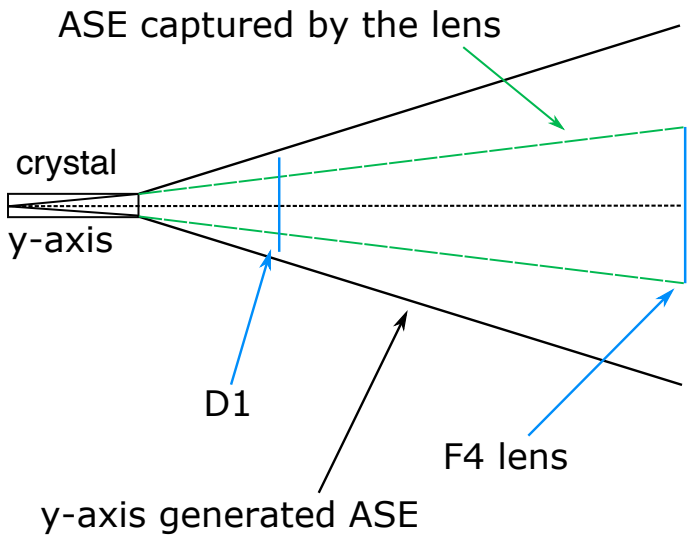

Figure 6.6: ASE collected by F4 collimating spherical lens. The ASE gathered by the F4 lens is not limited by the dichroic mirror D1 but by F4 acceptance angle.

The first aimed to reduce the ASE accepted by the lens by increasing the distance between the crystal's end facet and the collimating lens F4. Since ASE is a quasi-coherent process, is directionality properties are not equal to laser transition; an increase in the aforementioned distance reduced the ASE hitting the lens. The directionality of the generated ASE is different for x and y axes, since the crystal has not a symmetrical shape. The multipass setup depicted in figure 6.4 already presents the following improvements. In a previous configuration, the telescope in the retroinjection arm was composed by spherical lenses F4 with f= 200 mm and F5 with f= 100 mm. Through geometrical optics I estimated the total ASE gathered by the F4 lens with f= 200 mm to be $ASE_c \approx 3.7\%$. Successively, the spherical lens F4 focal length was changed from f= 200 mm to f= 300 mm. In a such multipass layout, the total ASE collected by the F4 lens I estimated to be $ASE_c \approx 1.4\%$. In such a way, the ASE which can be theoretically backscattered has been reduced by more than half. For the y axis, a qualitative sketch of the ASE collected by the F4 lens is drawn in figure 6.6.

The second aimed to reduce the retroinjected ASE and thus to directly reduce the positive feedback. In order to do that I positioned a physical mask, an iris, between the two lenses which composed the telescope in the retroinjection arm, leaving only a hole for the passage of the actual amplified seeder beam. The schematic picture of the iris is shown is figure 6.7. These implemented solutions drastically reduced the solid angle of the ASE backscattered.

In a high-gain multipass amplifier, a decrease in the incident seeder power increases the small signal gain provided to the signal, thus the threshold gain for ASE to transform in laser radiation can be reached. The 2-Pass Yb:YAG amplifier was tested trough amplification of a continuous wave signal to assess the minimum

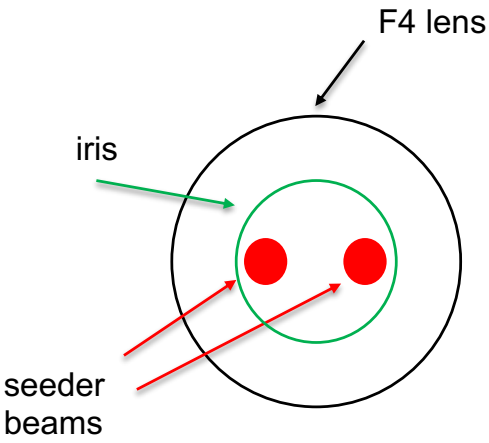

Figure 6.7: Iris implemented for ASE control.

incident seeder power necessary to self-lasing. The tests were carried out in three different amplifier configurations: without the implementation of the aforementioned countermeasures (Setup 1), with only the substitution of the collimating lens F4 (Setup 2) and also with the combination of the substituted F4 lens plus an iris (Setup 3). Moreover, the measurements were taken at three different incident pump power: 75 W, 85 W, and 95 W. The spectral components of the amplified beam were observed to understand whether the amplifier layout was self-lasing or not. Since ASE is a quasi-coherent process and exploits laser transitions, its wavelength peak will be matching with the peak of Yb:YAG emission cross section, which is at 1030 nm. Thus, the seeder wavelength was positioned slightly off peak ($\sim$ 0.5 nm) without compromising the amplification gain but enough to be able to discriminate between the amplifier beam laser radiation and self-lasing. In table 6.1 are described the self-lasing thresholds for the 2-Pass Yb:YAG amplifier without any countermeasures. The minimum incident seeder power is increased when there is an higher value of incident pump power due to the higher population inversion. At 95 W of incident pump power a thermal roll-off effect decreased the small signal gain g_0, which is $g_{0,1} \approx 800$ in the other two measurements. The minimum incident seeder power was P,inc,s = 27 mW at P,inc,p = 95 W. At this point the F4 lens was changed, which decreased the ASE backscattered into the crystal. The results are shown in table 6.2. Again, there is a thermal roll-off which decreased the g_0 at P,inc,p = 95 W, nonetheless the small signal gain $g_{0,2} \approx 1000$ in the three measurements. The implementation of this countermeasure increased significantly the g_0. Moreover, the related minimum seeder power has been reduced to P,inc,s = 13 mW at P,inc,p = 95 W. Finally I inserted the iris. The results are shown in table 6.3. The small signal gain took a huge step to $g_{0,3} \approx 1500$ reducing the minimum incident power to avoid self-lasing to P,inc,s = 7.5 mW at P,inc,p = 95 W. The latter is the 2-Pass Yb.YAG amplifier layout which has been exploited for continuous wave and ultrashort pulses amplification experiments.

An estimation of the threshold gain between Setup 2 and Setup 3 was done through equation 6.3. The threshold gain G_2 in a no mask configuration was known by experimental results, whereas Ω_2 and Ω_3 are not necessary as their absolute

Table 6.1: 2-Pass Yb:YAG Amplifier. Minimum Incident Seeder Power without Self-Lasing. No countermeasures were taken to control ASE.

Self-Lasing Threshold - Setup 1			
P, inc, p (W)	**P, inc, s (mW)**	**P, out (W)**	**Small signal gain g_0**
95	27	17	630
85	19	15.4	810
75	14	12	800

Table 6.2: 2-Pass Yb:YAG Amplifier. Minimum Incident Seeder Power without Self-Lasing. Changed F4 lens as countermeasure.

Self-Lasing Threshold - Setup 2			
P, inc, p (W)	**P, inc, s (mW)**	**P, out (W)**	**Small signal gain g_0**
95	13	12.2	940
85	7	7.8	1100
75	6	6.5	1080

Table 6.3: 2-Pass Yb:YAG Amplifier. Minimum Incident Seeder Power without Self-Lasing. Changed F4 lens plus iris as countermeasures.

Self-Lasing Threshold - Setup 3			
P, inc, p (W)	**P, inc, s (mW)**	**P, out (W)**	**Small signal gain g_0**
95	7.5	11	1470
85	5.1	8	1560
75	3.4	5.4	1600

value but as their ratio. Moreover, the solid angle is proportional to the illuminated area.Thus the threshold gain G_3 in a mask configuration could be estimated. Let us take for reference the setup described by the results in 6.2 in which the F4 lens was changed to decrease the ASE backscattered to the gain medium (Setup 2). In such a situation $\mathrm{ASE}_{c,2} \approx 1.4\%$. The setup which has to be compared to is the configuration with the iris added (Setup 3). By geometric calculations the iris further decreases the backreflected ASE by 40%. This means that:

$$\frac{ASE_{c,3}}{ASE_{c,2}} = 0.6 \tag{6.4}$$

which means that $\mathrm{ASE}_{c,3} \approx 0.8\%$. Since it is known that the Setup 2 has $g_{0,2} \approx 1000$

than the Setup 3 small signal gain can be estimated to be $g_{0,3} \approx 1500$ from:

$$\frac{g_{0,2}^2}{g_{0,3}^2}\sqrt{\frac{\ln\left(g_{0,3}^2\right)}{\ln\left(g_{0,2}^2\right)}} \approx 0.6 \tag{6.5}$$

This estimation, which has been carried out with the threshold gain for self-lasing formula, it is consistent with the results presented in table 6.3. Other physical masks were tested to further decrease the backscattered ASE, but they were discarded due to small improvements which carried drawbacks. Thus, the configuration described by Setup 3 has been exploited in the following amplification experiments due to its capacity to control self-lasing even at low incident seeder power.

6.4 Continuous Wave Amplification

The multipass Yb:YAG amplifier was tested exploiting a continuous wave Yb:KYW seeder described in section 6.1. The amplifier layout is represented in figure 6.4. It consisted in a Two-Pass Yb:YAG amplifier with the implemented countermeasures for self-lasing. The seeder wavelength was set to 1030 nm. The output power characteristic, which is shown in figure 6.9, was measured with three incident seeder power: 500 mW, 100 mW and 10 mW. The incident pump power was up to 95 W at 10 A of driving current and $\sim$ 80 W of absorbed pump power. In figure 6.10 is depicted the gain with respect to the incident seeder power at maximum pump power. At P,inc,s = 500 mW, the maximum output power was P,out = 28.75 W with a gain $G = 57.5$. At P,inc,s = 100 mW, the maximum output power was P,out = 21.6 W with a gain $G = 216$. At P,inc,s = 10 mW, the maximum output power was P,out = 14.8 W with a gain $G = 1480$. At low incident seeder power, the 2-Pass Yb:YAG amplifier reaches more than 30 dB of gain, without encountering self-lasing. At higher incident seeder power > 100 mW the amplifier reaches more than 20 W of output power.

The amplified seeder beam quality was measured by scanning a CCD camera along the focal plane of a spherical lens with a focal length of 100 mm. The incident seeder power was 10 mW while the incident pump power was at its maximum value, 95 W. The lens was positioned at the output of the HR 45° broadband plane mirror after the spherical lens F3 with f=250 mm. The beam passed through a polarizer beam splitter (PBS) in order to measure only the horizontal polarized beam quality, since it is the incident seeder polarization. The amplified beam quality was measured to be $M_x^2 \times M_y^2 = 1.47 \times 1.45$ and it is shown in figure 6.8. The seeder maintains a very good spatial beam quality along amplification.

The gain medium is a Yb:YAG crystal, which has a cubic, isotropic structure. Such a structure is particularly susceptible to all those processes which have asymmetric effects, such as thermo-optic effects. Thus, especially at high-powers, Yb:YAG amplifiers may exhibit a strong thermal lensing and depolarization losses due to induced birifringence. A depolarization measurement was carried out to understand the quantity of output power which had rotated polarization from the horizontal (π)

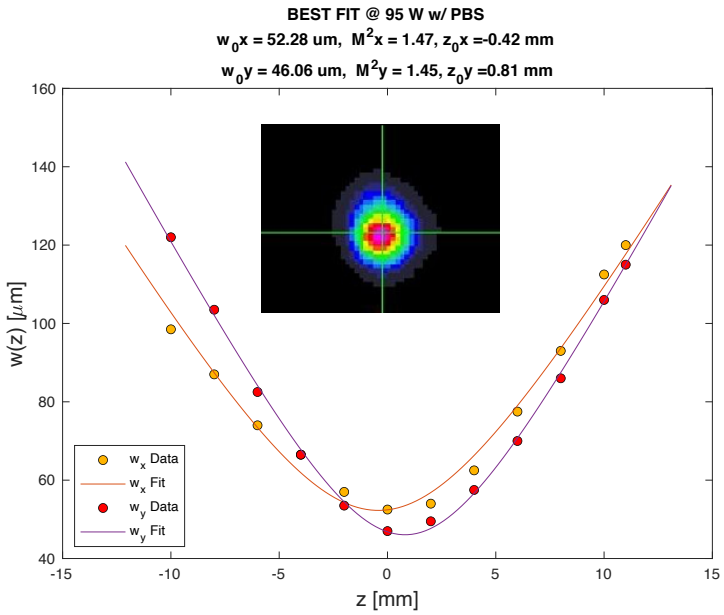

Figure 6.8: Continuous wave Yb:YAG amplifier output beam quality. Inset: intensity beam profile in the focus.

incident seeder polarization to vertical (σ) polarization:

$$\text{Depolarization} = \frac{P_{out,\sigma}}{P_{out,\sigma+\pi}} \tag{6.6}$$

At maximum pump power the depolarization losses has been measured to be $\approx 4\%$.

6.5 Thermal Lens Measurement

An additional detrimental effect which appears at high-powers in amplifiers is thermal lensing, as described in Section 4.5.4. In order to define the focal length of the thermal lens, the amplifier layout from picture 6.4 was slightly modified. Firstly, the HR mirror M3 in the retroinjection arm was substitute by an OC with very low transmittivity $T_{OC} > 99\%$. Subsequently, a telescope was set to reimage the seeder beam waist in the Yb:YAG crystal. The telescope was composed by two spherical lens (not depicted in the layout) F6, with f=100 mm and F7=300 mm, both AR coated at 1030 nm. Then, a CCD camera was moved along the focal plane of the spherical lens F7.
The spatial beam quality was measured with the pump switched off and the pump switched on at maximum output power. As mentioned in the previous section, the seeder presented a beam quality $M_x^2 \times M_y^2 = 1.09 \times 1.17$ with a slightly astigmatism. The same beam quality was measured also after the passage though the multipass amplifier. Once the pump module was switched on at 95 W of incident pump power, the amplified seeder beam quality measured was extremely similar to the previous evaluation, $M_x^2 \times M_y^2 = 1.47 \times 1.43$. This result demonstrates that the incident seeder beam was discretely preserved by the amplification process. The aforementioned

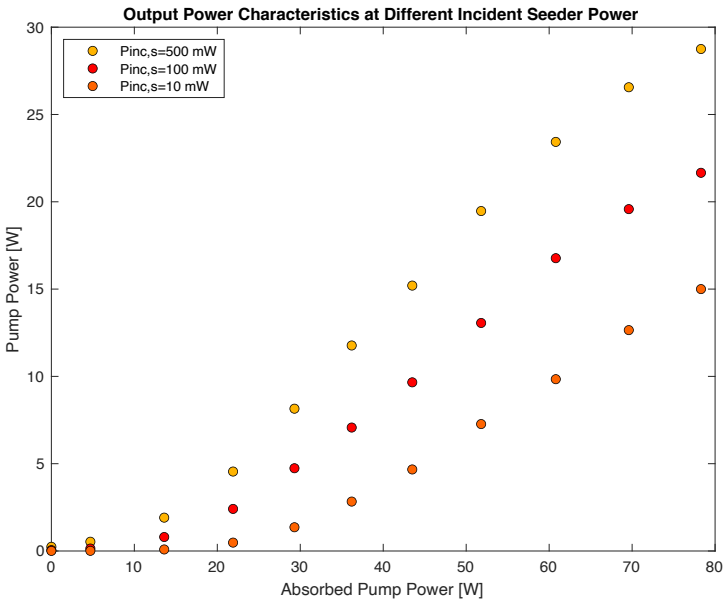

Figure 6.9: Continuous Wave Yb:YAG Amplifier at 500 mW, 100 mW and 10 mW of incident seeder power.

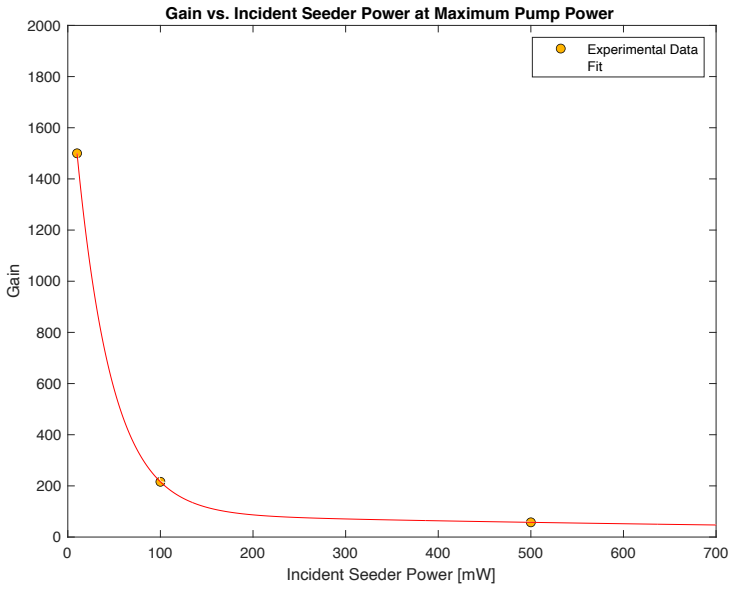

Figure 6.10: Gain in Continuous Wave Yb:YAG Amplifier with respect to incident seeder power.

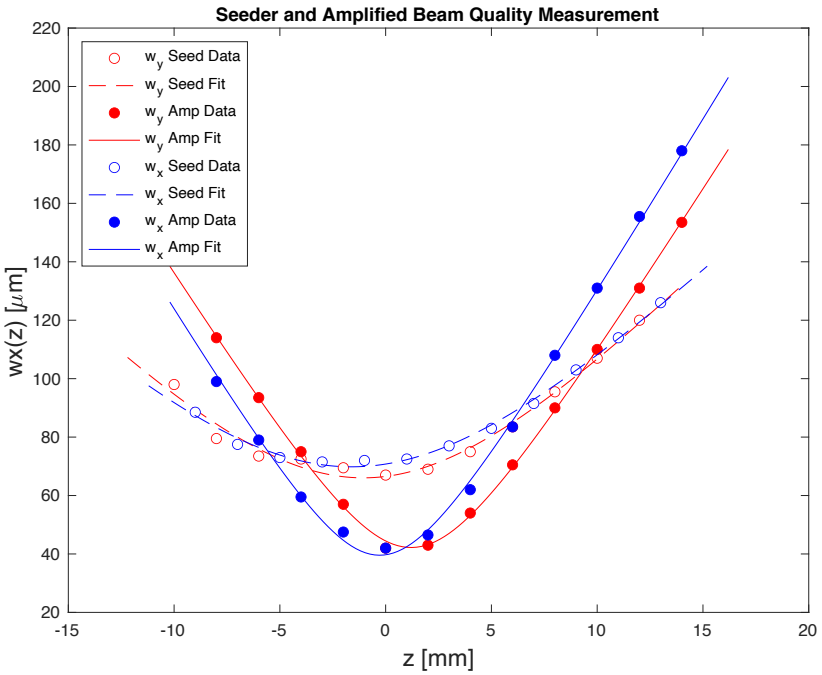

Figure 6.11: Thermal Lens in Yb:YAG Amplifier. Beam waist measurement of the seeder at the amplifier output with the pump switched off (empty circles) and with the pump switched on (full circles). The dashed and solid curves represent the result of the ABCD beam propagation best fit.

measurements of beam quality are shown in figure 6.11. From these measurements it is clear that a thermal effect was modifying the optical properties of the amplified seeder beam in both tangential and sagittal planes. Through an ABCD modeling of the amplifier setup it was studied the propagation of an almost perfectly Gaussian laser beam. In such a way it was possible to estimate the effective thermal focal length in the amplifier at 95 W of incident pump power. The best fit, which is depicted in figure 6.11 was a thermal lens with a focal length of $f_{th,x} = 12$ mm on x axis and $f_{th,y} = 10$ mm on y axis. The positive sign is consistent with the thermo-optic coefficients of Yb:YAG. Such thermal lens is strong, but the simple ABCD model showed that the amplifier layout is robust to this kind of perturbations. In fact, moving by few millimiters the HR 0° broadband mirror M3 in the retroinjection arm was enough to counteract the thermal lens in the gain medium.

6.6 Ultrashort Pulse Amplification

The 2-Pass Yb:YAG amplifier was tested exploiting a mode locked Yb:KYW seeder described in section 6.1. The amplifier layout is represented in figure 6.4. It consisted in a Two-Pass Yb:YAG amplifier with the implemented countermeasures for self-lasing. The seeder provided pulses of 200 fs of pulse duration, with a bandwidth FWHM of ~ 6 nm, up to 5 nJ of energy, an average output power up to 0.5 W, with a pulse repetition rate of 108 MHz and with a tunable peak wavelength from 1025 nm to 1036 nm. The pulse repetition rate of the seeder is such that $1/f_p \ll \tau_f$ which

means that the amplifier's medium has a fluorescence time much longer than the time between two signal pulses. In fact, Yb:YAG has a fluorescence time $\sim$ 1 ms whereas the seeder PRR is 108 MHz. It also means that the gain medium does not have enough 'resolution' to discriminate two signal pulses, and then it acts like the signal were CW. The only difference with the previous amplification measurements is that previously the seeder was operated in continuous wave regime so had a very narrow bandwidth (<0.5 nm) whereas now it is running in mode locking regime so it has a broad bandwidth ($\sim$ 6 nm). This is a great difference in terms of amplification gain since the Yb:YAG doesn't possess such broadband emission cross sections across the spectrum of the pulse to obtain an homogeneous gain. Thus, the overall amplification gain is lowered. The seeder peak wavelength was set at three different values: 1026 nm, 1030 nm and 1033 nm. The incident seeder power was set at 100 mW and 10 mW. The 10 mW incident seeder power was chosen as approximately corresponding to what is typically available from a mode locked oscillator after pulse picking at $\sim 1-2$ MHz. The amplification results at maximum pump power are shown in tables 6.4 and 6.5. At $P_{inc,s} = 100$ mW the average output power was 11.4 W, 13.6 W and 11.2 W for 1026 nm, 1030 nm and 1033 nm of central wavelength, respectively. The pulse duration increased from $\tau_p = 200$ fs to > 400 fs, and the pulse bandwidth FWHM decreased accordingly from $\sim$ 6 nm down to $<$ 3 nm. At lower incident seeder power $P_{inc,s} = 10$ mW the average output power was 6.8 W, 8.3 W and 6.2 W for 1026 nm, 1030 nm and 1033 nm of central wavelength, respectively. The pulse duration increased from $\tau_p = 200$ fs to > 600 fs, and the pulse bandwidth FWHM decreased accordingly from ~ 6 nm down to ≤ 2 nm. The best outcomes, in terms of output power, were obtained at a central wavelength of 1030 nm. This is consistent with the values of the Yb:YAG emission cross section σ_e.

Table 6.4: 2-Pass Yb:YAG Amplifier, Ultrashort Pulse Amplification. 100 mW Incident Seeder Power. Incident Pump Power 95 W. Seeder Peak Wavelength 1026 nm, 1030 nm, 1033 nm.

Ultrashort Pulse Amplification, 100 mW Seeder Power				
Property	**Unit**	**1026 nm**	**1030 nm**	**1033 nm**
$\tau_{p,inc}$	fs	200	200	200
$\tau_{p,amp}$	fs	430	600	680
BW_{inc}	nm	6.56	7.04	5.04
BW_{amp}	nm	2.72	2	2.24
$E_{p,out}$	nJ	105	125	103
P_{inc}	W	0.1	0.1	0.1
P_{out}	W	11.4	13.6	11.2
Gain	–	114	136	112

In the following experiments particular emphasis was given to amplification with low incident seeder power ($P_{inc,s} = 10$ mW). Thus I want to focus the attention to the results in table 6.5. At a central wavelength of 1026 nm, the amplified pulse duration was $\tau_{p,amp} = 673$ fs, with a BW FWHM of 2.08 nm, an average output power of 6.8 W, the resulted gain was 28.3 dB. At a central wavelength of 1030 nm, the amplified

Table 6.5: 2-Pass Yb:YAG Amplifier, Ultrashort Pulse Amplification. 10 mW Incident Seeder Power. Incident Pump Power 95 W. Seeder Peak Wavelength 1026 nm, 1030 nm, 1033 nm.

Ultrashort Pulse Amplification, 10 mW Seeder Power				
Property	**Unit**	**1026 nm**	**1030 nm**	**1033 nm**
$\tau_{p,inc}$	fs	200	200	200
$\tau_{p,amp}$	fs	673	744	814
BW_{inc}	nm	7	6.24	5.2
BW_{amp}	nm	2.08	1.84	1.68
$\mathrm{E}_{p,out}$	nJ	63	77	57
P_{inc}	W	0.01	0.01	0.01
P_{out}	W	6.8	8.3	6.2
Gain	–	680	830	620

pulse duration was $\tau_{p,amp} = 744$ fs, with a BW FWHM of 1.84 nm, an average output power of 8.3 W, the resulted gain was 29.2 dB. At a central wavelength of 1033 nm, the amplified pulse duration was $\tau_{p,amp} = 814$ fs, with a BW FWHM of 1.68 nm, an average output power of 6.2 W, the resulted gain was 27.9 dB. From these results it is clear that a detrimental process is reducing the useful bandwidth of the pulse and increasing its temporal duration. This process is gain narrowing, which has been explained in section 4.5.1, and is noticeable both for 10 mW and 100 mW of incident seeder power. The reduced bandwidth can be estimated from:

$$\Delta\omega_p \simeq \frac{\Delta\omega_{p0}}{\sqrt{\left(\frac{\omega_g}{\omega_i}\right)^2 + g(\omega_0)}} \tag{6.7}$$

Since the Gaussian pulse was nearly Fourier limited, the pulse duration increases too:

$$\tau_p \simeq \tau_{p0}\sqrt{1 + g(\omega_0)\left(\frac{\omega_i}{\omega_g}\right)^2} \tag{6.8}$$

The estimated amplified pulse for a gain of 29.2 dB, as in the experimental case of 10 mW of incident seeder power at 1030 nm of central wavelength, was with a BW FWHM $\approx$ 1.8 nm and a pulse duration $\tau_p \approx 600$ fs, which is consistent with the experimental data. The amplified seeder beam quality was measured by scanning a CCD camera along the focal plane of a spherical lens with a focal length of 80 mm. The incident seeder power was 10 mW while the incident pump power was at its maximum value, 95 W. The lens was positioned at the amplifier output. The beam passed through a polarizer beam splitter (PBS) in order to measure only the horizontal polarized beam quality, since it is the incident seeder polarization. The amplified beam quality was measured to be $\mathrm{M}_x^2 \times \mathrm{M}_y^2 = 1.36 \times 1.33$ and it is shown in figure 6.12. The outcome is consistent with the previous measurements. The depolarization losses were found to be $< 3.5\%$ at maximum pump power.

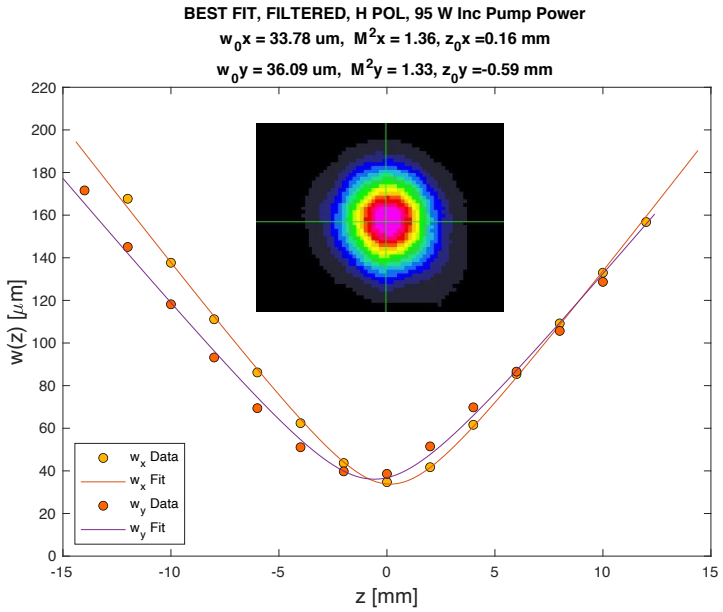

Figure 6.12: Ultrashort Pulses Yb:YAG amplifier output beam quality. Inset: intensity beam profile in the focus.

A FROG technique was exploited to measure the amplified ultrashort pulses. The device used was a GRENOUILLE 10-100 by Swamp-Optics. Its spectral resolution is 0.4 nm, which was enough, in this case, to efficiently retrieve the measurement. In figure 6.13 is shown the retrieved FROG trace and the spectral phase and intensity for a pulse centered at 1030 nm. The FROG measurement shows the amplified pulse is transform limited since it has a constant spectral phase. A polychromatic simulation of the amplification process was carried out through the numerical model previously described. In figures 6.20, 6.21 and 6.22 is presented a comparison between the experimental and simulated amplified pulse duration, through autocorrelation, and spectral intensity. A more detailed description of the numerical model and its implementation in this particular amplifier layout are found in section 4.3 and 6.11.

6.7 Spectral Shaping with a Lyot Filter

In order to mitigate gain narrowing a technique was exploited to modify the shape of the spectral intensity of the pulse, which originally is the Fourier transform of a sech^2 function. Thus it is possible to selectively decrease the intensity of the pulse spectral components, for example of those which reach high gains because of their matching with the peak of the Yb:YAG emission cross section. Such solution creates a *notch* in the pulse spectral shape of the pulse. The spectral shaping has been carried out exploiting a Lyot filter made by a 4 mm long LBO crystal, originally cut for Type-I Second Harmonic Generation (SHG) at 1064 nm, but used here well out of phase matching, i.e., with negligible SHG, and a polarization beam splitter (PBS). The power transmittivity T of the Lyot filter is wavelength dependent, according to equation 6.9 and 6.10 the LBO crystal has 3 degrees of freedom, that determine the

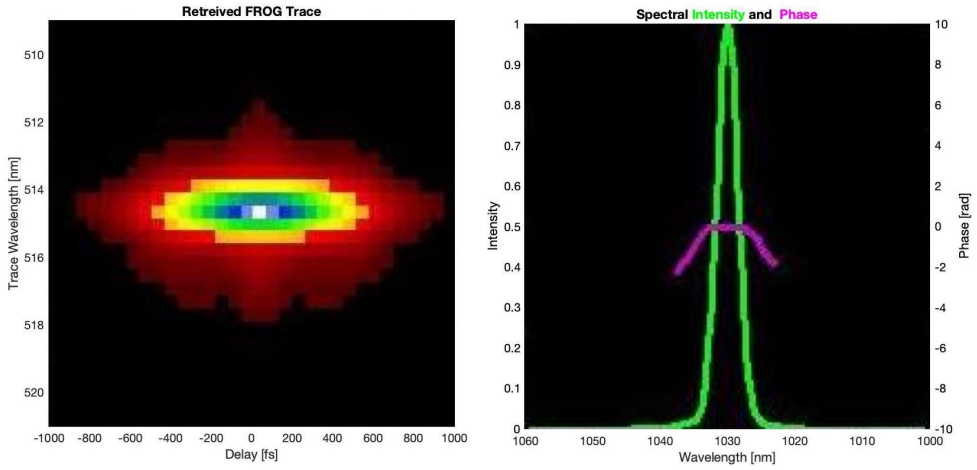

(a) **(b)**

Figure 6.13: FROG measurement of amplified pulse centered at 1030 nm. (a) Retrieved trace (b) Spectral intensity and phase.

central wavelength of the notch and its magnitude.

Group velocity mismatch between the two polarizations sets the maximum birefringent crystal length. Since mismatch is 50 fs/mm at 1030 nm in LBO, the maximum crystal length before an excessive temporal splitting of the polarizations takes place is about 4 mm for 200 fs input pulses. Shorter LBO crystals were unable to produce a sufficiently deep notch filter for effective spectral reshaping, given the input pulse spectrum and amplifier bandwidth.

The Lyot filter was mounted on an alignment stage with three degrees of freedom. While the θ angle is used to modulate the notch, the ϕ angle defines the notch wavelength. The equations that define the Lyot filter are the following:

$$T(\lambda) = \cos^4(\theta) + \sin^4(\theta) + 2\sin^2(\theta)\cos^2(\theta)\cos(\Delta\phi(\lambda)) \tag{6.9}$$

$$\Delta\phi(\lambda) = \frac{2\pi}{\lambda}\big(n_z - n_y\big)L \tag{6.10}$$

where L is the LBO crystal length, n_z and n_y are the refractive indexes of z and y axes, respectively. In Figure 6.15 it is presented the result of a simulation of the spectral shaping with 2 mm and 4 mm LBO crystals with a θ angle varying from 0° to 45° with 15° steps, when the input spectrum (blue curve of 6.15) has a FWHM = 6 nm and is centered at 1030 nm. As expected from equation 6.9, when $\theta = 0°/90°$ there is no spectral shaping. The ϕ angle is used to center the notch on the pulse central wavelength and it was kept constant in this simulation.

As it can be seen from the comparison, the 4 mm LBO crystal provides a more effective notch modulation and better energy transmission, hence it was chosen to be used in the amplification experiments with the Lyot filter.

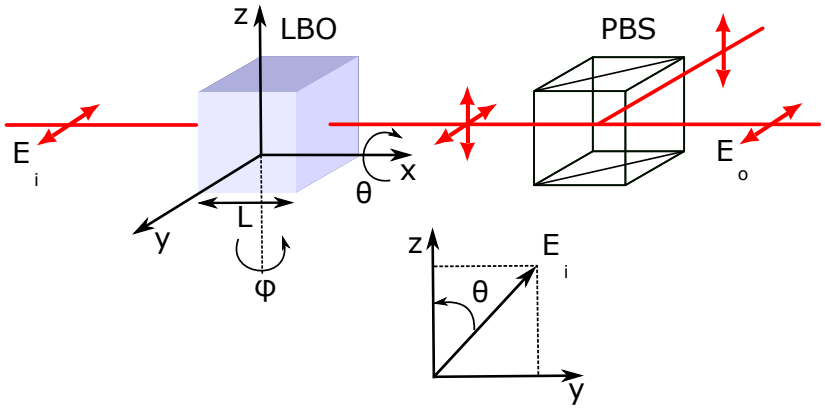

Figure 6.14: The Lyot filter. The LBO crystal was AR coated at 1040 nm. The PBS was a 1" N-SF1 polarizing beam splitter cube. The input laser polarization was along y axis, and the LBO crystal could be rotated around x-axis to vary θ angle and the Lyot filter transmission.

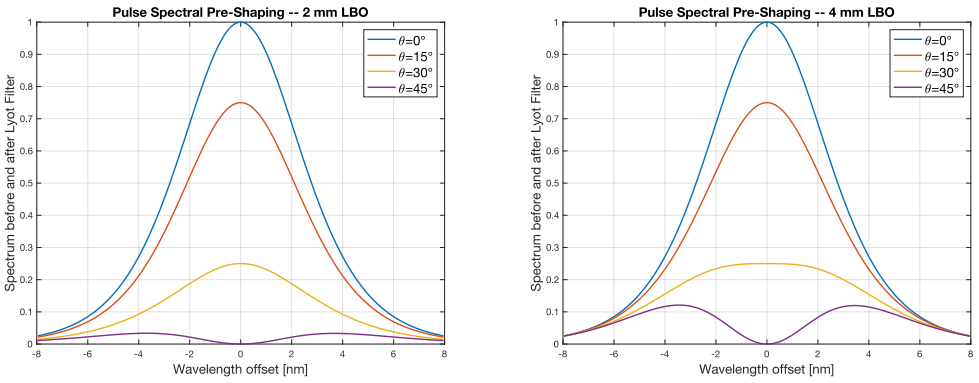

(a) **(b)**

Figure 6.15: Numerical simulation of a 200 fs, 6 nm, 1030 nm centered pulse, spectral preshaped by a Lyot filter with an LBO crystal of (a) 2 mm and (b) 4 mm length.

6.8 Ultrashort Pulse Amplification with Spectral Preshaping

The multipass Yb:YAG amplifier was tested exploiting a mode locked Yb:KYW seeder, described in section 6.1, and a Lyot filter for a spectrally preshaping of the pulses to minimize gain narrowing and preserve pulse duration during amplification. The amplifier layout is represented in figure 6.16. It consisted in a Two-Pass Yb:YAG amplifier with the implemented countermesures for self-lasing. The seeder provided pulses of 200 fs of pulse duration, with a bandwidth FWHM of $\sim$ 6 nm, up to 5 nJ of energy, an average output power up to 0.5 W, with a pulse repetition rate of 108 MHz and with a tunable peak wavelength from 1025 nm to 1036 nm. The seeder peak wavelength was set at three different values during the experiments: 1026 nm, 1030 nm and 1033 nm. The Lyot filter was positioned along the seeder optical path before the F3 spherical lens. The ϕ angle of the LBO crystal was rotated such that the notch was always centered at 1030 nm, since it is the wavelength which matches the peak of the Yb:YAG emission cross section. The notch was modulated through the rotation of θ angle which was set at $\theta = 40°$. The incident seeder power was set at 100 mW and 10 mW and it was measured after the Lyot filter. The transmission of the Lyot filter was 54%, 23% and 36% for 1026 nm, 1030 nm and 1033 nm of central wavelength, respectively. This means that, for example, to have 10 mW of incident seeder power with pulses preshaped and centered at 1026 nm, the Lyot filter input beam had to have 18.5 mW of average power. The amplification results at maximum pump power are shown in tables 6.6 and 6.7.

Table 6.6: 2-Pass Yb:YAG Amplifier, Ultrashort Pulse Amplification with Pre-Shaping. 100 mW Incident Seeder Power. Incident Pump Power 95 W. Seeder Peak Wavelength 1026 nm, 1030 nm, 1033 nm.

Ultrashort Pulse Amplification with Preshaping. 100 mW Seeder Power				
Property	**Unit**	**1026 nm**	**1030 nm**	**1033 nm**
$\tau_{p,inc}$	fs	200	200	200
$\tau_{p,amp}$	fs	300	900	960
BW_{inc}	nm	5.8	10.7	4.56
BW_{amp}	nm	5.2	3.28	3.04
$\mathrm{E}_{p,out}$	nJ	83	92	74
P_{inc}	W	0.1	0.1	0.1
P_{out}	W	9	10	8
Gain	–	90	100	80

The Lyot filter discards a variable fraction of the spectral components intensity. In particular, in these experiments the notch central wavelength was set to 1030 nm, which is the peak of Yb:YAG emission cross section. Since the other spectral components feel a lower emission cross section, it is straightforward to expect less amplified pulses. Regarding the experiments at 10 mW of incident seeder power the results are the following. At a central wavelength of 1026 nm, the amplified pulse duration was $\tau_{p,amp} = 304$ fs, with a BW FWHM of 6.1 nm, an average output

Table 6.7: 2-Pass Yb:YAG Amplifier, Ultrashort Pulse Amplification wiith Pre-Shaping. 10 mW Incident Seeder Power. Incident Pump Power 95 W. Seeder Peak Wavelength 1026 nm, 1030 nm, 1033 nm.

Ultrashort Pulse Amplification with Preshaping. 10 mW Seeder Power				
Property	**Unit**	**1026 nm**	**1030 nm**	**1033 nm**
$\tau_{p,inc}$	fs	200	200	200
$\tau_{p,amp}$	fs	304	426	478
BW_{inc}	nm	5.6	9.5	4.32
BW_{amp}	nm	6.1	2.24	2
$\mathrm{E}_{p,out}$	nJ	30	39	27
P_{inc}	W	0.01	0.01	0.01
P_{out}	W	3.23	4.2	2.9
Gain	–	323	420	290

power of 3.23 W, the resulted gain was 25.1 dB. At a central wavelength of 1030 nm, the amplified pulse duration was $\tau_{p,amp} = 426$ fs, with a BW FWHM of 2.24 nm, an average output power of 4.2 W, the resulted gain was 26.2 dB. At a central wavelength of 1033 nm, the amplified pulse duration was $\tau_{p,amp} = 478$ fs, with a BW FWHM of 4.32 nm, an average output power of 2.9 W, the resulted gain was 24.6 dB. A similar behaviour is found also when the incident seeder power is 100 mW.

Gain narrowing still limits the bandwidth at 1030 nm and 1033 nm of pulse peak wavelength. On the other hand an interesting effect appears at 1026 nm. The incident pulse centered at 1026 nm is amplified with a gain of 25.1 dB , and its amplified BW FWHM is not reduced accordingly to the gain narrowing formula for an homogeneous broadened laser transition lineshape, as happened to the not spectrally preshaped pulses. In fact, it is increased with respect to the incident BW FWHM. This effect will be addressed in the next section.

The amplified beam quality was measured to be $\mathrm{M}_x^2 \times \mathrm{M}_y^2 = 1.36 \times 1.33$ as in the ultrashort pulse amplification without spectral pre-shaping. Also, the depolarization losses were found to be $< 3.5\%$ at maximum pump power.

A FROG technique was tried to measure the amplified ultrashort pulses. The device used was a GRENOUILLE 10-100 by Swamp-Optics. Its spectral resolution is 0.4 nm. Unfortunately, such value was insufficient to clearly describe the notch generated by the Lyot filter, and thus the retrieved FROG figure and the related spectral phase and intensity were not useful to better describe the incident and amplified pulse. Thus, the pulse duration was measured by an APE Pulsecheck autocorrelator. In figures 6.23, 6.24 and 6.25 is presented a comparison between the experimental and simulated amplified pulse duration, through autocorrelation, and spectral intensity. A more detailed description of the numerical model and its implementation in this particular amplifier layout are found in section 4.3 and 6.11.

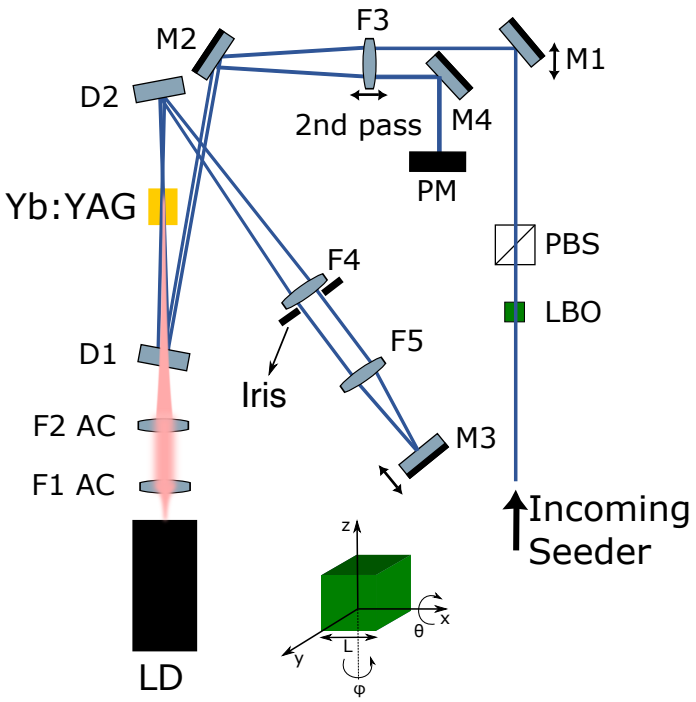

Figure 6.16: 2-Pass Yb:YAG amplifier with pulse spectral preshaping. F1, F2: achromatic lenses, f1=40 mm, f2=75 mm, AR coated; F3, F4, F5: spherical lenses, f3=250 mm, f4=300 mm, f5=100 mm, AR coated; M1, M2, M4: HR 45° broadband plane mirrors; M3: HR 0° broadband plane mirror; D1, D2: dichroic mirrors, HT at 976 nm and HR at 1000-1100 nm; PM: power meter; PBS: polarizer beam splitter; LBO: Lithium triborate crystal.

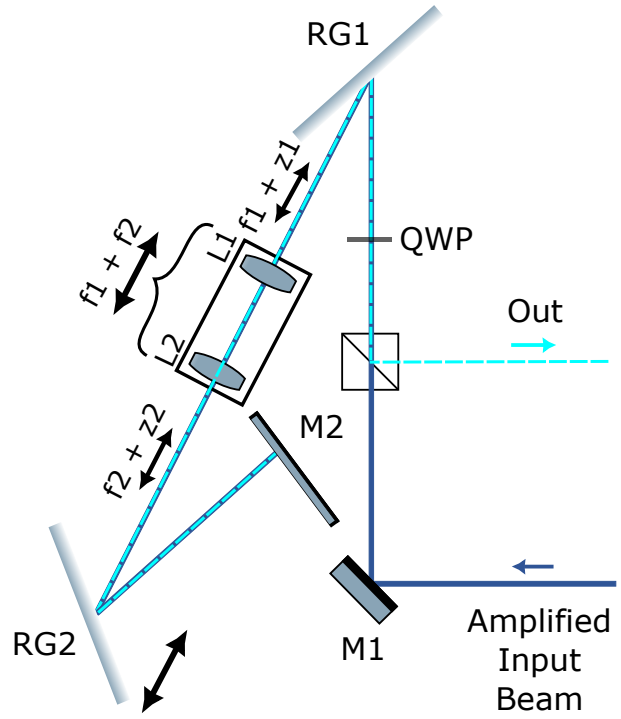

Figure 6.17: Martinez Stretcher and Compressor. L1, L2: spherical lenses, f1=f2=75 mm, AR coated; RG1, RG2: reflection grating, $\sim$ 1200 gooves/mm and $\theta_{1st} \approx 38°$ at 1030 nm; QWP: quarter wave plate; PBS: polarizer beam splitter; M1: HR 45° broadband plane mirror; M2: HR 0° broadband plane mirror.

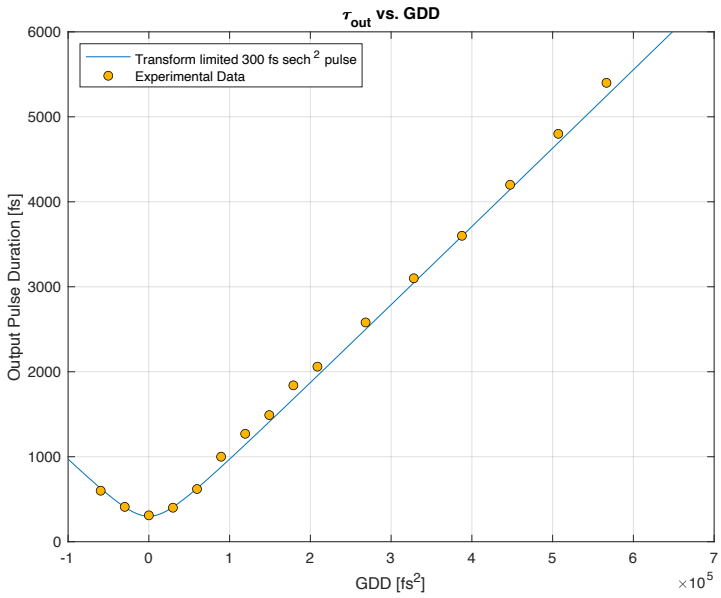

Figure 6.18: Spectrally Preshaped Pulse Compression. Empty circles: experimental data, solid line: fit of a 300 fs transform limited sech^2 pulse with an addition of GDD.

6.9 Gain Narrowing Reduction in Yb:YAG

In previous section the amplification of spectrally preshaped ultrashort pulses was addressed. A particular interest was raised by the preshaped pulse with a center wavelength at 1026, since the results are not in accordance with the mathematical model which describes gain narrowing. This behaviour lies in the asymmetrically broader spectral distribution of Yb:YAG emission cross section at wavelengths lower than 1030 nm. This spectroscopic characteristic sustains an amplified pulse which has a bandwidth comparable to the incident pulse (5.6 nm vs. 6.1 nm) even though the spectral shape further departs from a Fourier transform sech^2 function, as inferred from the time-bandwidth product (TBP) which increases from 0.4 to 0.52 (this is 0.315 for a Fourier limited pulse with a temporal sech^2 shape). So as to deepen the comprehension of this phenomenon an investigation was carried out to understand whether the pulse was further compressible or not.

In order to do that a Martinez stretcher and compressor was used (cit). The system contained two antiparallel diffraction gratings with a telescope in between, as depicted in figure (ref) Owing to the image inversion and transfer, it became possible to vary the dispersion from zero (when the gratings are arranged so that the image of one grating coincides with the position of the other, so $z_1 = z_2 = 0$) to any value, with both positive and negative second-order dispersion (when $z_1 \neq 0$ and $z_2 \neq 0$). In a such configuration, the output pulse has the spectral components spatially overlapped as the input pulse. The reflection gratings had ~ 1200 grooves/mm and $\theta_{1st,order} \approx 38°$ at 1030 nm. The telescope was composed by two spherical lens, L1 and L2, with a focal length of 75 mm and both AR coated at 1030 nm. The second

order dispersion provided by the Martinez configuration is:

$$\mathrm{GDD} = \frac{\lambda^3(z_1 + z_2)}{\pi c^2 d^2 \cos^2(\theta_d)} \tag{6.11}$$

where z_1 and z_2 are the relative distances between the focal plane of the related lens and the grating., d is the grating spacing, and θ_d is the reflection angle with was set equal to the first order angle. The reflection grating RG2 was positioned on a stage to freely move along the optical axis of several centimeters.
The compressor was set in order to have $z_1 = 0$, while the grating RG2 was moved in the nearby of the zero-dispersion point $z_2 = 0$. In such a way the Martinez configuration provided:

$$\mathrm{GVD} \simeq sgn(z_2) \cdot 6000\,\mathrm{fs}^2/\mathrm{mm} \tag{6.12}$$

The input pulse had a temporal duration of 304 fs with a BW FWHM of 6.1 nm centered at 1026 nm. The temporal duration of the output pulse with respect to the GDD provided by the compressor is depicted in figure 6.18. The pulse resulted already transform limited at 304 fs FWHM, and no residual chirp whatsoever was detected. This behaviour can be explained by the fact that, even though the TBP of the pulse was 0.52, its spectral shape was not the Fourier transform of a sech^2 function, and thus this is the transform limit for that given shape.

6.10 Thermal Measurements

Simultaneously with the amplification experiments described, I also tested the ultrashort pulses amplifier at different crystal temperature. The gain medium, Yb:YAG, presents good thermo-optic and excellent thermo-mechanic properties, but with a relatively narrow emission bandwidth. Due to the quasi-three level nature of Ytterbium ions, the expected result with an higher crystal temperature is a decrease in the absolute values of the Yb:YAG emission cross section and a broader bandwidth due to an increase of the lower laser level thermal population. The following temperature measurements aimed to define this process and understand the relationship between output power, gain narrowing, pulse duration and BW FWHM.

The amplifier layouts without the Lyot filter (figure 6.4) and with the Lyot filter (figure 6.16) were employed. An NTC thermistor was put in thermal contact with the water-cooled copper holder of the Yb:YAG crystal to measure its temperature. All the previous measurements were taken at an holder temperature of 25 °C. The water-cooling flow was reduced to obtain a temperature of 35 °C and 45 °C and carry out amplification experiments.
The incident seeder power was set at 10 mW. The amplifier layout was tested of central wavelength of 1030 nm without spectral preshaping, on the other hand it was tested at 1026 nm, 1030 nm and 1033 nm of central wavelength with spectral preshaping. The maximum output power with respect to temperature is shown in table 6.8. As expected, there is a significant drop in the output power, in most cases more than $> 50\%$. In the case of the spectrally preshaped pulse centered at 1026 nm, the output power goes from 3.23 W to 1.62 W with only 20 °C of temperature holder difference.

Table 6.8: 2-Pass Yb:YAG Amplifier, Ultrashort Pulse Amplification with Pre-Shaping. 10 mW Incident Seeder Power. Incident Pump Power 95 W. Seeder Peak Wavelength 1026 nm, 1030 nm, 1033 nm.

Output Power vs. Temperature				
Temp.	**With Preshaping**			**Without Preshaping**
	1026 nm	**1030 nm**	**1033 nm**	**1030 nm**
25 °C	3.23 W	4.2 W	2.9 W	8.3 W
35 °C	2.28 W	1.8 W	1.8 W	6.8 W
45 °C	1.62 W	1.2 W	1.4 W	4.9 W

Table 6.9: 2-Pass Yb:YAG Ultrashort Pulses Amplifier with Pre-Shaping, Temperature measurements. 10 mW Incident Seeder Power. Incident Pump Power 95 W. Seeder Peak Wavelength 1026 nm.

BW and Pulse Duration vs. Temperature, Preshaping, 1026 nm				
Temp.	**BW FWHM (nm)**		**Pulse Duration (fs)**	
	Inc.	**Amp.**	**Inc.**	**Amp.**
25 °C	5.6	6.16	200	304
35 °C	5.6	6.24	200	316
45 °C	5.6	5.52	200	301

Table 6.10: 2-Pass Yb:YAG Ultrashort Pulses Amplifier with Pre-Shaping, Temperature measurements 10 mW Incident Seeder Power. Incident Pump Power 95 W. Seeder Peak Wavelength 1030 nm.

BW and Pulse Duration vs. Temperature, Preshaping, 1030 nm				
Temp.	**BW FWHM (nm)**		**Pulse Duration (fs)**	
	Inc.	**Amp.**	**Inc.**	**Amp.**
25 °C	9.5	2.24	200	426
35 °C	9.5	2.72	200	426
45 °C	9.5	3.2	200	373

In tables 6.9, 6.10 and 6.11 are described the BW FWHM and pulse duration with respect to temperature when the incident pulses are preshaped, with 1026 nm, 1030 nm and 1033 nm of central wavelength. On the other hand, in table 6.12 the incident pulse is not preshaped, with a central wavelength of 1030 nm. All those measurements, which small exceptions, share the same trend when the gain medium temperature is increased. Not only the output power dramatically decreases, but the BW FWHM increases and the pulse duration decreases. Thus, a small gain in pulse duration has as drawback a huge drop in output power. In figure 6.19 is depicted the most

Table 6.11: 2-Pass Yb:YAG Ultrashort Pulses Amplifier with Pre-Shaping, Temperature measurements. 10 mW Incident Seeder Power. Incident Pump Power 95 W. Seeder Peak Wavelength 1033 nm.

BW and Pulse Duration vs. Temperature, Preshaping, 1033 nm				
Temp.	**BW FWHM (nm)**		**Pulse Duration (fs)**	
	Inc.	**Amp.**	**Inc.**	**Amp.**
25 °C	4.32	2	200	478
35 °C	4.32	1.95	200	488
45 °C	4.32	2.16	200	421

Table 6.12: 2-Pass Yb:YAG Ultrashort Pulses Amplifier without Pre-Shaping, Temperature measurements. 10 mW Incident Seeder Power. Incident Pump Power 95 W. Seeder Peak Wavelength 1030 nm.

BW and Pulse Duration vs. Temperature, No Preshaping, 1030 nm				
Temp.	**BW FWHM (nm)**		**Pulse Duration (fs)**	
	Inc.	**Amp.**	**Inc.**	**Amp.**
25 °C	6.24	1.84	200	744
35 °C	6.24	1.92	200	667
45 °C	6.24	2.16	200	573

representative trend of the temperature measurement which has been shown. The numerical model of the amplification gain with respect to the output pulse duration was simulated with an incident pulse with 7 nm , 8 nm and 9 nm of BW FWHM, respectively. Increasing the temperature decreases the amplifier gain, and the related output pulse behaves as it had an broader incident BW FWHM.

6.11 Numerical Model Investigation

An extensive work of numerical simulation of the amplification process has been carried out to validate the experimental results. In order to do that it has been exploited the polychromatic numerical model described in section 4.3. In the following tables 6.13 and 6.14 are shown the results with 10 mW of incident seeder power without spectral preshaping and with preshaping, respectively. In each simulation the real incident pulse was measured with an optical spectrum analyzer and was used as input pulse for the simulation. In figures 6.20, 6.21 and 6.22 is presented a comparison between the experimental and simulated autocorrelation trace and spectral intensity for not preshaped incident pulses. In figures 6.23, 6.24 and 6.25 is presented a comparison between the experimental and simulated autocorrelation trace and spectral intensity for preshaped incident pulses.
The figures shows on the left a comparison of the autocorrelation trace of the amplified pulse and the IFFT of its spectrum. On the right a comparison between the spectra

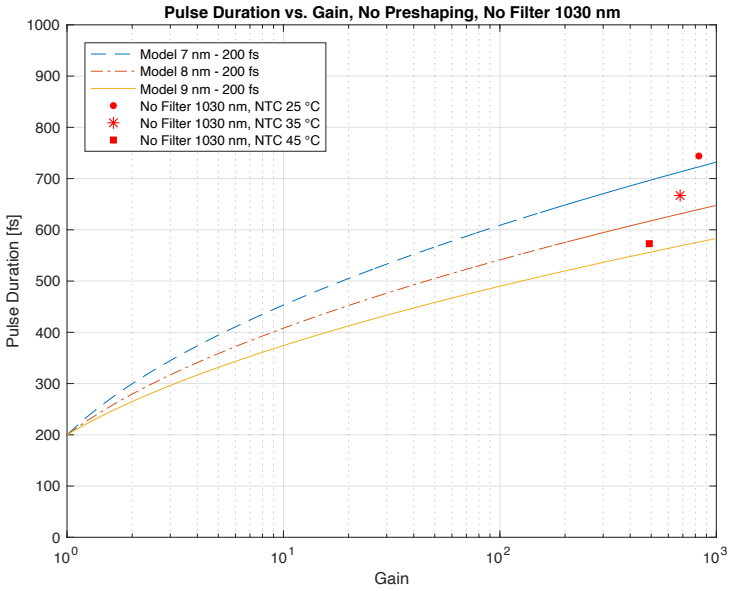

Figure 6.19: Pulse duration variation in temperature measurements. The numerical model of the amplification gain with respect to the output pulse duration was simulated with an incident pulse with 7 nm (dashed blue curve)), 8 nm (dashed red curve) and 9 nm (solid yellow curve) of BW FWHM, respectively.

Table 6.13: Simulation 2-Pass Yb:YAG Amplifier, Ultrashort Pulse Amplification. 10 mW Incident Seeder Power. Incident Pump Power 95 W. Seeder Peak Wavelength 1026 nm, 1030 nm, 1033 nm.

Simulation Ultrashort Pulse Amplification, No Pre-Shaping				
Property	**Unit**	**1026 nm**	**1030 nm**	**1033 nm**
$\tau_{p,inc}$	fs	200	200	200
$\tau_{p,amp}$	fs	662	452	486
BW_{inc}	nm	7	6.24	5.2
BW_{amp}	nm	1.75	1.84	1.6
$\mathrm{E}_{p,out}$	nJ	60	74	53
P_{inc}	W	0.01	0.01	0.01
P_{out}	W	6.5	8	5.8
Gain	–	650	800	580

of the experimental incident pulse, experimental amplified pulse and simulated amplified pulse. While the gain narrowing is evident and validated by simulations in most cases, this is not happening with the incident pulses spectrally preshaped and centered at 1026 nm. On the other hand, the numerical model supports the pulse bandwidth conservation and gain narrowing reduction at 1026 nm. This difference with respect to the amplification without a preshaped pulse clearly shows that the spectral shaping, combined with the asymmetric shape of the emission cross section, are the sole responsible for the generation of a spectrally broadened amplified pulse.

Table 6.14: Simulation of 2-Pass Yb:YAG Amplifier, Ultrashort Pulse Amplification with Pre-Shaping. 10 mW Incident Seeder Power. Incident Pump Power 95 W. Seeder Peak Wavelength 1026 nm, 1030 nm, 1033 nm.

Simulation Ultrashort Pulse Amplification, Pre-Shaping				
Property	**Unit**	**1026 nm**	**1030 nm**	**1033 nm**
$\tau_{p,inc}$	fs	200	200	200
$\tau_{p,amp}$	fs	266	310	320
BW_{inc}	nm	5.6	9.5	4.32
BW_{amp}	nm	6.65	1.65	1.55
$\mathrm{E}_{p,out}$	nJ	27	32	12
P_{inc}	W	0.01	0.01	0.01
P_{out}	W	2.9	3.5	1.32
Gain	–	290	350	132

Although the output power is reduced to about 50% with such preshaped seeder, simulations suggest that the same output power of 6.8 W (with no preshaping) can be achieved by increasing the pump power of about 20%, from 95 W to 115 W. More practically, the numerical model suggests that multipass gain optimization is the way to increase amplifier efficiency while exploiting this "blue-shifted" seed technique to compensate for gain narrowing at about 200-fs pulse width.

6.12 Conclusion

In this part of my PhD worked on a 2-Pass Yb:YAG amplifier. The first measurements were carried out in continuous wave, where it showed excellent amplification performances up to 34 dB with 10 mW of incident seeder power, a very good optical quality $M^2 < 1.5$ and a robustness to thermal effects such as thermal lensing and depolarization losses. Then, the 2-Pass Yb:YAG amplifier was tested in ultrashort pulse amplification. The pulses had a 200 fs pulse duration, a BW FMHW $\sim$ 6 nm and up to 5 nJ of energy. Their central wavelength was set at 1026 nm, 1030 nm and 1033 nm. The resulted gain was up to 29.2 dB at 10 mW of incident seeder power with the pulses centered at 1030 nm. In a such configuration, the pulses evidently suffered of gain narrowing, with a strongly decreased BW FWHM $\sim$ 2 nm and a longer pulse duration $\sim$ 700 fs. The beam quality was still very good $M^2 < 1.4$ with reduced depolarization losses. Subsequently, I implemented a technique of pulse spectral shaping through a Lyot filter with the aim of mitigate gain narrowing. While this method seemed to be noneffective or even deleterious in terms of output power and BW FWHM in some situations, it led to an interesting bandwidth conservation when the incident pulse was centered at 1026 nm. Thus, I investigated this unusual effect of bandwidth broadening in Yb:YAG, which counteracts the effect of the gain narrowing when the pulse is appropriately spectrally preshaped. A polychromatic simulation of the amplification process was carried out in order to help understanding the experimental results. This effect was present at $\lambda_s = 1026$ nm and was clearly related to the spectral gain asymmetry of the emission cross section of Yb:YAG. The

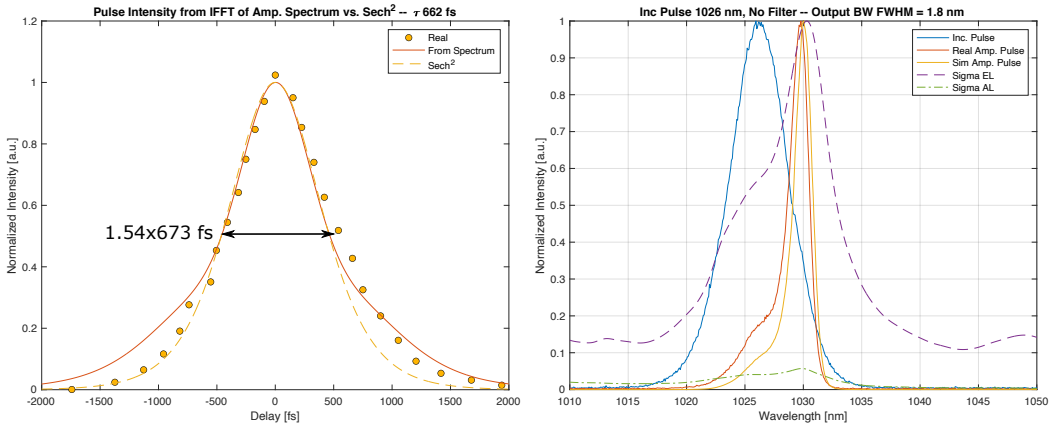

(a) (b)

Figure 6.20: Autocorrelation and spectral Intensity of a pulse not preshaped pulse centered at 1026 nm. Comparison between experimental and simulation results. In dash purple and green dash and dots are shown the emission and absorption cross section of Yb:YAG.

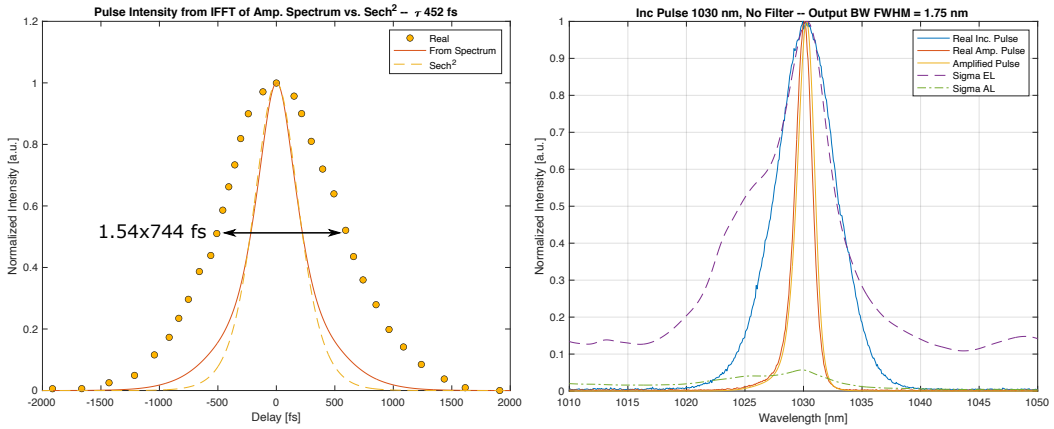

(a) (b)

Figure 6.21: Autocorrelation and spectral Intensity of a preshaped not pulse centered at 1030 nm. Comparison between experimental and simulation results. In dash purple and green dash and dots are shown the emission and absorption cross section of Yb:YAG.

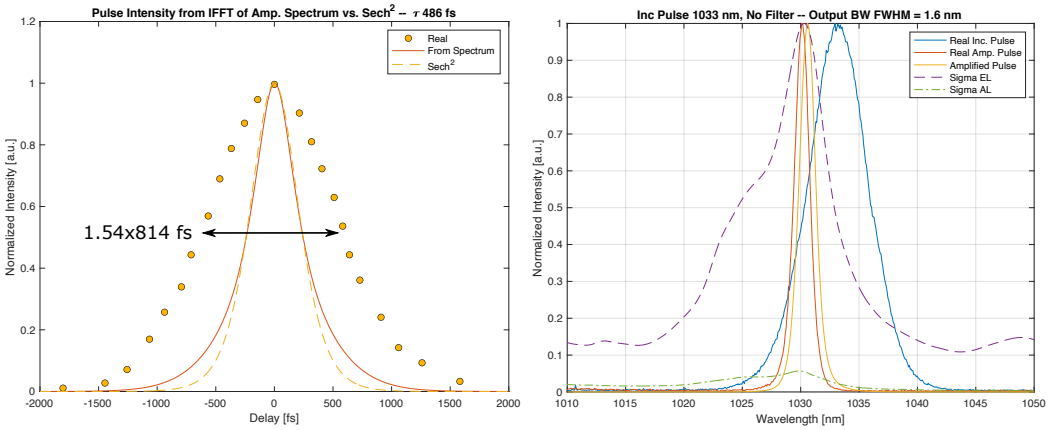

(a) (b)

Figure 6.22: Autocorrelation and spectral Intensity of a not preshaped pulse centered at 1033 nm. Comparison between experimental and simulation results. In dash purple and green dash and dots are shown the emission and absorption cross section of Yb:YAG.

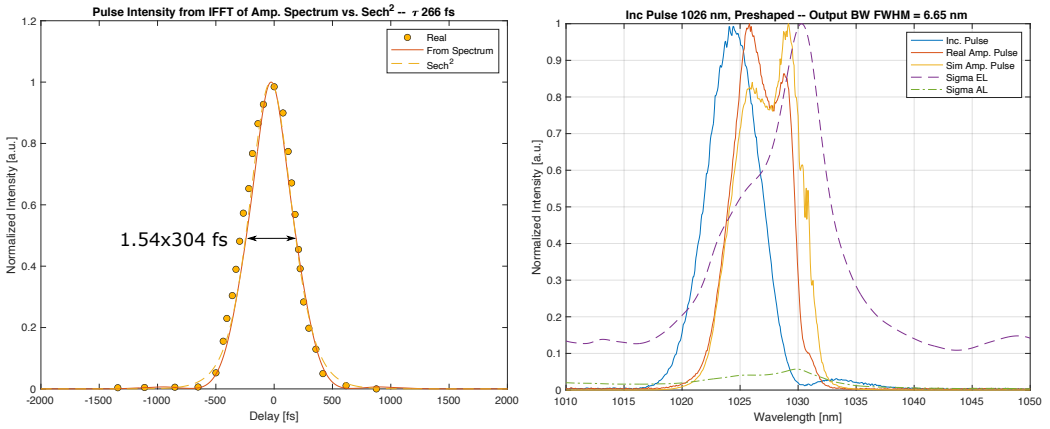

(a) (b)

Figure 6.23: Autocorrelation and spectral Intensity of a preshaped pulse centered at 1026 nm. Comparison between experimental and simulation results. In dash purple and green dash and dots are shown the emission and absorption cross section of Yb:YAG.

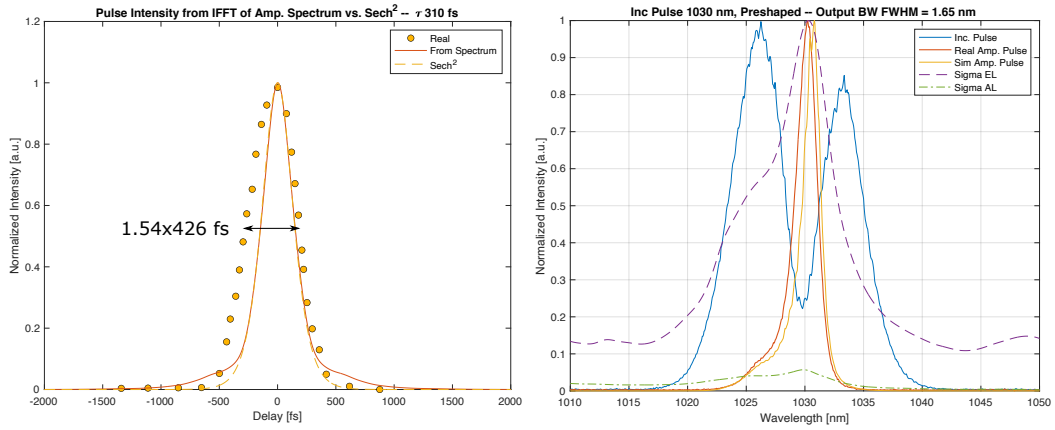

(a) (b)

Figure 6.24: Autocorrelation and spectral Intensity of a preshaped pulse centered at 1033 nm. Comparison between experimental and simulation results. In dash purple and green dash and dots are shown the emission and absorption cross section of Yb:YAG.

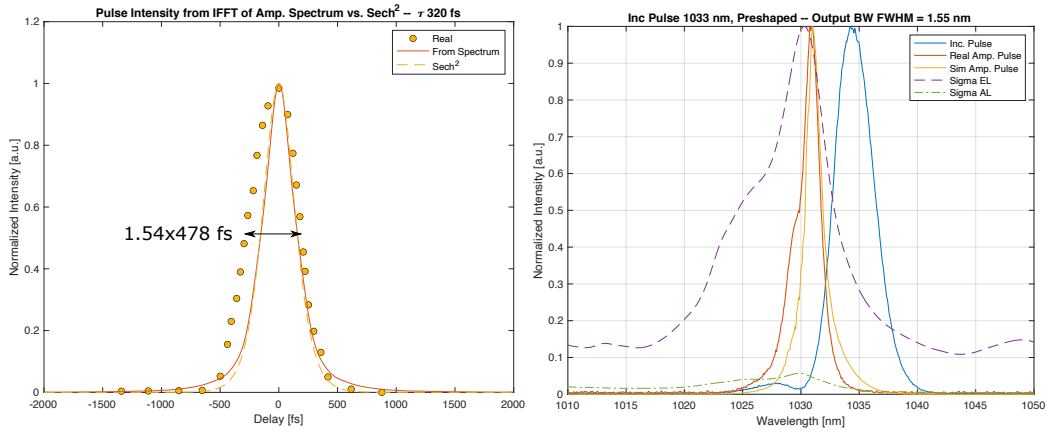

(a) (b)

Figure 6.25: Autocorrelation and spectral Intensity of a preshaped pulse centered at 1033 nm. Comparison between experimental and simulation results. In dash purple and green dash and dots are shown the emission and absorption cross section of Yb:YAG.

amplification of 200 fs pulses at 1030 nm, or longer peak wavelength, resulted in narrow bandwidth ($\sim$ 2 nm), $\sim$ 700 fs long pulses, due to severe gain narrowing effect. By seeding at 1026 nm with spectral shaping, bandwidth was completely preserved (from 5.6 nm to 6.1 nm FWHM), with only a moderate increase of the pulse duration from 200 fs to 304 fs, at an expense of a slight gain reduction from 29.2 to 25.1 dB at 10 mW of incident average power. The numerical simulations indicated that the gain reduction observed when seeding at 1026 nm with the spectral shaping, could be easily compensated by increasing amplifier gain through multipass optimization, still preserving the 300 fs output pulse duration. The demonstrated bandwidth broadening effect in Yb:YAG can be an incredible helpful solution to ultrashort pulse Yb:YAG multipass amplifiers for an industrial product, since the gain narrowing is one of the most detrimental effects. In fact, the results obtained during these experiments, as well as other parts of my PhD thesis, fall under a non-disclosure agreement, with an interest from Spectra-Physics to a possible patent.

Chapter 7

High-Power μ-PD Yb:$LiLuF_4$ Multipass Amplifier

Simultaneously with the work carried out in collaboration with Spectra-Physics on high-power Yb:YAG multipass amplifier for ultrashort pulses, I have worked on another high-power multipass amplifier which exploited as gain medium a single crystal fiber (SCF) Yb:$LiLuF_4$ (Yb:LLF) grown by the micro-pulling-down technique. Single crystal fibers (SCFs) grown by the micro-pulling-down (μ-PD) method are thin crystal rods with a variable diameter down to $\sim$ 1 mm and with a length up to $\sim$ 100 mm. Due to the length of the crystals, their doping concentration is low. Such crystal rods represent an interesting solution for a high-power solid state laser amplifiers since they possess a long absorption length and a very high surface to volume ratio, which lead to an elevate thermal dissipation [71]. With respect to the most common Czochralski method [72], the micro-pulling-down technique is faster, cheaper and produces single crystal fibers in a direct manner without the requirement of additional processes. This is an attractive feature since it avoids the challenging task of necessarily cut and polish several centimeter long and few mm thin rods. In detail, Yb:LLF crystal is particularly appealing for power scalability applications since it has a very reduce quantum defect ($\sim$ 4%), a weak and negative thermo-optic coefficient, low phonon energy reducing radiative cross relaxation processes, and a low refractive index, limiting nonlinear effects in ultrashort pulse amplifiers.

The single crystal fiber Yb:LLF which has been exploited for the following amplification experiments was grown at University of Pisa, Italy. In this work, I present a demonstration of a SCF amplifier based on a birefringent Yb:LLF crystal grown by the μ-PD technique. The following amplification measurements were taken in continuous wave, but given the spectroscopic properties of the gain medium a future investigation of the ultrashort pulse amplification performances will be certainly carried out.

7.1 Continuous Wave Yb:YLF Seeder

The seeder employed for CW amplification experiments was a three mirrors, V-shaped, fiber-coupled laser diode pumped Yb:YLF oscillator. The resonator layout is shown in figure 7.1. The pump diode was fiber-coupled emitting a maximum

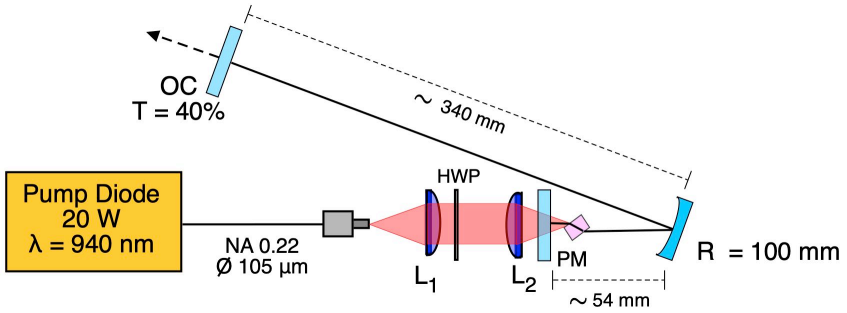

Figure 7.1: Continuous Wave Seeder Oscillator. L1, L2: Aspheric lens f1 = 25 mm, f2 = 20 mm Anti-Reflection (AR) coated at 976 nm. HWP: Half-Wave Plate Anti-Reflection (AR) coated at 980 nm. PM: Dichroic plane Pump Mirror, Anti-Reflection (AR) coated at 900-985 nm, HR coated at 1000-1100 nm.

output power of 20 W at $\lambda_p = 940$ nm. The fiber was multimode with a core diameter $2w = 105$ μm with an NA= 0.22. The beam quality was estimated to be $M^2 \simeq 38$. Due to the short length of the fiber ~ 10 cm, the output beam was elliptically polarized with a polarization extinction ratio of $\approx 4{:}1$.
The pump was collimated and then focused into the crystal by using two aspherical lenses: L1, with focal length 25 mm, and L2, with focal length 25 mm, both AR coated at 976 nm. Between them an half wave plate AR coated at 980 nm was positioned to modify the pump polarization and increase the absorption from the crystal, which is birefringent. The maximum measured pump absorption was approximately 50%. The gain medium was a 5.2 mm long, 10% doped Yb:YLF. The crystal was put at Brewster's angle to reduce insertion losses since the facets were polished and uncoated. The crystal was mounted on a water-cooled copper plate. The desired output wavelength was around 1020 nm. At this wavelength there is a peak of the emission cross sections of the amplifier gain medium, an Yb:LLF crystal. Due to the quasi-three level nature of Ytterbium ions, the desired wavelength was selected by properly choosing the OC mirror transmittivity. The seeder wavelength was 1021 nm with a $T_{OC} = 40\%$. In a such configuration, the maximum output power was about 1 W, with an almost circular beam and with a beam quality $M_x^2 \times M_y^2 = 1.06 \times 1.06$, shown in figure 7.2.

7.2 Continuous Wave Amplification

The experimental layout is represented in figure 7.3. It consisted in a Four-Pass Yb:LLF amplifier. The spectroscopic properties of Yb:LLF, which is a birefringent crystal, are described in Chapter 5. The c-axis of the crystal was orthogonal to the rod axis, and it presented an high optical quality free of cracks and micro bubbles. The gain medium was pumped by a fiber-coupled laser diode mounted on a water-cooled heat sink. The pump module provided a maximum power of 120 W in a multimode fiber with a core diameter $2w = 105$ μm with an NA= 0.22. The estimated beam quality was $M^2 \simeq 35$. The pump wavelength was stabilized at $\lambda_p = 976$ nm by means of a fiber Bragg grating (FBG) and with a bandwidth FWHM of ~ 0.5 nm. The wavelength stabilization was effective only near the maximum pump power, obtained

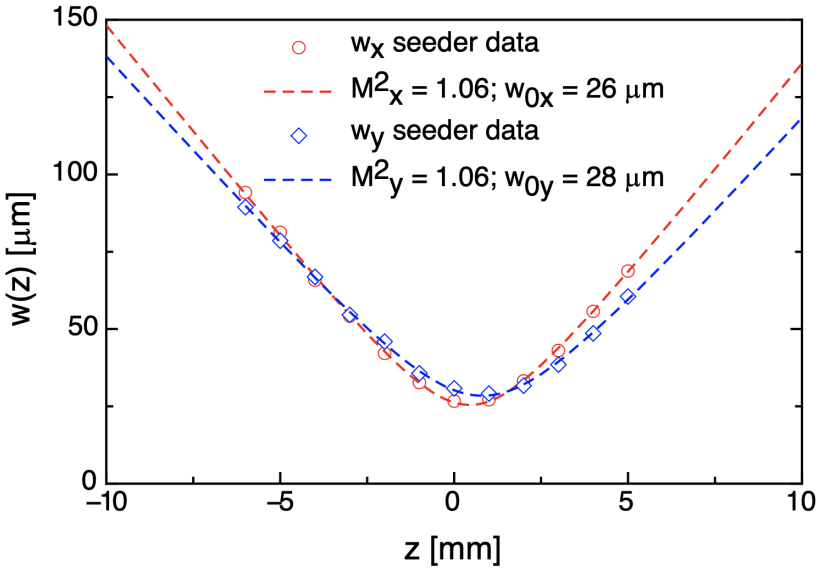

Figure 7.2: Spatial beam quality of the CW Yb:YLF oscillator.

at 12.5 A of driving current. For lower values of pump power, the wavelength was driving current dependent and drifted in a continuous manner from 965 nm at 70 W to 968 nm at 90 W with a bandwidth FWHM of 2.5 nm, above this level power the emission wavelength was locked at 976 nm.
The absorbed pump power characteristic is depicted in figure 7.4. Even though the pump module had an output wavelength drift before $\sim$ 100 W, the absorption power efficiency was only slightly affected, with a value always $\geq$ 88% also after the wavelength stabilization. This is an interesting feature since it means that the Yb:LLF crystal doesn't require a precise control over the pump wavelength to efficiently absorb energy.
The pump beam was coupled in the amplifier by using a telescope composed by two achromatic lenses, F1 with a focal length of 40 mm, F2 with a focal length of 150 mm, both AR coated at 976 nm. The spot radius realized in the active medium was $w_p = 200$ μm. The gain medium exploited by the amplifier was a 42 mm long, single crystal fiber (SCF) Yb:LLF 2% doped, grown by micro pulling down technique (μPD). The $\sim$ 2.8 mm diameter Yb:LLF SCF was wrapped in indium foils and then soldered in a water-cooled copper holder. The water was kept at a constant temperature of 4 °C.
The seeder output beam was collimated by using a spherical lens, which is not depicted in figure ref, with a focal length of 500 mm. Subsequently passed through a Faraday isolator (FI) with the sole purpose to optically isolate the seeder from the rest of the system. After the FI the seeder beam passed through an half wave plate (HWP) in order to be completely transmitted by the polarizer beam splitter (PBS). After the PBS the seeder beam polarization was linear and horizontal (π). Successively the seeder beam was focused into the amplifier gain medium by means of an AR coated spherical lens F3 with a focal length of 200 mm. The focusing lens yielded to a beam radius $w_s = 135$ μm into the SCF rod. The incident seeder power measured at the facet of the Yb:LLF was 0.8 W. The chosen seeder/pump beam

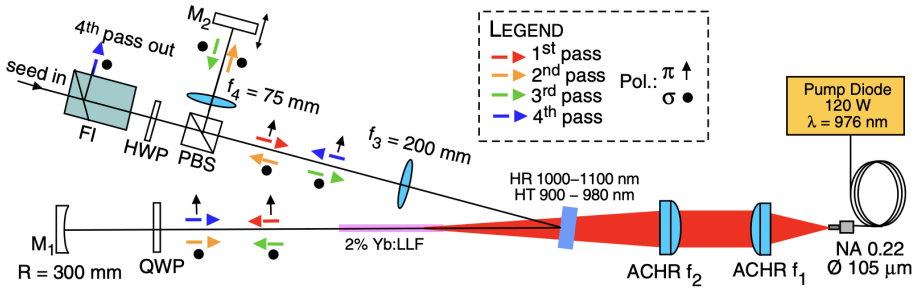

Figure 7.3: Yb:LLF Multipass amplifier setup. F1, F2: Achromatic lenses, f1=40 mm, f2=150mm, both AR coated at 976 nm; F3, F4: Spherical lenses, f3=200 mm, f4=75 mm, AR coated at 1020 nm; M1: High-Reflectivity (HR) broadband curved mirror, R=300 mm; M2: High-Reflectivity (HR) 0° broadband mirror; Half wave plate (HWP); Quarter wave plate (QWP); Polarized beam splitter (PBS); Faraday isolator (FI).

ratio ($w_s = 135$ μm, $w_p = 200$ μm) provided the best amplification gain and spatial beam quality.

The multipass amplifier exploits polarization to modify the seeder optical path and eventually to extract it. After a first pass in the amplifier, the seeder passes though a quarter wave plate (QWP), it is reflected back by a spherical, high reflectivity (HR) broadband mirror M1 with a radius of curvature of 300 mm. The mirror radius of curvature was chosen to re-image the beam into the Yb:LLF rod. Successively it goes though a second time the quarter wave plate (QWP). Thus, the seeder polarization is rotated by 90° before the second pass into the crystal. After the second pass, the F3 spherical lens collimates the beam, which is reflected by the polarizer beam splitter (PBS). The two passes amplified seeder beam goes into the retroinjection arm, which is composed by a spherical lens F4, with a focal length of 75 mm, AR coated, and a high reflectivity (HR) 0° broadband plane mirror M2. The retroinjection arm is used to back reflect the two passes amplified seeder beam into the amplifier for the third and fourth passes. Both the distances F4 lens−M2 mirror and Yb:LLF rod−M1 mirror were adjustable to take into account thermal lensing in the amplifier. After the fourth pass the beam seeder polarization was rotated by another 90° degrees, so it could be completely transmitted by the polarizer beam splitter (PBS) and being extracted by the Faraday isolator.

Since the Yb:LLF is a birefringent crystal the seeder beam experienced a different emission cross section with respect to its polarization. The first and the fourth passes had an horizontal (π) polarization and exploited the cross section parallel to the c-axis, $E \parallel c$. The second and the third passes had a vertical (σ) polarization and exploited the cross section perpendicular to the c-axis, $E \perp c$.

The multipass amplifier was firstly tested at low incident seeder power in order to assess the amplifier small signal gain in a situation far from saturation. The saturation power for π and σ polarizations were found by taking into account the spectroscopic properties of the SCF Yb:LLF, its fluorescence time [4] and the seeder

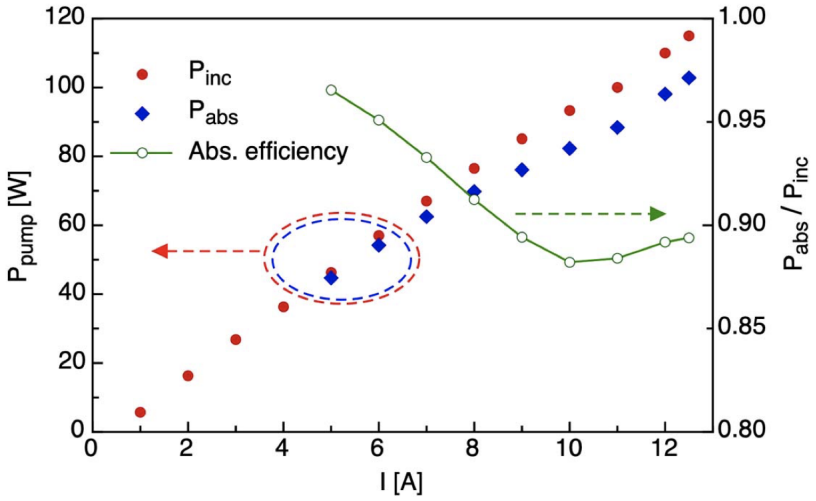

Figure 7.4: Incident and absorbed power in the multipass amplifier as a function of the laser diode current. For driving current above 10 A, the pump module stabilized the output wavelength at 976 nm though the FBG.

beam waist w_s:

$$P_{sat,\pi} = I_{sat,\pi} A_s = \frac{hc}{\lambda_s} \frac{\pi w_s^2}{\lambda_s(\sigma_{a,\pi} + \sigma_{e,\pi})\tau_f} = 6.5\,\mathrm{W} \tag{7.1}$$

$$P_{sat,\sigma} = I_{sat,\sigma} A_s = \frac{hc}{\lambda_s} \frac{\pi w_s^2}{\lambda_s(\sigma_{a,\sigma} + \sigma_{e,\sigma})\tau_f} = 13.5\,\mathrm{W} \tag{7.2}$$

where the seeder wavelength was $\lambda_s = 1021$ nm and the fluorescence time $\tau_f \simeq 2$ ms. The related values of intensity saturation were $I_{sat,\pi} = 11$ kW·cm^{-2} and $I_{sat,\sigma} = 23$ kW·cm^{-2}.

Above 80 W of absorbed pump power, the amplifier gain had a saturation-like effect, with a negligible increase of output power when increased the pump power. This is visible from figure 7.4 and happened at different seeder/output power levels. This indicated that saturation of the amplifier gain was likely due to parasitic thermal effects instead of gain saturation, since the saturation power of the SCF Yb:LLF of both polarizations was well above the output power. For this reason, in the following experiments the absorbed pump power was limited to 80 W, which corresponded to approximately 90 W of incident pump power. Moreover, at high incident pump power the multipass amplifier experienced a slow thermal drift which decreased the amplifier gain. The thermal steady state was reached after few minutes the pump was switched on.

These thermal parasitic effects affected the performance of the multipass amplifier. Thus, they were investigated with the procedure as follows. Firstly, the amplifier was aligned for maximum gain at low incident pump power ($\sim$ 40 W). Then, the gain medium was let cool down by switching off the pump diode. Lastly, the amplifier gain was measured two times: right after switching on the pump and after the thermal steady state was reached. This investigation, which is visible in figure 7.6, was carried out at different seeder and pump power levels. The results clearly show that the

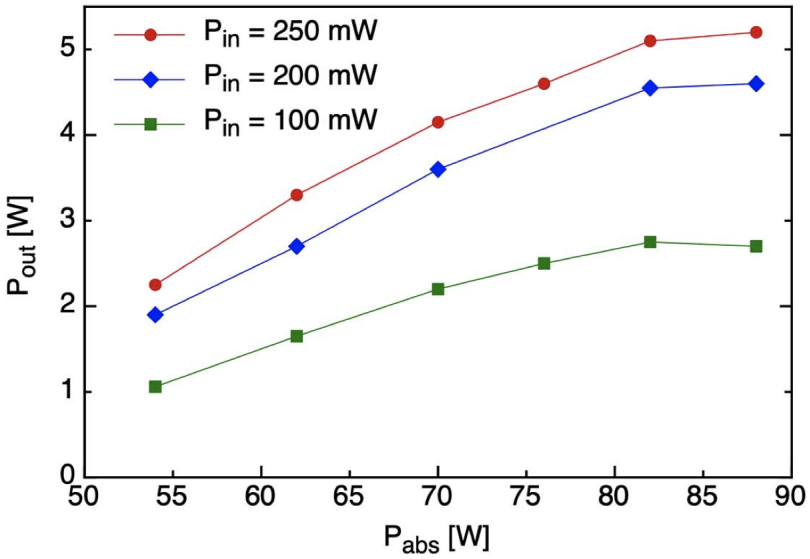

Figure 7.5: Four-passes output power as a function of the absorbed pump power for different values of the incident seeder power.

thermal effects significantly impacted on the amplifier performance when the incident pump power was above 60 W. At the maximum absorbed pump power, the gain drop was estimated to be about 15%. This behaviour was attributed to an increased temperature inside the crystal rod. Due to the quasi-three level nature of Ytterbium ions, an increased temperature led to a rise of the reabsorption losses due to the thermal population of the lower laser level transition. Moreover, it led to a reduction of the emission cross section peak value [73].

A second measurement of the multipass amplifier gain was carried out as a function of the incident seeder power for different absorbed pump power levels. This measurement, which is presented in figure 7.7, was performed right after the pump diode switched on, so in a so called "cold" condition. A maximum output power of 8.4 W was obtained with an incident seeder power of 0.8 W with a gain of 10.5. The maximum small signal gain was above 30 with an incident seeder power of 50 mW. No significant beam depolarization was witnessed at any incident pump power.

The amplified seeder beam quality was measured by scanning a CCD camera along the focal plane of a spherical lens with a focal length of 80 mm. The lens was positioned at the output of the Faraday isolator (FI). The spatial beam quality was measured with the pump switched off and the pump switched on. As mentioned in the previous section, the seeder presented a beam quality $M_x^2 \times M_y^2 = 1.06 \times 1.06$ with a slightly astigmatism. The same beam quality was measured also after the passage though the multipass amplifier. Once the pump module was switched on at 100 W of incident pump power, the amplified seeder beam quality measured was $M_x^2 \times M_y^2 = 1.15 \times 1.06$. This result demonstrates that the incident seeder beam quality was almost completely preserved and is an evidence of the exceptional optical quality of the SCF Yb:LLF rod exploited as gain medium.

The aforementioned measurements of beam quality are shown in figure 7.8. From

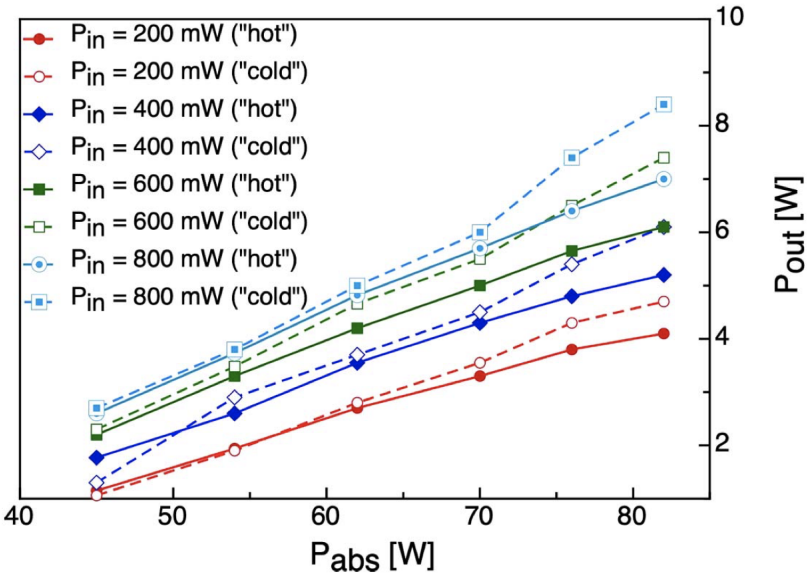

Figure 7.6: The temperature dependence of the amplifier gain. The characteristic defines the output power of the four-passes amplifier as a function of absorbed pump for different incident seeder power measured immediately after the pump was switched on ("cold", dashed line), and after thermal steady-state has been reached ("hot", solid line).

these measurements it is clear that a thermal effect was modifying the optical properties of the amplified seeder beam. Furthermore the amplifier produces a beam magnification along the CCD plane which makes more evident the astigmatism of the incident seeder beam. Through an ABCD modeling of the amplifier setup it was studied the propagation of an almost perfectly Gaussian laser beam. In such a way it was possible to estimate the effective thermal focal length in the amplifier at 100 W of incident pump power. The best fit, which is depicted in figure 7.8 was a thermal lens with a focal length of $f_{th} = -150$ mm. The sign thermal lens is concordant with the negative thermo-optic coefficients owned by fluorides crystals such as Yb:LLF. The simplified ABCD amplifier model didn't take into account the dependence of Yb:LLF thermo-optic properties from the seed polarization.

Despite that, the thermal focal length, which is calculated from equation 4.76, directly depends on the ratio between thermal conductivity and thermo-optic coefficient, which differs only $\sim 30\%$ for the two polarizations in the Yb:LLF rod [74]. Such a reduced difference may explain the consistency of the simulated to the experimental results. Furthermore, the calculated thermal lens of $f_{th} = -150$ mm is in agreement with the estimated thermal lens in an end-pumped rod with ideal radial heat flow [75]. Such a model allows to estimate a temperature difference between the center and the border of the Yb:LLF rod of ~ 50 °C. Nonetheless a thermal lens with a relatively short focal length, the amplified beam quality remained excellent. This result confirmed that the multipass amplifier layout is robust to such thermal effects. This propriety has been validated by the ABCD amplifier model, and the main reason is due to the re-imaging during the multipass amplification given by the retroinjection arm. It keeps the total spherical aberrations low and allows the seeder beam to

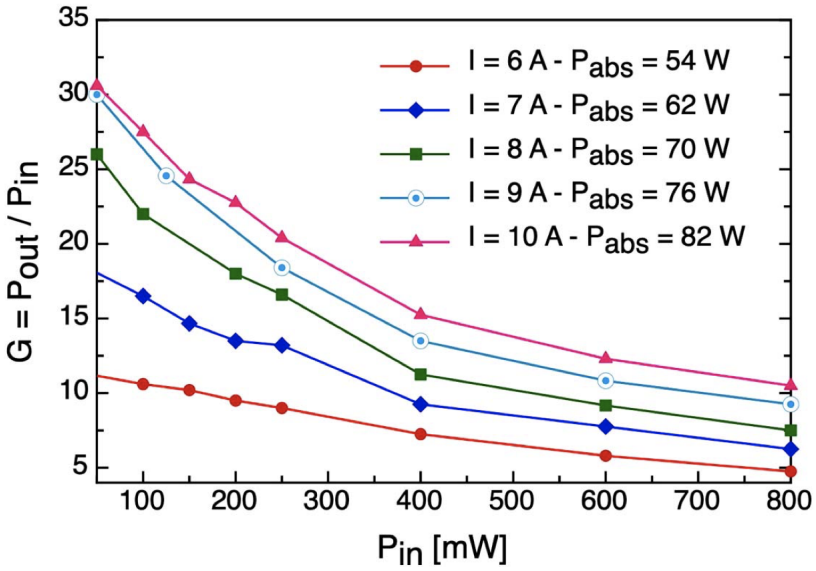

Figure 7.7: Measured gain as a function of the incident seeder power for different values of the absorbed pump power.

maintain a constant beam diameter along different passes of amplification.

7.3 Conclusion

During this work I exploited for the first time a single crystal fiber Yb:LLF grown by the μ-PD technique in a multipass amplifier. The amplifier setup consisted of four passes and exploited a CW Yb:YLF oscillator at $\lambda_s = 1021$ nm with ~ 1 W of output power as seeder. The maximum small signal gain measured was > 30 with an incident seeder power of 50 mW, an incident pump power of ~ 90 W and an absorbed pump power of 82 W. The maximum output power was found to be 8.4 W right after switching on the pump module, at 82 W of absorbed pump power with an incident pump power of 0.8 W. Even in this situation, the multipass amplifier preserved extremely well the spatial beam quality and the polarization of the seeder beam. The amplified seeder beam quality was measured to be $M_x^2 \times M_y^2 = 1.15 \times 1.06$ and with a thermal lens at maximum pump power of $f_{th} = -150$ mm. These measurements clearly show the high optical quality of the SCF Yb:LLF, the validity of the multipass amplifier layout and the usefulness of the spectroscopic characteristics of Yb:LLF for amplification.
Unfortunately, there were observed thermal parasitic effects which limited the amplifier gain at high pump power. In order to overcome this detrimental process, the most important actions which could be taken aim to reduce the temperature at the centre of the crystal rod. In particular, this can be done by further increase the high surface to volume ratio and by reducing the doping concentration, increase accordingly the crystal's length and its absorption length. In an industrial related product, a multipass amplifier of this kind has an interest as a final stage in an amplifier chain where the incident seeder power is ~ 1 W or above, in order to

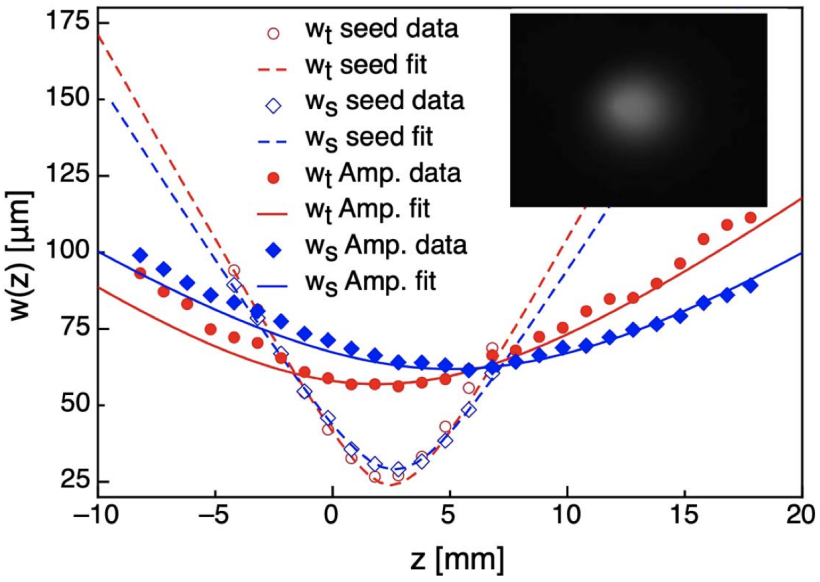

Figure 7.8: Beam waist measurement of the seeder at the amplifier output with the pump switched off (empty dots and diamonds) and with the pump switched on (full dots and diamonds). The dashed and solid curves represent the result of the ABCD beam propagation best fit. Inset: beam intensity profile of the amplified beam.

effectively exploit the relatively low emission cross sections of Yb:LLF crystal and the low small signal gain. This work led to a paper which has been published in the Optics Express Journal [8].

Chapter 8

High Brightness Diode Pumped Yb:CaF_2 Multipass Amplifier

The last part of my work has been devoted to the study of innovative tapered laser diodes (TLDs) with a low output power but high spectral radiance, more commonly called brightness. The development of these diodes has been funded through the European programme H2020 under the name of Eureka Eurostarts MiFeM, project no. 11440. It was a partnership between two research centres, Ferdinand-Braun-Institut (FBH) and Brilliance FAB Berlin (BFB), Berlin, Germany, and two companies, Pantec Engineering, Ruggell, Liechtenstein, and Spectra-Physics, Rankweil, Austria. The aim of the project was to provide to the market a compact, low cost and robust miniaturized laser diode with a high beam quality and output power, to operate in continuous wave or in pulsed regime, which could be used directly for material processing, such as micromachining, or to deliver their power to an active medium.

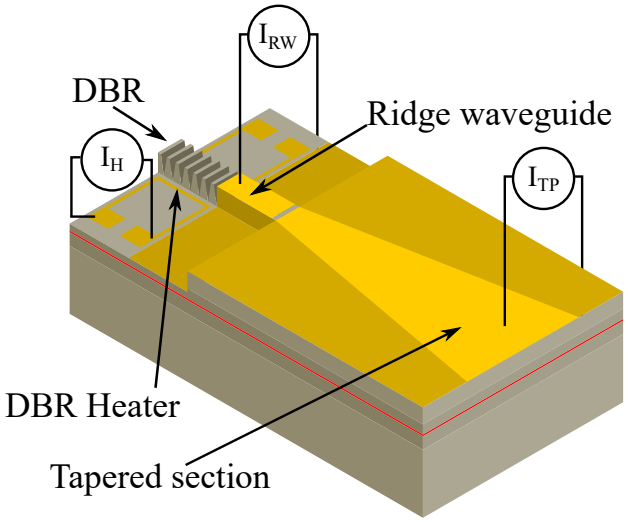

Figure 8.1: Schematic DBR tapered diode laser layout including additional DBR heater and corresponding current sources [7].

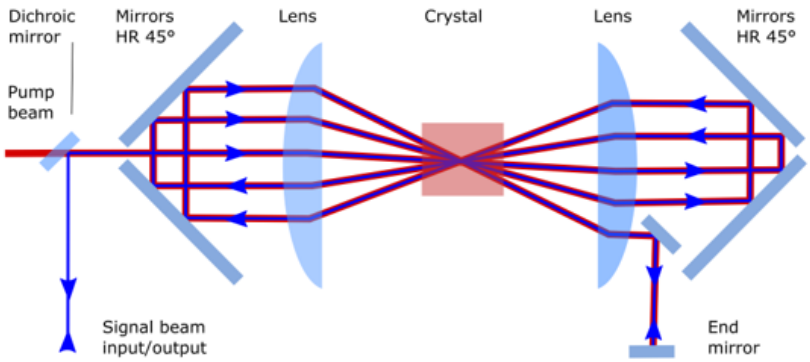

Figure 8.2: Theoretical design of a multipass amplifier exploiting a high brightness pump.

In the last years the Ferdinand-Braun-Institut developed a device called Base MiMo, which is composed by two tapered laser diodes combined by polarization coupling. The scope of my experiments was to investigate the feasibility of Base MiMos in continuous wave operation as a diode pump for pulse amplification exploiting a multipass configuration. While Base MiMos have a modest output power ~ 14 W, they have a very high beam quality $M^2 < 2$, which is comparable with the seeder's beam quality. This property paves the way to a completely different way to amplify pulses and to extract the energy stored in the gain medium.

In a common multipass amplifier setup the high power diode pump possesses a low brightness. The seeder beam waist in the active medium is slightly smaller than the pump beam waist in order to have high efficiency and avoid beam distortions. On the other hand, the volume of the gain medium in which the pump has stored energy is much more with respect to the volume in which the seeder propagates, since the pump beam quality is much lower. In a common multipass configuration such this, the seeder passes with slightly different angles several times through the gain medium, each time in those regions where it hasn't gone through before, and therefore where the energy stored hasn't been depleted yet. Doing that, more energy from the gain medium is extracted and the overlap efficiency between pump and seeder is increased.

On the other hand, Base MiMos have a high spatial quality. This means that not only its beam waist in the gain medium is comparable with the seeder beam waist, but also the volumes are similar. In a such way, the pump and the seeder can be co-propagating inside the gain medium with a very high overlap efficiency. In a multipass configuration with an high brightness diode pump, such as Base MiMo, both the seeder and the pump pass with slightly different angles several times through the gain medium while they are co-propagating. This leads to an higher efficiency since the volume of the active medium excited by the pump and not exploited by the seeder is very reduced.

While the premises of the Base MiMo as a diode pump are outstanding, their development still result in an immature stage, and as for now they are not a viable solution for an industrial product. In fact different Base MiMos have been used for

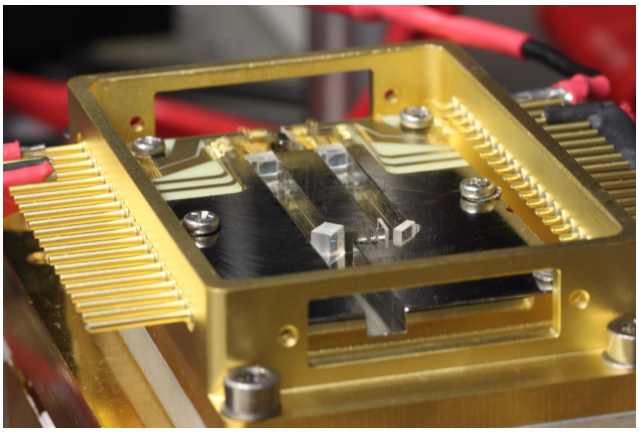

Figure 8.3: Photography of an operational Base MiMo composed by two tapered laser diodes combined by polarization coupling [7].

amplification experiments. Their overall stability, especially regarding the output power and the tapered laser diodes lifetime, was undermined by different problems. Nonetheless they represent a device under development with a great potential.
In the following experiments I present a novel Yb:CaF_2 multipass amplifier configuration exploiting a Base MiMo with only one of the two TLDs partially functioning, with an overall maximum output power of 6.4 W of which $\sim$ 4.5 W in the central lobe and a beam quality $M_x^2 \times M_y^2 = 2.6 \times 1.9$. Given its spectroscopic properties, Yb:CaF_2 is the perfect candidate for ultrashort pulse amplification.

8.1 Tapered Laser Diodes

A single-mode laser diode can achieve a high spatial beam quality but only with a low optical power in the milliwatt range. On the other hand, broad area laser diodes, or a stack of them (diode bars), can reach higher output powers, but with a reduced beam quality. An example are the laser diodes which has been used in the previous experiments, which have a very high output power ($\sim$ 100 W) but with a low beam quality ($M^2 = 30 - 50$). For this reason a new solution has been developed to overcome the low power provided by laser diodes with high optical quality, i.e. the tapered laser diodes.
A tapered laser diode consists in two separately contacted active regions: a ridge waveguide, which generates a low-power signal, and a tapered section, which increases the output power while maintaining an high beam quality.
The tapered laser diodes exploited in these experiments were developed by FBH and BFB in Berlin. The cavity is provided by a DBR-grating section with additional heater at the end of the ridge waveguide which also selects the emission wavelength [76]. The ridge waveguide has a width of 4 μm and a length of 1 mm. The full angle of the tapered section is set to 6° while its length is 4 mm. The overall length, including the DBR-grating is 6 mm. The laser tapered diode, depicted in figure 8.1, is capable of reaching an optical output power of approximately 8 W in a claimed long term operation ($>$ 2000h [77]). The laser is stabilized to a longitudinal single mode at each operating point ensuring a narrow spectral width below 20 pm. The spectral emission

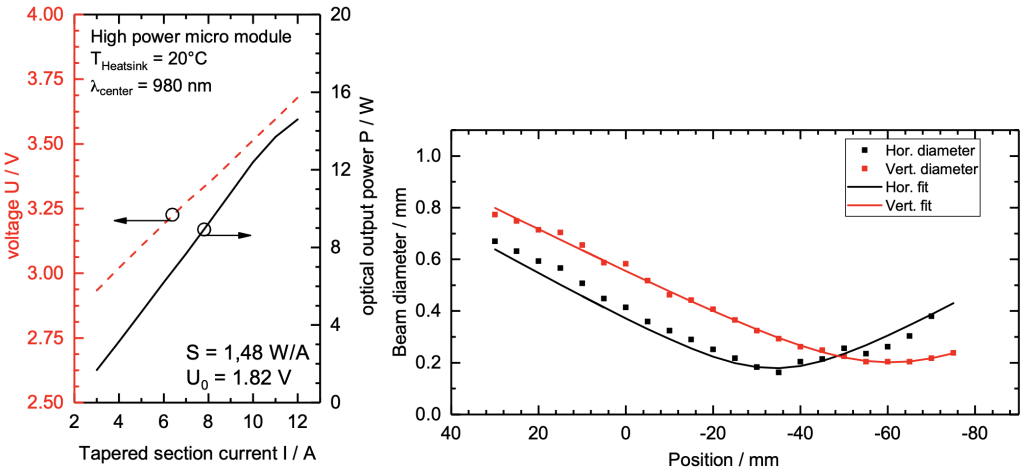

(a) **(b)**

Figure 8.4: Base MiMo Properties [7]. (a) Output Power and (b) Beam quality $M_x^2 \times M_y^2 = 1.11 \times 1.52$.

characteristics can be tuned by an heating element next to the DBR. While having a stable optical output power, the center emission wavelength can be modified by up to 2 nm [78]. Moreover, the output beam presents an linear horizontal polarization. While the total output power is approximately 8 W, only an estimated 70% lies in the central lobe, which is the part of the output beam with high spatial quality and of our interest.

8.2 Laser Micromachining Module: Base MiMo

In order to increase the output power two tapered laser diodes were combined by polarization coupling. In this configuration, the laser module was called Base MiMo. The characteristics of the micro module depend strongly on the optical, thermal and mechanical layout. An exemplary Base MiMo is shown in figure 8.3. All optical components were housed inside an inlay with a footprint of 58×34 mm^2. An extensive work has been done at FBH to provide thermal crosstalk between the single diode emitters. To collimate the output of the single emitters, specialized lenses developed by FBH and Pantec Engineering were used. They feature individual cylindrical shapes to reduce unavoidable aberrations. Since the output beam divergence on the fast axis depends on the current provided to the diode, the lens has been designed such that it collimates the beam at the maximum current level. The polarization coupling was accomplished by using a deflecting mirror, an half wave plate and a thin film polarizer featuring a dielectric coating. The output power of Base MiMo reached $\sim$ 14 W, at a sink temperature of 20 °C, a ridge waveguide current of $I_{RW} = 350$ mW, a tapered current of $I_{TP} = 12$ A and an emission wavelength of 980 nm. Only a fraction of the output power, approximately 10 W, are in the central lobe with a high beam quality. Hence, this is the output power of our interest for amplification experiments. The beam quality is $M_x^2 \times M_y^2 = 1.11 \times 1.52$ with a slightly astigmatism. The y axis is the fast axis and has a lower spatial quality. The output power and

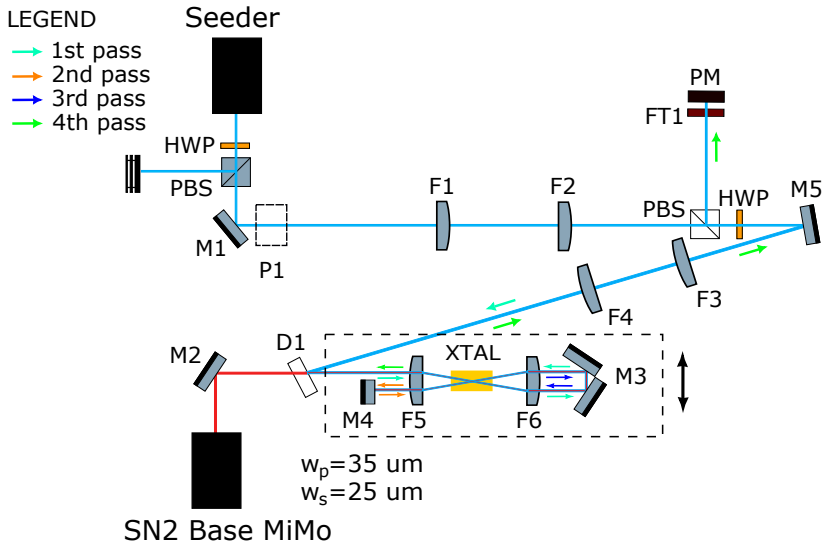

Figure 8.5: Double 2-Pass Yb:CaF_2 Amplifier Setup. P1: Periscope; M1, M2, M3: High reflectivity (HR) 45° broadband mirrors; M4, M5: HR 0° broadband plane mirrors; D1: Dichroic Mirror (DM) Highly Transmitting (HT) at 980 nm and HR at 1000-1100 nm; F1, F2: f=100 mm spherical lenses, AR coated at 980 nm; F3: f=75 mm spherical lens, AR coated at 980 nm ; F4: f=50 mm spherical lens, AR coated at 980 nm; F5, F6: f=30 mm achromatic lenses, AR coated at 980 nm; HWP: half-wave plate at 1030 nm; PBS: SF10 polarizer beam splitter; FT1: FEL1000 Longpass Filter, cut-on at 1000 nm.

beam quality are depicted in figure 8.4.
Unfortunately, during the experiments here described, the Base MiMo suffered a partial failure. So, the following results were obtained with a Base MiMo provided with only one of the two TLDs was functioning, with an output power of 6.4 W of which 4.5 W in the central lobe and a beam quality $M_x^2 \times M_y^2 = 2.6 \times 1.9$.

8.3 Numerical Model Investigation

An extensive work of numerical simulation has been carried out through the polychromatic numerical model described in section 4.3. In particular, the model has been modified to take into account that the seeder and the pump are actually co-propagating in the gain medium for all the passes. The initial part of the investigation was devoted to understand the amplification conditions to obtain the highest efficiency: the crystal's length, the beam waist and the number of passes with respect to a given pump power. This part is critical since the Ytterbium has a quasi-three level nature and there may be significant reabsorption losses if the residual pump is not considered. The information provided by the aforementioned analysis were used to design the multipass amplifier. The crystal chosen as gain medium for amplification experiments was an Yb:CaF_2. Even though it has a low emission cross section, leading to a reduced single pass gain, it possesses a very broad emission bandwidth. This is a favorable characteristic for an ultrashort pulse amplifier when is reached high-gain because the gain narrowing effect is reduced.

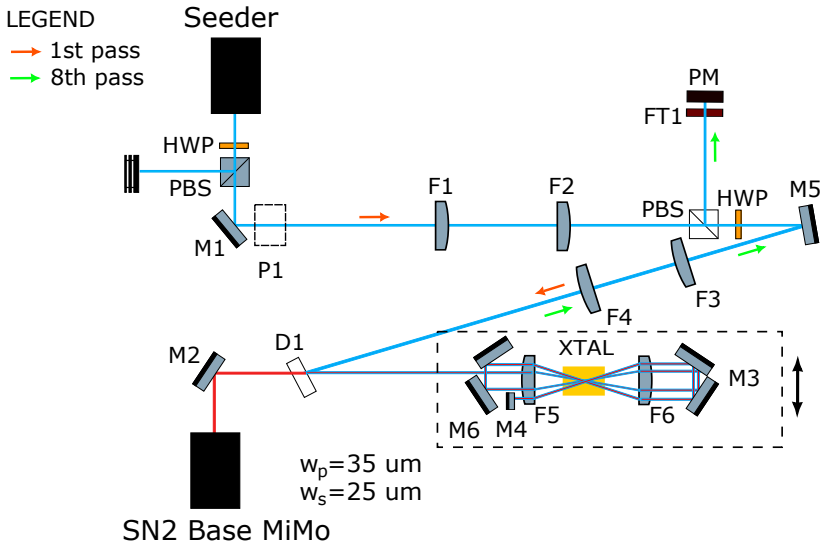

Figure 8.6: Theoretical Yb:CaF_2 Multipass Amplifier Setup. P1: Periscope; M1, M2, M3, M6: High reflectivity (HR) 45° broadband mirrors; M4, M5: HR 0° broadband plane mirrors; D1: Dichroic Mirror (DM) Highly Transmitting (HT) at 980 nm and HR at 1000-1100 nm; F1, F2: f=100 mm spherical lenses, AR coated at 980 nm; F3: f=75 mm spherical lens, AR coated at 980 nm ; F4: f=50 mm spherical lens, AR coated at 980 nm; F5, F6: f=30 mm achromatic lenses, AR coated at 980 nm; HWP: half-wave plate at 1030 nm; PBS: SF10 polarizer beam splitter; FT1: FEL1000 Longpass Filter, cut-on at 1000 nm.

With an output power provided by the Base MiMo of $\sim$ 14 W, and exploiting an Yb:CaF_2 3% doped crystal, the numerical study found the best solution to be an Yb:CaF_2 5 mm long crystal, with a pump beam waist $w_p \sim 30$ μm, a seeder beam waist $0.8 - 0.9 \cdot w_p$ and up to a double 4 pass configuration. The amplifier layout is shown in figure 8.6. In such a system, the simulated gain was 12.8 and 11.7 with 1 mW and 10 mW of incident seeder power, respectively.

An additional simulation was carried out to define the number of passes necessary to reach at least 30 dB of gain. Following the previous layout, the resulted number of passes was 24, with an incident pump power $>$ 30 W with an incident pump power of 1 mW. While the output power reached by the Base MiMo is not comparable, it is interesting to know the level of power required for future improvements. Moreover, such a high-gain would fully exploit the capabilites of Yb:CaF_2 in ultrashort pulse amplification.

Unfortunately, due to lifetime issues one of the two TLDs which composed the pump module stopped to work. The power provided by the Base MiMo dropped to approximately 4.5 W in the central lobe. The previous numerical simulation regarding the crystal's length and the beam and seeder spot sizes remained correct, but given the reduced amount of power the setup could be used only up to a double 2 pass configuration. The amplifier layout which was used for amplification measurements is shown in figure 8.6.

In the second part of the investigation I compared the simulation with the experimental results and to corroborate them.

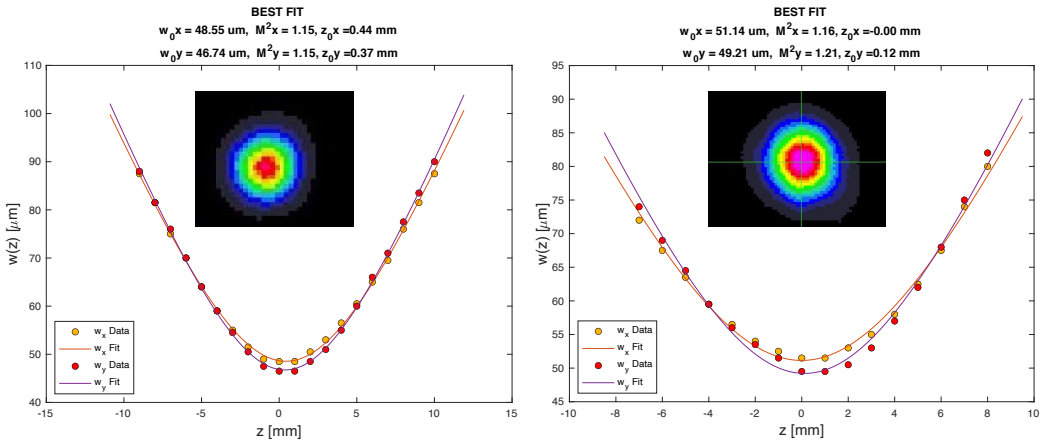

(a) **(b)**

Figure 8.7: Beam quality measurement of the output amplifier beam at 10 mW of incident seeder power when (a) the pump was switched off (b) the pump was switched on at maximum output power. Inset: beam profiles in the focus.

8.4 Ultrashort Pulses Amplification

The system used for measurements was a multipass amplifier which was employed in different configurations: 1-Pass, 2-Pass and Double 2-Pass. The system layout for a Double 2-Pass is shown in figure 8.5. While the layouts actually exploited were several, the following is the one which presented the best results in terms of validity of the Base MiMo potential and scalability. The system was composed by three parts: the Yb:KYW seeder and some optical components to manipulate its power and beam width, the Base MiMo used as pump, and the actual Yb:CaF_2 multipass amplifier.

The seeder, which is described in section 6.1, was a Yb:KYW based oscillator and was operating in a mode locking regime, providing pulses of 200 fs of pulse duration, with a bandwidth FWHM of $\sim$ 6 nm, up to 5 nJ of energy, an average output power up to 0.5 W, with a pulse repetition rate of 108 MHz and with a tunable peak wavelength from 1025 nm to 1036 nm. The seeder wavelength was set for these experiments at $\lambda_s = 1030$ nm to match the peak of the emission cross section of Yb:CaF_2 which is $\sigma_e \sim 0.16{\cdot}10^{-20}$ cm^2. It had a linear horizontal polarization and a beam quality $M_x^2 \times M_y^2 = 1.09 \times 1.17$. The resonant mode had a beam radius of $w_s \approx 400$ μm on the OC.

The pump was a Base MiMo with only one of the two TLDs partially functioning. It had an overall maximum output power of 6.4 W of which $\sim$ 4.5 W in the central lobe, a beam quality $M_x^2 \times M_y^2 = 2.6 \times 1.9$ and an emission wavelength at maximum output power of $\lambda_p = 981.6$ nm. At this wavelength it matched the peak of the absorption cross section of Yb:CaF_2 which is $\sigma_a \sim 0.50{\cdot}10^{-20}$ cm^2. The pump module was mounted on a water-cooled copper heat sink at 20 °C.

The multipass scheme, which is visible in figure 8.5, was designed such that an achromatic lens (F5) focused both the seeder and the pump; after the first pass the beams are then collimated by an achromatic lens (F6) reflected back by two broadband HR 45° mirrors (M3) and refocused by the same achromatic lens into the

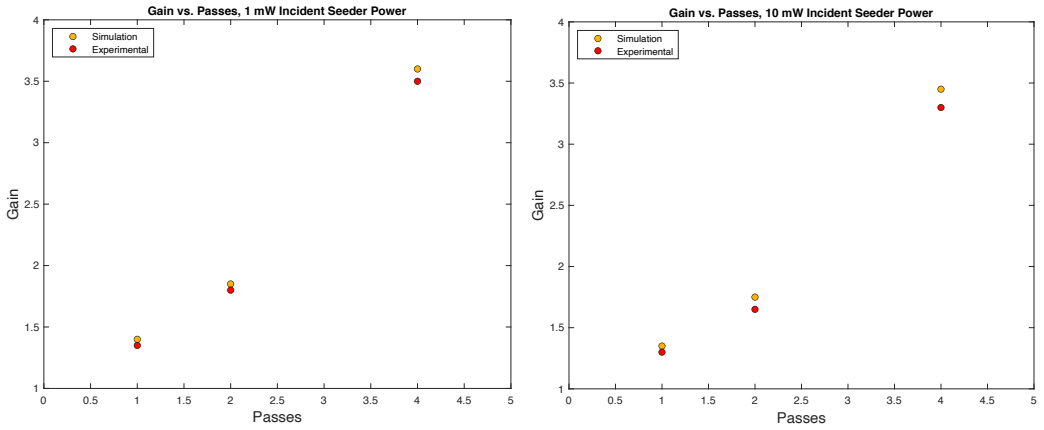

(a) **(b)**

Figure 8.8: A comparison of the gain with respect to passes in the active medium, simulation and experimental results. The incident seeder power is (a) 1 mW and (b) 10 mW.

crystal. In a such configuration, the pump beam waist in the gain medium focused by lens F5 was $w_p = 35$ μm whereas the seeder beam waist was $w_s = 25$ μm. Such small spot sizes require a very fine adjustment of the seeder beam over the pump, especially since no additional optics is used among the passes to modify the beam properties. The double passage was done through a broadband HR 0° mirror (M4) which retroinjected the seed and pump beams into the amplifier gain medium.
The key point of the following multipass configuration is to have the pump and the seeder co-propagating and focusing in the same spot in the gain medium. Due to a similar beam quality, their beam widths and wavefronts on the focusing achromatic lens F5 have to be comparable. Thus, two telescopes were used to modify the beam width and the wavefront of the seeder before injecting it into the amplifier. The first telescope was composed by two spherical lenses, F1 and F2 both with 100 mm of focal length and B coated. The second telescope was also composed by two spherical lenses, F3 with 75 mm of focal length, F4 with 50 mm of focal length, both B coated. The seeder was inserted in the multipass amplifier by using a dichroic mirror (D1) which was HT at 980 nm and HR at $1000 - 1100$ nm. The amplified signal was then extracted by exploiting polarization, using a polarizer beam splitter (PBS) ad a half wave plate (HWP).
The crystal was a 5 mm long, 3% doped Yb:CaF_2. It was wrapped around indium foils and then soldered in a copper holder to increase thermal conductivity. The holder was water-cooled at 15 °C. The amplification measurements were carried out at low incident seeder power, 1 mW and 10 mW. The output power of the seeder was set by using a polarizer beam splitter (PBS) ad a half wave plate (HWP). The system layout was tested in 1-Pass, 2-Pass and Double 2-Pass. The experimental results at maximum pump power of 4.5 W, which are compared to the numerical model results, are shown in tables 8.1, 8.2 and 8.3. The single pass configuration presents a gain of 1.35 with respect to a simulated value of 1.4 when the incident seeder power is 1 mW and a gain of 1.3 with respect to a simulated value of 1.35 when the incident seeder power is 10 mW. In a Double 2-Pass configuration, the output power is 3.5

mW (3.5 gain) and 33 mW (3.3 gain) with 1 mW and 10 mW of incident seeder power, respectively. Again, the output data provided by the numerical model are close, with 3.6 mW (3.6 gain) and 34.5 mW (3.45) for 1 mW and 10 mW of incident seeder power.

Table 8.1: Comparison Between Simulation and Experimental Results of 1-Pass Yb:CaF_2 Amplifier

1-Pass Yb:CaF_2 - Simulation				
P, inc, s (mW)	**P, inc, p, CL (W)**	**P, res, p (W)**	**P, out (mW)**	**Gain**
1	4.5	3.4	1.4	1.4
10	4.5	3.4	13.5	1.35
1-Pass Yb:CaF_2 - Experimental				
P, inc, s (mW)	**P, inc, p, CL (W)**	**P, res, p (W)**	**P, out (mW)**	**Gain**
1	4.5	3.6	1.35	1.35
10	4.5	3.6	13	1.3

Table 8.2: Comparison Between Simulation and Experimental Results of 2-Pass Yb:CaF_2 Amplifier

2-Pass Yb:CaF_2 - Simulation				
P, inc, s (mW)	**P, inc, p, CL (W)**	**P, res, p (W)**	**P, out (mW)**	**Gain**
1	4.5	2.25	1.85	1.85
10	4.5	2.25	17.5	1.75
2-Pass Yb:CaF_2 - Experimental				
P, inc, s (mW)	**P, inc, p, CL (W)**	**P, res, p (W)**	**P, out (mW)**	**Gain**
1	4.5	2.4	1.8	1.8
10	4.5	2.4	16.5	1.65

In figure 8.8 there is a comparison of the gain provided over the passages between the experimental setup and the numerical model. The graphs clearly shows that the gain increase linearly with respect to passages and that te experimental and simulated results adhere.
The beam quality, as shown in figure 8.7, remains excellent even after a Double 2-Pass configuration. It was measured by scanning a CCD camera along the focal plane of a spherical lens with a focal length of 100 mm. When the pump module was switched on, the output beam quality measured was $M_x^2 \times M_y^2 = 1.15 \times 1.15$. Once the laser diode was switched on at maximum output power, the spatial beam quality resulted was $M_x^2 \times M_y^2 = 1.16 \times 1.21$. The pulse duration and its bandwidth are not affected by the amplification since the Yb:CaF_2 has broadband emission cross sections and the gain provided is not enough to provide bandwidth reduction whatsoever. Thus

Table 8.3: Comparison Between Simulation and Experimental Results of Double 2-Pass Yb:CaF_2 Amplifier

Double 2-Pass Yb:CaF_2 - Simulation				
P, inc, s (mW)	**P, inc, p, CL (W)**	**P, res, p (W)**	**P, out (mW)**	**Gain**
1	4.5	0.1	3.6	3.6
10	4.5	0.1	34.5	3.45
Double 2-Pass Yb:CaF_2 - Experimental				
P, inc, s (mW)	**P, inc, p, CL (W)**	**P, res, p (W)**	**P, out (mW)**	**Gain**
1	4.5	0.1	3.5	3.5
10	4.5	0.1	33	3.3

the amplified pulse was still 200 fs of pulse duration and with a bandwidth FWHM of $\sim$ 6 nm.

8.5 Conclusion

During this work I demonstrated a novel setup of multipass amplifier which involves an high brightness diode pump, called Base MiMo, developed thanks to an European funding through H2020. Its main properties are a good output power $\sim$ 14 W, an high beam quality $M^2 < 2$ and a very narrow emission linewidth. Additional features of industrial interest are a compact size, a low cost and robustness. These unique characteristics leads to a new way to design multipass amplifiers and efficiently extract the energy stored by the laser diode. An intensive investigation has been carried out to validate this statement and to find the boundary conditions to optimize the amplification. Unfortunately, the experimental results were undermined by the lifetime and assembly issues that affect the Base MiMo.
Nonetheless, some important results were obtained using a Base MiMo with only one of the two TLDs partially in function. In this situation, the amplification setup, based on a Yb:CaF_2 5 mm long 3% doped, was tested in 1-Pass, 2-Pass and Double 2-Pass amplification with low incident seeder power, 1 mW and 10 mW. In particular, the Double 2-Pass setup verified that the gain scalability over the passages is linear, as it is clear from the experimental results. The Double 2-Pass Yb:CaF_2 amplifier provided 33 mW of output power (3.3 gain) with an incident seeder power of 10 mW, and 3.5 mW (3.5 gain) with an incident seeder power of 1 mW, exploiting an incident pump power of 6.4 W, of which approximately 4.5 W in the central lobe. The experimental measurements are consistent with the output data provided by the amplification model. These results provided a milestone for the future experiments of this novel multipass amplifier setup with a more powerful Base MiMo. My work to the development of the Base MiMo led to a be a contributor in a paper which has been presented at Photonic West, 2020 [7].

Chapter 9

Conclusion

During my PhD I investigated different high-power multipass amplifiers with the aim to find a high gain-cost ratio solution for an industrial product. Given the industrial nature of my PhD I focused my attention also to consolidated amplifier designs and materials but with the goal to provide useful results for an implementation in a future industrial solution. I tested various crystals, with their own spectroscopic properties, which required diverse amplifier layouts to be exploited. A particular emphasis was given to simulations of the amplification processes through the implementation of a numerical model.

The first part of my work has been devoted to the study of a high-power Yb:YAG multipass amplifier. The gain medium, an Yb:YAG, is a well-known crystal which presents high emission cross section and a modest emission bandwidth. The system amplifier showed excellent amplification performances, a very good optical quality and a robustness to thermal effects such as thermal lensing and depolarization losses. Moreover I investigated an unusual effect of bandwidth broadening in Yb:YAG in ultrashort pulse amplification. This effect counteracts the bandwidth reduction of gain narrowing when the pulse is appropriately spectrally preshaped. A polychromatic simulation of the amplification process was carried out in order to help understanding the experimental results. This effect was present at $\lambda_s = 1026$ nm and was clearly related to the spectral gain asymmetry of the emission cross section of Yb:YAG. The amplification of 200 fs pulses at 1030 nm, or longer peak wavelength, resulted in narrow bandwidth ($\sim$ 2 nm), $\sim$ 700 fs long pulses, due to severe gain narrowing effect. By seeding at 1026 nm with spectral shaping, bandwidth was completely preserved (from 5.6 nm to 6.1 nm FWHM), with only a moderate increase of the pulse duration from 200 fs to 304 fs, at an expense of a slight gain reduction from 29.2 to 25.1 dB at 10 mW of incident average power. The numerical simulations indicated that the gain reduction observed when seeding at 1026 nm with the spectral shaping, could be easily compensated by increasing amplifier gain through multipass optimization, still preserving the 300 fs output pulse duration. The demonstrated bandwidth broadening effect in Yb:YAG can be an incredible helpful solution to ultrashort pulse Yb:YAG multipass amplifiers for an industrial product, since the gain narrowing is one of the most detrimental effects that limit amplification while maintaining the original BW FWHM of the pulse. A thorough search of the relevant literature yielded to no papers related to this effect.

Successively, I exploited for the first time a single crystal fiber Yb:LLF grown by

the μ-PD technique in a multipass amplifier. Here I presented preliminary results in continuous wave amplification. The maximum small signal gain measured was > 30 with an incident seeder power of 50 mW, an incident pump power of ~ 90 W and an absorbed pump power of 82 W. The maximum output power was found to be 8.4 W right after switching on the pump module, at 82 W of absorbed pump power with an incident pump power of 0.8 W. The multipass amplifier preserved extremely well the spatial beam quality and the polarization of the seeder beam. All the measurements which have been carried out proved the high optical quality of the SCF Yb:LLF, the validity of the multipass amplifier layout. Unfortunately, there were observed thermal parasitic effects which limited the amplifier gain at high pump power. In order to overcome this detrimental process, different actions can be taken to certainly improve the system. In an industrial related product, a multipass amplifier of this kind has an interest as a final stage in an amplifier chain where the incident seeder power is ~ 1 W or above, in order to effectively exploit the relatively low emission cross sections of Yb:LLF crystal and the low small signal gain.
Lastly, I demonstrated a novel setup of multipass amplifier which involves an high brightness diode pump, called Base MiMo, developed thanks to an European funding through H2020. Its main properties are a good output power ~ 14 W, an high beam quality $M^2 < 2$ and a very narrow emission linewidth. Unfortunately, the experimental results were undermined by the lifetime and assembly issues that affect the Base MiMo. Nonetheless, some important results were obtained using a Base MiMo with only one of the two TLDs partially in function. In this situation, the amplification setup, based on a Yb:CaF_2 5 mm long 3% doped, was tested in different multipass configurations. In particular, the Double 2-Pass setup verified that the gain scalability over the passages is linear, as it is clear from the experimental results. The Double 2-Pass Yb:CaF_2 amplifier provided 33 mW of output power (3.3 gain) with an incident seeder power of 10 mW, and 3.5 mW (3.5 gain) with an incident seeder power of 1 mW, exploiting an incident pump power of 6.4 W, of which approximately 4.5 W in the central lobe. The experimental measurements were consistent with the output data provided by the amplification process simulated by the implemented numerical model. These results provided a milestone for the future experiments of this novel multipass amplifier setup with a more powerful Base MiMo.
The results obtained during my PhD thesis has been seen with great interest by Spectra-Physics Rankweil. Thus, my thesis falls under a non-disclosure agreement.

Appendices

Appendix A

Geometrical Optics and Wave Propagation

During centuries different theories have been defined to describe the light. Geometrical optics is the simplest of them, and involves the propagation of light along distances and interaction with objects whose physical dimensions are incomparably greater than the wavelength of the light. Hence, the light behaviour is not defined by its wavelength, which is neglected. It is focused on the location and direction of light. Geometrical optics has some postulates:

- Light propagation is described under the form of rays.
- The optical medium in which the light propagates has a refractive index $n \geq 1$ such that the speed of light in the medium is $c_n = c/n$ where c is the speed of light in the vacuum. Thus, the time of travel between two points is $d/c_n = nd/c$ where d is the distance between them. The value nd is called *optical path length*.
- In an inhomogeneous medium the refractive index, and thus the optical path length, depend on the position.
- It follows the *Fermat's principle* which defines the optical path as the minimum or maximum of all possible solutions between two points.

Two phenomena arise when the light encounters an interface with a different refractive index, reflection and refraction, and the ray is splitted in two. The incident ray and the normal to the interface generate the so called *plane of incidence*.

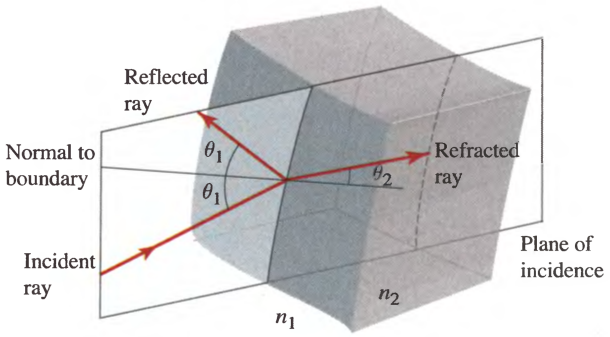

Figure 1: Reflection and refraction at an interface [79].

The incident ray, the reflected ray and the normal to the interface all lie on the plane of incidence. Moreover the incident ray and the reflected ray make with the normal the same angle, $\theta_i = \theta_r$, but opposite with respect to the normal. Refraction is described dy the *Snell's law*:

$$n_1 \sin(\theta_1) = n_2 \sin(\theta_2) \tag{1}$$

where n_1 and n_2 are the respective refractive indexes of the media, θ_1 is the angle between the incident ray and the normal, whereas is the angle between the refracted ray and the normal. If $n_1 > n_2$, then there is not a refracted ray above a certain angle $\theta_c = \arcsin(n_2/n_1)$ called *critical angle*.
Let us now focus on the most common objects and their behaviour. A lens is an optical component whose goal is to bend the rays of the incident light upon it. Depending on the lens shape, the refracted rays diverge or converge. The shape is defined by the radius of curvature R of the surfaces normal to the light propagation. Lenses with paraboloidal shape have the ability to focus the incoming rays to a single point, called *focus*, but they are complex to build. On the other hand, spherical lenses are very simple. Their surface reproduce partially the surface of a paraboloid. Their shape is not optimal to focus rays in a single point. Nonetheless, rays which are parallel and close to the optic axis of a spherical lens are approximately focused to a single point, ie. as in a paraboloidal lens.

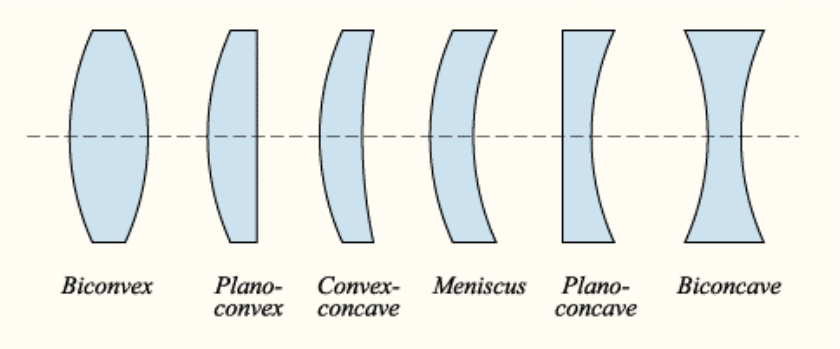

Figure 2: Spherical lenses [79].

In order to obtain a paraboloidal-like behaviour, spherical lenses has to sustain the *paraxial approximation*, which defines that the incoming rays make a small angle with respect to the optic axis, $\sinh(\theta) \approx \theta$. If this approximation holds, the focusing property of a spherical lens is equiparated to the one of a paraboloid lens. So, from now on will be exploited. The aberrations generated by a spherical lens without the paraxial approximation will be addressed later. Spherical lenses can have a planar, a convex or a concave shape, or a mix of them. Their radius of curvature is equal to the radius of the sphere which they partially recreate. The lens's behaviour is defined by the *Lensmaker's equation*:

$$\frac{1}{f} = (n-1)\left[\frac{1}{R_1} - \frac{1}{R_2} + \frac{(n-1)d}{nR_1R_2}\right] \tag{2}$$

where f is the focal length, n the refractive index of the lens's material, d is the

lens's thickness along the lens axis, R_1 and R_2 the radius of curvature of the closer and farther surface to the incoming light, respectively. By definition, the radius of curvature R_1 is positive when it is convex, negative when concave, whereas for the radius of curvature R_2 the opposite. When the thickness $d \ll R_1$ and $d \ll R_2$ then the *thin lens approximation* can be made, and equation 2 becomes:

$$\frac{1}{f} = (n-1)\left[\frac{1}{R_1} - \frac{1}{R_2}\right] \tag{3}$$

Let us define the starting point $P_1 = (z_1, y_1)$ and the arrival point $P_2 = (z_2, y_2)$.

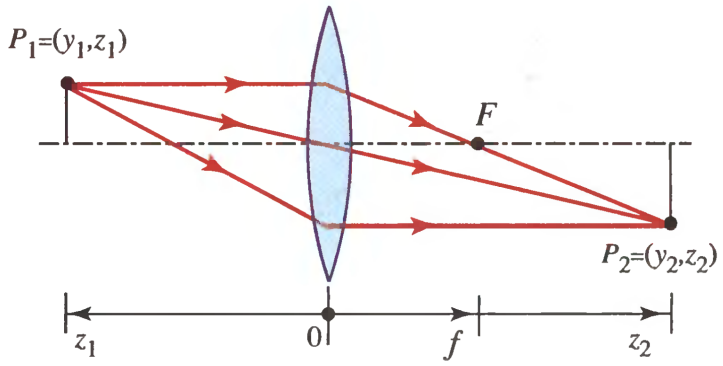

Figure 3: Thin lens [79].

Therefore:

$$\frac{1}{f} = \frac{1}{z_1} + \frac{1}{z_2} \tag{4}$$

when an object is put at a distance equal to the focal length, it is imaged at infinity. The magnification of the object is:

$$M = \frac{y_2}{y_1} = -\frac{z_2}{z_1} = \frac{f}{f - z_1} \tag{5}$$

A set of more than one lens can be taken into account. For two lenses:

$$\frac{1}{f} = \frac{1}{f_1} + \frac{1}{f_2} - \frac{d}{f_1 f_2} \tag{6}$$

where d is the distances between the lenses. If $d = f_1 + f_2$ then they form the simplest type of optical telescope and its magnification is:

$$M = -\frac{f_2}{f_1} \tag{7}$$

This telescope images an object put at infinite before the first lens to infinite after the second lens, with a magnification M. On the other hand, if the object is put at f_1 before the first lens, then the distance d between them is not a variable and the object will be imaged in the focal point of the second lens with magnification M.
Another important optical component is the spherical mirror. As for lenses, the spherical mirror approximates a paraboloid mirror in the paraxial approximation

with a focal length $f = R/2$ where R is the radius of curvature of the spherical mirror.

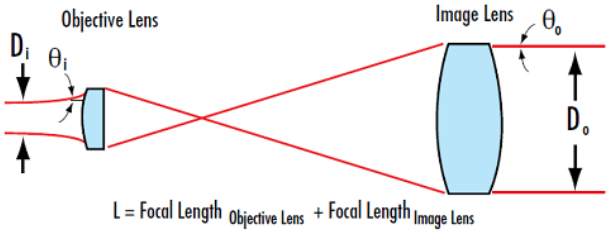

(a) Keplerian Telescope

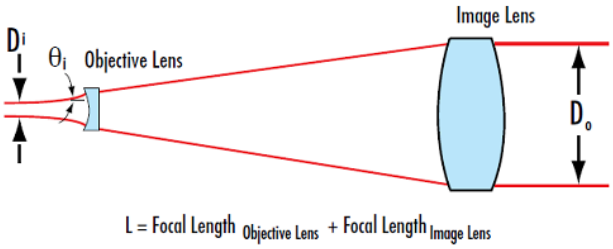

(b) Galileian Telescope

Figure 4: Lenses Telescope [80].

Thus:

$$-\frac{2}{R} = \frac{1}{z_1} + \frac{1}{z_2} \tag{8}$$

which means that an object at infinity is imaged at a distance $z_2 = -R/2$, which is the focal length:

$$f = -\frac{R}{2} \tag{9}$$

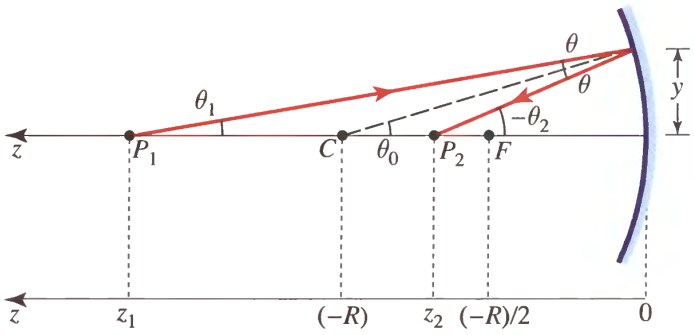

Figure 5: Spherical Mirror [79].

and then equation 8 becomes:

$$\frac{1}{f} = \frac{1}{z_1} + \frac{1}{z_2} \tag{10}$$

which is equal to equation 8. It means that a spherical mirror behaves like a thin lens.
The spherical lenses suffer from aberrations. The most important in our case are:

- **Chromatic Aberration**

  The lens's material has a wavelength dependent refractive index n_ω, i.e. suffers from dispersion. This leads to different focal lengths with respect to wavelength.

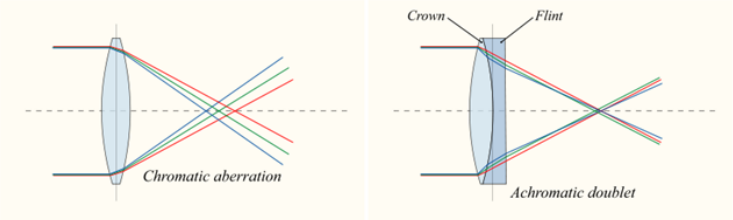

Figure 6: Chromatic Aberration [81].

  This problem is counteracted over a range of wavelengths with an achromat, a set composed by two lenses stuck together and made by materials with different dispersion.

- **Astigmatism**

  It occurs when a perfectly spherical lens is hit by a ray far from the optical axis. In this case, the tangential plane, which is the plane on which the lens lies, sees a reduced focal length; on the other hand the sagittal plane, which is perpendicular to tangential plane, sees an increased focal length. The result is a different focus after the lens for the two planes.

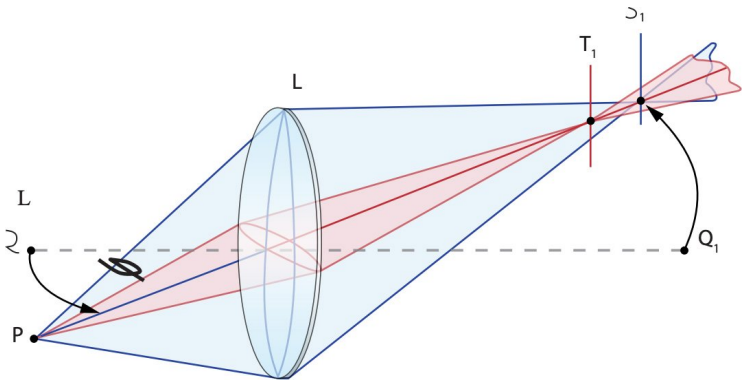

Figure 7: Astigmatism [79].

  Astigmatism may happen also for lenses which do not possess a circular symmetry, which means that the lens's radius of curvature is different in tangential an sagittal plane, which still results in different focal length.

- **Spherical Aberration**

  The paraxial approximation allows to define the behaviour of a spherical lens as a paraboloid lens if the former is hit by rays near the optical axis. If this is not happening, the spherical lens focuses the incoming rays at different point, creating an aberration called spherical.

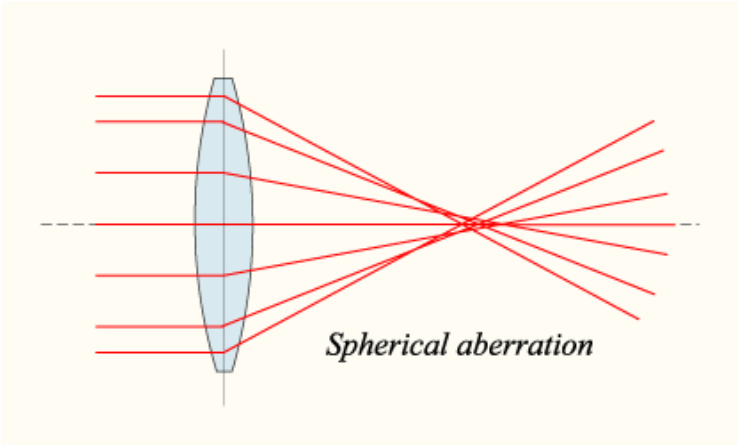

Figure 8: Spherical Aberration [81].

Matrix Optics

Let us now introduce the *Matrix* formalism for geometrical optics. Consider a ray in paraxial approximation which lies in the plane of the optical axis and propagates on it. It can be described by two parameters: the distance with respect to the optical axis y and the angle θ with respect to it.

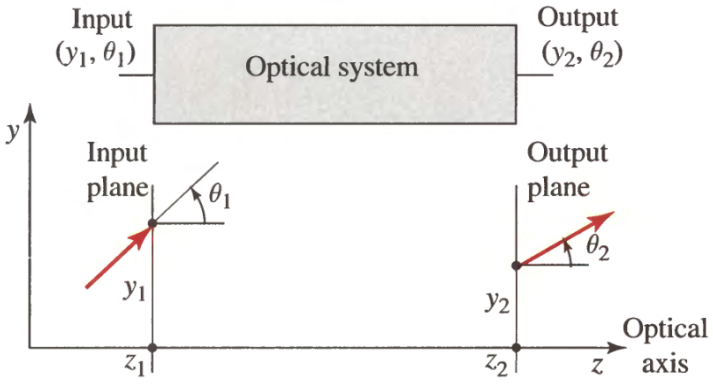

Figure 9: Matrix Optics [82].

Thus, the propagation of the rays in an optical system is defined by two parameters which are the variables of two linear algebraic equations:

$$\begin{cases} y_2 = Ay_1 + B\theta_1 \\ \theta_2 = Cy_1 + D\theta_1 \end{cases} \tag{11}$$

where A, B, C, D are real numbers. They can be described as a 2 by 2 matrix. In matricial form:

$$\begin{bmatrix} y_2 \\ \theta_2 \end{bmatrix} = \begin{bmatrix} A & B \\ C & D \end{bmatrix} \begin{bmatrix} y_1 \\ \theta_1 \end{bmatrix} \tag{12}$$

The ABCD matrix is called *ray-transfer matrix* M and defines the propagation of a ray though an optical component. Let us define the M matrix for simple optical components:

- **Free-Space Propagation**

  Here, the theta angle is unaffected along the d propagation distance, which means that $\theta_2 = \theta_1$ and $y_2 = y_1 + \theta_1 d/n$, thus:

$$M = \begin{bmatrix} 1 & d/n \\ 0 & 1 \end{bmatrix} \tag{13}$$

- **Refraction Through Thin Lens**

  Since the paraxial approximation holds, at lens interface the height of the ray remains the same, and thus $y_2 = y_1$, whereas $\theta_2 = -y_1/f + \theta_1$:

$$M = \begin{bmatrix} 1 & 0 \\ -1/f & 1 \end{bmatrix} \tag{14}$$

- **Reflection from a Planar Mirror**

  The ray position with respect to optical axis is not changed, thus $y_2 = y_1$, moreover the angle remains the same $\theta_2 = \theta_1$, so:

$$M = \begin{bmatrix} 1 & 0 \\ 0 & 1 \end{bmatrix} \tag{15}$$

  which is the identity matrix.

- **Reflection from a Spherical Mirror**

  Following the consideration made previously about a spherical mirror, $f = -R/2$, $y_2 = y_1$, and $\theta_2 = y_1 2/R + \theta_1$:

$$M = \begin{bmatrix} 1 & 0 \\ 2/R & 1 \end{bmatrix} \tag{16}$$

  A mirror with R as radius of curvature behaves as a thin lens with a focal length $f = -R/2$.

- **Cascaded Optical Components**

It is straightforward the creation of optical systems with more than one optical component. In this case, the matrix M which defines the system is the matricial product of the single matrices M_i:

$$M = \prod_{i=N}^{1} M_i \tag{17}$$

The order of the matrix multiplication is inverted with respect to the physical positioning of the components in the system.

Wave Optics

Light can be described by a single scalar wavefunction. Geometrical optics is an approximation of wave optics in which the wavelength tends to zero. Let us recall some properties of light:

$$c_n = \frac{c}{n} \qquad c = \lambda\nu \qquad k = \frac{2\pi}{\lambda} \qquad \omega = 2\pi\nu \tag{18}$$

where n is the medium refractive index, ν is the frequency, ω the angular frequency, k the wavenumber, λ the wavelength. An optical wave, which depends on time t and space $\boldsymbol{r} = (x, y, z)$, can be described by a scalar quantity $U(r, t)$.

$$U(\boldsymbol{r}, t) = A(\boldsymbol{r})e^{j\varphi(\boldsymbol{r})}e^{j2\pi\nu t} = U(\boldsymbol{r})e^{j2\pi\nu t} \tag{19}$$

where $U(\boldsymbol{r}, t)$ is called *complex wavefunction* and the time-independent factor $U(\boldsymbol{r})$ is called *complex amplitude*. The real wavefunction is:

$$u(\boldsymbol{r}, t) = \mathrm{Re}\{U(\boldsymbol{r})e^{j2\pi\nu t}\} = \frac{1}{2}\left[U(\boldsymbol{r})e^{j2\pi\nu t} + U^*(\boldsymbol{r})e^{-j2\pi\nu t}\right] \tag{20}$$

where $U^*(\boldsymbol{r})$ is the complex conjugate. The complex wavefunction is a solution of the so called *wave equation*:

$$\nabla^2 U(\boldsymbol{r}, t) = \frac{1}{c^2}\frac{\partial^2 U(\boldsymbol{r}, t)}{\partial t^2} \tag{21}$$

where $\nabla^2 = \frac{\partial^2 u}{\partial x^2} + \frac{\partial^2}{\partial y^2} + \frac{\partial^2}{\partial z^2}$ is the Laplacian operator, which gives a scalar quantity. The wave equation is linear, and thus it holds the principle of superposition. The complex amplitude must satisfy the *Helmholtz equation*:

$$\nabla^2 U(\boldsymbol{r}) = -k^2 U(\boldsymbol{r}) \tag{22}$$

where k is the wavenumber. The simplest solution of this equation are the *plane wave* and the *spherical wave*.
A plane wave has a complex amplitude:

$$U(\boldsymbol{r}) = Ae^{-j\boldsymbol{k}\cdot\boldsymbol{r}} = Ae^{-j(k_x x + k_y y + k_z z)} \tag{23}$$

where A is the *complex envelope* and $\boldsymbol{k}$ is the *wavevector* such that $\boldsymbol{k} = (k_x, k_y, k_z)$. It is called plane wave because it defines parallel planes which propagate perpendicular

to the wavevector $\boldsymbol{k}$, which also describes the frequency of oscillation. The real wavefunction, if $\boldsymbol{k}$ is taken along z axis, is:

$$u(\boldsymbol{r},t) = |A|\cos(2\pi\nu t - kz + \arg\{A\}) = |A|\cos(2\pi\nu(t - z/c) + \arg\{A\}) \tag{24}$$

In time has a period $T = 1/\nu$ and in space has a period $2\pi k = \lambda$.
Another solution of Helmholtz equation is spherical wave, which has a complex amplitude:

$$U(\boldsymbol{r}) = \frac{A_0}{r}e^{-jkr} \tag{25}$$

where $U(\boldsymbol{r})$ is in spherical coordinates, k is the wavenumber, r is the distance from the origin, and A_0 is a constant. It defines a series of concentric spheres whose distance between each other is $2\pi k = \lambda$.

In the framework of wave optics, the paraxial approximation can be made. If it is supposed that z is the axis of propagation, then the complex amplitude is:

$$U(\boldsymbol{r}) = A(\boldsymbol{r})e^{-jkz} \tag{26}$$

The envelope and its derivative must vary slowly with respect to the axis of propagation z, which means $\Delta A \ll A$ thus:

$$\frac{\partial A}{\partial z} \ll kA \qquad\qquad \frac{\partial^2 A}{\partial z^2} \ll k^2 A \tag{27}$$

Then the Helmholtz equation 22 with the paraxial wave from 25 becomes:

$$\nabla_T^2 A = j2k\frac{\partial A}{\partial z} \tag{28}$$

where $\nabla_T^2 = \frac{\partial^2}{\partial x^2} + \frac{\partial^2}{\partial y^2}$ is the transverse Laplacian operator. The equation 28 is the paraxial Helmholtz equation in the slowly varying envelope approximation (SVEA). From our point of view, the most interesting is the Gaussian beam:

$$U(\boldsymbol{r}) = A(\boldsymbol{r})e^{-jkz} \tag{29}$$

$$A(\boldsymbol{r}) = \frac{A_1}{q(z)}e^{-jk\frac{\rho^2}{2q(z)}} \tag{30}$$

$$q(z) = z + jz_r \tag{31}$$

where $\rho^2 = x^2 + y^2$ defines the radial position, A_1 is a constant, q is the generalized curvature ray, which can be separated in its real an imaginary parts. The imaginary part z_r is called *Rayleigh length*:

$$z_r = \frac{\pi w^2(z)}{\lambda} \tag{32}$$

Thus:

$$\frac{1}{q(z)} = \frac{1}{R(z)} - j\frac{\lambda}{\pi w^2(z)} \tag{33}$$

where $R(z)$ is the wavefront radius of curvature and $W(z)$ is the beam width. The complex amplitude $U(\boldsymbol{r})$ which describes a Gaussian beam is then obtained from equation 29 exploiting equation 33:

$$U(\boldsymbol{r}) = A_0 \frac{w_0}{w(z)} e^{-\frac{\rho^2}{w^2(z)}} e^{-jkz - jk\frac{\rho^2}{2R(z)} + j\zeta} \tag{34}$$

where $A_0 = A_1/jz_r$ and w_0 is the beam with at $z = 0$. The complex amplitude has explicated the amplitude and phase. Moreover each of these components has a relationship with the Rayleigh length z_r. Regarding the beam width $w(z)$:

$$w(z) = w_0 \sqrt{1 + \left(\frac{z}{z_r}\right)^2} \tag{35}$$

which is a fundamental equation in beam propagation. The beam width at $z = z_r$ is equal to $w(z_r) = \sqrt{2}w_0$; when $w(z)$ lies within $-z_r < z < z_r$ it is defined in the Rayleigh range and $w(z) \approx w_0$, which means that the beam remains substantially collimated.

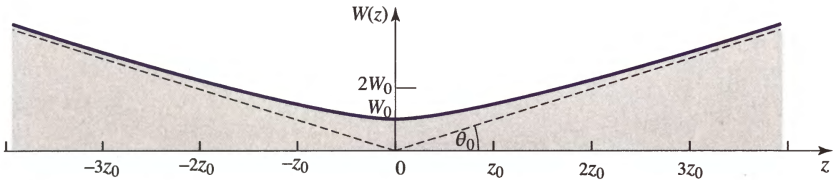

Figure 10: Gaussian beam width [82].

The ray of curvature $R(z)$:

$$R(z) = z\left[1 + \left(\frac{z_r}{z}\right)^2\right] \tag{36}$$

for small values of z, $R(z) \approx \infty$, at Rayleigh length $R(z_r) = 2z_r$.

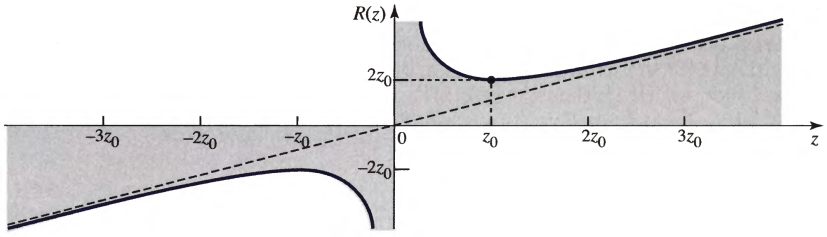

Figure 11: Gaussian ray of curvature [82].

The value $\zeta(z)$ is called *Gouy phase* and describes the phase difference of a Gaussian beam with respect to a plane or a spherical wave:

$$\zeta(z) = \arctan\left(\frac{z}{z_r}\right) \tag{37}$$

At $-\infty$ there is a phase delay of $-\pi/2$ whereas at $+\infty$ a phase delay of $+\pi/2$. The phase of the Gaussian beam is given by:

$$\varphi(\rho, z) = kz - \zeta(z) + \frac{k\rho^2}{2R(z)} \tag{38}$$

where the first term kz is the phase of the plane wave, the second term $\zeta(z)$ is the Gouy phase, and the third term $k\rho^2/2R(z)$ is the off-axis phase.

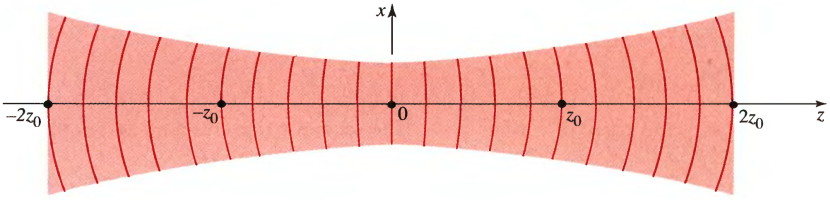

Figure 12: Wavefronts of a Gaussian beam [82].

The beam width w_0 at $z = 0$ is given by:

$$W_0 = \sqrt{\frac{\lambda z_r}{\pi}} \tag{39}$$

which means that a Gaussian beam with a bigger initial beam width has a longer Rayleigh length z_r and thus the beam remains collimated over a longer distance. The beam half-angle divergence θ_0 can be calculated when $z \gg z_r$, then:

$$w(z) \approx w_0 \frac{z}{z_r} = \theta_0 z \tag{40}$$

$$\theta_0 = \frac{w_0}{z_r} = \frac{\lambda}{\pi w_0} \tag{41}$$

The beam full-angle divergence is:

$$2\theta_0 = \frac{4\lambda}{2\pi w_0} \tag{42}$$

The beam divergence can be used to compare a real Gaussian beam to a perfect Gaussian beam. The beam quality M^2 is the ratio between the product of full-angle divergence $2\theta_m$ and the beam diameter $2w_m$ of the real beam with respect to the same product of a perfect Gaussian beam, which is $4\lambda/\pi$:

$$M^2 = \frac{2W_m 2\theta_m}{4\lambda/\pi} = \frac{\theta_m}{\theta_0} \tag{43}$$

In an alternative way it can be seen as the ratio of the half-angle divergence. The M^2 factor will be 1 when the beam is perfectly Gaussian, otherwise it will be higher than 1.

The paraxial Helmholtz equation from 28 has another set of solution of great importance: the Hermite-Gaussian beams. They are interesting because they can

oscillate without alteration in an optical cavity, they are called the *transversal modes* of the resonator. The complex amplitude for a Hermite-Gaussian beam is:

$$U_{l,m}(\boldsymbol{r}) = A_{l,m}\left[\frac{w_0}{w(z)}\right]G_l\left[\frac{\sqrt{2}x}{w(z)}\right]G_m\left[\frac{\sqrt{2}y}{w(z)}\right]e^{-jkz-jk\frac{\rho^2}{2R(z)}+j(l+m+1)\zeta} \tag{44}$$

where l, m are indexes which define the beam, $w(z)$ the beam width, $R(z)$ the radius of curvature, $\zeta(z)$ the Gouy phase, and $A_{l,m}$ is a constant.

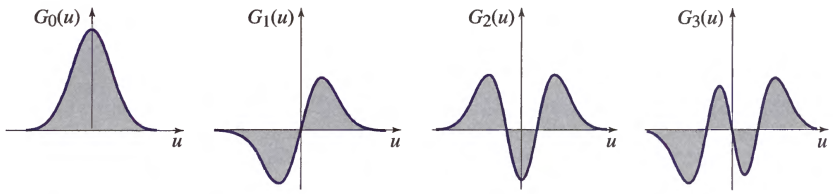

Figure 13: Hermite-Gaussian functions [82].

Moreover the function G of l or m order follows:

$$G_i(u) = H_i(u)e^{-\frac{u^2}{2}} \tag{45}$$

and is called Hermite-Gaussian function of order i, where H_i is the Hermite polinomial of order i. The fundamental mode of the Hermite-Gaussian beam is $l = m = 0$ which gives:

$$U_{0,0}(\boldsymbol{r}) = A_{0,0}\frac{w_0}{w(z)}e^{-\frac{\rho^2}{w^2(z)}}e^{-jkz-jk\frac{\rho^2}{2R(z)}+j\zeta} \tag{46}$$

which is a Gaussian beam.

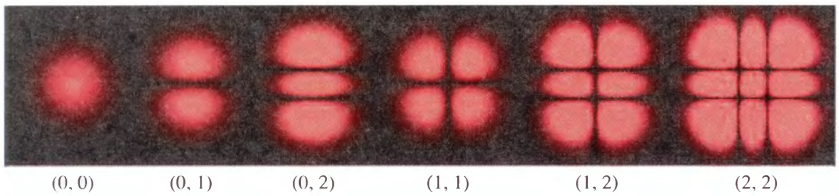

Figure 14: Intensity distribution of Hermite-Gaussian beams [82].

Matrix Optics and Gaussian Beams

The strength of the Matrix Optics introduced before is that a Gaussian beam can be defined by it since it holds the paraxial approximation. Since:

$$R_1 \simeq \frac{y_1}{\theta_1} \qquad R_2 \simeq \frac{y_2}{\theta_2} \tag{47}$$

where R_1 is the incident wavefront ray of curvature and R_2 is the transmitted wavefront ray of curvature, which can also be written as:

$$R_2 = \frac{Ay_1 + B\theta_1}{Cy_1 + D\theta_1} = \frac{AR_1 + B}{CR_1 + D} \tag{48}$$

This relation can be exploited also for the generalized ray of curvature q:

$$q_2 = \frac{Aq_1 + B}{Cq_1 + D} \tag{49}$$

and the same $ABCD$ matrices hold for optical elements, such as the free propagation:

$$M = \begin{bmatrix} 1 & d/n \\ 0 & 1 \end{bmatrix} \tag{50}$$

or the thin lens:

$$M = \begin{bmatrix} 1 & 0 \\ -1/f & 1 \end{bmatrix} \tag{51}$$

or the spherical mirror:

$$M = \begin{bmatrix} 1 & 0 \\ 2/R & 1 \end{bmatrix} \tag{52}$$

As before, the matrix formalism can e applied to the description of a system with more than one optical component. For example, with two optical components:

$$q_2 = \frac{A_1 q_1 + B_1}{C_1 q_1 + D_1} \qquad q_3 = \frac{A_2 q_2 + B_2}{C_2 q_2 + D_2} \tag{53}$$

The matrix which describes the system is the product of the single matrices with inverted order with respect to the related objects on the optical path:

$$M = \begin{bmatrix} A & B \\ C & D \end{bmatrix} = M_2 M_1 \tag{54}$$

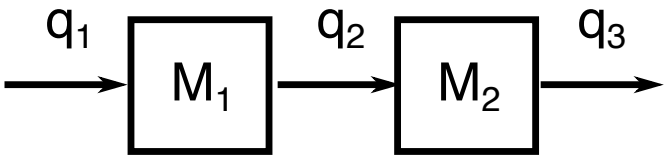

Figure 15: Overall Matrix of Optical Components

+Then the transmitted generalized ray of curvature can be defined with respect to the incident:

$$q_3 = \frac{Aq_1 + B}{Cq_1 + D} \tag{55}$$

This property is of fundamental importance, since it gives the chance to define a complete matrix for an optical resonator. In this case, the complete matrix M is the product of two matrices M_+ and M_-, which defines the forward and backward propagation inside the cavity.

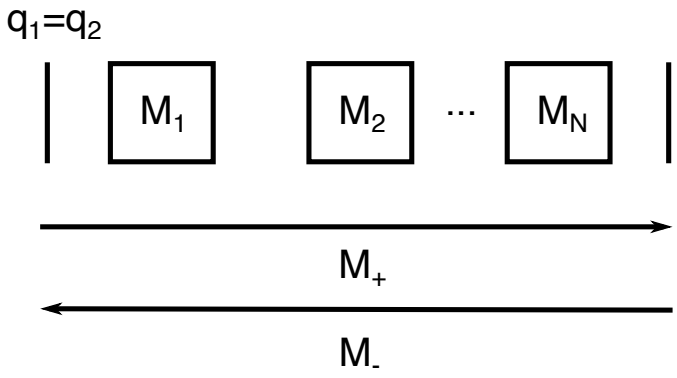

Figure 16: Optical cavity

Their product creates the *round-trip* matrix M:

$$M = \begin{bmatrix} A & B \\ C & D \end{bmatrix} = M_- M_+ \tag{56}$$

where:

$$M_+ = \prod_{i=N}^{1} M_i \qquad M_- = \prod_{i=1}^{N} M_i \tag{57}$$

Moreover the difference between the two matrices is the diagonal, which is interchanged:

$$M_- M_+ = \begin{bmatrix} D_+ & B_+ \\ C_+ & A_+ \end{bmatrix} \begin{bmatrix} A_+ & B_+ \\ C_+ & D_+ \end{bmatrix} \tag{58}$$

Since one of the requirements of an optical resonator is the relationship between the beam before and after a roundtrip, it is possible to write that, at the first mirror:

$$q_1 = q_2 = q \tag{59}$$

where q_2 is the output generalized ray of curvature and q_1 is the input one. This means that:

$$q_2 = \frac{Aq_1 + B}{Cq_1 + D} = \frac{Aq + B}{Cq + D} \tag{60}$$

which lead to the following condition to be satisfied:

$$Cq^2 + (D - A)q - B = 0 \tag{61}$$

This equation defines the conditions to obtain a stable optical resonator. Dividing for $1/q^2$:

$$\frac{B}{q^2} + \frac{(D-A)}{q} + C = 0 \tag{62}$$

thus:

$$\frac{1}{q} = -\frac{(A-D) \pm \sqrt{(A-D)^2 + 4BC}}{2B} = \frac{1}{R} - j\frac{\lambda}{\pi w^2} \tag{63}$$

so:

$$\frac{D-A}{2B} \pm \frac{1}{B}\sqrt{\left(\frac{A+D}{2}\right)^2 - 1} = \frac{1}{R} - j\frac{\lambda}{\pi w^2} \tag{64}$$

The beam waist exists if the argument of the square root is negative, since the imaginary part must be obtained:

$$\frac{\lambda}{\pi w^2} = \frac{1}{|B|}\sqrt{1 - \left(\frac{A+D}{2}\right)^2} \qquad -1 < \frac{A+D}{2} < 1 \tag{65}$$

The stability condition for the optical resonator is:

$$-1 < \frac{A+D}{2} < 1 \tag{66}$$

Appendix B

Pulse Propagation in Dispersive Optical Media

The velocity at which an electromagnetic wave with frequency ν propagates depends on the refractive index of the medium in which the propagation takes place. In the vacuum, the velocity of light is:

$$c = \frac{1}{\sqrt{\epsilon_0 \mu_0}} \tag{67}$$

where c is the velocity of light, whose value is $2.99{\cdot}10^8$ m$\cdot$s^{-1}, ϵ_0 is the electric permittivity in vacuum and μ_0 the magnetic permittivity in vacuum. Their value is $8.85{\cdot}10^{-12}$ with dimensions F$\cdot$m^{-1} for the electric permittivity and $4\pi{\cdot}10^{-7}$ with dimensions T$\cdot$m$\cdot$A^{-1} for the magnetic permittivity. On the other hand, when the wave is in a medium different from vacuum:

$$c_n = \frac{c}{n} = \frac{c}{\sqrt{\epsilon_r \mu_r}} = \frac{1}{\sqrt{\epsilon_r \epsilon_0 \mu_r \mu_0}} \tag{68}$$

where c_n is the velocity of light in the medium whose refractive index is n. The parameter ϵ_r is called relative electric permittivity, whereas μ_r is the relative magnetic permeability, such that:

$$n = \sqrt{\epsilon_r \mu_r} \tag{69}$$

They are a property of every material and they depend on wavelength. Thus, also the refractive index of the medium depends on wavelength. This is a characteristic of fundamental importance for pulse propagation, whose wavelength is not unique. An investigation of the dependence of the light propagation with respect to wavelength is then necessary. The refractive index wavelength dependence can be found experimentally for each material, and it is described by the *Sellmeier's formula*:

$$n(\lambda) = \sqrt{1 + \sum_j \frac{A_j \lambda^2}{\lambda^2 - B_j}} \tag{70}$$

where A_j and B_j are coefficients which have to be found experimentally.
Let us recall some definitions of electromagnetic waves in vacuum:

$$c = \lambda \nu \qquad \omega = 2\pi\nu \qquad k = \frac{2\pi}{\lambda} \tag{71}$$

where λ is the wavelength, ν is the frequency, ω is the angular frequency, k is the wavenumber. For the propagation in a medium:

$$c_n = \frac{\lambda\nu}{n} = \lambda_n\nu \qquad \omega = 2\pi\nu = c_n k \qquad k_n = kn = \frac{2\pi n}{\lambda} = \frac{2\pi}{\lambda_n} \tag{72}$$

and it is possible to define the wavenumber in a medium k_n as:

$$\beta = k_n = kn \tag{73}$$

and call it *propagation constant*. Then it is possible to describe the velocity of light in another way:

$$c = \frac{\omega}{k} \tag{74}$$

It takes also the definition of *phase velocity* because it describes the velocity of the phase of a given frequency through the propagation. This definition is useful when the light is composed by more frequencies such as a pulse. The phase velocity in a medium is then:

$$c_n = \frac{\omega}{k_n} = \frac{\omega}{\beta} \tag{75}$$

The definition 74 is particularly interesting because it allows to describe electromagnetic wave with a given frequency with its velocity c_n.

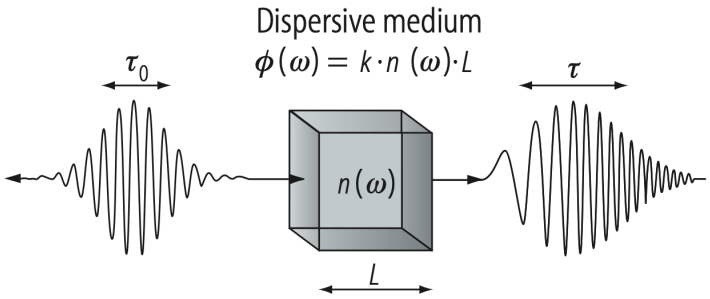

Figure 17: Dispersive Medium [50].

The wavenumber k_n depends on the refractive index, and then it is frequency-dependent. Let us define ω_0 as the central angular frequency of a pulse with bandwidth $\Delta\omega$. Then, the wavenumber k_n can be written as the Taylor expansion:

$$k_n(\omega)\big|_{\omega_0} = k_0 + \frac{\partial k}{\partial \omega}\bigg|_{\omega_0}(\omega-\omega_0) + \frac{1}{2}\frac{\partial^2 k}{\partial \omega^2}\bigg|_{\omega_0}(\omega-\omega_0)^2 + \frac{1}{6}\frac{\partial^3 k}{\partial \omega^3}\bigg|_{\omega_0}(\omega-\omega_0)^3 + \ldots \tag{76}$$

where k_0 is the wavenumber at ω_0 and it is the zero-order dispersion. The second term is the first-order dispersion:

$$\frac{\partial k}{\partial \omega}\bigg|_{\omega_0} = \frac{1}{v_g} \tag{77}$$

is the inverse of what is called *group velocity* and defines the velocity of the pulse envelope. It is the actual velocity of the pulse propagating through the medium of refractive index n. It is also defined as the *group delay per unit length* since it describes a time frame with respect to a length. The third term is the second-order dispersion:

$$\left.\frac{\partial^2 k}{\partial \omega^2}\right|_{\omega_0} = \frac{\partial}{\partial \omega}\frac{\partial k}{\partial \omega} = \frac{\partial}{\partial \omega}\left(\frac{1}{v_g}\right) = k'' = \text{GVD} \tag{78}$$

is called *Group Velocity Dispersion* (GVD) and it is defined by the parameter k''. It describes the dispersion of the group velocity v_g with respect to the angular frequency. Its dimensions are $s^2 \cdot m$. It also defines the *Group Delay Dispersion* (GDD) per unit length. Whereas the GVD gives the relative amount of second-order dispersion, GDD gives the absolute amount, since it is defined over a given distance. The GVD is also called *chromatic dispersion*. The fourth term is the third-order dispersion:

$$\left.\frac{\partial^3 k}{\partial \omega^3}\right|_{\omega_0} = k''' = \text{TOD} \tag{79}$$

and it is just called *Third-Order Dispersion* (TOD) and defined by the parameter k'''. Its dimensions are $s^3 \cdot m$.

Regarding the chromatic dispersion, it is called *normal dispersion* if it is $k'' > 0$. In normal dispersion the group velocity decreases with respect to angular frequency. This means that the phase velocity at a given wavelength it is lower when the wavelength increases. Thus the 'blue' wavelengths will be at the tail of the pulse, whereas the 'red' wavelengths at the leading edge of the pulse. This is the most common behaviour of materials. On the other hand, the chromatic dispersion it is called *anomalous dispersion* if it is $k'' < 0$. In anomalous dispersion the behaviour is the other way around. The group velocity increases with respect to angular frequency, and thus the 'blue' wavelengths will be at the leading edge of the pulse, whereas the 'red' wavelengths at the tail of the pulse. A chromatic dispersion different from zero creates in pulses what are called *chirp*, since the wavelengths travel at different velocities within the pulse.

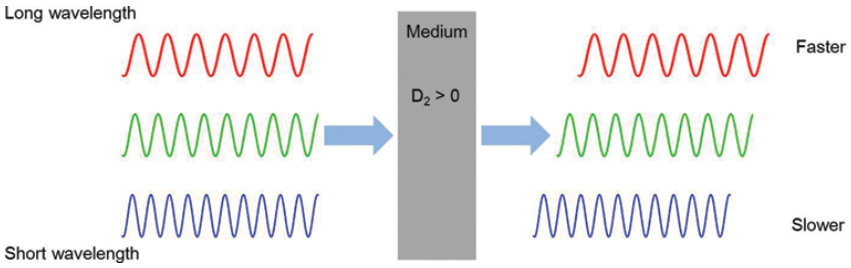

Figure 18: Chromatic Dispersion [83].

The equations just shown can be exploited also with respect to the phase of a given wavelength. The phase offset of a pulse with respect to its central wavelength ω_0,

accumulated over a path of length z is:

$$\phi(\omega)\big|_{\omega_0} = \phi_0 + \frac{\partial\phi}{\partial\omega}\bigg|_{\omega_0}(\omega-\omega_0) + \frac{1}{2}\frac{\partial^2\phi}{\partial\omega^2}\bigg|_{\omega_0}(\omega-\omega_0)^2 + \frac{1}{6}\frac{\partial^3\phi}{\partial\omega^3}\bigg|_{\omega_0}(\omega-\omega_0)^3 + \dots \quad (80)$$

where $\phi_0 = k_n(\omega)z$ is the zero-dispersion phase, whereas:

$$\phi^{'}(\omega_0) = \frac{\partial\phi}{\partial\omega}\bigg|_{\omega_0} = z\frac{\partial k}{\partial\omega}\bigg|_{\omega_0} = \frac{z}{v_g} \quad (81)$$

The same can be applied to the second order:

$$\phi^{''}(\omega_0) = \frac{\partial^2\phi}{\partial\omega^2}\bigg|_{\omega_0} = z\frac{\partial^2 k}{\partial\omega^2}\bigg|_{\omega_0} = \frac{\partial\phi^{'}}{\partial\omega}\bigg|_{\omega_0} \quad (82)$$

The parameter $\phi^{''}(\omega_0)$ is the GVD multiplied by a length, and thus it is the GDD. In fact, it defines the delay with respect to the group velocity.
Let us now describe the propagation of a pulse in a dispersive, linear and transparent media. The shape of the pulse has been set as Gaussian, since it has a very similar behaviour with respect to an hyperbolic secant, but it is much easier to manipulate. Nonetheless, all the results in a qualitative way can be transposed to hyperbolic secant pulses. Thus, the Gaussian electric field is, for an unchirped pulse:

$$\mathcal{E}(t, z=0) = \mathcal{E}_0 \exp\left(-\frac{t^2}{\tau_p^2}\right) \quad (83)$$

where τ_p is initial pulse duration such that $\tau_F = 1.17\tau_p$ is the pulse duration at FWHM, and $\mathcal{E}_0$ is the complex amplitude. Moreover:

$$\Delta\nu\tau_F = 0.441 \quad (84)$$

which means that the Gaussian pulse is Fourier-limited. In order to obtain the temporal evolution of the Gaussian pulse it is convenient to go to the frequency domain, since in this domain the dispersion affects only the phase of the pulse. Thus, the Fourier transform the pulse:

$$\tilde{\mathcal{E}}(w, z=0) = \tilde{\mathcal{E}}_0 \exp\left(-\frac{\omega^2\tau_p^2}{4}\right) \quad (85)$$

where $\tilde{\mathcal{E}}_0 = \mathcal{E}_0\sqrt{\pi}\tau_p$. Then multiply it by the propagation along the dispersive medium. Since a good approximation of the pulse propagation is given by the Taylor expansion until second order:

$$\tilde{\mathcal{E}}(w, z) = \tilde{\mathcal{E}}_0 \exp\left(-\frac{\omega^2\tau_p^2}{4}\right)\exp\left(-j\frac{1}{2}k^{''2}\omega^2 z\right) \quad (86)$$

where the second exponential is given by the GDD in frequency domain. Only dispersion order above the second contribute to pulse temporal broadening. The first-order, which is the group delay, gives the delay of the peak envelope. Then a

Fourier anti-transform is carried out, the time dependent electric field of the Gaussian pulse propagating in a dispersive media is:

$$\mathcal{E}(t,z) = \mathcal{E}_0 \exp\left(-\frac{t^2}{\tau_p^2 + \frac{4k''^2 z^2}{\tau_p^2}}\right) \exp\left(-j\frac{k'' z}{\frac{\tau_p^4}{2} + 2k''^2 z^2} t^2\right) \tag{87}$$

It is clear that the temporal shape of the pulse has been modified by the passage in the dispersive medium, as well as the phase. The pulse duration is, along the z position:

$$\tau_p(z) = \sqrt{\tau_p^2 + \frac{4k''^2 z^2}{\tau_p^2}} \tag{88}$$

and the phase:

$$\phi(t,z) = -\frac{k'' z}{\frac{\tau_p^4}{2} + 2k''^2 z^2} t^2 \tag{89}$$

Then they can be rewritten as:

$$\tau_p(z) = \tau_p \sqrt{1 + \left(\frac{z}{z_d}\right)^2} \tag{90}$$

$$\phi(t,z) = -\left(\frac{t^2}{\tau_p^2}\right) \frac{2z/z_d}{1 + \left(z/z_d\right)^2} \mathrm{sgn}\left(k''\right) \tag{91}$$

$$\frac{\partial^2 \phi(t,z)}{\partial t^2} = -\left(\frac{1}{\tau_p^2}\right) \frac{2z/z_d}{1 + \left(z/z_d\right)^2} \mathrm{sgn}\left(k''\right) \tag{92}$$

where the dispersion length z_d is:

$$z_d = \frac{\tau_p^2}{2|k''|} \tag{93}$$

The temporal evolution of a Gaussian pulse in a dispersive medium has a behaviour similar to the spatial propagation from the beam waist of the Gaussian pulse due to diffraction. The dispersion length z_d is equal to the Rayleigh distance z_r. When $z = z_d$, the pulse duration is increased by $\sqrt{2}$. The dispersion length depends on the GVD of the material, which is the variation of the group velocity with respect to the angular frequency. When it is stronger, the dispersion length is smaller. The equation 92 gives an exact view of the temporal evolution of the phase, where the function sgn gives the sign of the second temporal derivative. The instantaneous angular frequency of the pulse is given by:

$$\omega(t) = \frac{\partial(\omega_0 t - \phi(t,z))}{\partial t} \tag{94}$$

Thus, since the variation of angular frequency can be seen as the temporal variation of the instantaneous phase:

$$\frac{\partial\phi(t,z)}{\partial t} = \Delta\omega \tag{95}$$

Equation 92 can be rewritten with respect to the angular frequency:

$$\frac{\partial\omega}{\partial t} = -\left(\frac{1}{\tau_p^2}\right)\frac{2z/z_d}{1+\left(z/z_d\right)^2}\mathrm{sgn}\left(k''\right) \tag{96}$$

This means that the instantaneous angular frequency has a temporal variation, i.e. there are frequencies which travel with different velocities. This means that when an unchirped Gaussian pulse propagates along a dispersive, linear and transparent media, it broadens in time and a chirp is created. The equation 94 becomes:

$$\omega(t) = \omega_0 + \left(\frac{t}{\tau_p^2}\right)\frac{2z/z_d}{1+\left(z/z_d\right)^2}\mathrm{sgn}\left(k''\right) \tag{97}$$

From this equation is clear that the pulse acquires a chirp which is linear in time, it is positive when $k'' > 0$, so the material has a normal dispersion, it is negative when $k'' < 0$, so the material has an anomalous dispersion.

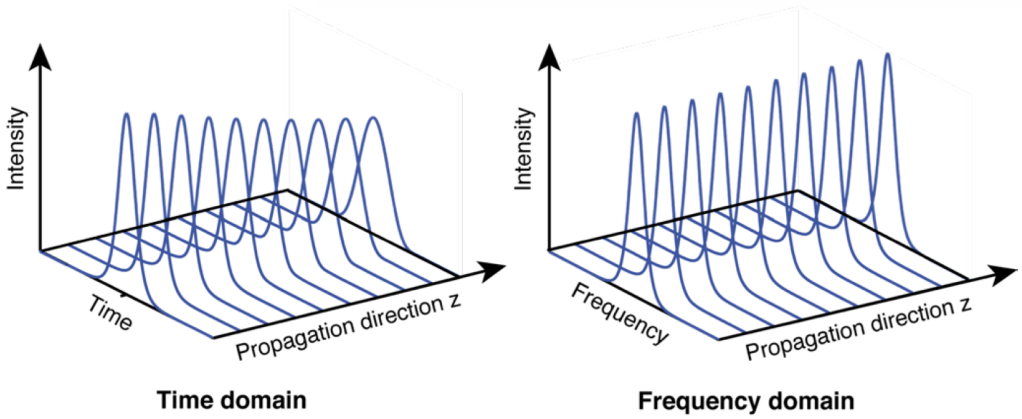

Figure 19: Group Velocity Dispersion on Pulse Propagation [50].

This behaviour is interesting and can be exploited. If the input Gaussian pulse is linearly chirped, it can be written as:

$$\mathcal{E}(t, z=0) = \mathcal{E}_0 \exp\left(1+ja\right)\exp\left(-\frac{t^2}{\tau_p^2}\right)\exp\left(j\phi(t, z=0)\right) \tag{98}$$

The chirp is represented by the parameter a, when a is positive there is a negative (or down) chirp, when a is negative there is a positive (or up) chirp:

$$\frac{\partial\phi}{\partial t} = -2a\frac{t}{\tau_p^2} \tag{99}$$

The chirp adds frequencies to the pulse, which means that it is not Fourier-limited anymore:

$$\Delta\nu\tau_F = 0.441\sqrt{1+a^2} \tag{100}$$

where the BW and τ_F are defined at FWHM. The results from equation 88 and equation 89 become:

$$\tau_p(z) = \sqrt{\frac{4}{x}\Big(x^2 + y^2(z)\Big)} \tag{101}$$

$$\phi(t,z) = -\frac{y(z)}{4\Big(x^2 + y^2(z)\Big)}t^2 \tag{102}$$

where:

$$x = \frac{\tau_p^2}{4(1+a^2)} \qquad y(z) = \frac{a\tau_p^2}{4(1+a^2)} - \frac{1}{2}k^{''}z \tag{103}$$

Then the propagation in the dispersive medium depends on the sign of the chirp and $k^{''}$. If there is a positive chirp (a negative) and a positive $k^{''}$, or there is a negative chirp (a positive) and a negative $k^{''}$, then the pulse broadens in time because the effect of the chirp and chromatic dispersion is the same.

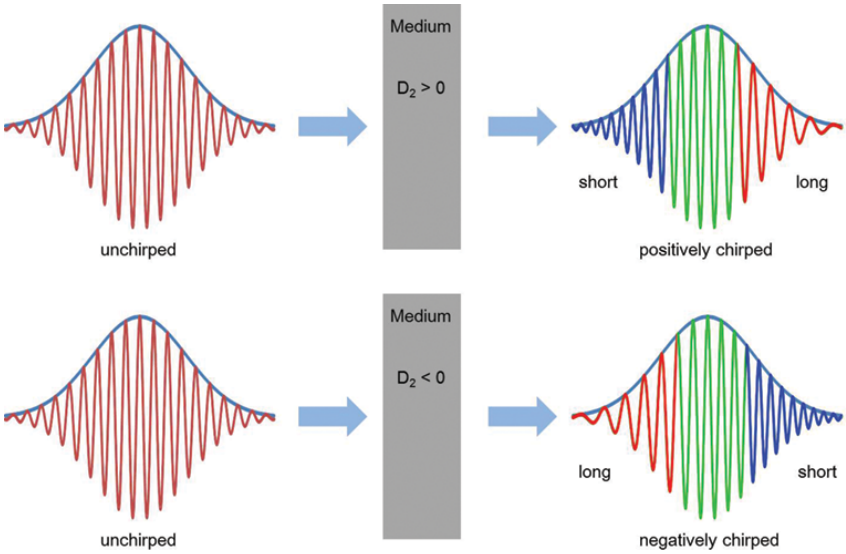

Figure 20: Pulse Chirp [83].

This can be seen from $y(z)$ equation 103 and equation 101. When $y^2(z)$ increases along z, then the pulse broadens along z. On the other hand, when the sign of a and $k^{''}$ is the same, i.e. positive chirp (a negative) and negative $k^{''}$, or negative chirp (a positive) and negative $k^{''}$, then $y^2(z)$ decreases until it becomes zero at a distance:

$$z_d = \frac{a\tau_p^2}{2|k^{''}|(1+a^2)} \tag{104}$$

which is the distance needed to obtain an unchirped Gaussian pulse, bandwidth limited:

$$\tau_p(z_d) = \frac{\tau_p}{\sqrt{1+a^2}} \tag{105}$$

and from equation 100:

$$\Delta\nu\tau_F = 0.441 \tag{106}$$

which describes a Fourier-limited Gaussian pulse. This effect is of fundamental importance, because a chirped pulse contains more frequencies than its counterpart Fourier-limited gaussian pulse, which means that a chirped pulse can be shortened in time through a dispersive media. The creation of a chirped pulsed from an unchirped one can be done through nonlinear processes, such as described in Appendix D.

Appendix C

Pulse Propagation in Nonlinear Optical Media

The propagation in vacuum of an electromagnetic wave is described by the wave equation:

$$\nabla^2 \mathcal{E} = \frac{1}{c^2} \frac{\partial \mathcal{E}}{\partial t} \tag{107}$$

where c is the velocity of light in the vacuum:

$$c = \frac{1}{\sqrt{\mu_0 \epsilon_0}} \tag{108}$$

where μ_0 is the magnetic permeability and ϵ_0 is the electric permittivity. On the other hand, when the electromagnetic wave propagates in a medium, the material modifies the wave behaviour and then the wave equation:

$$\nabla^2 \mathcal{E} = \frac{1}{c_n^2} \frac{\partial^2 \mathcal{E}}{\partial t^2} \tag{109}$$

where c_n is the velocity of the light in the medium:

$$c_n = \frac{c}{n_0(\omega)} \qquad c_n = \frac{1}{\sqrt{\mu \epsilon}} \tag{110}$$

where μ and ϵ are the total permeability and permittivity, whereas $n_0(\omega)$ is the medium's refractive index. They value:

$$\mu = \mu_r \mu_0 \approx \mu_0 \qquad \epsilon = \epsilon_r \epsilon_0 \tag{111}$$

where μ_r and ϵ_r are the relative permeability and permittivity of the material. So, the wave equation is:

$$\nabla^2 \mathcal{E} = \frac{\epsilon_r}{c^2} \frac{\partial^2 \mathcal{E}}{\partial t^2} \qquad n_0(\omega) = \sqrt{\epsilon_r} \tag{112}$$

This is the wave equation for a linear medium. The relative permittivity can be written as:

$$\epsilon_r = 1 + \chi \qquad n_0(\omega) = \sqrt{1 + \chi} \tag{113}$$

where χ is the electric susceptibility of the material, and it is dimensionless. The latter, as well as the refractive index, is wavelength dependent. Thus, the wave equation can be described as:

$$\nabla^2\mathcal{E} = \frac{1}{c^2}\frac{\partial^2\mathcal{E}}{\partial t^2} + \frac{\chi}{c^2}\frac{\partial\mathcal{E}}{\partial t} \tag{114}$$

The electric susceptibiliy describes the degree of polarization of the material with respect to an applied electric field. In fact, the linear scalar polarization of a material is defined as:

$$P = \epsilon_0\chi\mathcal{E} \tag{115}$$

It describes the density of the field-induced dipole moments in the material due to the electromagnetic wave. In a vectorial form, the polarization can be expressed in three dimensions, x, y and z, as well as the electric field $\mathcal{E}$. So, the electric susceptibility χ is defined by 9 components. The linear polarization can be written as:

$$P_i = \epsilon_0\sum_i \chi_{i,j}\mathcal{E}_j \tag{116}$$

where $i, j = x, y, z$. If the applied electric field is intense enough, such as in the case of a light pulse, the scalar polarization can be written as a power series:

$$P = \epsilon_0\chi^{(1)}\mathcal{E} + \epsilon_0\chi^{(2)}\mathcal{E}\mathcal{E} + \epsilon_0\chi^{(3)}\mathcal{E}\mathcal{E}\mathcal{E}\ldots \tag{117}$$

and each $\chi^{(i)}$ has dimensions $\mathrm{m}^{i-1}\cdot\mathrm{V}^{1-i}$. As well as before, exists a vectorial form of the polarization. Since the $\chi^{(2)}$ and $\chi^{(3)}$ describes also the interaction between two and three electric fields, they respectively have 27 and 81 components. Thus:

$$P_i^{(1)} = \epsilon_0\sum_i \chi_{i,j}^{(1)}\mathcal{E}_j \tag{118}$$

$$P_i^{(2)} = \epsilon_0\sum_i \chi_{i,j,k}^{(2)}\mathcal{E}_j\mathcal{E}_k \tag{119}$$

$$P_i^{(3)} = \epsilon_0\sum_i \chi_{i,j,k,l}^{(3)}\mathcal{E}_j\mathcal{E}_k\mathcal{E}_l \tag{120}$$

where $i, j = x, y, z$. Not all the components of the susceptibility are non-zero, and some of them might be equal to each other. Since they are vector based, they depend also on the crystal's structure. For example, a centrosymmetrical crystal does possess a $\chi^{(2)} = 0$, which means that cannot be exploited for second order nonlinear processes. Given these consideration, the wave equation becomes:

$$\nabla^2\mathcal{E} = \frac{1}{c_n^2}\frac{\partial^2\mathcal{E}}{\partial t^2} + \frac{1}{c^2}\frac{\partial}{\partial t}\left(\chi^{(2)}\mathcal{E}\mathcal{E} + \chi^{(3)}\mathcal{E}\mathcal{E}\mathcal{E}\ldots\right) \tag{121}$$

This is the wave equation for a nonlinear medium. The nonlinear susceptibility $\chi^{(2)}$ is responsible of second order nonlinear processes, such as *second harmonic generation* (SHG), *sum frequency generation* (SFG), *difference frequency generation* (DFG). On the other hand $\chi^{(3)}$ is responsible of third order nonlinear processes, such

as *third harmonic generation* (THG) or the *optical Kerr effect*. The latter is the most interesting process for our topic.
Let us focus on third order nonlinear processes. Suppose to have a monochromatic wave:

$$\mathcal{E}(z,t) = \frac{1}{2}\left(\hat{\mathcal{E}}(z)e^{-j\omega_0 t} + c.c.\right) \qquad \hat{\mathcal{E}}(z) = \hat{\mathcal{E}}_0 e^{jkz} e_i \tag{122}$$

where e_i is the unitary vector describing the wave propagation direction and $\hat{\mathcal{E}}_0$ is the complex amplitude. Thus, the scalar third order polarization is:

$$P^{(3)} = \frac{3}{4}\chi^{(3)}|\hat{\mathcal{E}}|^2\mathcal{E} \tag{123}$$

The wave equation, regarding only the $\chi^{(3)}$, can also be written as:

$$\nabla^2\mathcal{E} = \frac{1}{c^2}\frac{\partial\mathcal{E}}{\partial t}\left(n_0^2(\omega) + \chi^{(3)}|\hat{\mathcal{E}}|^2\right) \tag{124}$$

where $n_0(\omega)$ is the linear refractive index of the medium. Then:

$$\nabla^2\mathcal{E} = \frac{(n_0^2(\omega) + \frac{3}{4}\chi^{(3)}|\hat{\mathcal{E}}|^2)}{c^2}\frac{\partial^2\mathcal{E}}{\partial t^2} \tag{125}$$

So the new refractive index is:

$$n^2 = n_0^2(\omega) + \frac{3}{4}\chi^{(3)}|\hat{\mathcal{E}}|^2 \tag{126}$$

Since the term in is small, an approximation can be done, thus:

$$n = n_0(\omega) + \frac{3}{8n_0}\chi^{(3)}|\hat{\mathcal{E}}|^2 = n_0(\omega) + n_2(\omega)I \tag{127}$$

where:

$$I = \frac{1}{2}\epsilon_0 c n_0 |\hat{\mathcal{E}}|^2 \tag{128}$$

and n_2 is the nonlinear refractive index and it is measured in $\mathrm{m}^2\cdot\mathrm{W}$. The nonlinear index worth:

$$n_2(\omega) = \frac{3\chi^{(3)}}{4\epsilon_0 c n_0^2(\omega)} \tag{129}$$

So now the wave equation can be written in a compact form as:

$$\nabla^2\mathcal{E} = \frac{n^2(\omega, I)}{c^2}\frac{\partial^2\mathcal{E}}{\partial t^2} \tag{130}$$

After lengthy passages and after the exploitation of the SVEA approximation, the result is the NSE:

$$j\frac{\partial A_0}{\partial z} = -\gamma|A_0|^2 A_0 + \frac{1}{2}k''\frac{\partial^2 A_0}{\partial t^2} \tag{131}$$

where A_0 is the wave amplitude envelope, $\gamma = \omega n_2/cA_{eff}$ is the nonlinear coefficient, and k'' is the GVD. Let us now describe the $\chi^{(3)}$ effect produced by the optical Kerr effect.

Self Phase Modulation

A gaussian pulse has an intensity profile described as:

$$I(x,y,z,t) = I_p \frac{w_0}{w(z)} e^{-2t^2/\tau_p^2} e^{-\frac{x^2+y^2}{w^2(z)}} e^{j\omega_0 t - jk_0 n(\omega,I) z - jk\frac{x^2+y^2}{2R(z)} + j\zeta} \tag{132}$$

where w_0 is the beam waist, k is the wavenumber, $n(\omega, I)$ is the medium's refractive index, $R(z)$ is the radius of curvature, ζ is the Guoy phase, ω_0 is the angular frequency, τ_p is the pulse duration and z is the propagation axis. The refractive index is intensity dependent:

$$n(\omega, I) = n_0(\omega) + n_2 I(x,y,z,t) \tag{133}$$

and since the wavenumber is refractive index dependent, also the phase it will be. It means that parts of the pulse travel at a different velocity, thus they accumulate a phase difference among each other. Let us focus on the intensity at the peak of the transversal plane and on a given z position. This effect is called Self-Phase Modulation (SPM):

$$\phi_{tot}(t) = \phi_0(t) + \phi_{SPM}(t) = \omega_0 t - n(\omega, I) k_0 z = \omega_0 t - (n_0(\omega) + n_2 I(t)) k_0 z \tag{134}$$

The additional phase is then:

$$\phi_{SPM}(t) = -k_0 n_2 I(t) z \tag{135}$$

where z is the propagation length in the nonlinear medium. The added phase depends on the intensity pulse shape. The term $\delta = k_0 n_2 z$ is called SPM coefficient. Since the intensity gaussian profile is:

$$I(t) = I_p e^{-2t^2/\tau_p^2} \tag{136}$$

The SPM phase is:

$$\phi_{SPM}(t) = -k_0 n_2 I_p e^{-2t^2/\tau_p^2} z \tag{137}$$

Since the temporal variation of the phase is the instantaneous angular frequency:

$$\omega(t) = \frac{\partial \phi_{tot}(t)}{\partial t} = \omega_0 t - k n(\omega, I) z \tag{138}$$

The latter can be described as:

$$\omega(t) = \omega_0 + \frac{2t k_0 n_2 I_p z}{\tau_p^2} e^{-2t^2/\tau_p^2} \tag{139}$$

There are two considerations. The wavelengths in the pulse travel at different velocities depending on the sign of the nonlinear refractive index n_2. When it is positive, $ln_2 > 0$, longer wavelengths 'redder' are at the leading edge of the pulse, and shorter wavelengths 'bluer' at the trailing edge. When it is negative, $n_2 < 0$, longer wavelengths 'redder' are at the trailing edge of the pulse, and shorter wavelengths 'bluer' at the leading edge.

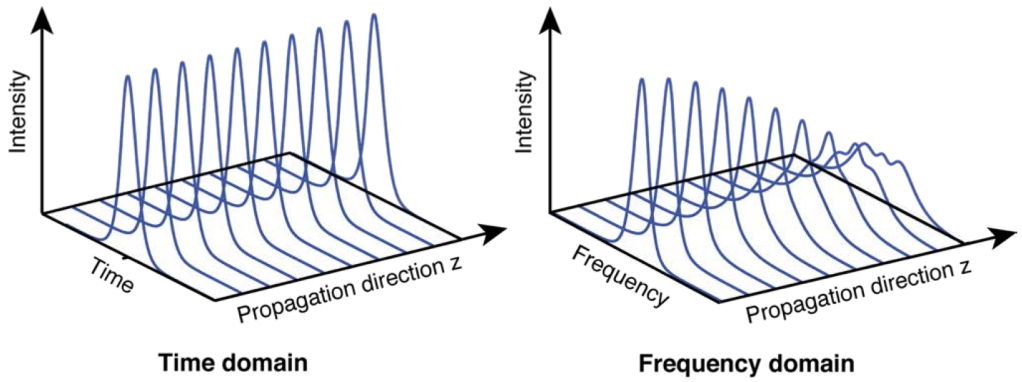

Figure 21: Self Phase Modulation on Pulse Propagation [50].

The pulse has a *chirp*, which means that its instantaneous frequency increases with time, if is called up chirp, or decreases, if it is called down chirp. The chirp obviously depends on the nonlinear refractive index n_2:

$$\omega(t) = \omega_0 + \alpha t \qquad \alpha = \frac{\partial \omega(t)}{\partial t} = \frac{2tk_0 n_2 I_p z}{\tau_p^2} e^{-2t^2/\tau_p^2} \tag{140}$$

The effect of the SPM can be counteracted by a dispersive medium which would create a dispersion with a chirp of the opposite sign.
Moreover, there is a generation of new wavelengths, i.e. the spectrum of the pulse broadens, symmetrically with respect to the central frequency ω_0. In the time domain the pulse shape is not modified.

Self Focusing

Let us suppose to have a gaussian pulse. Then, its transversal intensity is:

$$I(r) = I_p e^{-2\frac{r^2}{w^2}} \tag{141}$$

where I_p is the intensity at the center, so the peak pulse intensity, and $r^2 = x^2 + y^2$ is the radius.
While propagating in a medium, the pulse has a varying refracting index following the known equation:

$$n(\omega, I) = n_0(\omega) + n_2(\omega) I(x, y, z, t) \tag{142}$$

which means that the pulse will experience a different refractive index along the transverse plane of propagation, since the intensity is not constant. The refractive index at the center of the peak is:

$$n_p = n_0(\omega) + n_2(\omega) I_p \tag{143}$$

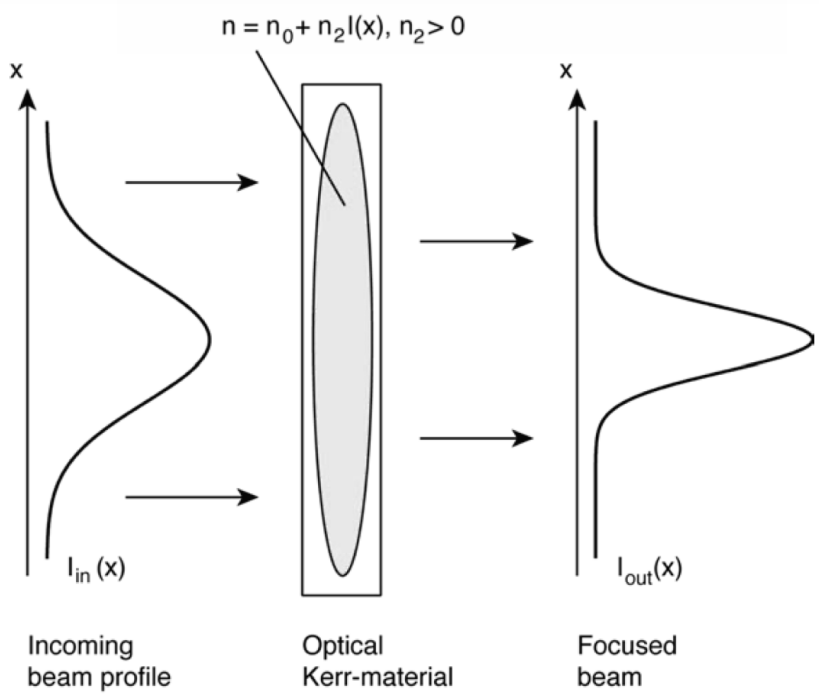

Figure 22: Self Focusing [50].

Near the center of the pulse, where ($r^2 \ll w^2$) the variation of refractive index is:

$$n(r) \approx n_p - 2\Delta n_p \frac{r^2}{w^2} \tag{144}$$

The corresponding added phase along the radial position:

$$\phi_{SPM}(r) = k_0 n_2 I(r) z \approx k_0 n_2 z \left(1 - 2\frac{r^2}{w^2}\right) \tag{145}$$

and then the behaviour of the pulse propagating in the medium is like if it were propagating along a lens with a positive focal length of:

$$f = -\left(\frac{\partial \phi_{SPM}(r)}{\partial r}\right)^{-1} = \frac{w^2}{4\Delta n_p z} \tag{146}$$

where z is the medium's length. This effect is called *Self-focusing*.

Self Steepening

Another phenomena due to optical Kerr effect is the so called *Self steepening*. Since there is a intensity dependent refractive index, and that the group velocity depends on the refractive index:

$$\frac{1}{v_g} = \frac{\partial k_0 n(\omega, I)}{\partial \omega} \tag{147}$$

it means that the pulse in time will travel with a velocity depending on the spatial intensity in the nonlinear medium. If the nonlinear refractive index n_2 is positive, the intensity peak moves towards the trailing edge, it it is negative it moves towards the leading edge. So, let us focus on the center of the pulse:

$$\frac{1}{v_g} = \frac{\partial k_0 n_0}{\partial \omega} + \frac{\partial k_0 n_2 I(t)}{\partial \omega} \tag{148}$$

where:

$$I(t) = I_p e^{-2t^2/\tau_p^2} \tag{149}$$

So the temporal variation of the group velocity is:

$$\frac{\partial v_g}{\partial t} = \frac{\partial \omega}{\partial k_0} \frac{\partial}{\partial t} \left(\frac{1}{n_2 I(t)} \right) \tag{150}$$

The result is a pulse peak which shifts towards the edges depending on the sign of the nonlinear index.

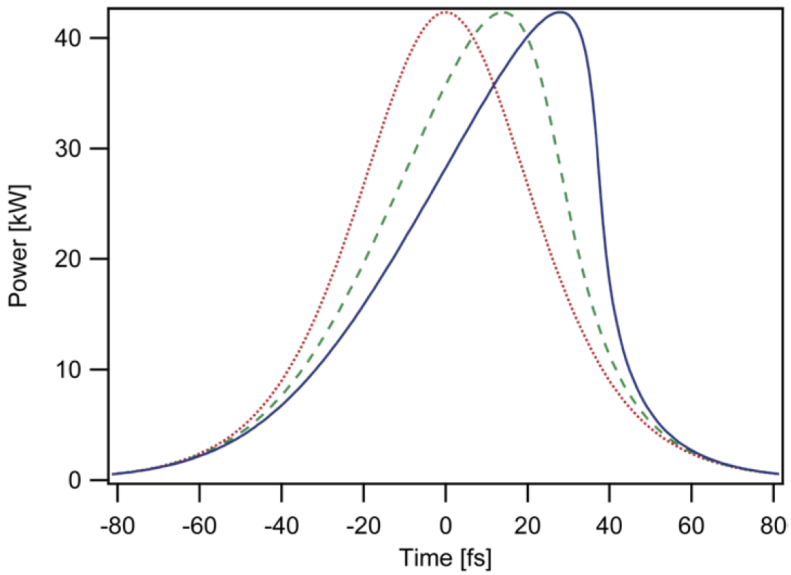

Figure 23: Self Steepening [50].

Publication List

Parts of this thesis are published in the following journal papers and conference proceedings:

1. Federico Pirzio, Shu Jun, Simone Tacchini, Alberto Di Lieto, Giuliano Piccinno, Mauro Tonelli, and Antonio Agnesi, "Multi-watt amplification in a birefringent Yb:$LiLuF_4$ single crystal fiber grown by micro-pulling-down", Opt. Lett. 44, 4095-4098 (2019)

2. Philipp Hildenstein, Alexander Sahm, David Feise, Martin Gorjan, Simone Tacchini, Katrin Paschke, Günther Tränkle, "High-power, high-beam quality miniaturized laser module for pumping of solid state lasers at 980 nm", Conference Paper, Photonic West (2020)

Bibliography

[1] E. Caracciolo. *Femtosecond regenerative amplifier systems with high power and high energy.* Phd thesis, Università degli Studi di Pavia, 2015.

[2] J. Saikawa, Y. Sato, T. Taira, and A. Ikesue. Absorption, emission spectrum properties, and efficient laser performances of Yb:$Y_3ScAl_4O_{12}$ ceramics. *Applied Physics Letters*, 85(11):1898–1900, 2004.

[3] F. Druon, S. Ricaud, D. N. Papadopoulos, A. Pellegrina, P. Camy, J. L. Doualan, R. Moncorgé, A. Courjaud, E. Mottay, and P. Georges. On Yb:CaF_2 and Yb:SrF_2: review of spectroscopic and thermal properties and their impact on femtosecond and high power laser performance . *Opt. Mater. Express*, 1(3):489–502, 2011.

[4] H. Lin, F. Pirzio, A. Volpi, G. Cittadino, A. Di Lieto, M. Tonelli, and A. Agnesi. Crystal growth, spectroscopic characterization, and sub-100 femtosecond mode-locked operation of a Yb:$LiLuF_4$ laser. *J. Opt. Soc. Am. B*, 33(11):2350–2356, 2016.

[5] A. S. Yasyukevich, A. V. Mandrik, N. V. Kuleshov, E. Yu. Gordeev, S. L. Korableva, A. K. Naumov, V. V. Semashko, and P. A. Popov. Spectral kinetic properties of Yb^{3+}:$Na_4Y_6F_{22}$ and Yb^{3+}:$LiLuF_4$ crystals. *Journal of Applied Spectroscopy*, 74(6):844, 2007.

[6] G. Huber, C. Kränkel, and K. Petermann. Solid-state lasers: status and future. *J. Opt. Soc. Am. B*, 27(11):B93–B105, 2010.

[7] P. Hildenstein, A. Sahm, D. Feise, M. Gorjan, S. Tacchini, K. Paschke, and G. Tränkle. High-power, high-beam quality miniaturized laser module for pumping of solid state lasers at 980 nm. 2020.

[8] F. Pirzio, S. Jun, S. Tacchini, A. Di Lieto, G. Piccinno, M. Tonelli, and A. Agnesi. Multi-watt amplification in a birefringent Yb:$LiLuF_4$ single crystal fiber grown by micro-pulling-down. *Opt. Lett.*, 44(17):4095–4098, 2019.

[9] A. L. Schawlow and C. H. Townes. Infrared and optical masers. *Phys. Rev.*, 112:1940–1949, 1958.

[10] J. Hecht. Short history of laser development. *Optical Engineering*, 49(9):1–23, 2010.

[11] T.H. Maiman. Stimulated optical radiation in ruby. *Nature*, 187:493–494, 1960.

[12] B. Ajay and S. Klepper. Submarkets, Industry Dynamics, and the Evolution of the U.S. Laser Industry. 2008.

[13] R. J. Keyes and T. M. Quist. Injection luminescent pumping of CaF_2U^{3+} with GaAs diode lasers. *Applied Physics Letters*, 4(3):50–52, 1964.

[14] P. Moulton. Ti-doped sapphire: tunable solid-state laser. *Optics News*, 8(6):9–9, 1982.

[15] N. Sarukura, Y. Ishida, H. Nakano, and Y. Yamamoto. CW passive mode locking of a Ti:sapphire laser. *Applied Physics Letters*, 56(9):814–815, 1990.

[16] D. E. Spence, P. N. Kean, and W. Sibbett. 60-fsec pulse generation from a self-mode-locked Ti:sapphire laser. *Opt. Lett.*, 16(1):42–44, 1991.

[17] U. Keller. Ultrafast all-solid-state laser technology. *Applied Physics B*, 58(5):347–363, 1994.

[18] U. Keller, K. J. Weingarten, F. X. Kartner, D. Kopf, B. Braun, I. D. Jung, R. Fluck, C. Honninger, N. Matuschek, and J. Aus der Au. Semiconductor saturable absorber mirrors (SESAM's) for femtosecond to nanosecond pulse generation in solid-state lasers. *IEEE Journal of Selected Topics in Quantum Electronics*, 2(3):435–453, 1996.

[19] W. F. Krupke. Ytterbium solid-state lasers. the first decade. *IEEE Journal of Selected Topics in Quantum Electronics*, 6(6):1287–1296, 2000.

[20] C. Hönninger, R. Paschotta, M. Graf, F. Morier-Genoud, G. Zhang, M. Moser, S. Biswal, J. Nees, A. Braun, G. A. Mourou, I. Johannsen, A. Giesen, W. Seeber, and U. Keller. Ultrafast ytterbium-doped bulk lasers and laser amplifiers. *Applied Physics B*, 69(1):3–17, 1999.

[21] Inc. Spectra-Physics. https://www.spectra-physics.com/f/spirit-femtosecond-laser, 2020.

[22] D. Strickland and G. Mourou. Compression of amplified chirped optical pulses. *Optics Communications*, 56(3):219–221, 1985.

[23] BBC Research. Ultrafast lasers: Technologies and global markets. https://www.bccresearch.com/market-research/photonics/ultrafast-lasers-technologies-global-markets.html, 2018.

[24] T. Gunaratne and B. Clark. Ultrashort pulse laser micromachining: History and future opportunities, industrial lasers solutions for manufacturing. 2014.

[25] J. Cheng, C. Liu, S. Shang, D. Liu, W. Perrie, G. Dearden, and K. Watkins. A review of ultrafast laser materials micromachining. *Optics and Laser Technology*, 46:88–102, 2013.

[26] K. Sugioka and Y. Cheng. Ultrafast lasers - reliable tools for advanced materials processing. *Light: Science & Applications*, 3(4):e149–e149, 2014.

[27] J.C. Diels and R. Wolfgang. *Ultrashort Laser Pulse Phenomena (Second Edition)*, pages 457–489. Academic Press, 2006.

[28] Laser Spectroscopy Lab. https://www.chem.uci.edu/~dmitryf/Equipment/curiousmolly.html, 2020.

[29] K. H. Leitz, B. Redlingshöfer, Y. Reg, A. Otto, and M. Schmidt. Metal ablation with short and ultrashort laser pulses. *Physics Procedia*, 12:230–238, 2011.

[30] C. Momma, S. Nolte, B. N. Chichkov, F. V. Alvensleben, and A. Tünnermann. Precise laser ablation with femtosecond pulses. In *Conference on Lasers and Electro-Optics*. Optical Society of America, 1997.

[31] R. Srinivasan, Bodil Braren, and Kelly G. Casey. Nature of "incubation pulses" in the ultraviolet laser ablation of polymethyl methacrylate. *Journal of Applied Physics*, 68(4):1842–1847, 1990.

[32] S. Küper and M. Stuke. Femtosecond uv excimer laser ablation. *Applied Physics B*, 44(4):199–204, 1987.

[33] D. Breitling, Sergey Klimentov, and F. Dausinger. *Femtosecond Technology for Technical and Medical Applications*. Springer, 2004.

[34] DS Choy. History of lasers in medicine. *The Thoracic and cardiovascular surgeon*, 36 Suppl 2:114—117, 1988.

[35] F. P. Campbell. Retinal Vein Occlusion: An Experimental Study. *Archives of Ophthalmology*, 65(1):2–10, 1961.

[36] L. Goldman and R. A. Schwartz. *Current Developments in Laser Surgery for Skin Cancer*. Springer New York, 1988.

[37] P. E. McGuff, D. Bushnell, H. S. Soroff, and R. A. Deterling, Jr. Studies of the surgical applications of laser (light amplification by stimulated emission of radiation). *Surg. Forum*, 143-5(14), 1963.

[38] A. Fermann, M. E.and Galvanauskas and G. Sucha. *Ultrafast Lasers - Technology and Applications*. CRC Press, 2003.

[39] D. Huang, E. A. Swanson, C. P. Lin, J. S. Schuman, W. G. Stinson, W. Chang, M. R. Hee, T. Flotte, K. Gregory, C. A. Puliafito, and et al. Optical coherence tomography. *Science (New York, N.Y.)*, 254(5035):1178–1181, 1991.

[40] G. Franssen, H. Schleijpen, J. Heuvel, H. Buersing, B. Eberle, and D Walter. Femtosecond lasers for countermeasure applications. *Proceedings of SPIE - The International Society for Optical Engineering*, 7483, 2009.

[41] Leonardo Company. https://www.leonardocompany.com/en/products/miysis-dircm-3, 2020.

[42] X. Briottet, Y. Boucher, A. Dimmeler, A. Malaplate, A. Cini, M. Diani, H. Bekman, P. Schwering, T. Skauli, I. Kasen, I. Renhorn, L. Klasén, M. Gilmore, and D. Oxford. Military applications of hyperspectral imagery. In *Targets and Backgrounds XII: Characterization and Representation*, volume 6239, pages 82 – 89. SPIE, 2006.

[43] A. Braun, X. Liu, G. Mourou, D. Kopf, and U. Keller. Diode-pumped Nd:glass kilohertz regenerative amplifier for subpicosecond microjoule level pulses. *Appl. Opt.*, (18):4163–4167, 1997.

[44] O. Svelto. *Principles of Lasers*. Springer US, 2010.

[45] Anthony E. Siegman. *Lasers*. University Science Books, 1986.

[46] G. Zhu, X. Zhu, Y. Huang, H. Wang, and C. Zhu. Numerical analysis of an end-pumped Yb:YAG thin disk laser with variation of a fractional thermal load. *Appl. Opt.*, 53(19):4349–4358, 2014.

[47] F. Kärtner. Ultrafast Optics. https://ocw.mit.edu, 2015.

[48] Optique Ingenieur. http://www.optique-ingenieur.org/en/courses/OPI_ang_M01_C03/co/Contenu_05.html, 2020.

[49] M. Hercher. An analysis of saturable absorbers. *Appl. Opt.*, 6(5):947–954, 1967.

[50] U. Keller. *Landolt Börnstein, Group VIII, Laser Physics and Applications. Subvolume B: Laser Systems*. Springer Verlag, 2007.

[51] F. X. Kartner, J. A. der Au, and U. Keller. Mode-locking with slow and fast saturable absorbers-what's the difference? *IEEE Journal of Selected Topics in Quantum Electronics*, 4(2):159–168, 1998.

[52] U. Keller and L. Gallmann. Ultrafast Laser Physics. https://ulp.ethz.ch/education/lectures/ultrafast-laser-physics.html, 2020.

[53] F. X. Kartner, I. D. Jung, and U. Keller. Soliton mode-locking with saturable absorbers. *IEEE Journal of Selected Topics in Quantum Electronics*, 2(3):540–556, 1996.

[54] C. Hönninger, R. Paschotta, F. Morier-Genoud, M. Moser, and U. Keller. Q-switching stability limits of continuous-wave passive mode locking. *J. Opt. Soc. Am. B*, 16(1):46–56, 1999.

[55] L. M. Frantz and J. S. Nodvik. Theory of Pulse Propagation in a Laser Amplifier. *Journal of Applied Physics*, 34(8):2346–2349, 1963.

[56] P. Kroetz, A. Ruehl, K. Murari, H. Cankaya, F. X. Kärtner, I. Hartl, and R.J.D. Miller. Numerical study of spectral shaping in high energy Ho:YLF amplifiers. *Opt. Express*, 24(9):9905–9921, 2016.

[57] RP Photonics. https://www.rp-photonics.com/thermal_lensing.html, 2020.

[58] S. Chénais, F. Druon, S. Forget, F. Balembois, and P. Georges. On thermal effects in solid-state lasers: The case of ytterbium-doped materials. *Progress in Quantum Electronics*, 30(4):89 – 153, 2006.

[59] W. Koechner. *Solid-State Laser Engineering*. Springer Verlag New York, 2006.

[60] T. Y. Fan. Heat generation in Nd:YAG and Yb:YAG. *IEEE Journal of Quantum Electronics*, 29(6):1457–1459, 1993.

[61] R. Gaumé, B. Viana, D. Vivien, J. P. Roger, and D. Fournier. A simple model for the prediction of thermal conductivity in pure and doped insulating crystals. *Applied Physics Letters*, 83(7):1355–1357, 2003.

[62] P. Klopp, V. Petrov, U. Griebner, and G. Erbert. Passively mode-locked Yb:KYW laser pumped by a tapered diode laser. *Opt. Express*, 10(2):108–113, 2002.

[63] A. A. Kaminskii, P. V. Klevtsov, L. Li, and A. A. Pavlyuk. Stimulated emission from ky$(wo_4)_2$: Nd^{3+} crystal laser. *physica status solidi (a)*, 5(2):K79–K81, 1971.

[64] N. V. Kuleshov, A. A. Lagatsky, V. G. Shcherbitsky, V. P. Mikhailov, E. Heumann, T. Jensen, A. Diening, and G. Huber. CW laser performance of Yb and Er,Yb doped tungstates. *Applied Physics B*, 64(4):409–413, 1997.

[65] P. A. Loiko, K. V. Yumashev, N. V. Kuleshov, and A. A. Pavlyuk. Thermo-optical properties of pure and Yb-doped monoclinic $KY(WO_4)_2$ crystals. *Applied Physics B*, 106(3):663–668, 2012.

[66] P. Lacovara, H. K. Choi, C. A. Wang, R. L. Aggarwal, and T. Y. Fan. Room-temperature diode-pumped Yb:YAG laser. *Opt. Lett.*, 16(14):1089–1091, 1991.

[67] M. Siebold, S. Bock, U. Schramm, B. Xu, J. L. Doualan, P. Camy, and R. Moncorgé. Yb:CaF_2 a new old laser crystal. *Applied Physics B*, 97(2):327–338, 2009.

[68] A. Bensalah, Y. Guyot, A. Brenier, H. Sato, T. Fukuda, and G. Boulon. Spectroscopic properties of Yb^{3+}: $LuLiF_4$ crystal grown by the Czochralski method for laser applications and evaluation of quenching processes: a comparison with Yb^{3+}: $YLiF_4$. *Journal of Alloys and Compounds*, 380(1):15–26, 2004.

[69] Efficient and stable pulsed laser operation of Ce:$LiLuF_4$ around 308 nm. *Optics Communications*, 146(1).

[70] D. Kopf, G. J. Spühler, K. J. Weingarten, and U. Keller. Mode-locked laser cavities with a single prism for dispersion compensation. *Appl. Opt.*, 35(6):912–915, 1996.

[71] F. Lesparre, J. T. Gomes, X. Délen, I. Martial, J. Didierjean, W. Pallmann, B. Resan, M. Eckerle, T. Graf, M. A. Ahmed, F. Druon, F. Balembois, and P. Georges. High-power Yb:YAG single-crystal fiber amplifiers for femtosecond lasers in cylindrical polarization. *Opt. Lett.*, 40(11):2517–2520, 2015.

[72] T. Fukuda and V. I. Chani. *Shaped Crystals: Growth by Micro-Pulling-Down Technique*. Springer Verlag Berlin Heidelberg, 2007.

[73] J. Koerner, C. Vorholt, H. Liebetrau, M. Kahle, D. Kloepfel, R. Seifert, J. Hein, and M. C. Kaluza. Measurement of temperature-dependent absorption and emission spectra of Yb:YAG, Yb:LuAG, and Yb:CaF_2 between 20 °C and 200 °C and predictions on their influence on laser performance. *J. Opt. Soc. Am. B*, 29(9):2493–2502, 2012.

[74] R. L. Aggarwal, D. J. Ripin, J. R. Ochoa, and T. Y. Fan. Measurement of thermo-optic properties of $Y_3Al_5O_{12}$, $Lu_3Al_5O_12$, $YAIO_3$, $LiYF_4$, $LiLuF_4$, BaY_2F_8, $KGd(WO_4)_2$, and $KY(WO_4)_2$ laser crystals in the 80–300K temperature range. *Journal of Applied Physics*, 98(10):103514, 2005.

[75] W A Clarkson. Thermal effects and their mitigation in end-pumped solid-state lasers. *Journal of Physics D: Applied Physics*, 34(16):2381–2395, 2001.

[76] C. Fiebig, G. Blume, M. Uebernickel, D. Feise, C. Kaspari, K. Paschke, J. Fricke, H. Wenzel, and G. Erbert. High-Power DBR-Tapered Laser at 980 nm for Single-Path Second Harmonic Generation. *IEEE Journal of Selected Topics in Quantum Electronics*, 15(3):978–983, 2009.

[77] C. Fiebig, S. Pekarek, K. Paschke, M. Fischer, T. Südmeyer, U. Keller, and G. Erbert. High-brightness distributed-Bragg-reflector tapered diode lasers: pushing your application to the next level. *Proceedings of SPIE - The International Society for Optical Engineering*, 7918, 2011.

[78] K. Paschke, G. Blume, O. Brox, F. Bugge, J. Fricke, D. Feise, J. Hofmann, H. Wenzel, and G. Erbert. Watt-level continuous-wave diode lasers at 1180 nm with high spectral brightness. *Proceedings of SPIE - The International Society for Optical Engineering*, 9348:93480X–1, 2015.

[79] *Fundamentals of Photonics*, chapter 1, pages 1–40. John Wiley and Sons, Ltd, 1991.

[80] Edmund Optics. Laser beam Expanders. https://www.edmundoptics.de/knowledge-center/application-notes/lasers/beam-expanders/, 2020.

[81] Wikipedia. Achromatic Lenses. https://en.wikipedia.org/wiki/Achromatic_lens, 2020.

[82] *Fundamentals of Photonics*, chapter 2, pages 41–79. John Wiley and Sons, Ltd, 1991.

[83] IntechOpen. Generation of High-Intensity Laser Pulses and their Applications, High Energy and Short Pulse Lasers. https://www.intechopen.com/books/high-energy-and-short-pulse-lasers/generation-of-high-intensity-laser-pulses-and-their-applications, 2016.